24/4-2055

05/7/95 ~~P2 20.49~~ 4:49.

06/7/95. 16.55

418
16.55

THE IMPACT TOUGHNESS OF IRON MANGANESE ALLOYS

by

MICHAEL D. BRAMHALL BSc.(HONS) MET.

A THESIS SUBMITTED TO THE COUNCIL FOR NATIONAL ACADEMIC AWARDS IN PARTIAL FULFILMENT OF THE REQUIREMENTS FOR THE DEGREE OF DOCTOR OF PHILOSOPHY

Collaborating Establishment: British Steel Corporation
Swinden Laboratories,
Rotherham

Sponsoring Establishment: Department of Metals and Materials Engineering,
Sheffield City Polytechnic

DATE: MARCH 1989

PREFACE

This thesis is submitted to the Council for National Academic Awards for the degree of Doctor of Philosophy.

The research was carried out during the period October 1983 to September 1986 at the Department of Metals and Materials Engineering, Sheffield City Polytechnic.

A Post-graduate course was attended at the Sheffield City Polytechnic during the above period in Computer Programming and Numerical Analysis. The Author has attended a conference on 'Optical and Electron Microscopy' held at Sheffield University in September 1984,and a conference on 'Bainite' held at The Institute of Metals,London,April 1985.

The author would like to express his appreciation to BSC Swinden Laboratories for carrying out comparative Dilatometry and X-ray diffraction work, and to Rotherham Engineering Steels for supplying the 9%Ni and 5%Ni steels.

Also, grateful acknowledgement is made to Dr.D.Dulieu, industrial supervisor,for numerous helpful discussions.

Thanks also to Dr.S.Thorpe ,formerly of Applied Physics, Sheffield City Polytechnic,for carrying out the Mossbauer work.

Many thanks to the technicians,administrative staff and lecturing staff of the Department of Metals and Materials Engineering for their help and support.Thanks also to Professor A.W.D.Hills for his support.

Grateful thanks are sincerely expressed to Dr.E.A.Wilson for his interest,guidance and constant encouragement throughout the course of this work.

Thanks are also expressed to Gillian Simmonite for patiently typing the majority of this thesis.

Finally, I would like to pay tribute to my wife,Bridget, for her patience,support and constant encouragement.

The results obtained and the theories developed are,to the best of my knowledge, original except where reference is made to the work of others. No part of this thesis has been submitted for a degree at any other university or college.

M.D.Bramhall.

M.D.BRAMHALL
March 1989

Dept. of Metals & Materials Engineering
Sheffield City Polytechnic

THE IMPACT TOUGHNESS OF IRON -MANGANESE ALLOYS

by

Michael D. Bramhall

Synopsis

Fe-8Mn alloys may form the basis of a cryogenic steel similar to Fe-9Ni steels,but at a cost much more economical as manganese is cheaper than nickel.However,Fe-Mn alloys are susceptible to temper embrittlement through segregation of Mn,N and P to prior austenite grain boundaries.

The present investigation shows that impact toughness can be improved by tempering to produce small amounts of reverted austenite into the structure.

In quantifying the percentages of reverted austenite in these structures, X-ray and Mössbauer studies have shown that the phase analysis of these alloys varies from the surface of specimens into the bulk,and is thought to be due to deformation induced transformation of $\gamma \rightarrow \varepsilon$ during sample preparation.It was concluded that bulk austenite and epsilon concentrations are best obtained after 2 minutes electro--polishing.

Additions of 0.1%Ti and 0.1%Al to 'pure' alloys,in order to getter nitrogen,have been found to improve impact properties by reducing intergranular embrittlement.These additions also lead to a 'massive ferrite' structure not previously found in alloys of this manganese level. This is thought to be due to the lower interstitial levels in solid solution favouring formation of massive ferrite rather than lath martensite at a higher cooling rate and lower transformation temperature.

A further considerable improvement in toughness has been achieved by water quenching rather than air cooling from the austenitisation temparature. Auger electron spectroscopy studies have shown that air cooling results in segregation of phosphorus and nitrogen to prior austenite grain boundaries. An addition of 0.5%Mo to these alloys was found not to be completely effective in reducing intergranular embrittlement.

Commercially 'impure' alloys were found to exhibit inferior impact properties compared to 'pure' alloys. A further comp--arison with 9% nickel and 5% nickel steels has shown that pure Fe-8Mn alloys could be used as a low temperature steel down to ~ -100°C.

A'novel' heat treatment to an Fe-8Mn-0.2V alloy,consisting of a solution treatment followed by low temperature ageing has shown that vanadium carbide precipitation produces a significant reduction in grain size upon re-austenitisation due to particle pinning of grain boundaries.

1.0 INTRODUCTION

Iron-manganese alloys containing up to 10% manganese transform to lath martensite on air cooling, similar to iron-nickel alloys containing 9 to 25% nickel. It is therefore believed that iron-8% manganese may form the basis of cryogenic steel similar to 9% nickel steels, but at a cost more economical as manganese is relatively cheap and is widely distributed in natural resources.

However, previous investigations (1) (2) (3) have shown that Fe-Mn alloys based on 6-10% Mn are susceptible to temper embrittlement due to segregations of Mn and N to the prior austenite grain boundaries (1). Other work (2) (4) has shown that the toughness can be considerably improved by tempering at 500-600°C to produce reverted austenite. The precise mechanism by which reverted austenite improves toughness, however, is not very clear.

1.1 Objectives of Present Research

(i) To investigate the mechanisms by which austenite may act as a sink for impurities and improve toughness.

(ii) By investigating both high purity and commercial purity alloys determine whether Nitrogen and

residual elements have a significant effect on toughness. The effect of stabilisation and grain refinement with Ti and Al was also to be investigated.

(iii) Investigate the effect of cooling rate on toughness.

(iv) Investigate the role of Molybdenum additions on toughness.

(v) To determine whether an improvement in toughness can be obtained by a reduction in grain size through particle pinning of grain boundaries by ageing an Fe8MnO.2V alloy at low temperatures.

(vi) Determine the role of Epsilon martensite on toughness.

2.0 LITERATURE REVIEW

2.1 Cryogenic Steels

2.1.1 Introduction

Liquids that are normally stored in bulk can be classified into four temperature ranges as follows (5):

Design Temperature	Typical Temperature Range	Products
Ambient	+20°C to -10°C	Crude oil, petroleum products to pentane.
Low temperatures	-5°C to -50°C	Butane, propane, ammonia, chlorine.
Very low temperatures	-90°C to -110°C	Ethylene, ethane.
Cryogenic	-160°C to -196°C	Liquid natural gas, liquid oxygen and nitrogen.

The last two ranges are usually classified together because of similar materials of construction and a need for a different form of insulation compared with the less onerous categories.

Common to all these substances is the fact that their vapour pressures are in excess of atmospheric pressure and therefore if stored as a liquid they are kept in pressure vessels or refrigerated.

The materials of construction depend on the design temperature. Conventional oil storage design is applicable for ambient temperatures and down to $-10^{\circ}C$. Over this temperature range the strength and impact properties of semi-killed steels for plate up to 20mm thick and fully killed steels above this thickness are satisfactory.

The $-30^{\circ}C$ to $-50^{\circ}C$ range generally requires the best C-Mn steel possible including silicon killing, aluminium refining and micro-alloying to give good notch toughness at low temperature (6). Quenched and tempered steels are also in use. The use of $3\frac{1}{2}$, 5 or 9% nickel steels is not considered necessary until the temperature is below $-50^{\circ}C$.

At $-100^{\circ}C$ and below the normal materials of construction are 5% nickel steel, 9% nickel steel, austentic stainless steel and Al-Mg alloy. Ultra-fine grained structural steels in bar form can also be produced for operation down to $-120^{\circ}C$. Figure 1 shows the lowest operating temperatures of some cryogenic steels.

2.1.2 Metallurgical Factors

Changes in the impact transition temperature or Ductile-Brittle Transition temperature (DBTT) can be produced by changes in the chemical composition and/or micro-structure of the steel. The impact properties are impaired by raising the carbon content as carbides contribute to embrittlement both mechanically and chemically (7). Mechanically they act as barriers to dislocation movement so helping to initiate intergranular cracks. Chemically, carbides can be rejectors of impurities, so enriching the grain boundaries with them. Sulphur, phosphorus and nitrogen are also generally regarded as detrimental to toughness due to their segregation to grain boundaries.

Early work by Rees and Hopkins (8) indicated that oxygen also reduces the intergranular strength of iron. However, work by Pickard, Rieu and Goux (9) found that oxygen did not affect intergranular brittleness. They declared that previous studies on iron (10) for the influence of oxygen occurred where the sulphur concentration was already sufficient to cause embrittlement, see figures 2 and 3.

Nickel is accepted to be beneficial to toughness (11, 12). Apart from its grain refining action nickel is thought to lower the ductile-brittle transition temperature (DBTT) by a solid solution effect allowing cross-slip to occur at low temperatures (13).

Grain size has a strong effect on transition temperature because grain boundaries act as barriers to crack propagation (14). An increase of one ASTM number in the ferrite grain size can result in a decrease in transition temperature of approximately 15°C (15). Many of the variables concerned with the processing of mild steel affect the ferrite grain size and therefore the transition temperature, such as normalising and rolling, figure 4.

The notch toughness of steel is greatly influenced by microstructure. Tempered martensite is the best condition in ferritic steels when compared with poor impact values in a completely pearlite structure or intermediate values with a bainitic structure (16). Low carbon ferrites in the quenched and tempered condition are also tough (6).

In contrast to body-centred cubic structures which show a ductile-brittle transition, the ductility and impact behaviour of face-centred cubic metals such as the austenitic steels are high and are relatively unaffected by lowering the temperature.

2.1.3 Controlled Rolled Steels

High strength and low temperature toughness can be produced in carbon-manganese steels by controlled rolling and microalloying to produce a small ferrite

grain size. Additions of aluminium, niobium, vanadium and titanium, either singly or in combination are made to combine with carbon and/or nitrogen to form carbide, nitride or carbo-nitride precipitates which are used to restrict recrystallisation and grain growth during rolling and, apart from ALN, provide precipitation strengthening. ALN when present as large precipitates at prior austenite grain boundaries provides little strengthening and embrittles the steels (6). The best combinations of strength and toughness are found in steels given reasonably high reheat temperatures ($\sim$ 1125°C), to take most alloy carbides and nitrides into solution, with low finish rolling temperatures ($\sim$ 800°C) and fast cooling rates (6,15). Typical results in a C-Mn-Nb, 20mm diameter bar are 55 Joules at -50°C charpy impact strength (6).

2.1.4 Quenched and Tempered Steels

Good low temperature properties can be obtained from a low carbon-manganese steel by rapid quenching from the mill after rolling. Good yield strengths can be obtained with sub-zero impact transition temperatures. Quenched and tempered steels may have reduced carbon contents and an increased manganese content compared with many structural steels. In the basic composition the structure formed on quenching after rolling to 950°C is principally acicular ferrite which is transformed from a small austenite grain size (15). Such a structure contributes towards improved toughness. The yield strength may be increased by a tempering treatment

if a precipitation strengthening alloy addition is present in the steel. The steels usually have a low hardenability but additions of alloys such as copper and molybdenum have a marked effect on this property. Recent evidence suggests that uniform properties can be obtained in plates up to 65mm thick (15). A typical result from a C-Mn-V-Cu steel quenched from 950°C and tempered at 600°C gives a proof strength of 460 N/MM^2 with 100 Joules at -40°C charpy 2mm V.

2.1.5 Nickel Steels

A range of nickel steels are available for service temperatures from ambient down to -196°C. The recognised nickel steels are 3½, 5 and 9% nickel steels. In addition to these, 36% nickel-iron alloys may be used down to-269°C in applications where a low coefficient of expansion is a design requirement. This alloy is fully austenitic (17), and the explanation for the low coefficient of expansion is thought to involve the Curie transition of these F.C.C. alloys which is a minimum in the region of 36% nickel. On heating just below the Curie temperature there is a contraction due to demagnetisation which opposes normal thermal expansion, but once the Curie temperature is exceeded the expansion coefficient rises rapidly to the normal value. A further contribution to the unusual behaviour results from cold working of these alloys which further reduces the expansion coefficient to values near or even below zero.

3½ per-cent nickel steel is a weldable low carbon steel which has good strength and notch toughness down to approximately -100°C. It has been used for containing, at atmospheric pressure, liquid ethylene and liquified gases of higher boiling points such as ethane, acetylene, carbon dioxide and propane. It is used in the normalised & tempered and in the quenched & tempered conditions. Normalising or quenching is usually in the range 870-900°C with a subsequent temper at 600°C ± 20°C. The microstructure consists of martensite or ferrite/carbide. In the normalised and tempered condition 3½% Ni steel plate in 13mm section gives 110 Joules charpy 2mm V at 20°C with a yield strength of 387 N/mm^2, and 40 Joules at -100°C (17).

5% nickel steel is used as a wrought material for service down to approximately -120°C. The high level of toughness shown by the steel at this temperature enables it to be used for the fabrication of welded vessels for handling and storage of liquid ethylene in land-based plant and marine tankers. Typical normalised (870-900°C) and tempered (~600°C) properties are (17):

20°C -	Yield Stress 460 N/mm^2 -	194J, charpy 2mmV
-140°C -		- 35J, charpy 2mmV
-196°C -		- 10J, charpy 2mmV

9% nickel steel is an economic steel for fabricating vessels and plant for processing, transportation and storage of liquified gases down to -196°C, the temperature of liquid nitrogen. The required properties of 9% nickel steel are produced by double normalising and tempering (NNT) or by water quenching and tempering (WQT). Temperatures for NNT are 900°C, 790°C, 575°C respectively; WQT are 800°C followed by tempering at 560-600°C. The presence of a small volume fraction of stable austenite produced by either of these treatments contributes to the excellent notch toughness of the steel at cryogenic temperatures. The effect of the second normalising or quenching is to produce martensite which, because of its composition, has a high degree of tensile ductility and notch toughness. Re-heating the steel to about 580°C not only tempers the martensite but also produces the small amount of stable austenite, the stability of which is dependent upon the time and temperature of tempering. Typical properties of 13mm plate (17) in NNT or WQT conditions are as follows:

WQT	20°C	Yield Strength	600 N/MM^2	150J	Charpy 2mmV
	-196°C	Yield Strength	950 N/MM^2	75J	Charpy 2mmV
NNT	20°C	Yield Strength	590 N/MM^2	125J	Charpy 2mmV
	-196°C	Yield Strength	850 N/MM^2	75J	Charpy 2mmV

2.1.6 Austenitic Stainless Steels

Austenitic steels fracture in a ductile manner even at temperatures far below ambient, due to the f.c.c. structure not undergoing a ductile-brittle transition as b.c.c. steels.

The standard grades of austenitic stainless steel are used over a wide range of temperatures and exhibit good ductility and ductile fracture behaviour down to liquid helium temperatures. The most popular grade is AlSl 304, while types 316, 321 and 347 may also be used (see Table 1). These alloys show a slight increase in proof strength at sub-zero temperatures and a marked increase in tensile strength. The basic 304 composition (.03%C, 18%Cr, 10% Ni) produces a relatively unstable austenite which becomes more unstable as the temperature decreases. In consequence, transformation to martensite can be triggered off by tensile testing at low temperatures, producing a volume expansion which influences the stress/strain curve (18). This unstable austenite leads to lower % elongations and reduced impact toughness (18).

If small quantities of nitrogen are present a significant increase in proof stress occurs as the temperature is decreased due to solid solution strengthening, as well as stabilising the austenite to low temperatures, since N is an austenite stabiliser (18).

Properties of standard AlSl 304 and Hi-Proof 304 are: (18) -

Standard 304	0.2% Proof Stress:	260 N/MM^2 20°C to -196°C
	Charpy 2mmV:	100 Joules at -196°C
Hi-Proof 304 (0.018%N)	0.2% Proof Stress:	350N/MM^2 (20°C) rising to 700N/MM^2 (-196)
	Charpy 2mmV:	27 Joules at -196°C

2.2 IRON MANGANESE ALLOYS - CONSTITUTION AND TRANSFORMATIONS

2.2.1 Equilibrium Diagrams

The Fe-Mn equilibrium diagram is shown in figure 5, with the metastable phase diagram showing non-equilibrium α and ε martensitic transformation temperatures in figure 6 (19). The corresponding and similar Fe-Ni equilibrium diagrams are shown in figures 7 and 8 (19). Manganese depresses the $\alpha + \gamma / \gamma$ phase boundary more severely than nickel. At lower temperatures the equilibrium phases are ferrite and austenite over a wide range of alloy contents. Due to the slow nature of the equilibrium reaction the equilibrium phases are not formed and a variety of transformation products can be formed on cooling from austenite.

2.2.2 Phase Transformations

According to Wilson (20) (21) (22) there are believed

to be five basic transformation modes of austenite established for low interstitial alloys although other workers do not agree with this interpretation (23) (24) (25) (26).

Equiaxed Ferrite

This reaction occurs at small degrees of undercooling. It is thought to be nucleated at grain corners with incoherent boundaries and negligible strain energy. In order to aid nucleation it is possible that one or more of the interfaces may be coherent or semi-coherent. This transformation was originally discovered by Owen and Gilbert (27) in dilute substitutional alloys and is thought to occur by a massive transformation by movement of the incoherent boundaries, and rapid atom transfer across the boundaries.

Massive Ferrite

This transformation occurs at higher cooling rates and at a lower temperature than equiaxed ferrite. It is also thought to form by a massive transformation to give grains of ragged outline and high dislocation density (22). See figure 9. The nucleus is thought to form at grain boundaries with one incoherent surface and a semi-coherent interface parallel to the grain boundary. Strain energy is produced in the nucleus due to coherency strain and the greater volume change appearing as a higher dislocation density (22). Thus

the strain energy opposes transformation so the transformation occurs at a lower temperature than equiaxed ferrite.

As with equiaxed ferrite, growth is thought to occur by movement of the incoherent boundary with rapid atom transfer across the boundary. However, in this case the movement of the boundary is thought to be hindered by solute drag at the interface pinning the moving boundary at various points along its length, giving rise to the ragged grain structure.

Bainitic Ferrite

This consists of a cellular structure, similar to lath martensite, but having wider and more irregular laths (28) (22). Since the degree of undercooling is fairly large, nucleation of the transformation is thought to be intragranular. Growth of the bainitic nucleus probably occurs by the movement of ledges (29). Such a growth mechanism would give rise to surface tilts on pre-polished surfaces and the transformation could mistakenly be thought to be martensitic (23).

Lath Martensite

This is otherwise known as 'massive' 'self-accomodating' or 'slipped' martensite (30). It is the product of austenite decomposition to body-centred cubic ferrite via a shear mode of transformation. Parallel laths are

formed of high dislocation density. Thus in this class of martensite the lattice invariant shear is thought to occur by slip, although recent theory suggests there are at least two slip modes (31).

The laths have dimensions ~ 0.3 x 3 x 100μm with a habit plane close to $\{575\}_\gamma$, ~4.5° from $\{111\}_\gamma$ and form in packets with low angle boundaries (up to 2°) between individual laths (32) (33).

It was first observed in plain carbon steels in the range 0 - 0.6 mass % carbon (34) (35).

In Fe-Ni alloys it occurs at moderate cooling rates in the range 9 - 18 mass % Ni (36).

Twinned Martensite

Lenticular plates are formed in the microstructure whose internal structure is cross-hatched by transformation twins (34). It is formed in Fe-Ni alloys in the range 30 - 34 mass % nickel below room temperature. Fe-C alloys (35) and in Fe-N alloys in the range 0.7 - 2.7 mass % N (37).

Epsilon Martensite

This is a close-packed hexagonal phase which occurs mainly in steels of low stacking fault energy such as austenitic stainless (18/8) (38). In Fe-Mn alloys it

mainly occurs in the composition range 10-30% Mn (39) and it forms in parallel sided bands bounded by the (111) austenite planes. It is generally believed that it is an intermediate stage in the decomposition of austenite to ferrite (40), i.e. $\gamma \rightarrow \varepsilon \rightarrow \alpha$.

Many researchers disagree about the nature of the forward and reverse transformation of ε martensite.

Schumann (4)) reports a $\gamma \rightarrow \varepsilon \rightarrow \alpha$ transformation for the forward reaction and $\varepsilon \rightarrow \gamma$ for the reverse, with at about 300°C higher than this, $\alpha \rightarrow \gamma$ on heating. He also reports a direct $\gamma \rightarrow \alpha$ forward transformation.

Bogachev (41) does not agree that ε is the first to form and states that this is not consistant with the presence of retained austenite between the α crystals or the concentration and temperature ranges in which the block-like α' structure appears.

Andryushchenko and Georgieva (42) report a $\gamma \rightleftharpoons \alpha$ transformation for alloys of 1.7 → 12% Mn. In the range 12-14% Mn they report both $\gamma \rightleftharpoons \alpha$ transformation and $\varepsilon \rightarrow \gamma$ on heating, but rule out the possibility of a reverse $\varepsilon \rightarrow \alpha$ transformation. They proved this by heating a specimen containing $\gamma + \alpha + \varepsilon$ with the amount of α known, until the ε disappeared, after which the amount of α martensite was again determined at room temperature. Since the results of the first and second

measurements of α coincided they concluded that the reverse $\varepsilon \rightarrow \gamma$ and not the $\varepsilon \rightarrow \alpha$ transformation had taken place. This observation is confirmed by Bogachev (43). They also confirmed that in higher (>14% Mn) manganese alloys that the $\gamma \rightarrow \varepsilon$ and $\varepsilon \rightarrow \alpha$ transformations occured during cooling. Finally, they concluded that in alloys containing ~16 to 30% Mn only the $\gamma \rightleftharpoons \varepsilon$ transformations occur.

Gulyaev (44) similarly reports a $\gamma \rightarrow \varepsilon$ and $\varepsilon \rightarrow \alpha$ transformation in 11.5 - 15.7% Mn alloys together with a $\gamma \rightarrow \alpha'$ martensite transformation. In the range 15.7 - 29% Mn $\gamma \rightleftharpoons \varepsilon$ only was found giving a mixed structure consisting of $\gamma + \varepsilon$. He also found that increasing purity of the alloys increases the temperature at which the transformation $\gamma \rightarrow \varepsilon$ starts and thus more ε is formed. He reports 85% ε in a 17% Mn alloy of high purity.

Giles and Marder (45) report that there is either a $\gamma \rightarrow \varepsilon$ or a $\gamma \rightarrow \alpha \rightarrow \varepsilon$ transformation sequence under induced pressure in an Fe - 17.7% Mn alloy. For the $\gamma \rightarrow \alpha \rightarrow \varepsilon$ sequence they propose that the f.c.c. phase first shears to b.c.c. This b.c.c. then transforms immediately to h.c.p. because the b.c.c. phase is unstable at this high pressure. It has also been reported that the transformation $\gamma \rightarrow \varepsilon$ on impact testing may improve toughness (46, 47).

2.3 PROPERTIES OF FERRITIC FE-MN ALLOYS

2.3.1 Introduction

Manganese resembles nickel in many of its chemical and microstructural effects. Its use has been mainly in low alloy steels and Hadfield's manganese steel. Due to its abundance, its similarities with nickel and its low cost it has been studied by many workers as a substitute for nickel in high alloy steels. Schumann (48) and Holden (39) have studied the mechanical properties of binary Fe-Mn alloys. Its use, however, as a cryogenic steel has been limited due to its brittleness (1), (2).

Fe-Mn and Fe-Ni alloys exhibit similar structures over the composition ranges 0-10% Mn and 0-25% Ni combined with Fe. Both manganese and nickel depress the transformation temperature; manganese greater than nickel, as shown in figures 2-5. A lath martensite structure is obtained with Fe-Mn (4-10%) and Fe-Ni (9-25%) alloys and is a shear dominated product in both systems, being structurally identical in the same heat-treated condition.

2.3.2 Structure and Morphology

Holden, Bolton and Petty (39) found that Fe-Mn alloys containing up to 10% Mn are entirely ferritic.

Alloys between 10-15% give a mixed structure of $\alpha' + \varepsilon$ martensite with varying amounts of each phase depending upon composition. Manganese levels from 0-2%, 2-6%, 6-10% produce structures of equiaxed ferrite, upper bainite and lath martensite respectively. Roberts (49) observed similar structures at 2% and at 9% manganese but, depending on grain size or cooling rate, found massive ferrite or massive martensite at 5% Mn instead of the bainitic reaction as reported by Holden (39).

Holden et al (39) reported that there is a difference in morphology between the martensite formed above and below 10% manganese. Below 10% Mn the structure was lath martensite. In common with many previous observations, the lath martensite forms on a habit plane close to $\{111\}_\gamma$ with laths separated by a low angle boundary.

In alloys containing more than 10% Mn two different morphologies of martensite exist, which are also associated with ε-martensite. They both differ crystallographically from normal lath martensite. One morphology has laths which are straight-sided bounded by $\{111\}$ planes. In contrast to normal lath martensite each lath is broken up into a series of blocks. These blocks arise due to mis-orientation along the lath and are separated by a common $\{112\}_\gamma$ plane. These observations are in common for low stacking fault

energy austenitic steels such as 18/8 (38) (50) (51). It has been suggested (39) that this type is almost certainly nucleated by ε-martensite.

2.3.3 Embrittlement in Ferritic Fe-Mn Alloys

Work carried out in the department (2) (52) has shown that ferritic iron-manganese allows failure by an intergranular manner akin to temper embrittlement.

Temper embrittlement is discussed in this section and compared and contrasted with the intergranular embrittlement found in iron-manganese alloys.

Temper-brittleness is generally found in low alloy steels and usually occurs on slow cooling or re-heating in the temperature range 350-550°C. The characteristics of temper-brittleness include a rise in the ductile-brittle transition temperature of notched-bar impact tests with an intergranular brittle fracture. It follows a 'C' curve behaviour when plotted against time and temperature with maximum embrittlement occuring in the region 450 to 550°C (53). See figures 10, 11, 12. At low tempering temperatures ($\sim$ 350°C) embrittlement only occurs after long holding times whilst at higher temperatures above 550°C de-embrittlement occurs. Embrittlement is caused by certain impurity elements such as antimony, phosphorus, tin and arsenic

segregating to grain boundaries. Manganese and silicon can also embrittle in large amounts (54), although this is thought to be due to an impurity - Mn interaction at the austenite grain boundaries (2). The main characteristic of temper-brittleness is that it is reversible. A severely embrittled steel can be de-embrittled by tempering above 550°C and re-embrittled by tempering below 550°C (53). De-embrittlement above 550°C is thought to be due to impurity elements being 'boiled off' from the grain boundary (53). However, in the case of Fe-8Mn alloys it must also be due to the formation of reverted austenite (see figure 12) (2). This austenite will be relatively stable on tempering below 550°C and therefore in the case of iron-manganese alloys the grain boundary embrittlement is not reversible.

Susceptibility to embrittlement is enhanced by alloy content such as chromium, manganese and nickel (55) and also increases with a change in structure of the order pearlite, bainite and martensite (56).

Edwards and Eyre et al (57) (58) have carried out extensive studies on an En30A steel. They found that embrittlement was due to Ni, Sn and P segregation to prior austenite grain boundaries. Figure 13 shows the variation in grain boundary nickel concentration as a function of ageing temperature and time. A non-

equilibrium segregation of nickel was observed on ageing at 450°C and 500°C. The composition profiles obtained as a function of distance from the fracture surface are shown in figure 14. The enhanced P and Sn concentrations were confined to within the first few monolayers of the boundary whereas nickel's segregation profile was much broader approaching that of the bulk at a distance of ~ 20nm. An interesting feature of the composition profiles was the build-up of carbon content adjacent to the fracture surface.

Rees and Hopkins (10) experienced brittleness in Fe-5% Mn alloys on examination of tensile and impact properties. They also examined Fe-Ni alloys which exhibited similar characteristics of brittleness. They concluded that some kind of grain boundary weakening through impurity segregation was responsible for the brittleness in both sets of alloys. Nikonenko (59) observed brittleness in Fe-8% Mn on cold working but it was suggested that possibly this brittleness was due to transformations of retained ε martensite to α martensite. Boniszewski (60) reported extreme brittleness in Fe-7% Mn compared with its counterpart Fe-9% Ni. He suggested that in Fe-Mn alloys twinned martensite was responsible for this brittleness whereas in Fe-9% Ni, lath martensite was taking place. F. G. Wilson (61) also thought that the presence of twinned martensite was responsible for this brittleness in Fe-Mn alloys while

studying replacement of nickel by manganese in maraging steel. However, recent studies (39) have not shown any evidence of twinned martensite in Fe-Mn alloys.

Bolton (1) thought that the main cause of embrittlement in Fe-Mn alloys was reversible temper embrittlement although it was difficult to decide from the available evidence which impurity was responsible for the embrittlement. Bolton speculated that for Fe-Mn alloys containing trace impurities that the Mn/Si levels could possibly control the susceptibility to temper-embrittlement. Further evidence which favoured silicon as being responsible was that a 0.5%Mo addition failed to restrict the embrittlement which had also been shown to occur with other steels (62, 63) where silicon was responsible for embrittlement. The evidence for silicon was not conclusive however as Preece and Carter (55) had suggested that phosphorus was also a source of embrittlement at concentrations as little as 0.001% P when in combination with manganese. Bolton's alloys contained 0.002%P to 0.005%P. It was thought that nitrogen (1) could also be responsible for increasing embrittlement. Capus (62) showed that nitrogen seriously enhanced 350°C embrittlement. Moreover it had also been found that low-carbon Fe-Mn alloys which contained aluminium to scavage the nitrogen were less brittle than straight Fe-Mn alloys (64).

Thus, from this research work it became obvious that possible impurities were P, N or Si, although the exact interaction was not clear nor whether manganese could cause embrittlement on its own.

More recently, Nasim (2) (3) concluded from his work in the department on 8% Mn alloys that intergranular embrittlement was due to N and P segregation in the austenitic field, enhanced on air cooling and shown to be associated with Mn and N cosegregation at the grain boundaries.

A 'C' curve for embrittlement in Fe-8 Mn (K1525) was obtained by Nasim (2) from tensile ductility tests at -78°C as a function of tempering time and temperature, see figures 11 and 12. Before tempering the alloy had been austenitised for 1 hour at 1000°C followed by water quenching. De-embrittlement occured above 500°C, but was associated with the formation of reverted austenite and epsilon martensite.

Further work by Nasim (2) and Nickbakht (65) showed that considerable embrittlement occurred in the first 6 minutes tempering of ice brine quenched charpy specimens at 450°C, see figure 15. In each case this was accompanied by a slight increase in hardness, figure 15 (b), although it was thought this hardening was only a secondary factor in producing embrittlement.

It seems likely as suggested by Squires and Wilson (66) that segregation of Mn and N occurs to prior austenite grain boundaries, weakening the grain boundary. During this period the yield strength of the matrix increases to a critical value which exceeds the fracture strength of the prior austenite grain boundaries.

In contrast Lee and Morris (67) used a scanning Auger to investigate intergranular fracture in as-quenched Fe-12% Mn to reinforce the theory that intergranular fracture modes in Fe-Mn alloys are microstructurally determined (68). In this interpretation the intergranular failure is not due to any catastrophic weakness of the grain boundary, but rather to the fact that the toughening of the matrix has the consequence that the intergranular fracture path is the "weak-link" in the alloy or the easiest path for fracture. Auger studies failed to reveal any consistent chemical segregation on the grain boundaries and so they concluded that the intergranular fracture path is inherently the easiest path for fracture.

However, Nickbakht (65) and Nasim (2) found that if Fe-8Mn is cooled more rapidly by quenching in ice-brine then the ductile-brittle transition temperature is lowered, compared with water quenched samples. Water

quenching produced intergranular fractures with segregation of Mn, P and N whereas ice-brine quenched samples gave cleavage transgranular fractures.

Also, Duchateau and Guttmann (69) found in their 6% and 9% Mn steels in the austenitised and doubly tempered condition that intergranular brittleness was due to plain temper embrittlement caused by P and Mn co-segregation to prior austenite grain boundaries.

The failure of Lee and Morris to find any embrittling elements may be due to the fact that they water quenched from the austenitising temperature giving only slight segregation below the limits of detection. The fact that Nasim found that ice-brine quenching suppressed intergranular fracture suggests that grain boundary fracture is not 'microstructurally determined'.

Duchateau and Guttmann found that the segregation could be suppressed by a small Mo addition of less than 1% as did Bolton et al (1). The role of molybdenum in preventing temper embrittlement will now be discussed in more detail.

2.3.4 The Role of Molybdenum in Preventing Temper Embrittlement

It has long been recognised that molybdenum in amounts

of the order of 0.5% drastically reduces or eliminates the susceptibility of alloy steels to temper embrittlement. Greaves and Jones (70) reported that it was not advantageous to add molybdenum in amounts much greater than about 0.5% and later work has shown that higher concentrations can be detrimental (71). Molybdenum appears to be effective in counteracting all four of the embrittling impurities Sb, As, P and Sn.

The precise mechanism has been under much speculation for the effect of molybdenum. Some workers suggest that it slows down the rate of embrittlement (71), and others suggest that it decreases the equilibrium amount of embrittlement (55, 72).

Austin, Entwisle and Smith (72) suggested that molybdenum decreases the grain-boundary segregation. Capus (73) proposed that molybdenum acts by decreasing the rate of phosphorus diffusion in iron. Restaino and McMahon (74) suggested that the strong carbide-forming tendencies of molybdenum resulted in more bulk carbide formation and less carbide at the grain boundaries.

Thus, there is less intergranular solute segregation caused by the solute rejection by the carbides. This mechanism is represented in figure 16. It is assumed that embrittling metalloid elements have negligible solubility in Fe_3C; a precipitating carbide would tend to reject such foreign atoms. The impurities would tend to build-up in the ferrite alongside the carbide-ferrite interface (75).

Joshi and Stein (76) suggested that molybdenum produced a smaller specific volume of molybdenum carbides, as opposed to other carbides, to explain the molybdenum effect.

Several investigations have been concerned with the effects on temper embrittlement of carbide-forming elements other than molybdenum, notably vanadium and tungsten. It has been found that a vanadium addition increases the susceptibility to temper embrittlement (70, 71), and tungsten has a beneficial effect similar to that of molybdenum at similar atomic percentages (70, 71). A combined Mo-V addition has also been reported as having a beneficial effect (71).

The mechanism by which molybdenum prevents temper embrittlement is still not fully understood. The use of Auger electron spectroscopy has helped to clarify the situation to some extent.

Viswanathan and Sherlock (77) found molybdenum levels on fracture surfaces above bulk levels in a 3.5% Ni, 1.8% Cr, 0.5% Mo steel of industrial purity (200 ppm P) after long embrittlement treatments. Inoue (78) found that an addition of 0.4% Mo to a 3% Mn, 240 ppm P steel resulted in a decrease in P segregation in both the as-quenched and embrittled conditions. Joshi and Stein (76) found no molybdenum segregation in some embrittled steels containing molybdenum.

McMahon, Cianelli and Feng (79) found that ageing for up to 1000 hours at 475°C, 0.5% Mo completely prevented embrittlement at a P content of 240 ppm, whereas at 600 ppm P the embrittlement was slight. During ageing at 500°C the embrittlement of the 240 ppm steel was eliminated by the Mo addition. However, the higher P steel exhibited a rise in transition temperature throughout the 1000 hour ageing period and AES revealed that this was accompanied by a rise in intergranular nickel and phosphorus contents with no intergranular molybdenum reported. This behaviour was attributed to the formation of molybdenum bearing alloy carbides, reducing the amount of Mo in solution.

The Guttmann theory (80) of temper embrittlement considers the effects of segregation in ternary systems such as iron-alloy element-impurity element (Fe-M-I) and takes into account the effects of the strength of the M-I interaction. This interaction tends to increase the segregation tendencies of both M and I and to correspondingly reduce the limits of solid solubility of M and I in iron.

Thus in an Fe-Ni-P alloy, the presence of nickel causes a decrease in the solubility of phosphorus and an increase in its segregation. However, the Ni-P interaction energy is about one-third as strong as Cr-P and one-sixth as strong as Mo-P. The effect of molybdenum in the Fe-Mo-P system could be strong enough to lower the limit of P solid solubility below the P concentration actually present in the steel; thus some of the P would form

clusters or precipitate as a molybdenum-rich phosphide, e.g. $(Mo,Fe)_3P$. The phosphorus which remains in solution would have a strong tendency to segregate, but its concentration drops quickly as the molybdenum concentration increases. It has thus been suggested that molybdenum's role is to immobilise P by tying up some of it as a phosphide or a Mo-P complex of some kind and that a small amount of P left in solution is insufficient to cause embrittlement.

The effect of increasing Mo content would therefore be to increase the amount of phosphorus which is removed from solution as phosphide. It is observed, however, that embrittlement susceptibility increases with increasing molybdenum content above about 0.5 to 0.8% Mo. There are two possible reasons for this. The first is that increasing Mo increases the amount of P at the grain boundary. This seems unlikely as experi mental work (81) has shown that the opposite occurs. The more likely explanation is that for the high molybdenum effect the reduction in impurity segregation is more than compensated for by the increase in hardness which molybdenum imparts to the steel due to solid solution hardening. This would increase embrittlement susceptibility. Experimental work has shown (81) that P segregation at 2% Mo is only of the order of 10 per-cent less than at 0.5% Mo whereas the hardness effect alone would cause a continuous increase in embrittlement

with increasing Mo. A minimum in embrittlement susceptibility would therefore be in the region of 0.5% Mo.

2.3.5 Mechanical Properties

Bolton et al (1) found that low carbon Fe-Mn lath martensites gave poor impact properties compared to Fe-Ni alloys. Iron-manganese alloys in the range 4-10% Mn were brittle in the as-quenched condition due to weakness at prior austenite grain boundaries. Good properties were achieved by tempering at 600°C with transgranular fracture but with some loss in tensile strength. They concluded that to improve impact toughness alloys needed to be grain refined with additions of scavenging elements.

Roberts (49) reported that yield strength versus ferrite grain size or martensite packet size could be represented by a Petch relationship. Properties were shown to be independent of sub-structure or Mn concentrations. Solid solution strengthening by Mn was found to be small and remains constant greater than 5% Mn. Only the martensite packet size and massive ferrite grain size controlled the impact transition temperature. Manganese in solid solution having little effect on the DBTT. This is in contrast to the work of Jolley (82) on Fe-Ni alloys who reported that in addition to grain refinement, that the DBTT is also lowered by the addition of nickel because nickel permits cross-slip to occur at low temperatures.

Holden, Bolton and Petty (39) found that 0-2% Mn produced low strengths and high ductilities, typical of annealed ferritic iron alloys. At 4-6% Mn bainitic structures produced on slow cooling had tensile strengths higher than those of annealed ferritic iron alloys. 6-10% Mn lath martensite structures gave high strength levels. 10-15% Mn with mixed $\alpha' + \varepsilon$ structures produced the highest strength levels obtained throughout the alloy range up to 36% Mn. Tensile and impact properties are shown in figures 17 and 18.

Charlesworth (4) has investigated two Fe-8% Mn alloys, one containing 0.1% Ti and 0.1% Al. By a combination of low austenitising temperature and the formation of reverted austenite after quenching, impact energies over 70 Joules were obtained at -100°C on half-size charpy specimens. See figures 19, 20, 21. This confirmed the early Russian work of Charushnikova (64).

2.3.6 Methods of Improving Low Temperature Toughness

Intercritical Heat-Treatment

In Fe-Ni alloys it was found (83) that by re-heating iron rich alloys into the two phase region ($\alpha+\gamma$) that austenite is formed by a diffusion controlled decomposition reaction:

$$\alpha_2 = \alpha + \gamma$$

where: α_2 = martensite

α = low nickel BCC phase

γ = nickel enriched FCC phase - reverted austenite

The reverted nickel-enriched austenite will transform wholly or in-part to martensite upon cooling to room temperature if the nickel enrichment corresponds to an Ms above room temperature. The ageing treatment, therefore, should be for a temperature and time sufficient to produce enough nickel in the austenite so that it is stable above room temperature. In 9% nickel steels used in the water quenched and tempered (WQT) or doubled normalised and tempered (NNT) conditions reverted austenite is formed and serves the following purposes:

(i) The austenite islands act as a sink for impurity atoms and cause a scavenging effect during tempering.

(ii) The austenite islands act as shock absorbers as FCC alloys have excellent toughness at low temperatures.

(iii) Grain refinement of the ferrite matrix takes place by formation of finely dispersed austenite islands during tempering.

(iv) Formation of austenite islands at prior austenite grain boundaries can also decrease temper embrittlement.

It is clear that if good cryogenic toughness is to be obtained, the reverted austenite should be stable at temperatures down to -196°C(84-88). This can be achieved by adding appropriate alloying elements or by suitable heat treatment.

In Fe-Ni alloys of this type the optimum tempering temperature is usually 570/580°C (9% Ni). Below 500°C temper embrittlement occurs and above 600°C the austenite islands become unstable due to their low nickel content, transforming to martensite on cooling (89).

Many investigations of the intercritical tempering of 6% Ni and 9% Ni steels have shown that a few per-cent of precipitated austenite into the lath martensite structure reduces the impact transition temperature (90-93). The austenite is formed as slightly elongated particles of sub-micron dimensions between martensite laths and along prior austenite grain boundaries.

Transformation-induced plasticity (TRIP) is frequently observed in materials in which phase transformations occur during deformation. In the Fe-Mn system,

however, in spite of considerable fractions of $\gamma \rightarrow \varepsilon$ and $\varepsilon \rightarrow \alpha'$ martensitic transformations during deformation, the TRIP phenomenon is not clearly observed. This is thought to be due to the difficulty in obtaining a suitable transformation rate as a function of strain (94), but since ε generation is effective in increasing the work hardening rate, more prominent TRIP may be achieved by the addition of other elements to obtain optimum ε formation rates (94).

To suppress impact transition temperature in Fe-Mn alloys the austenite should therefore possess stability against the martensitic transformation (90, 91, 95). Therefore, the austenite must be stable upon exposure to cryogenic temperatures and the austenite be at least stable during mechanical deformation at cryogenic temperatures. The degree of mechanical stability required for good toughness is not fully understood.

Explanations of how precipitated austenite affects fracture toughness involve considerations of when the austenite transforms during the fracture process (84, 90, 91, 92, 93, 95). For example, some early explanations proposed that the austenite was sufficiently stable so that it would directly interfere with crack propagation. Mossbauer spectrometry studies of fracture surfaces of 9% nickel steel have recently been carried out (85, 86) and have dispelled these explanations.

These studies have shown that no austenite remained at the fracture surface so the crack could not be blunted by the ductile austenite phase. In the case of 6% nickel steel, however, austenite particles were observed in extremely close proximity to fracture surfaces of impact specimens. Haga in this study (92) used constrained-fatigue-notched impact specimens (CFN) as shown in figure 22. These were used so that a thoroughly brittle fracture surface was obtained on impact testing at -196°C. Thus, a valid comparison between samples of different levels of austenite could be made. Using standard 2 mm V notch charpy test pieces a ductile fracture surface was found at -196°C due to the material's excellent toughness. So CFN specimens were used to produce a brittle fracture. Haga found that the transformation of austenite occurred no further than 10μm from the fracture surface, suggesting that the austenite may directly interfere with crack propagation.

Fultz and Morris decided to examine this theory using their own commercial 6% nickel steel (87). They used a heat-treatment of 1 hr. 800 WQ +1 hr. 670 WQ + 1 hr. 600 WQ. Large plastic deformations and variations in crystallographic texture led them to use mossbauer spectroscopy instead of X-ray diffractometry for measuring amounts of austenite near the fracture surfaces.

^{57}Fe mossbauer spectra were obtained on constrained-fatigue-notched impact specimens (CFN) at -196°C and RT together with charpy 2mm V specimens for comparison.

They found that no austenite was ever observed on the fracture surface of any specimen. Although the austenite particles were not completely mechanically stable they were all thermally stable with respect to immersion in liquid nitrogen. Depth profiles of austenite below the fracture surfaces had the same shape (figure 23) but shifted to increasing depth in the order CFN impact tested at -196°C, CFN impact tested at room temperature, charpy impact tested at-196°C and charpy impact tested at room temperature. This sequence is the same as their sequence in impact energy, which largely reflects the amount of plastic deformation during fracture. They also found that none of the austenite transformed in regions distant from the fracture surface (bulk austenite being 10.5%).

The work by Haga (92) fits into this trend as his CFN specimen broken at -196°C had a low impact energy and low transformation depth (10μm).

Fultz and Morris (87) therefore concluded from their work that transformation of precipitated austenite in 6% nickel steel is primarily a function of plastic deformation and not temperature. The depth of transformation below a fracture surface is greater

for those specimens that are tougher and exhibit more plastic deformation. They also concluded that when good fracture toughness is exhibited the austenite has transformed before it can interact directly with a propogating crack.

In Fe-Mn alloys the formation of reverted austenite has also been found to be beneficial in improving impact properties (2, 4, 69, 88, 96, 97).

Stannard and Baker (88) have investigated 6-12% Mn alloys. They found that good toughness was produced on tempering, producing $\alpha' + \gamma$. They state that the austenite content must be limited to prevent production of a continuous grain boundary film leading to intergranular fracture. Smaller amounts of reverted austenite are extremely beneficial, acting as a sink for impurities and retarding the ductile-brittle transition. They found that the volume and distribution of austenite retained after tempering was controlled by composition and heat-treatment of the steel.

The role of epsilon martensite is controversial. Duchateau and Guttmann (69) found that properties in a 9% Mn steel are controlled by the volume fraction of $(\gamma + \varepsilon)$. They found that ε phase was not embrittling but that fresh α' martensite was strongly embrittling.

Hwang and Morris (96) found that the presence of ε suppresses the DBTT in 12% Mn alloys, although at

the expense of yield strength. Clearly further work is required to clarify the exact effect of ε martensite on toughness.

Nikura and Morris (97) found that thermal treatment combining grain refinement with an intercritical temper gave good strength and toughness as low as -196°C in an Fe.5%Mn0.2%Nb steel.

Grain Refinement

It is well known that grain refinement can be used to strengthen material and improve toughness.

Hall and Petch (98) proposed the basic relationship between strength and grain size of any engineering steel:

$$\sigma_y = \sigma_i + d^{-1/2} K_y$$

where: σ_y = yield stress

σ_i = lattice friction stress (≡ yield stress of a constrained single crystal

d = half grain diameter

K_y = constant, related to difficulty of spreading slip from one grain to another.

In the case of brittle failure by cleavage, grain boundaries act as barriers to propagation of brittle cracks and thus a finer grain size increases toughness.

Where brittle failure occurs along grain boundaries due to segregation of impurities, the amount of segregate/ unit area of grain boundary is thought to be reduced as the grain size is refined.

As already discussed in the previous section, reversion annealing can refine the grain size. Niikura and Morris (97) added 0.2% Nb to their 5% Mn steel producing grain refinement and improving toughness. Reuben and Baker (99) have also used a Nb addition of 0.1% in a 4% Mn steel and found a similar grain refinement effect improving toughness. A great improvement in toughness due to grain refinement is produced by thermal cycling,

Thermal Cycling

This technique involves repetitive austenitising treatments of very short duration and temperatures barely sufficient to austenitise (100). The grain refining effect of austenite transformation and the tendency for each ferrite grain to transform on rapid heating to a single austenite grain, is utilised to develop ultra-fine grains. The extent of grain refinement and its effect on mechanical properties depends upon the number of cycles.

The cyclic treatment consists of holding the alloy in the austenite range just above the Af temperature

followed by holding in the ($\alpha+\gamma$) phase region just below the As temperature. The austenitising temperature should be as low as possible to minimise grain growth, whilst tempering in the ($\alpha+\gamma$) region should be high enough to maximise the rate of decomposition. In the first part of the cycle when the austenite transforms to ferrite through shear transformation, the grain refinement effect is presumably through relieving the internal strain built up during the shear transformation. During holding in the ($\alpha+\gamma$) phase region nucleation of reverted austenite takes place through a diffusional growth process. The microstructure is divided up by the nucleation of this reverted austenite at the boundaries of the martensite plates or prior austenite grain boundaries. Time of holding during each cycle influences the extent of grain refinement and mechanical properties of the alloy.

Jin, Hwang and Morris (101) found in an 8% Ni, 2% Mn, 0.15% Ti alloy that a four step thermal treatment lowered the transition temperature by 162°C. Grain refinement was from 38μm to 1.5μm. A small amount of reverted austenite introduced into this structure reduced the transition temperature by an additional 120-150°C.

Nasim and Wilson (102) found that in an Fe-8% Mn alloy a reduction in impact transition temperature from 115°C to -60°C was produced using a four step thermal cycling treatment, see figures 24 and 25. The thermal cycling

treatment consisted of 2 hours at 740°C AC, 2 hours at 655°C AC, then repeated. The austenite grain size was reduced from 80-90μm to 10-15μm. According to Roberts' work (49) this corresponded to a shift in DBTT ~50°C while the presence of 33% ($\gamma+\varepsilon$) produced a shift in DBTT of ~45°C according to the data of M. J. Schanfein et al (103). The additional unaccounted shift in DBTT of 80°C was suggested to be due to synergistic interaction between the introduction of ductile phase ($\gamma+\varepsilon$) and grain refinement. Another possible explanation is that as the brittle fracture in the original water quenched specimen was intergranular, with a DBTT of +115°C, that a change to a brittle cleavage fracture may decrease DBTT as well. In fact Nikbakht (65) observed a DBTT of +40°C with brittle cleavage fracture on ice-brine quenching an Fe-8Mn alloy.

The brittle fractures of thermally cycled material were complex, figure 26 , but the ductile areas in the fractograph were thought to correspond to the areas of austenite at prior austenite grain boundaries, figure 27.

Grain Refinement due to Pinning by Precipitates

Zener considered the relation between the size of spherical grains, R, and the size of spherical precipitate particles, r (104). By anology with surface

tension, he showed that the maximum force, B, exerted by a particle on a boundary would be:

$$B = \pi r \sigma$$

where: σ = surface energy per unit area of boundary.

The driving force for grain growth was assumed to be $2\sigma/R_0$. This force, however, relates to a contracting spherical interface with no attached interfaces. Thus, Zener's ultimate criterion:

$$R = \frac{4}{3} r/f$$

or $$D = \frac{8r}{3f}$$

where: D = grain diameter

f = volume fraction of precipitate particles

This model may be expected to over-estimate the driving force for grain growth, because the diminution of one interface usually involves the expansion of some other attached interfaces. Thus, substitution of typical particle sizes and volume fractions into the Zener equation indicates a much larger equilibrium grain size than is observed.

Hillert (105) considered the relation between the rate of growth of metal grains and the energy changes involved. It was recognised that large grains would grow at the expense of small grains. Gladman (106) further expanded this theory to give the critical particle radius, r* for pinning grains as:

$$r^* = \frac{6\,R_o f}{\pi}\left(\frac{3}{2} - \frac{2}{Z}\right)^{-1}$$

where: f = volume fraction of precipitate

R_o = matrix grain size = ½ x diameter

Z = ratio of the radii of the growing grain and its neighbour

Gladman and Pickering (107) determined that Z values between 2 and $\sqrt{2}$ would not be unreasonable and give excellent agreement with experimental results. The physical significance of the Z ratio is that only large grains may grow in a polycrystalline structure. The larger the value of Z (i.e. the larger the value of the grain radius in a matrix of mean radius, R_o); the greater the tendency of the grain to grow, and hence more pinning particles will be required. The value of Z must not be inordinately large, however, or the criterion of grain coarsening would be unsatisfactory due to the 'fine-grained' austenite containing many large grains before coarsening. Hillert (105) deduced that Z ratios of 1.5 may be perpetuated throughout the growth process.

Thermo-Mechanical Treatments

Hwang and Morris (108) found that cold work enhances the improvement in cryogenic properties produced in a reversion anneal in a 12% Mn alloy. This is achieved by cold working prior to the anneal which increases the decomposition rate

and thereby increases sites for the new phase, thereby producing a refinement of the grain size and introduction of a uniform distribution of retained austenite. In their work a large improvement in ductile-brittle transition termperatures was obtained. As quenched material gave a transition temperature of approximately -50°C compared to -196°C after 50% cold work followed by a reversion anneal.

Miller (109) achieved ultrafine-grained microstructures in a variety of alloy steels by cold working followed by annealing in the ($\alpha+\gamma$) two phase region of manganese and nickel steels. Grain sizes in the range 0.3 to 1.1μm were obtained. This was due to the low annealing temperature and the recrystallised structure being two phased thereby restricting grain growth.

Additions to Base Composition

Additions of Mo, Ni, B can help to improve the impact toughness and strength of Fe-Mn alloys.

Titanium and aluminium (2, 4, 64) can be added as nitrogen getters to reduce temper embrittlement. The addition of Mo is well known in reducing temper brittleness of alloys and has been discussed in section 2.3.5.

Duchateau and Guttmann (69) found in a 9% Mn alloy that a Mo addition of less than 1% suppressed intergranular

brittleness of P and Mn cosegregation. They also found that Mo favours the strain induced $\gamma \rightarrow \varepsilon$ transformation at the expense of $\gamma \rightarrow \alpha'$.

Niikura and Morris (97) found that in their 5% Mn alloy that an addition of Ni of 1-3% was found to increase strength at -196°C without loss of toughness.

Hwang and Morris (96) found that an addition of 0.002 to 0.01% Boron prevented intergranular fracture in a 12% Mn alloy. Boron segregated to the austenite grain boundary during annealing at temperatures near 1000°C. The toughness is further improved on tempering. Embrittlement only occurred when tempering temperatures were used resulting in the dissolution of Boron from the grain boundary thereby re-establishing intergranular embrittlement. They found that on tempering between 550 and 650°C that reverted austenite and epsilon were produced resulting in increased toughness, although ε phase reduced yield strength. Tempering between 680°C and 700°C resulted in embrittlement, due to fresh austenite grain boundaries and too low a temperature for re-segregation of boron in a reasonable tempering time.

Summary of Methods for Improving Toughness

For iron-manganese alloys inter-critical heat-treatments to produce reverted austenite provide the greatest benefits in reducing impact transition temperatures. Its

formation along prior austenite grain boundaries counteracts the effects of temper embrittlement which these alloys are prone to. Thermal cycling produces ultra-fine grains and hence great reductions in impact transition temperature. However, the cost commercially would probably be too high to be feasible in a production environment. Grain refinement by additions of Nb, Ti or particle pinning ageing treatments may produce a cheaper alternative. Additions also of Mo, Ni and B in conjunction with thermo-mechanical treatments may produce commercial alloys of high strength and low temperature toughness. Clearly, there is a great deal of research that is required to identify optimum compositions and heat-treatments for these alloys.

2.4 AUSTENITIC IRON-MANGANESE ALLOYS

2.4.1 Introduction

Commercial austenitic stainless steels are generally accepted as ductile metals with excellent corrosion resistance and high temperature stability because of their large chromium content ranging from 15-25% in the Fe-Ni matrix. These austenitic steels fracture in a ductile manner even at temperatures far below ambient, due to the f.c.c. structure not undergoing a ductile-brittle transition as b.c.c. steels.

Austenite Cr-Ni stainless steels are, therefore, popular for non-magnetic and cryogenic applications. However,

material cost is high when compared to austenitic high manganese steels. For non-magnetic structural applications material requirements are low magnetic permeability, enhanced strength, improved weldability and good machinability. Also, for cryogenic applications such as for storage and transportation of Liquid Natural Gas (LNG) and for superconducting technology, materials require low temperature toughness. There has been relatively little development of new steels to meet these requirements (110, 111, 112, 113, 114).

In order to provide good low temperature mechanical properties and to reduce nickel and chromium, a low carbon content and high manganese content is necessary. Manganese is an austenite former and thus in sufficient quantities stabilises austenite to low temperatures giving excellent low temperature impact toughness (4, 39); see figures 17 and 18. Carbon also extends the austenite phase region of the Fe-C equilibrium diagram and thus is an austenite stabiliser. However, too high a carbon content results in a decrease in toughness with a rise in the ductile-brittle transition temperature. Therefore, carbon has to be kept relatively low with a high Mn content.

The austenitic iron-manganese alloys studies by most researchers to date are:

(i) low carbon binary Fe-Mn

(ii) Fe-Mn-Al

(iii) Fe-Mn-Cr

(iv) Fe-Mn-Cr-Ni

2.4.2 Binary Austenitic Fe-Mn Alloys

The microstructure of Fe-Mn binary alloys is strongly dependent on manganese content. Despite mechanical property determinations by Holden et al (39), much has remained poorly understood.

Holden (39) examined Fe-Mn alloys containing up to 40% manganese, correlating structure with properties (figure 17). He found that alloys containing 15-28% Mn contain mixed $\gamma+\varepsilon$ structures and are fully austenitic above 28% Mn on cooling to room termperature. Holden found that between 15 and 20% Mn the ε phase was predominant and increased strengths were observed (880-1080 Nmm^{-2} tensile stress) due to the duplex structure and work hardening by the mechanically induced transformation of austenite during tensile testing. Beyond 20% Mn the austenite phase is more predominant, and as austenite has the lowest strength of all of the phases, the 20-28% Mn range showed decreasing tensile strengths (590-690 Nmm^{-2}). In the range 28-37% Mn stable austenitic structures were produced and hence low strength levels (490 Nmm^{-2} tensile stress).

Impact strengths for compositions greater than 15% Mn were very good, giving ductile fractures (figure 18).

Recent work in the department by Charlesworth (4) found in 20% Mn alloys a reasonable impact resistance down to -100°C in the as-quenched condition, figure 28. The structure consisted of austenite plus epsilon martensite. It does not attain the maximum toughness values of 8% Mn alloys, but is resistant to embrittlement over a wide range of temperatures and times, figures 28 and 29.

Charlesworth (4) studied the effect of ageing at various temperatures on a 40% Mn alloy. Figure 30 shows the hardness before and after ageing with the -196°C impact energy. He found that ageing above about 500°C resulted in a sharp decrease in impact energy at -196°C. Schumann (40) observed a sudden decrease in resilience at -196°C in a 40% Mn alloy. He attributed this to the presence of α manganese. Bogachev et al (115) also report an FCC → FCT transition below -100°C in Fe-Mn alloys in the range 30-40% Mn.

Tomota and Morris (116) identified the microstructure dependence of the tensile properties in 16-36% Mn steels. They found that transformations of $\gamma \rightarrow \varepsilon$ and/or $\varepsilon \rightarrow \alpha'$ martensite were induced under deformation (figure 31). As the Mn content was decreased from 36% to 25%, work hardening rapidly increased. Both the 1% flow stress

and tensile stress were also remarkably increased (figure 32). This was thought to be due to the intrusion of ε martensite. Although appropriate ε formation during deformation enhances uniform elongation as transformation induced plasticity (TRIP), large amounts of ε martensite deteriorate the ductility drastically. From 20 to 16% Mn, α' martensite is also induced by deformation which lowered the work-hardening and increased the ductility due to the large number of possible slip systems in α' compared to fcc γ or hcp ε (94).

Figure 33 shows ductile-brittle transition curves of Fe-Mn alloys as found by Tomota (117). From this data he deduced that ε martensite is detrimental to toughness whether it is formed in the as-quenched condition or formed during deformation. The 25% Mn alloy clearly shows that large amounts of ε lead to low elongation and a high impact transition temperature (figures 31, 32, 33) of $\sim 150^{\circ}C$. This high transition temperature is attributed to the reverse $\varepsilon \rightarrow \gamma$ transformation at elevated temperatures. Also, α' martensite, deformation induced, enhances toughness, but too much α' formation leads to a ductile-brittle transition associated with the fracture mode change from transgranular to intergranular. The alloys with more than 36% Mn also showed intergranular fracture at low temperatures for reasons unclear as Auger electron spectroscopy showed no clear evidence of segregation, although manganese enrichment was observed.

Bogachev (118) has studied Fe-Mn alloys in the range 18-20% Mn. He carried out thermomechanical treatments in the temperature range 100-400°C ($\gamma + \varepsilon$ region). Deformation in this temperature range changes the phase composition of the alloy and increases the imperfection, causing block refinement and growth of microstrains in the austenite and epsilon. He found that a large increase in strength results from this deformation, particularly in the temperature range of the ε phase of 100-180°C.

2.4.3 Fe-Mn-C Alloys

Hadfield's manganese steel of approximately 13% Mn and 1% carbon is fully austenitic and is chiefly used where grinding and gouging abrasion occur. To prevent brittleness caused by precipitation of carbides through slow cooling, the alloy is usually water quenched from 1050°C in order to keep the carbon in solution. Maratray and Norman (110) have found that better abrasian resistance is obtained with high carbon and low manganese contents of the Hadfield's type. An austenite microstructure showing a carbide dispersion develops good resistance to gouging abrasion, while resistance to grinding abrasion calls for a fully austenitic structure. Service tests show that the service life of 12% Mn - 2% Mo steel containing dispersed carbides is 50% larger than that of the Hadfield's steel composition.

Ohno et al (119) have developed a new type of 0.9%C, 14% Mn non-magnetic bar for concrete reinforcement with superior tensile strength and elongation to ordinary reinforcing steel, with very satisfactory non-magnetic characteristics.

Ouchi et al (120) have examined 24% Mn alloys with low carbon contents of 0.25% for use as hot rolled structural steel. As compared with the machinability of conventional high carbon low manganese steel, the low carbon high manganese steel is improved. It also has excellent toughness for low temperature use as a non-magnetic steel.

White and Honeycombe (121) studied a 13% Mn, 1.15%C steel and found that the austenite phase was stable in conditions of severe cold work at -196°C. On lowering the carbon content α and ε martensites are formed. The presence of epsilon suggests that the stacking fault energy of the austenite is low. They investigated the stability of these phases between -196°C and 400°C in the undeformed and deformed states and deduced that the properties of Hadfield's mnaganese steel are considered to arise from the presence of stacking faults and the interaction of solute elements with them.

2.4.4 Fe-Mn-Al Alloys

Charles and Berghezan et al (122-126) have studied Fe-(20-40%)Mn alloys with and without aluminium. In a

binary series of Fe-(20-40%)Mn alloys in the annealed condition they found that in alloys less than 28% Mn that epsilon martensite is responsible for a hardening effect and a decrease in ductility; whereas Fe36%Mn with its stable austenite phase gives good cryogenic properties but its yield strength is too low at 130 N/mm^2.

The addition of 5% Al to Fe-(20-40%)Mn enhances stability of the austenite phase and suppresses the $\gamma \rightarrow \varepsilon$ transformation. Since aluminium is a ferrite former it must be restricted to 5% particularly with lower manganese levels to avoid formation of ferrite. The solid solution hardening effect of aluminium gives an increase in toughness and elongation. Due to a large reserve of ductility 0.2-0.9% carbon was added. All the carbon went into interstitial solid solution, which is attributed to the absence of any strong carbide-forming elements, thus giving an increase in solid solution hardening. The hardening was found to be proportional to the carbon content added without an important decrease in ductility.

2.4.5 Fe-Mn-Ti Alloys

Chang and Morris (127) have studied Fe-28Mn-2Ti and Fe-20Mn-2Ti alloys. The titanium addition stabilises the austenitic phase in Fe-Mn alloys. The enhancement of mechanical properties were achieved through a

combination of cold work, precipitation and mechanically induced transformation. Cold rolling after solution annealing provides sufficient nucleation sites beneficial to subsequent ageing. Cold deformation produced a $\gamma \rightarrow \varepsilon$ transformation in the 28% Mn alloy, while a $\gamma \rightarrow \alpha'$ transformation was predominant in the 20% Mn alloy. A large number of very fine precipitates of $Fe_2(Ti,Mn)$ were found to form randomly in the matrix after a short ageing period. The cold work plus ageing treatment resulted in an increase in yield strength. The improvement in mechanical properties was due to the randomly distributed precipitates combined with the high defect density and fine substructure.

2.4.6 Fe-Mn-Cr Alloys

Several nickel-free alloys have been developed as possible replacements for the conventional austenitic stainless steels used in cryogenic temperature applications.

Experimental work has shown (128) that alloys based on Fe-16Mn-13Cr can give excellent properties over a range of temperatures following hot working at 1200°C, re-austenitising at 900°C and air cooling. The basic composition comprises three phases, γ (31%), ε (33%) and α (36%) giving the following properties:

Yield strength	275 - 450 N/mm^2
Tensile strength	690 - 860 N/mm^2
Elongation	45 - 75%
Charpy 'v' notch	250J
Upper shelf	
DBTT	- 160°C

The addition of 0.13% nitrogen introduces a stabilising effect on the phase transformations (83% γ, 17% ε) and although embrittlement occurs at -196°C the properties are acceptable at -160°C.

One problem in the use of austenitic stainless steels of the conventional type for cryogenic applications is their relatively large thermal expansion coefficients (12-14 x 10^{-6} /°C). Recent work in Japan (129) has shown that attractive combinations of strength and toughness combined with an expansion coefficient of 7 x 10^{-6} /°C is achieved with an Fe-25Mn-5Cr-1Ni steel. Additions of Nb, V or Ti to the optimum base composition refine the austenite grain size but decrease the toughness to a limited extent due to an increase in strength. The processing conditions are based on the rolling of ingot to 13 mm plate from 1250°C followed by re-austenitising at 1050°C and water quenching. Typical results are:

Fe-25Mn-5Cr-1Ni	:	0.2%PS 218N/mm^2, 148J @-196°C
Fe-25Mn-5Cr-1Ni 0.1Nb:		0.2%PS 324N/mm^2, 83J @-196°C

Sasaki (113) has developed a range of non-magnetic high manganese containing steels of 17-30% with 3-5% Cr that can be employed to extensive applications ranging from cryogenic to elevated temperature uses. These steels can maintain a non-magnetic state even when worked or heat-treated. Their thermal expansion coefficient can be controlled from that of austentitc stainless steel to that of low carbon steel. High strength can be obtained with good mechanical properties at low temperatures. Ordinary Hadfield steel has the disadvantages of being unstable when worked or heat-treated, of large thermal expansion coefficients, and of showing poor hot or cold workability.

Takahashi (111) has shown that good low temperature toughness comparable to 9% nickel steel can be obtained in a 0.45%C, 19%Mn, 5%Cr steel even in the as hot rolled condition.

Miura (112) has studied 18%Mn, 5%Cr austenitic steel at cryogenic temperatures, normally used for retaining rings of generators. He found that good low temperature toughness was obtained down to -196°C.

Sipos et al (114) have studied a Fe20Mn-4Cr0.5C steel. They found that mechanical properties were closely related to the strain induced $\gamma \rightarrow \varepsilon$ transformation. The strengthening effect produced by this phase change is limited by brittle fracture below room temperature. Brittle behaviour is associated with stress

concentrations produced by impinging ε platelets on the grain boundaries and ε phase transformation saturation. Tensile predeformation carried out at 100°C and 500°C showed that properties were considerably improved. This beneficial effect, especially on low temperature ductility is mainly attributed to austenite stabilisation by predeformation. The reduction of the amount of strain induced ε phase is due to the block-refining of the austenite grains, as twins and dislocation cells limit the growth of ε platelets.

Horiuchi et al (130) has evaluated the cryogenic mechanical properties of two kinds of high manganese steel, nitrogen strengthened high Mn stainless and high carbon, high Mn steel in an attempt to develop a new cryogenic steel for use down to 4K, with a higher yield strength than 304LN or 316LN. They showed that the optimum ranges of N-strengthened high Mn stainless steel ($>$0.25%N) having good ductility and toughness at 4K are:

Mn 18-28%
Cr 13-18%
Ni $>$ 5%

The austenitic phase is stabilised in this range of each element. Fracture toughness of high C, high Mn steels (0.6%C) increases with increase in Mn, Ni and Cu

contents due to increased austenite stability. Additions of chromium enhances the yield strength, but deteriorates the fracture toughness due to the retention of delta ferrite in the structure.

Optimum compositions for the two steels are:

High Mn stainless:	0.3%C, 18%Mn, 5%Ni, 14%Cr, 0.23%N
High C, high Mn:	0.6%C, 18%Mn, 3%Cu, 3%Ni

Ogawa and Morris (131) have carried out similar research on a 18Mn5Ni16Cr-.024C,.22N steel for use at 4 K.

They concluded that a very promising combination of yield strength, fracture toughness and fatigue resistance at 4K can be obtained, although the alloy should be kept free of δ ferrite and the carbon content kept to a low value. The alloy's strength can be increased by adding nitrogen.

Ishikawa et al (132) have also done studies on Fe(10-20)Mn-15Ni-15Cr-5Mo alloys. Proof strengths of 500N/mm^2 and 130J at liquid helium temperatures (4K) are very promising.

2.4.7 Effect of Epsilon Martensite, ε on Toughness

Holden et al (39) found in Fe-15-20%Mn increased tensile

strength due to work hardening and mechanically induced transformation of austenite to epsilon martensite during testing. Impact properties were high giving ductile fractures. Tomota and Morris (116) have found that the epsilon martensite which is induced under deformation by $\gamma \rightarrow \varepsilon$ increases work hardening and the formation during deformation enhances uniform elongation as transformation induced plasticity (TRIP). However, they found that large amounts of ε deteriorate ductility drastically and it is detrimental to toughness whether formed in the as-quenched condition or during deformation. In a 25% Mn alloy with large amounts of epsilon low elongations and a high impact transition temperature were found.

Charles and Berghezan (122-126) found that a 5% aluminium addition suppressed the $\gamma \rightarrow \varepsilon$ transformation as epsilon was responsible for a hardening effect and a decrease in ductility.

Sipos et al (114) found in an Fe20Mn 4Cr0.5C alloy that the strain induced $\gamma \rightarrow \varepsilon$ transformation had a strengthening effect but brittle fracture was observed below room temperature due to stress concentrations produced by impinging epsilon platelets on grain boundaries and epsilon phase saturation. This lead to a decrease in low temperature ductility.

Bogachev (133) found in Fe14-18%Mn alloys that an increase in γ and ε phases gave an increase in ductility which raised the tensile strength.

Hwang and Morris (96,108) found in Fe-12Mn alloys that tempering at 650°C introduced epsilon martensite into the structure which seriously decreased the yield strength and claimed this to be due to premature yielding through stress-assisted transformation of $\gamma \rightarrow \alpha'$ martensite. An increase in impact energy at -196°C was also found and thought to be due to the decrease in yield strength which usually gives a decrease in impact transition temperature.

Duchateau and Guttmann (69), however, found that epsilon martensite was not embrittling if it was in the extremely dispersed morphology within small isolated austenite islands. They deduced that its effect was rather beneficial and not distinguishable from that of austenite in their 6% and 9% Mn alloys. They found that an increase in ($\gamma+\varepsilon$) gave an increase in strain hardening capacity and a decrease in impact transition temperature.

Therefore, in summary, it appears that epsilon martensite can lead to low yield strengths and can enhance elongation by the TRIP effect. In small amounts depending on its morphology it can be beneficial to toughness but in large amounts it is detrimental to toughness and can reduce ductility dramatically.

2.4.8 Summary of Properties of Fe-Mn Alloys Consisting of (γ+ε) and γ Structures

The recent development of cryogenic engineering has demanded high strength, high toughness materials. Up-to-date various kinds of high manganese steels have been newly developed for low or very low temperature service. The binary Fe-Mn alloys tend to show intergranular fracture at high Mn levels and also tend to have low yield strengths. It is still unclear whether intergranular brittleness is inherent in the microstructure or is due to segregation of elements to grain boundaries. Of the newly developed alloys such as Fe-Mn-Al and Fe-Mn-Ti improved properties have been obtained. By far the most research is being carried out on the manganese stainless steels. However, these commercially developed high Mn alloys tend to have complicated chemical compositions and much has remained unclear concerning the optimum alloy design and mechanical behaviour with many aspects of the metallurgy of these alloys remaining poorly understood.

3.0 EXPERIMENTAL METHOD

3.1 Alloy Preparation

Fe-8Mn was chosen as an alloy base for this and previous studies since this gives a lath martensite structure relatively free of epsilon martensite on air cooling from the austenitising temperature. The cast numbers and composition of the steels studied are given in table 2.

Alloys 181 and 193 were previously prepared by Nikbakht (65); alloy K1525 by Nasim (2). In addition, two alloys of nickel steel were obtained from B.S.C. Rotherham Works, M176 (9% Nickel) and H5405 (5% nickel). M176 was in the form of 37mm square forged bar and H5405 was 48mm diameter as-rolled bar.

Several new Fe-8Mn laboratory casts were made. Initially, four 10Kg laboratory casts were made following discussions with British Steel Corporation regarding commercial compositions. Two 'pure' alloy casts were made using electrolytic manganese and Japanese electrolytic iron by vacuum melting (alloys 273 and 275). The other two casts were made to commercial impurities using mild steel billet supplied by B.S.C. Swinden Laboratories (alloys 277 and 278). Subsequently three more laboratory casts were made containing a 0.5% Mo addition. Alloys 317 and 318 were made to 'commercial' impurity levels and alloy 325 was made to a 'pure' specification. Molybdenum additions to Fe-8Mn were made because Bolton's work (1) and French work (69) indicated this addition reduced temper

embrittlement similar to its effect in low alloy steels (70). The pure alloy 275, the commercial alloy 278 and molybdenum alloys 317B, 318A, 318B, 325B had additions of Titanium and Aluminium to tie-up residual carbon and nitrogen, as Nasim's work (2, 3) has shown that free nitrogen can aggravate embrittlement in Fe-8Mn.

Alloy 277 contained ~0.2% vanadium in order to produce a fine dispersion of vanadium carbide to refine the grain size.

All the alloys were prepared by vacuum melting. Two ingots of approximately 4Kg each were produced from each cast. These were all surface 'scalped' and any pipe removed prior to rolling. All ingots were re-heated to 1100°C and upset-cross forged to a 2cm x 6cm section to break up the cast structure. Ingots were then homogenised in boxes sealed with clay for 50 hours at 1100°C, followed by air cooling. Ingots were then re-heated to 1100°C and hot rolled to 7mm plate by approximately 65mm width. Material so heat-treated was relatively free of banding.

3.2 Heat Treatment

Austenitisation treatments were carried out in muffle furnaces. Samples were coated in an oxidation retarding compound, Berkatec. Heat treatment was carried out on 7mm plates approximately 60mm long and were subsequently machined into sub-standard 10mm x 5mm x 55mm charpy specimens with a 2mm V notch perpendicular to the broad face of the plate.

An austenitising temperature of 850°C was used on most material and alloys were either air cooled (AC), water quenched (WQ) or ice brine quenched (IBQ) from the austenitising temperature. A low austenitising treatment was used to give a small austenite grain size to aid impact toughness. However, in early work repeating Nasim's and Charlesworth's studies on K1525, 181 and 193 an austenitising temperature of 1000°C was used.

Where it was desired to take all carbides and nitrides into solid solution an austenitising temperature of 1160°C was used. This was calculated from the solid solubility product for V_4C_3 and VN in low alloy steels (134) with 50°C superheat.

Tempering treatments were carried out in neutral salt baths on either plates or charpy specimen blanks. In the case of these blanks final machining to size and notching with 2mm V was carried out after all heat treatments.

3.3 Impact Toughness Testing

Sub-standard charpy (5 x 10 x 55mm) 2 mm V notch specimens were impact tested in various heat-treated conditions to determine ductile-brittle transition curves.

Low temperature impact tests were carried out after immersion for 15 minutes in various solutions depending on temperature:

0	to -10°C	ice/sodium chloride
-10	to -50°C	solid CO_2/methanol

-50	to	-78°C	solid CO_2 /acetone
-78	to	-129°C	liquid nitrogen/low b.pt. petroleum ether
-129	to	-159°C	liquid N_2/iso-pentane
-196°C			liquid N_2

Tests above room temperature were carried out by using a Carbolite convector oven.

Testing was carried out within 5 seconds of removing the sample from its temperature environment.

3.4 Tensile Testing

Tensile specimens were machined out of broken half charpy specimens according to the dimensions shown in figure 34.

The samples were tested at a strain rate of $0.5 min^{-1}$ at room temperature and -78°C using an Instron testing machine. The low temperature was attained by surrounding the testing jig with acetone and cardice contained in a vacuum flask.

3.5 Metallographic Examination

Specimens after each heat treatment were examined metallographically for general structure and prior austenite grain size. Etching in 2% Nital Solution was found to be sufficient for examination of general structure. Different etching techniques were tried for revealing the prior austenite. The best technique was first to temper the samples for 2-4 hours at 600°C, to precipitate austenite at the prior austenite grain

boundaries. This was followed by etching in 2% Nital for 15-30 seconds. The grain size was measured using the mean linear intercept method on a Vickers Projection Microscope, at a magnification of $\sim$500.

The mean linear intercept, m.l.i., is often given the symbol $\bar{d}$, where:

$$\bar{d} = \frac{L}{n}$$

where:

L = length of the random line on the planar surface

n = number of grains occupying this line

Intercepts in the order of 200 to 250 were recorded so that an accuracy of $\pm$10% with 95% confidence limits could be obtained.

The grain size quoted is the mean true grain diameter $\bar{D}$ given by;

$$\bar{D} = 1.75\ \bar{d} \quad (135)$$

Hardness measurements were taken using a Vickers hardness machine (Diamond) with a 30kg load, averaging over 3, 5 or 10 impressions, according to the degree of scatter between individual impressions.

3.6 Transmission Electron Microscopy (T.E.M.)

Thin foils were prepared from 3mm diameter rods machined from broken charpy samples. Discs of 0.1 to 0.2mm were prepared by slitting and then grinding on 600 grade paper. Samples were then electropolished in a solution of 6 per-cent perchloric acid in methanol (anhydrous). The temperature in the Struers electropolishing tank was kept at -20°C to -50°C using liquid nitrogen, so that oxide contamination of samples was eliminated. With samples containing reverted austenite polishing was carried out at -20 to -25°C as lower temperatures resulted in preferential attack of the austenite.

After thinning the foils were examined using a JEOL 100CX electron microscope with a side entry eucentric uniaxial tilt stage.

Carbon Replicas

To examine carbides from polished samples a carbon extraction replica technique was used:

(1) Micro samples were mounted in bakelite and polished down to 1 μm diamond followed by a light etch in 2% nital.

(2) A carbon layer was deposited on the micros by evaporation under vacuum.

(3) The layer of carbon was scribed with a scalpel into 2mm square grids.

(4) Micros were immersed into 6 per-cent nital for 30 to 60 minutes in order to loosen the carbon film.

(5) Washing was carried out in alcohol followed by plunging at 45° into distilled water, which resulted in the 2mm square replicas floating in the distilled water.

(6) Replicas were then mounted on copper grids of 150/200 mesh.

After mounting, the replicas were examined in the transmission electron microscope with EDAX (energy dispersive analysis by X-rays) to identify the particles.

3.7 Scanning Electron Microscopy

Charpy fracture surfaces were examined using a Philips PSEM500 Scanning Electron Microscope with an Energy Dispersive X-ray Analysis attachment, coupled to a LINK analyser and plotter.

Fracture surfaces were kept in a dessicator prior to examination to prevent oxide contamination.

3.8 X-Ray Diffraction

This was carried out on a Philips X-ray Diffractometer with a graphite monochromator using Cobalt K_α and Copper K_α radiation. Previous phase analysis by Nasim (2) and Charlesworth (4) used Cu.K_α only, which gives high background noise due to fluorescence. Cobalt radiation gives much better resolution of the peaks examined, particularly without a monochromator. With a monochromator both radiations can be used.

Some work was carried out at Swinden Laboratories for comparison.

Samples examined were $1cm^2$ by 5mm thick and were first electropolished using a Struers electropolishing unit in Struers A2 electrolyte for 2 minutes.

The integrated intensities of various reflecting planes (hkl) of α and ε and γ was needed to calculate the percentage of each phase.

The theoretical integrated intensity I (hkl) of a diffraction line (hkl) is given by (136):

$$I\ (hkl) = n^2.V.m.(L.P.)\,e^{-2m}\,(F)^2$$

where:

n = no. of cells in $1cm^2$

V = volume exposed to x-ray beam

- L.P. = Lorentz polorisation factor

m = multiplicity of (hkl)

e^{-2m} = Debye-Waller temperature factor

F = Structure factor x atomic scattering factor (f)

For n^2V it is possible to substitute V/v^2 where v is the volume of the unit cell.

If Ri = theoretical intensity for phase i of a particular reflection angle:

$$Ri = \frac{1}{v^2}.m.(L.P.).e^{-2m}.(F)^2$$

then, for three phases $\alpha, \gamma, \varepsilon$ in random orientation:

Vol fraction of ε phase $$V_\varepsilon = \frac{I_\varepsilon / R_\varepsilon}{\frac{I\alpha}{R\alpha} + \frac{I\gamma}{R\gamma} + \frac{I\varepsilon}{R\varepsilon}}$$

Assumptions:

(1) Debye-temperature = 420K (137)

(2) Lattice parameters for ε martensite a = 2.564Å, c = 4.06Å (2)

The table of theoretical (Ri) intensities has been calculated and are shown in Table 3 for Cobalt radiation, and Table 4 (ref. 2) for Copper radiation.

Each X-ray diffractometer run was carried out over the range 54° to 115° 2θ for Co K_α radiation and 44° to 95° 2θ for Cu K_α radiation. The following six integrated intensities could be calculated from the peak areas:

$(200)_\alpha$, $(211)_\alpha$

$(200)_\gamma$, $(220)_\gamma$, $(311)_\gamma$

$(10.1)_\varepsilon$

The six peak areas were measured using an OPTOMAX image analyser.

The peak ratios for α and γ, I_α/R_α and I_γ/R_γ were averaged out in the calculation to minimise preferred orientation errors. The accuracy of the determination was probably $\pm$ 1% for austenite and epsilon martensite. The lower limit of detection of austenite was $\sim$ 2%.

X-Ray Penetration

The penetrations of X-rays of different radiations can be calculated using the following relationship (138):

$$x = \frac{K_x . \sin\theta}{2\mu}$$

where: x = penetration

$$K_x = \ln \left(\frac{1}{(1-G_x)} \right)$$

G_x = the fraction of the total diffracted intensity which is contributed by a surface layer of depth x

$\sin\theta$ = depends on the wavelength (λ) and d-spacing according to Bragg's Law, $n\lambda = 2d.\sin\theta$

μ = linear absorption coefficient

= $2550cm^{-1}$ for CuK_α in Fe)
= $301{\cdot}4cm^{-1}$ for MoK_α in Fe) ref. (138)
= $442.69cm^{-1}$ for CoK_α in Fe)

If 99% of the diffracted intensity is arbitrarily assumed to come from the surface layer of depth x and the remaining 1% from below x is ignored, then $G_x = 0.99$ and $K_x = 4.6$. Inserting these values together with the values of the other parameters into the above equation yields the penetration distances for MoK_α, CuK_α and CoK_α as shown in Table 5.

It should be noted that penetration x is not a precise value because the intensity of the incident beam does not suddenly decrease to zero at a critical depth but rather decreases exponentially with distance below the surface. Consequently the majority of the crystals contributing to the calculated phase contents lie much nearer the surface than indicated by the respective penetration value. Nevertheless, the relative difference in penetration of the Cu, Mo and Co radiations still applies.

3.9 Mossbauer Spectroscopy

This technique was used as a comparison of phase analysis

with X-ray diffraction. Early in the experimental work discrepancies were observed in the amount of austenite determined by Nasim (2) and Charlesworth (4). The advantage of the Mossbauer technique is that both absorption spectra for X-rays (~25/30μm depth) and absorption spectra for electrons (~0.3μm depth) can be obtained. This can therefore give a comparison of surface and sub-surface phase analysis.

Work at Harwell (139) had indicated that there was a difference in the concentration of epsilon martensite, ε, between the interior and surface layers in 321 austenitic stainless steel. It was possible that such an effect was responsible for the discrepancy between the present investigation and Charlesworth's. The effect being due to different electropolishing times to Nasim's and Charlesworth's studies. It was for this reason that Mossbauer studies were carried out in the present work.

Alloys 181 (Fe.8Mn) and 273 (Fe.8Mn) were heat treated to produce large volumes of epsilon and austenite for comparison with X-ray diffraction. The treatment chosen was 1 hour 1000°C air cooled followed by 2 hours at 650°C air cooled. Heat treatment of alloy 273 was carried out under vacuum to prevent surface oxidation. Alloy 181 was electropolished for 10 seconds to remove surface oxidation. Absorption spectra for X-rays and electrons were then obtained.

A Mossbauer spectrum is obtained by passing a beam of gamma rays from a suitable radioactive source through a thin

sample which contains nuclei of the same species as those of the source. In the case of ^{57}Fe Mossbauer spectroscopy, the radioactive source normally derives from ^{57}Co alloyed into a non-magnetic rhodium matrix.

The ^{57}Co atom decays to an excited state of ^{57}Fe which in turn decays by successive emission of a 12.3keV gamma ray and a 14.4keV gamma ray; the latter is used for Mossbauer spectroscopy.

An absorption spectrum is produced by plotting the number of gamma counts against energy (Doppler velocity).

A process called Internal Electron Conversion was used to examine the surfaces of materials under the present investigation. Only 10 per-cent of the 14.4keV re-emitted resonant gamma rays escape the nucleus. The remainder may strike a K shell electron which is ejected with an energy of 7.3keV. At the same time though an X-ray of energy 6.5keV may be produced if an electron from the L shell of the atom falls into the K shell vacancy. The X-ray generated in the latter process has in turn a high probability of producing an Auger electron before it leaves the atom. There is thus a copious supply of particles leaving the nucleus. The 7.3keV electrons can easily be selectively detected by a helium-filled proportional counter. Since the penetration of these electrons is only about 500 nanometres, this provides a convenient means of studying the surface composition of such a sample. The X-rays are easily detected by replacing the helium with argon gas, and useful information can be obtained by

comparing the spectra produced from the sample by different particles. Figure 35 shows a schematic representation of the process.

3.10 Dilatometric Analysis

To determine the austenite and martensite transformation temperatures of alloys 181 and 193, dilatrometric analysis was performed on specimens 3mm diameter by 10mm length, using a "LINSEIS" horizontal dilatometer. A simultaneous recording was made of the dilatation and temperature on a 2 pen recorder. Samples were heated to 850°C/900°C at 20°C or 50°C per minute followed by air cooling or water quenching. Plots of dilatation versus temperature were made to determine As, Af, Ms and Mf temperatures. In addition runs of pure iron were made in an attempt to calibrate the dilatometer.

Further dilatometry work was carried out at Swinden Laboratories for comparison on alloys 273 and 275.

3.11 Auger Electron Spectroscopy

Auger electron spectroscopy was used to analyse fracture surface chemistry of alloys subjected to various heat-treatments, which exhibited differing fracture modes. Specimens were machined from broken extra long sub-standard charpies of dimensions 5mm diameter by 30mm length with a 1mm deep V-notch around the centre.

The samples were cooled to -196°C and fractured in situ at pressures $\sim 10^{-10}$ torr in the VG Microlab 500. Differential

energy spectra were recorded at a primary electron energy of 10 KeV and a specimen current of 10nA and a spot size of 1 μm.

Argon-ion sputtering was used to remove mono-layers progressively from the surface, thus allowing the determination of the composition profile of the elements as a function of distance from the fracture surface. Each ion bombardment comprised 15 μA-minutes at 5.Kv. A 20 second sputter was approximated to a removal of $\sim$5 monolayers.

Quantification of AES Spectra

It is well established that to a good approximation the amplitude of an Auger peak in the dN(E)/dE spectrum is proportional to the atomic concentration of the element giving rise to that peak (140). Problems of absolute quantification can be avoided by expressing results as ratios of prominent peaks of alloying or impurity elements to a chosen prominent peak of the matrix, provided that the matrix element always dominates the surface composition. The peak heights were therefore expressed as percentage ratios of the Fe(703eV) peak.

Conversion from such peak ratios to approximate atomic percentages requires information about relative elemental sensitivities. A widely used and comparatively simple approach to the conversion is to use the elemental spectra and scale factors in the "Handbook of Auger Electron Spectroscopy" (141).

The relative sensitivity, Sx, between any element x and silver is given by:

$$Sx = \frac{(A + B)}{(A)} \frac{I_x^H}{Kx \cdot I_{Ag}^H}$$

where: Sx = relative sensitivity of element x, at a particular primary beam energy (eg.3,5 or 10 KeV)

I_x^H = peak-to-peak amplitude from the handbook spectra of element x (with the desired primary beam energy)

I_{Ag}^H = Peak-to-peakamplitude from handbook for silver

Kx = handbook scale factor (KAg = 1), printed above the portion of the spectrum of interest

A&B = chemical formula indices of compound X_AY_B

Expressing peak heights as ratios of the Fe(703ev) peak the atomic concentration, Cx, of element x can be expressed as:

$$Cx = \frac{Ix/Sx}{Ife/Sfe}$$

where: Ix = peak-to-peak height of element x

Ife = peak-to-peak height of Fe(703ev) peak

Sfe = relative sensitivity of iron

Thus, atomic % concentration of element x, %Cx, is given by:

$$\%Cx = \%\ \text{of Fe(703ev) peak (for element x)} \times \frac{Sfe}{Sx}$$

There are pitfalls in using the spectra published in the "AES handbook" (141). The spectra almost all refer to pure bulk elements or to convenient compounds so that where the chosen prominent Auger peak is at several hundred eV kinetic energy, the sampling depth would be several atomic layers. In solid solution alloys in which the elements of interest are likely to be distributed uniformly over the maximum sampling depth, direct quantification by use of the Handbook should be feasible. However, in cases where the elements in question are segregated and therefore most probably not distributed uniformly in depth quantification can only be approximate and not absolute.

For carbon, errors in quantification can be quite high. Different spectra are obtained for carbon present in the form of graphite or amorphous carbon compared with carbon present as carbide. The handbook gives spectra for free carbon and for TiC.

Quantification of the atomic percent manganese on the fracture surface was not possible as the 542 eV peak was used. This is not the main peak, which is at 589 eV and overlaps with Fe. A 10Kev spectrum on pure manganese is necessary so that the ratio of Mn589 and 542 can be determined and hence the sensitivity factor for the 542 eV peak calculated. A 10KeV spectrum on pure manganese is not yet available.

4.0 EXPERIMENTAL RESULTS

4.1 Phase Analysis by X-Ray Diffraction and Mossbauer Spectroscopy

X-Ray Diffraction

Discrepancies in early experimental work were observed for the amounts of ε and γ when compared with Nasim (2) and Charlesworth (4), using X-Ray diffraction. Analysis of alloys 181 (Fe-7.89Mn) and 193 (Fe-8.54Mn-0.17Ti-0.18Al) was carried out on samples previously examined by Charlesworth (4) in an attempt to reproduce his results of phase analysis after an 850°C WQ, 600°C temper, followed by an embrittlement treatment at 450°C for 0.1 to 10 hours. As shown in Tables 6 and 7, initial results for percentage epsilon were much lower than Charlesworth's in both the aged and un-aged conditions. Table 8 outlines results obtained using the diffractometer at BSC Swinden Laboratories together with results on the same samples examined at the Polytechnic.

Even after re-preparation of the samples the results still differed greatly from Charlesworth. He obtained 39.4% epsilon phase compared with 3.2% and 3.7% epsilon obtained at Swinden Laboratories and the Polytechnic respectively on the binary alloy 181.

Tables 6 and 7 also highlight differences in results due to electropolishing times. Although not qualified in Charlesworth's

work it is assumed that he carried out a 10 second electro-polish on all his samples prior to X-Ray diffraction.

Table 9 details results after re-heat-treatment with samples air cooled or water quenched from 850°C for a comparison of cooling rate. Significantly lower amounts of austenite were found compared to samples originally heat treated by Charlesworth in the water quenched condition. Air cooling from 850°C produced slightly higher amounts of austenite and epsilon.

Table 10 shows the comparison of phases present after austenitising at 1000°C and either air cooling or water quenching followed by tempering at 650°C. A variation in electropolishing times is also shown. Samples were polished for 30 secs, 2 minutes, 5 minutes, then re-ground and polished for 30 seconds; all followed by X-Ray diffraction using Cobalt K_{α} radiation.

The effect of air cooling appears to produce larger amounts of epsilon than on water quenching. For example, alloy 181 after a 30 second electropolish indicated the presence of 22.5% epsilon on air cooling from 1000°C compared to 13.8% on water quenching.

Alloy 193 (Ti stabilised alloy) produced smaller amounts of epsilon than alloy 181 but the cooling rate had a similar effect in that 11.3% epsilon was produced on air cooling compared to 1.9% on water quenching after a 30 second electropolish.

Table 10 also compares the effect of electropolishing time on phase content. Results suggest that the amount of epsilon is greater at the surface of the sample after heat treatment compared to the bulk phase content. Figure 36 converts electropolishing time to depth of polish. It should be noted, as shown on the graph, the centre of the polished area was removed at a greater rate than the outer edges of the polished area.

Figures 37 and 38 show the variation of phase content with electropolishing time for the binary alloy 181 and the stabilised alloy 193 respectively in the air cooled from 1000°C and tempered and the water quenched from 1000°C and tempered conditions. In all cases the amount of epsilon was greater at the surface regions reducing to a constant level after 2 minutes and 5 minutes electropolish. Re-grinding after 5 minutes polish followed by a 30 second polish tended to increase the amount of epsilon slightly, indicating a deformation induced transformation.

Charlesworth carried out all his X-Ray diffraction using Cu K_α radiation. In the present research Co K_α radiation was principally used. Table 11 details a comparison of X-Ray data for both radiation sources. Results indicate that samples polished well back give similar phase contents using the two radiations.

Mossbauer Spectroscopy

For comparative purposes Mossbauer spectroscopy was carried

out on samples of the binary alloys 181 and 273 to determine the phase content. The heat treatment chosen of 1 hr. 1000°C AC + 2 hr. 650°C AC was to obtain large amounts of epsilon martensite and reverted austenite. Determination of Mossbauer X-Ray and Mossbauer electron spectra for the samples in the heat treated condition gave a comparison of penetration depth as Mossbauer electron spectra penetrates $< 1\mu m$ and Mossbauer X-Ray spectra penetrates approximately $30\mu m$.
Figures 39 to 44 show the Mossbauer spectra obtained and Table 12 details Mossbauer and comparative X-Ray diffraction data.

Both austenite and epsilon martensite are non-magnetic (113) and therefore appear as one peak at zero velocity on the spectra. Ferrite being magnetic shows a characteristic six peaks, three each side of the central non-magnetic peak. The splitting of the ferrite peaks which is more pronounced on the largest of the peaks is due to the interaction of manganese in the iron lattice (87,142).

The phase analysis was calculated by taking the integrated intensities of all the peaks as a ratio of the phase content, i.e. the area of the six alpha ferrite peaks totalled, compared to the area under the central austenite and epsilon peak.

Firstly, comparing Mossbauer electron spectra with Mossbauer X-Ray spectra for both alloys it is clear that the amounts of $\varepsilon + \gamma$ are lower at the surface of the sample than at a depth of approximately $30\mu m$. Alloy 181 did oxidise slightly

and was electropolished for 10 seconds to remove a thin layer. Decarburisation or partial oxidation at the very surface may account for the very low $\varepsilon+\gamma$ level of 1.2%. A further 5μm removal of the surface still showed a difference between X-Ray and electron Mossbauer spectra for $\varepsilon+\gamma$.

Alloy 273 was heat treated under vacuum to overcome oxidation and decarburisation problems. Again Mossbauer spectra in the as-heat-treated condition with no electropolish showed lower amounts of $\varepsilon+\gamma$ at the surface than at a depth of up to 30μm, i.e. 7.8% ($\varepsilon+\gamma$) compared to 22.7% ($\varepsilon+\gamma$) respectively.

Complementing the Mossbauer technique with X-Ray diffraction provided a clearer analysis of the phases (Table 12). It has been assumed that Cu K_α penetrates up to a depth of $\sim$6μm and Co K_α penetrates $\sim$30μm. For alloy 273 there is an excellent agreement between the two phase analysis techniques. Comparing Mossbauer X-Ray spectra with X-Ray diffraction using cobalt radiation the amounts of ($\varepsilon+\gamma$) are 22.7% and 22.0% respectively. Both techniques analyse to approximately the same depth. Comparing this result with that of the bulk phase content (i.e. phase analysis of the centre of the sample after a 2 minute polish) it is clear that ε phase increases from the surface layers and γ decreases, and ferrite remaining approximately the same. This indicates a $\gamma \rightarrow \varepsilon$ transformation, in the surface layers, probably due to deformation produced by initial mechanical polishing.

At first sight it appears that the X-Ray results and Mossbauer studies are contradictory; X-Ray results reveal

greater ε in the surface layers of samples compared with the interior, while Mossbauer electron spectra, Table 12, indicate less $(\varepsilon+\gamma)$ in the surface layers. However, the penetration depth of Mossbauer electron spectra is $< 1\mu m$ while that of Cu K_α is $\sim 6\mu m$. Thus it is possible that ε is greater in the outermost surface layers ($> 1\mu m$), decreases over the next $6\mu m$ and reaches a plateau at $\sim 30\mu m$ which is characteristic of the bulk. The point is discussed further in section 5.1.

(Fe-7.89Mn) and Alloy 193 (Fe-8.54Mn-0.17Ti-0.18Al)

Charpy samples tested by Charlesworth (4) were examined by optical and electron microscopy. Impact transition curves for these alloys, binary alloy 181 and stabilised alloy 193, are shown in figure 19. Results of grain size and hardness are shown in Table 13.

Alloy 181 in both the air-cooled and water-quenched conditions from 850°C exhibited a lath martensite structure as shown by optical and electron micrographs, figures 45 and 47.

Alloy 193 appeared to exhibit a "massive ferrite" structure as shown by optical and electron micrographs in figures 46, 48 and 49 in the air-cooled condition. The water quenched samples possibly consisted of a mixed structure of massive ferrite and lath martensite, figure 46 (b). In the 1h850°CAC+2h600°CWQ condition reverted austenite of 1-2μm length and 0.1-0.15μm thickness could be observed in the structure, figure 50. Figure 51 shows the bright and dark field images of reverted austenite within a massive ferrite structure.

Austenitising at 850°C produced a prior austenite grain size for alloy 181 of 33μm to 50μm in water-quenched and air-cooled samples respectively. Alloy 193 was slightly finer and taking the mean values in Table 13 varied from 28μm to 44μm. This scatter is probably due to using samples previously heat-treated.

Austenitising at 900°C on alloy 181 produced a grain size of 69μm to 76μm, whereas in alloy 193 it produced a grain size of 57μm to 70μm.

Additions of 0.17%Ti and 0.18% Al in alloy 193 appear to have resulted in alloy 193 having a finer grain size.

Hardness measurements were as expected and compare well with Charlesworth (4) - see Table 13. In general the addition of Ti and Al to alloy 193 has gettered residual C and N resulting in less interstitial solid solution hardening.

4.3 Dilatometric Analysis

Table 14 details the dilatometric results obtained on alloys 181 and 193 at the Polytechnic. Samples were soaked for 5 minutes at 850°C before being air cooled or water quenched.

On air cooling the initial cooling rate between 850°C and 400°C was found to be approximately 450°C/min reducing to 150°C/min over the Ms to Mf range. Water quenched samples had a cooling rate over the Ms to Mf range of approximately 350°C/min.

Problems were encountered with variability of results. This variability was mainly due to specimen size of 3mm diameter compared to the silica tube size that they were inserted into of 10mm diameter. The specimens therefore tended to slip during expansion and contraction.

Further dilatometric analysis on alloys 273 and 275 was carried out at BSC Swinden Laboratories and Table 15 details the transformation temperatures. Table 16 details transformation temperatures in Fe-Mn alloys determined by other workers, and these results are plotted in figure 52. It is apparent that there is good agreement that the Ms for lath martensite in alloy K1525, 193 and 275 is 355±10°C. The higher arrest temperature of 390°C in alloy 273 at 500°C/Min may be due to the formation of massive ferrite rather than lath martensite.

4.4 Impact Toughness of Pure Alloys 273 (Fe-7.85Mn) and 275 (Fe-8Mn -0.13Ti-0.104Al)

4.4.1 Air Cooling and Water Quenching from 850°C

The impact transition data and corresponding curves for the binary alloy 273 and stabilised alloy 275 after 1 hour at 850°C followed by air cooling and water quenching are shown in Table 17 and figure 53. Results indicate that impact transition temperature is reduced by water quenching from 850°C compared to air cooling. Alloy 275 also exhibits a lower transition temperature compared to alloy 273 and must be due to the grain refinement effect of the 0.13%Ti and 0.104% Al additions and removal of interstitials from solid solution. Alloys 181 (Fe-7.89%Mn) and 193 (Fe-8.54%Mn-0.17%Ti-0.18%Al) followed the same curve (4) in the as WQ and AC conditions - (see figure 19) and are shown in figure 53 for comparison. In this case insufficient data were determined by Charlesworth to distinguish between the binary alloy 181 and the stabilised alloy 193.

4.4.2 Tempering at 600°C

Tempering at the optimum temperature of 600°C (4) was carried out for both alloys in the as-air-cooled and water quenched conditions. Tempering was followed by water quenching in all cases. Tables 18 and 19 and figures 54 to 57 detail the charpy impact data and transition curves in the AC&T and WQ+T conditions for alloys 273 and 275. Figures 58 and 59 illustrate the effect of cooling rate from 850°C and tempering at 600°C on DBTT of both alloys. It is clear that cooling rate from 850°C has a significant effect on transition temperature in that

water quenching lowers the DBTT. Tempering at 600°C further reduces the DBTT and this must be due to the reverted austenite which is formed during this treatment. Table 20 details the impact transition temperatures for both alloys in all the heat-treated conditions.

Figure 60 shows the effect of grain refinement on DBTT in the WQ and WQ&T conditions. In the as-quenched condition alloy 275 has a lower DBTT than 273 due to the grain refinement produced by Ti and Al additions to alloy 275. However, in the WQ+T condition alloy 273 has the lower DBTT of -125°C compared to -82°C in the stabilised alloy 275. This can be explained by the amount of reverted austenite present as shown by X-Ray diffraction data, Table 21. Alloy 273 has slightly more austenite present, 3.6% at room temperature compared to 1.9% in alloy 275. This slightly greater amount of austenite is thought to counterbalance the effect of grain size. Table 22 details the grain sizes and alloy 273 has a prior austenite grain size of 39μm compared to 31μm in 275 in the WQ+T condition.

However, in the AC and AC+T conditions as shown in figure 61 the reduction in DBTT is as expected. Alloy 273 in the as-air-cooled condition has a DBTT of +210°C compared to +26°C in the grain refined alloy 275 after the same heat treatment. Tempering at 600°C reduces the DBTT to -96°C in alloy 273 and -70°C in alloy 275; the reverted austenite level being 2.0% and 2.5% respectively at room temperature. (Note: in figures 54 to 60, impact tests were repeated for temperatures at

-100°C and -120°C due to an anomaly in the results. It is believed that the low temperature thermometer used in the initial tests gave inaccurate readings).

4.4.3 Fractrography

Details of fractographic appearance are shown in Table 20 for the binary alloy 273 and stabilised alloy 275, together with details of impact transition temperature.

Alloy 273 exhibited a predominantly intergranular fracture mode at the lower shelf energy in both the air cooled and water quenched conditions. There were some cleavage areas of approximately 10% in the 1 hr. 850°C air cooled, figure 62, and 20% in the 1 hr. 850°C WQ samples, figure 63. Upper shelf fracture appearance was in all cases ductile dimples. Figure 64 shows a typical fractograph.

The stabilised alloy 275 again exhibited predominantly intergranular fracture in the 1 hr. 850°C air cooled condition with approximately 10-15% quasi-cleavage facets, figure 65. In the water quenched condition the fracture mode was 100% cleavage, figure 66. Ductile dimples were exhibited at the upper shelf in both conditions of similar appearance to figure 64.

Tempering for 2 hours at 600°C produced a marked change in fracture appearance particularly in alloy 273 which in the air cooled and tempered and in the water quenched and tempered

conditions exhibited cleavage rather than intergranular fracture with approximately 35% ductile areas, at the lower shelf. These ductile areas could be described as "ductile tearing", difficult to resolve at relatively low magnifications, figure 67, but quite clear at X3200 as shown in figure 68.

In comparison, alloy 275 in the air cooled and tempered condition exhibited a 100% cleavage fracture mode at the lower shelf energy, having a similar appearance to figure 66. In the water quenched and tempered condition the lower shelf was again cleavage but showed about 5% ductile areas.

All upper shelf fracture morphologies exhibited ductile dimples.

The improvement in fracture appearance from intergranular to cleavage after tempering, plus the appearance of ductile-tearing can be explained by the presence of reverted austenite produced by the tempering treatment.

4.4.4 X-Ray Diffraction

Results are shown in Table 21 for alloys 273 (Fe-7.85Mn) and 275 (Fe-8Mn-0.13Ti-0.104Al). Both alloys gave similar levels of reverted austenite in the air cooled and tempered condition ~2.5%. In the water quenched and tempered condition alloy 275 gave slightly less austenite than alloy 273. Cobalt radiation was mainly used as the X-Ray source but details of results using Copper radiation are also given (in the same samples, after cooling to room temperature). These results were slightly different and may be explained by the differences in depth of penetration of the X-Ray sources. No evidence of epsilon martensite was found in the two alloys in these heat-treated conditions.

Room temperature X-Ray samples were cooled to -78°C and -196°C to check austenite stability. Thirty minutes at these temperatures failed to reduce the austenite levels of both alloys proving the austenite to be thermally stable down to liquid nitrogen temperatures.

4.4.5 Hardness and Grain Size

Details of hardness and prior austenite grain size are shown in Table 22. Alloy 275 has a slightly finer prior austenite grain size of 27-31μm compared to 39μm for alloy 273. This can be explained by the small additions of aluminium and titanium acting as grain refiners.

Hardnesses were very similar, alloy 273 being slightly higher than the stabilised alloy 275 overall. This is presumably due

to the reduction of interstitials in solid solution in alloy 275. A similar effect was noticed for binary alloy 181 and stabilised alloy 193 as mentioned in section 4.2.

4.4.6 Optical and Electron Microscopy

Alloy 273 (Fe-7.85Mn)

This alloy appears to exhibit a mixed microstructure of lath martensite and massive ferrite in both the 1 hr. 850°C AC and 1 hr. 850°C WQ conditions. The actual proportions of each phase in each heat treated condition is very difficult to measure, particularly from the optical micrographs, figures 69 and 70. A tentative estimate using optical and transmission electron microscope images gives 20% massive ferrite in the water quenched condition and 50% massive ferrite in the air cooled condition.

Transmission electron micrographs show clearly both the highly dislocated massive ferrite structure and the lath martensite structure, figures 71, 72, 73 and 74. In the tempered condition the reverted austenite was seen mainly as fine elongated 'islands' of dimensions approximately 2μm by 0.1μm. The austenite appears to have nucleated in between martensite laths and at prior austenite grain boundaries, figures 75 and 76. The optical microstructure also reveals austenite precipitated at the grain boundaries, figure 77. Occasionally, small islands of reverted austenite were observed; figures 78(a) and (b) show the bright and dark field images of such an island. Figure 79 shows the bright and

dark field image of a single elongated austenite island with the corresponding diffraction pattern of zone axis $\langle \bar{1}22 \rangle$.

Alloy 275 (Fe-7.85Mn-0.13Ti-0.104Al)

The microstructure of alloy 275 also exhibited mixed structures in both the air cooled and water quenched conditions. It was estimated that in the 1 hr. 850°C WQ condition the structure consisted of 50% massive ferrite and 50% lath martensite compared to 80% massive ferrite and 20% lath martensite in the 1 hr. 850°C AC condition. Figures 80 and 81 show typical optical microstructures in the as quenched and quenched and tempered conditions. Figure 82 shows a transmission electron micrograph of a typical area of massive ferrite revealing the heavy dislocation network, while figures 83 and 84 show dislocation substructures. The typical morphology of reverted austenite in the form of elongated islands are shown in figure 85. This is further illustrated in the bright and dark field images of reverted austenite precipitated along lath boundaries in figure 86. Figure 87 shows a titanium carbide precipitate in a massive ferrite structure with the corresponding dark field and diffraction patterns.

4.4.7 Embrittlement Treatment at 450°C

The effect of ageing at 450°C on impact toughness in the optimum heat treated condition (1 hr. 850°C WQ+2hr.600°CWQ) was studied as a good measure of toughness and the heat treated alloys' resistance to temper embrittlement.

Samples were aged for 0.1, 1.0, 10.0 and 100 hours at 450°C and then impact tested. Initially, samples were fractured at -78°C. Alloy 273 showed no significant differences in impact strength or changes in hardness, see figure 88 and Table 23. Alloy 275 however, showed a rise in energy after 1 hour at 450°C which dropped off after 100 hours at 450°C. No corresponding rise or fall in hardness was noted. However, -78°C is close to the impact transition temperature of this alloy at -82°C which explains the sharp difference between the 0.1 and 1.0 hour results, i.e. alloy 275 was brittle in the as quenched condition after 0.1h at 450°C.

Alloy 273 on the other hand did not show this effect, energy remaining fairly constant, due to its impact transition temperature for this alloy being much lower at -125°C. Further samples were therefore aged at 450°C and tested at -40°C which is on the edge of the upper shelf energy of alloy 275.

Analysis of fracture surfaces by scanning electron microscopy revealed no significant differences on ageing at 450°C. At -40°C both alloys exhibited a mixture of cleavage and ductile areas in the ratio 20:80 respectively, as shown typically in figures 89 and 90. At -78°C fracture surfaces were all quasi-

cleavage as shown by figure 91, with small ductile areas between 5 and 10% in both alloys.

It therefore appears that both alloys in this heat-treated condition (1 hr.850°CWQ+2hr.600°CWQ) are largely resistant to temper embrittlement on ageing at 450°C.

Both alloys showed a slight rise in hardness after tempering for 6 minutes, compared to the optimum heat treated condition. The hardness then appeared to remain level up to 100 hours at 450°C.

X-Ray diffraction analysis of phase content is shown in Table 24. No significant variation in austenite levels was found. It is apparent that the prior austenite formed at 600°C has not nucleated any further austenite on ageing at 450°C. This point is further discussed in section 5.6.

4.5 Effect of Tempering Time at 600°C and 650°C on Tensile and Impact Properties of Alloy 273 (Fe-7.85Mn) and Alloy 275 (Fe-8Mn-0.13Ti-0.104Al)

Nasim (2) found unusual stress strain curves in alloy K1525 after thermal cycling which gave a sharp increase in stress as deformation proceeded. This "kink" in the stress strain curve was attributed to deformation-induced transformations of austenite and/or epsilon phase.

To fully investigate the above phenomenon tensile properties were determined after tempering at 600°C and 650°C for 2, 4, 8 and 16 hours to produce various amounts of austenite and epsilon phase in alloys 273 and 275.

The effect of phase content could therefore be related to tensile properties at room temperature and -78°C and compared with impact strength at -78°C. The effect of deformation on phase content could be examined by X-Ray diffraction on samples before and after tensile testing. Samples were also given a two stage and a four stage thermal cycling treatment to compare directly with Nasim's results.

Tempering at 600°C

Tensile curves followed a normal shape and showed no unusual "kinks". Soon after reaching the maximum load samples underwent quite large amounts of necking resulting in reductions of area in the region of 80%.

Table 25 details tensile results at room temperature (RT) and

-78°C for alloys 273 and 275 after tempering at 600°C.

Alloy 273 (Fe-7.85Mn) showed an increase in tensile stress as expected at -78°C compared to room temperature, figure 92. However, as can be seen the tensile strength remained fairly constant at both testing temperatures over the range of tempering times from 2 hours up to 16 hours. Conversely, the 0.2% proof stress remained level up to 4 hours and then fell after both 8 and 16 hours. This fall corresponded to an increase in reverted austenite after 8 hours and 16 hours. No epsilon phase was found after 2 hours but appeared after 4 hours at 600°C and increased very slightly from 1.3% at 4 hours up to 2.5% after 16 hours, Table 26. This increase in γ and ε phases may account for the fall in the 0.2% proof stress on increasing the tempering time. The ductility remained fairly constant over the tempering times involved at a level of ~32%. Hardness (Table 27), however, showed a slight peak after 8 hours at 600°C, but this may be within experimental error. Impact energy at -78°C for the range of tempering times used is shown in Table 27 and graphically in figure 93. Impact energy initially increases sharply from 2 hours to 4 hours at 600°C with a gradual increase from 4 up to 16 hours. The fracture appearance was predominantly cleavage with increasing amounts of ductile tearing areas of ~15% after 2 hours up to ~50% ductile after 16 hours. Figures 94 and 95 show typical SEM photographs revealing cleavage and ductile tearing areas. This increase in ductile areas and improvement in impact strength may be accounted for by the larger amounts of reverted austenite produced on tempering for longer times.

For alloy 275 (Fe-8Mn-0.13Ti-0.104Al) tempered at 600°C tensile behaviour was very similar to the binary alloy 273, although at -78°C there was an increase in tensile and proof strength after 16 hours compared to 8 hours, whereas at room temperature the proof strength continued to fall, figure 96. The phase content as shown in Table 26 and figure 96 remained fairly constant with 2.8%ε and 7.8%δ after 16 hours at 600°C. Hardness was overall higher than alloy 273 and possibly showed a slight peak after 8 hours similar to 273. Impact energies were higher than alloy 273 but showed the same sharp increase in energy at 4 hours compared to 2 hours at 600°C. The fracture appearance was again cleavage with between 5% and 20% ductile dimples depending on time at 600°C. It is worth noting that for this alloy the ductile areas were dimples rather than ductile tearing, figures 97 and 98. Alloy 273 exhibited ductile tearing at the same test temperature. At the lower shelf of both alloys the fracture surface consisted of cleavage and ductile tearing areas, as discussed in section 4.5.3, in the WQ+T condition. It is suggested that alloy 275 exhibits dimples rather than ductile tears at -78°C due to the presence of 0.1%Al and 0.1%Ti. Dimples nucleate at inclusions of TiC/N and AlN whereas in pure alloy 273 which does not contain these additions dimples would form at higher temperatures and tearing would occur more easily below the upper shelf. (The above inclusions were verified by Edax.)

Tempering at 650°C

Alloy 273 exhibited similar trends as at 600°C with regard to tensile properties and results are detailed in Table 28 and

figure 99. A small peak was observed in tensile properties after 4 hours at 650°C, particularly noticeable at -78°C. Hardness went through a minimum after 8 hours at 650°C compared to a peak at 600°C. Phase content however after 8 hours at 650°C revealed peaks in austenite and epsilon phase corresponding to this minimum in hardness level, Table 29, figure 99. Impact strength at -78°C tended to increase on tempering, with only a slight drop after 4 hours at 650°C corresponding to the peak in tensile properties, figure 95. Overall, compared to tempering at 600°C the tensile strengths were higher at 650°C and impact energies lower. This is expected as higher tensile strengths tend to lead to lower impact energies.

Table 30 details impact energies and fracture appearance details. The mode of fracture was again similar to those at 600°C with a cleavage mode and between 5 and 10% ductile tearing, figure 100; ductile areas being less than at 600°C which may be due to a decrease in reverted austenite after long times at 650°C compared to 600°C where austenite levels increased with longer times.

For alloy 275 tempered at 650°C, figure 101 and Tables 28, 29 and 30, tensile strength at room temperature peaked after 4 hours, corresponding to a peak in austenite which rose from 3.6% after 2 hours at 650°C to 9.6% after 4 hours. Conversely, tensile strength at -78°C was approximately constant with a possible minimum after 4 hours at 650°C. Proof stresses followed a similar trend to their corresponding tensile

stresses with properties at -78°C continually increasing on tempering whereas at room temperature, proof stresses reached a maximum at 8 hours and then levelled off. Elongation again remained fairly level throughout the tempering times involved. Hardness, however continually increased up to a maximum after 16 hours, going from 223 up to 241 Hv30. Impact energy at -78°C, figure 93 and Table 30, was very low from 2 hours to 8 hours at 650°C with a sharp increase at 16 hours. Fracture surfaces exhibited a cleavage fracture mode or quasi-cleavage after 2 hours and 4 hours at 650°C respectively. After 8 hours the fracture surface consisted of cleavage and 10% ductile dimples, figure 102. After 16 hours at 650°C the fracture surface contained 80% ductile dimples.

In summary, tensile strengths are relatively unaffected by tempering times greated than 2 hours. Proof stresses tend to fall off with increasing tempering time corresponding to a general increase in γ and ε levels. Impact energies tended to increase with tempering time. Elongation was relatively unaffected by time at 600°C or 650°C.

Alloy 273 was slightly higher in tensile strength than alloy 275. Hardnesses also tended to be higher in 273 than 275. Impact strength at -78°C was higher in alloy 275 after tempering at 600°C than 273 but at 650°C the opposite was the case; the only exception being the result on 275 after 16 hours at 650°C. This result throws doubt onto the three results at 2, 4 and 8 hours at 650°C. These were tested at -78°C, near to the DBTT of -82°C, obtained after 1 hour 850°CWQ+2hr.600°CWQ and so may well be brittle.

Increasing tempering temperature from 600°C to 650°C tended to increase tensile and proof strengths for both alloys with corresponding increases in hardness levels. Impact energies were also correspondingly lower at 650°C compared to 600°C. These observations are discussed further in section 5.7.

4.6 Effect of Deformation on Phase Content

No evidence of deformation-induced transformations was found on load-elongation curves as found by Nasim (2). Alloys 273 and 275 tempered for varying times at 600°C and 650°C were examined by X-Ray diffraction in the as heat treated condition. Tensile samples were then examined after tensile testing at room temperature and -78°C by X-Ray diffraction to determine whether deformation had induced a change in phase content. Tables 26 and 29 detail the results of X-Ray phase analysis on tensile specimens. In all cases the analysis was taken on the deformed gauge length.

It is clear from the results that epsilon and austenite tended to transform to α' martensite on testing, i.e. $\varepsilon \rightarrow \alpha$ and $\gamma \rightarrow \alpha$ transformations took place.

There was no direct evidence of an $\gamma \rightarrow \varepsilon$ transformation which would have been indicated by an increase in ε phase on deformation corresponding to a decrease in γ.

There were several notable exceptions to the general case of $\gamma \rightarrow \alpha$ and $\varepsilon \rightarrow \alpha$. For example, in alloy 273 after 2 hours and 4 hours at 600°C the γ phase was stable at -78°C but transformed during the room temperature test. There was also some evidence that ε was stable in both alloys after tempering at 650°C, particularly after room temperature testing. In alloy 275 tempered for 16 hours at 600°C both the γ and ε phases were stable after room temperature and -78°C testing.

In summary, longer tempering times produced greated stability of γ and ε . ε phase tended to be more stable than γ after tempering at 650°C. This is possibly due to the theory that ε is an intermediate decomposition product in the $\gamma \rightarrow \varepsilon \rightarrow \alpha$ transformation (40) so that although $\varepsilon \rightarrow \alpha$ may have taken place as well as $\gamma \rightarrow \alpha$, some γ may have transformed to ε rather than α i.e. the transformation $\gamma \rightarrow \varepsilon$ and $\gamma \rightarrow \alpha$ may have taken place leaving only ε and α in the structure.

4.7 Effect of Thermal Cycling Treatments on Deformation Properties

To further investigate the unusual stress strain curves found by Nasim (2) on thermal cycling of K1525 alloy 273 of a similar composition was put through two thermal cycling treatments similar to those used by Nasim. Tensile tests were then carried out followed by X-Ray diffraction phase analysis.

The two thermal cycling treatments given to alloy 273 were a first cycle comprising of ($I_A + I_B$) stages as shown in figure 24 and a second treatment comprising of ($I_A + I_B + II_A + II_B$) stages also shown in figure 24. Prior to thermal cycling the samples were given 1 hour at 1000°CWQ.

Table 31 details tensile results at room temperature and -78°C. Comparing them with results after tempering from 2 hours to 16 hours at 600°C and 650°C, Tables 25 and 28, it can be seen that thermal cycling improves tensile stress. Alloy 273 after 1 hr 850°CWQ+2hr650°C resulted in a tensile stress at room temperature of 655 Nmm^{-2} compared to 719 Nmm^{-2} after a $I_A + I_B$ cycle and 720 Nmm^{-2} after a $I_A + I_B + II_A + II_B$ cycle. The increased strength tended to lead to a slight loss in elongation. The phase analysis for both cycles is detailed in Table 32 including analysis on deformed tensiles at room temperature and -78°C. In the $I_A + I_B$ condition only 1.8% ε and 5.3% γ was produced compared to 5.8% γ and 28.0% ε in K1525 found by Nasim (2). After completion of the second cycle $II_A + II_B$ Nasim obtained 8.0% γ and 24.6% ε compared to 8.9% γ and no epsilon in alloy 273. This difference in phase analysis may account for Nasim's unusual stress strain curves. He suggested that during tensile ...

testing at -78°C the ε phase transformed to α contributing to low yield strength but an increase in elongation. Examination of alloy 273 by X-Ray analysis after tensile testing at room temperature and -78°C resulted in austenite transforming to alpha martenite and also $\varepsilon \rightarrow \alpha'$. It is worth noting that after the second cycle $\Pi_A + \Pi_B$ where no ε was found after heat treatment (only 8.9% γ), that 1.2% ε and 1.5% ε were found after deformation at room temperature and -78°C respectively, suggesting a $\gamma \rightarrow \varepsilon$ transformation.

Figure 27 shows an optical micrograph of K1525 in the thermally cycled condition. Figure 103 is an optical of alloy 273 in the fully thermally cycled condition, shown for comparison. These show that K1525 has a greater precipitation of reverted austenite at the prior austenite grain boundaries.

4.8 Impact Toughness of Commercially Impure Alloy 278

An impure alloy was investigated to compare properties with the pure alloys 273 and 275. Alloy 278 contained 0.028%C compared to 0.005% in 275 and higher residual levels. Nitrogen was also much higher at 0.012% compared with 0.0017% in 275. Due to this high nitrogen level, 0.19%Ti was added as a nitrogen getter as nitrogen has been shown to segregate to the prior austenite grain boundaries in Fe-Mn alloys (2), causing embrittlement.

A similar range of heat treatments to 273 and 275 were carried out for comparison.

4.8.1 Impact Transition Curves

Table 33 and figure 104 detail the impact transition data and curves for alloy 278. As found in alloys 273 and 278, water quenching rather than air cooling from 850°C improves impact properties, the impact transition temperature being reduced by 60°C on water quenching, Table 34; in the air cooled condition the DBTT was +140°C compared to +80°C on water quenching.

As expected on tempering at 600°C, producing reverted austenite, the DBTT was further reduced to 0°C after air cooling and tempering for 2 h at 600°C, while after water quenching and tempering for 2 h at 600°C it was reduced to -40°C. In comparison for the 'pure' binary alloy 273 the DBTT varied from +210°C down to

-125°C, depending on heat treatment. In the case of alloy 275, titanium treated (as alloy 278), the DBTT varied from +26°C down to -82°C.

A further temper of 4 hours at 600°C was carried out on water quenched material to determine whether an improvement in properties could be achieved. It was thought that previous samples tempered for 2 hours may not have been soaked long enough at temperature to give the benefits of reverted austenite. However, the DBTT was only reduced a further 10°C to -50°C.

4.8.2 Fractography

All upper shelf fractures were ductile dimples as shown in figure 105, with numerous inclusions visible in the dimples. Edax analysis on these inclusions revealed them to be aluminium and titanium rich, e.g. probably Al_2O_3 and TiC/TiN particles, figures 106 to 109. Modes of fracture, Table 34, were predominantly quasi-cleavage, figure 110, becoming quasi-cleavage and ductile tearing, figure 111, with the intrusion of reverted austenite on tempering.

4.8.3 X-Ray Diffraction

X-Ray diffraction, using cobalt radiation and a 2 minute electropolish, was carried out on samples in all the heat treated conditions, Table 35. In the air cooled and tempered condition, 2% ε and 11.5% γ were observed, whereas in the WQ+T condition 3.5% ε and 10.0% γ were observed. This level of γ is high compared to pure alloys 273 and 275 which ranged in γ from 1.9 to 3.6% with no ε phase present.

Further tempering of alloy 278 for 4 hours rather than 2 hours at 600°C produced 17.4% δ . The higher level of δ after this treatment explains the slightly lower DBTT and greater ductile areas at the lower shelf temperature. Alloy 278 in the optimum heat treated condition of 1 hr.850°CWQ+2hr.600°CWQ compared to 275 in this condition had ~ 50% ductile tearing areas compared to only ~5% in 275.

4.8.4 Optical and Electron Microscopy

Figures 112 and 113 show typical optical microstructures. Figures 114, 115 and 116 show TEM microstructures. The structure consists of lath martensite which upon tempering produces reverted austenite at the lath boundaries. Along these lath/austenite boundaries, epsilon martensite was observed, figure 116.

4.8.5 Grain Size and Hardness

Details of grain size, hardness and phase content of alloy 278 in various heat treated conditions are shown in Table 35. In addition the results obtained for the stabilised 'pure' alloy 275 are compared with those of the commercially pure alloy 278. It will be seen that in general hardness levels of 278 are higher than those of 275. This is probably due to the higher carbon levels in alloy 278 giving rise to a heavier dispersion of TiC and carbon in solid solution. On tempering, further TiC will precipitate giving rise to an increase in hardness. These hardness levels in alloy 278 are also higher than found in stabilised alloy 193.

4.8.6 Summary

Alloy 278 gave inferior impact properties compared with pure alloys 273 and 275. The finer grain size and higher austenite level of 278 should have produced improved impact properties. However, alloy 278 contained a small amount of ε martensite, generally considered to be a brittle phase. It also had a higher hardness than 273 and 275, which may also account for inferior impact properties. Fractographic evidence indicated that properties should have been better as the lower shelf contained more ductile areas than 273 or 275. However, the higher impurity levels may account for the poorer properties and Auger electron spectroscopy of fracture surfaces of these alloys will be discussed in the next section.

4.9 Auger Electron Spectroscopy

Alloys 273, 275, 277 and 278 were examined by Auger electron spectroscopy to determine whether any embrittling elements were present on fracture surfaces after various heat treatments. Nasim (2) found P and manganese-nitrogen co-segregation to intergranular fracture surfaces in alloy K1525 after ageing at 450°C, following a water quench. In the water quenched condition only N and P were detected in the intergranular condition, but in the case of another WQ sample enrichment of Mn and N were detected on the grain boundaries (2). Presumably this particular specimen had undergone a slower quench. Nasim suggested that these elements accounted for the intergranular fracture mode causing embrittlement, in the as-quenched and aged conditions.

'Pure' Binary Alloy 273 - 1h850°CWQ
DBTT + 66°C, Intergranular Fracture

In-situ fracture at -196°C exhibited intergranular fracture and results of AES on as-fractured and sputtered fracture surfaces are shown in Table 36 and figures 117-120. On the as-fractured surface the peak height ratio of Mn was 12.9% with 8.9%Si. After sputtering to remove surface layers Mn decreased to 7.2% and both C and O increased, falling off after ~ 30 monolayers removed, figure 120.

'Pure' Binary Alloy 273 - 1h850°CAC
DBTT+210°C, Intergranular Fracture

This sample exhibited an intergranular fracture mode. Results are detailed in Table 37 and figures 121-129. C, O, N, Si all

increased to a maximum on sputtering back the fracture surface and then fell off after ~ 20 monolayers removal. Mn however increased steadily from a peak ratio with Fe703 of 8.3% on the fracture surface up to 11.9% suggesting Mn desegregation at the grain boundary. Phosphorus was present at the grain boundary at a level of 5.1% peak ratio (2.6 atomic %) dropping off to zero after ~ 10 monolayers removed, figure 129. Table 37 and figure 125 also detail results of AES on a precipitate found on the fracture surface. This is thought to be a carbide as the C peak in figure 125 revealed a pre-carbon peak hump, typical of a carbide.

Stabilised Pure Alloy 275-1h850°CAC
DBTT+26°C, Intergranular Fracture

This sample exhibited an intergranular fracture surface on testing in-situ. Results are detailed in Table 38 and figures 130 to 136. Again C and O rose to a peak at ~ 20 monolayers and then fell off. On the fracture surface no carbon or oxygen was present. Silicon was also found to increase on sputtering to a maximum at ~ 20 monolayers and then falling off to 200 at ~ 25 monolayers, figure 136. Phosphorus was also present at the fracture surface at a peak ratio concentration of 5.1% (~2.6 atomic %) increasing slightly on sputtering to a ratio of 7.1% (~3.6 atomic %) then dropping off completely after ~ 25 monolayers removal.

Pure Binary Alloy 273 - 1hr850°CAC+2hr600°CWQ
DBTT-96°C, Cleavage and Ductile Fracture

This sample was chosen as its lower shelf fracture mode exhibited ductile-tearing and cleavage fracture areas. The

ductile areas are thought to be reverted austenite and so AES on both cleavage and ductile areas was carried out to try and identify differences in impurity levels as Mn and N being austenite stabilisers thought to segregate to reverted austenite.

Results are shown in Table 39 and figures 137-146. The cleavage fracture surface contained a high level of nitrogen and some phosphorus. After sputtering nitrogen gradually fell, figure 145, and phosphorus fell until after ~ 15 monolayers it had disappeared. Carbon and oxygen again rose to a peak at ~ 10 monoloayers and then started to fall off. Manganese remained fairly level, showing a slight drop after ~ 5 monolayers removal.

The ductile fracture surface was high in silicon and again there was a small amount of phosphorus on the grain boundary as fractured, figure 146. Manganese was also present. After sputtering the Mn remained fairly constant, but the Si and P levels dropped off. Silicon dropped sharply after the first sputter but was still present after ~ 15 monolayers removed. P however did not fall off and remained until ~ 15 monolayers when it was not observed. The phosphorus level behaved exactly as shown on the cleavage fracture and superimposing the two sputtering profiles shown in figures 145 and 146 would show extreme similarity.

Comparing C and O levels on both ductile and cleavage fracture surfaces, both increased to the same levels upon sputtering from zero at the fracture surface.

In summary, comparing cleavage and ductile areas phosphorus shows no difference and is present on both fracture surfaces,

C and O are present only after sputtering and show similar profiles in both cases. Manganese exhibits generally a slightly higher level in the ductile area compared to the cleavage area. Nitrogen was present on the cleavage fracture but not on the ductile fracture area. Also, silicon is at a lower level on the cleavage fracture and only rises to the as-fractured ductile level after sputtering, followed by a sharp fall.

Commercial Alloy 278 (1hr.850°CAC)

This sample exhibited a cleavage fracture and results are detailed in Table 40 and figures 147 to 150.

Again carbon and oxygen were not observed on the fracture surface but increased to high levels after sputtering. Manganese was present on the fracture surface at a peak height ratio of 13.4% gradually dropping off to 8.5% after sputtering. Phosphorus was also present at the fracture surface and fell off to zero after removal of ~ 30 monolayers, figure 150.

Alloy 277 (1hr.1160°CIBQ)

This alloy exhibited intergranular fracture due to the severe quench. Details of AES are shown in Table 41 and figures 151-154.

Again, carbon and oxygen both increased on sputtering as previously found. Manganese increased and then fell off, figure 154. No other elements were observed on the fracture surface.

General Summary of AES Results

The increase in carbon and oxygen on sputtering is thought to be due to contamination of the Argon, used for the profiling, with hydrocarbons. The same trend of both elements increasing to high levels after surface removal was observed on all sputtering profiles.

Phosphorus was the only embrittling element consistently observed on fracture surfaces but was detected on both cleavage and intergranular fractures.

4.10 Grain Refinement of Commercial Alloy 277 (FE-8MN-0.2V)

In an attempt to grain refine Fe8Mn alloys an addition of ~ 0.2%V was made in order to investigate the role of ultra-fine prior austenite grain size on toughness. The theory behind this heat treatment was as follows:

The alloy would be first austenitised above the carbide/nitride solvus temperature at 1160°C to dissolve all the second phase particles, followed by quenching in iced-brine to retain all the solute in solution. The material would then be tempered in the range 450°C to 600°C to precipitate a fine dispersion of vanadium carbide which upon re-austenitisation at the normal temperature of 850°C would then pin the grain boundaries.

Impact toughness, fractography and optical/transmission electron microscopy were all used to monitor this heat treatment.

4.10.1 Solution-Treated Toughness

Solution-treatment was carried out at 1160°C for 1 hour followed by iced-brine quenching. The impact transition curve is shown in figure 155. Data is detailed in Table 42. The curve for solution-treated + 1 hour at 850°C water quenched is also shown. This second austenitisation resulted in a reduction of impact transition temperature from ~+170°C to ~+140°C. Thus, without any grain refinement heat treatment the impact toughness was very poor. Scanning electron micrography revealed an inter-granular fracture mode at the lower shelf of the IBQ sample, figure 156 with a quasi-cleavage fracture mode for the IBQ+850°CWQ sample, figure 157. The upper shelf fracture mode was ductile dimples in both cases, shown typically in figure 158.

Transmission electron microscopy revealed a fully lath martensite structure as shown in figure 159.

The difference in austenitisation temperature was reflected in the size of the prior austenite grains. Table 43 details hardnesses and grain size of alloy 277 in various heat treated conditions, together with impact transition temperatures. In the IBQ condition the hardness was fairly high at 358Hv compared to 345Hv after a further 1 hour at 850°CWQ. Grain size was reduced on the second austenitisation quite markedly from 55μm to 31μm, explaining the slightly improved transition temperature.

4.10.2 Age-Hardening Curves (450-600°C)

Samples were ice-brine quenched from 1160°C followed by ageing at temperature of 450°C, 500°C, 550°C and 600°C. At each temperature one sample was progressively aged and hardness tested up to a maximum of 100000 minutes until the secondary hardening peak was passed. Figure 160 shows the resultant ageing curves.

The curve for 450°C was repeated using seven samples aged for times up to 60000 minutes as a large hardening peak was originally found after 30000 minutes. The second curve did not follow the trend of the first one and it is suggested that the first sample had reacted with the salt in the salt bath. For the second curve fresh salt was used for the heat treatments.

As can be seen, for successively higher tempering temperatures the hardness after peak hardening fell off to quite low levels, particularly at the upper end of the tempering range.

Figure 161 shows the effect of ageing temperature on hardness for 3, 10 and 30 hours. The curve for 3 hours peaked at 550°C and all peaks fell off rapidly at 600°C.

Figure 162 and Table 44 detail phase analysis results by X-Ray diffraction of samples aged in figure 160. Results show that epsilon martensite is not present on ageing long times at 450°C and 500°C. Reverted austenite increases with tempering temperature. At 600°C the total content of austenite plus

epsilon martensite is equal to the equilibrium amount of austenite expected according to the equilibrium diagram, figure 5.

4.10.3 Grain Refinement Heat Treatment

Impact Toughness

From the age-hardening results an ageing temperature of 550°C was chosen and samples were aged for 3, 10, 18 and 30 hours for assessment.

After solution treatment (1160°CIBQ) and ageing at 550°C, samples were re-austenitised at 850°C for 1 hour followed by a water quench. An impact transition curve was produced for samples aged for 3 hours at 550°C, Table 42 and figure 155. Details of hardness, grain size and impact transition temperature are shown in Table 43. The 3 hour treatment at 550°C resulted in a reduction in prior austenite grain size from 31 μm (for IBQ+850°CWQ) to 12.5 μm with a corresponding reduction in impact transition temperature from +140°C to +115°C.

Scanning electron micrographs are shown in figures 163 and 164 of lower shelf fracture surfaces. The fracture mode in all cases was fine quasi-cleavage with some evidence of intergranular cracks. Upper shelf fractures were all of ductile dimple mode.

Optical and Transmission Electron Microscopy

Figures 165 and 166 show optical microstructures of samples grain refined. These show the fine martensite structure.

Figure 165 also shows intergranular cracking believed to be due to the severe iced-brine quench.

Figures 167 to 170 show the transmission electron microstructures. A lath martensitic structure is seen in figure 167, while figure 168 reveals precipitates of vanadium carbide at the grain boundary. Figure 170 shows the morphology of the reverted austenite.

Phase Content

The amount of reverted austenite present after ageing at 550°C was measured prior to the second austenitisation at 850°C. It is thought that this austenite may contribute to the grain refinement on subsequent austenitisation. Figure 171 shows the effect of ageing time at 550°C on the amount of reverted austenite, hardness and grain size. The amount of austenite increases with ageing time at 550°C (no epsilon was present). A corresponding decrease in grain size was noted. The hardness decreased after 18 hours, where it peaked. This was probably due to overageing of the vanadium carbide precipitates.

Carbon Replicas

Carbon replicas were produced from samples aged for 3, 10, 18 and 30 hours at 550°C.

Figure 172 shows a typical distribution of carbides after 3 hours of 550°C. Figure 173 shows the bright and dark field images of the carbides with the corresponding diffraction

pattern corresponding to $\langle 111 \rangle$ V_4C_3. Figure 174 shows a large precipitate of (V,Ti) C as verified by EDAX. Figure 174(c) is a typical EDAX trace of the majority of fine particles, proving them to be vanadium carbides.

Figures 175, 176 and 177 show typical replicas for 10, 18 and 30 hours at 550°C. Figures 175 and 176 show the carbides at the grain boundaries.

Vanadium Carbide Size Distribution

Precipitate size was measured from 10 photomicrographs of replicas. A total of 790 precipitates were measured and the distribution of sizes up to 0.04 microns is shown in figure 178. Figure 179 shows a histogram of the full size distribution for the 3 hours at 550°C treatment. The mean particle size was found to be 0.027 microns although the median in figure 178 is 0.016 microns.

4.11 Impact Toughness of Pure Alloys 325A and B Containing 0.5%Mo

An addition of Molybdenum has been found to be beneficial in reducing temper embrittlement in steels (see section 2.3.4) and in Fe8Mn (147). Two alloys of pure composition were made, one containing 0.1%Al, 0.1%Ti, in order to investigate toughness.

Table 45 details impact toughness for both alloys in the as-water quenched (1hr.850^{o}CWQ) and in the optimum heat treated condition (1hr.850^{o}CWQ+2hr.600^{o}CWQ). Impact transition curves are shown in figure 180. Table 46 details fracture mode, DBTT, phase content, hardness and grain size. Figure 181 shows the as-quenched fracture mode which exhibited a mixture of cleavage and intergranular fracture. It should be noted that there is still some intergranular fracture, which suggests that the 0.5%Mo addition has not been completely effective in combatting temper embrittlement.

As expected, tempering at 600^{o}C improved DBTT by the addition of reverted austenite to the microstructure. Alloy 325B had additions of Al and Ti to tie-up excess nitrogen but this alloy had poorer as-quenched properties compared to 325A. This may be explained by the much larger grain size of 325B of 33μm compared to 17μm in 325A. In the tempered condition 325B exhibited a lower DBTT of -86^{o}C compared to -64^{o}C in 325A. This is probably due to a slightly higher amount of austenite in 325B at 5.8% compared to 3.3% in 325A.

Figure 182 shows the optical microstructure of 325B in the quenched and tempered condition believed to be lath martensite.

4.12 Impact Toughness of Commercially Impure Alloys 317 and 318, Containing 0.5% Mo and Various Levels of Titanium

Two alloys containing commercial impurities were made to the same Fe8Mn0.5Mo base composition so that four sub-casts could be attained, containing o, 0.05, 0.16 and 0.30%Ti.

Impact data is shown in Table 47 and curves are shown in figures 182 and 184. Table 48 details DBTT, phase content, hardness and grain size. Figure 185 shows the typical fracture mode of quasi-cleavage/ductile morphology. Figure 186 shows an optical of the lath martensite structure in 318B, typical of these alloys.

It was expected that an increase in titanium would lead to an increase in impact toughness, i.e. a decrease in the DBTT. However, the DBTT did not decrease with an increase in titanium, Table 48. The grain size was also expected to decrease with increasing titanium, but this did not occur. Hardness peaked at 0.05%Ti as did DBTT (lowest at -100°C). A small amount of titanium (0.05%) gave the largest amount of austenite (36.6%) which then decreased with increasing titanium. Epsilon martensite was not present in the alloy without titanium (317A) but was a maximum in 318B at 7.9%.

The DBTT is probably affected by all the above factors. A large amount of austenite, small grain size, low hardness and low epsilon would be expected to give the lowest DBTT. Alloy 318A fits this definition apart from hardness. The variability of the results is probably due to a combination of the above factors. These points are discussed further in section 5.8.

4.13 Impact Toughness of 5%Ni and 9%Ni Steels

Commercial alloys of 5% and 9% Ni were obtained from BSC Rotherham works for a comparison of properties. Table 49 and figure 187 detail the impact transition results for both alloys. The 9% Ni alloy was tested in two heat treated conditions, double normalised and tempered, NNT, and water quenched and tempered, WQ+T. Table 50 details the lower-shelf fracture mode, DBTT, phase content, hardness and grain size. The results were as expected, with the 9%Ni alloy giving a much lower DBTT than the 5%Ni alloy, being lower than -160°C compared to ~ -70°C. The 5% nickel alloy had a larger grain size and higher hardness and contained no austenite. The 9% nickel alloy contained 9.4% and 11.5% austenite in the two heat treated conditions, with a finer grain size, thereby improving impact toughness.

5.1 Phase Analysis by X-Ray Diffraction and Mossbauer Spectroscopy

X-Ray and Mossbauer results have been stated in Section 4.1. Extensive X-Ray analysis has been carried out using both cobalt and copper sources for diffraction. Mossbauer spectroscopy was used on alloys 181 and 273 for comparison with the X-Ray diffraction studies. All this analysis was carried out due to discrepancies in early experimental work which highlighted differences in phase content between the present investigation and that of Charlesworth (4) and Nasim (2).

The following factors were found to affect the measured phase content:

(i) X-Ray source used for diffraction.

(ii) Depth of electropolish.

(iii) Austenitisation temperature and cooling rate from heat-treatment, i.e. air cooling or water quenching from austenitising or tempering temperature.

(i) and (ii) refer to the method of measurement whereas (iii) leads to a variation in phase content dependent only on heat-treatment conditions.

The penetration of different X-Ray sources has already been discussed, Section 3.8. Charlesworth (4) used $Cu\ K_{\alpha}$ radiation for his X-Ray diffraction studies as did Nasim (2). The present

investigation has used both radiations although for bulk phase analysis it has been found that Cobalt radiation is best used.

The early discrepancies between Charlesworth and the present investigation are typified for alloy 181, Table 8. Charlesworth obtained 39.4% epsilon phase comparied to 3.7% epsilon in the present investigation for the same heat-treatment.

The main difference between the two methods of measurement was the X-Ray source radiation used. Charlesworth used Cu radiation of penetration $\sim 6\mu m$ whereas the present investigation used Co radiation of penetration $\sim 30\mu m$. The large variation of results may also be explained by the effect of electropolishing time. Charlesworth, it is assumed, used a polishing time of $\sim$10 seconds. Figures 37 and 38 show the variation of phase content with electropolishing time. These studies have shown that the amount of epsilon phase is greater in the surface layers of the sample reducing to a constant level after about 2 minutes polish. In general, regrinding and polishing after a long electropolish resulted in a slight increase in epsilon phase indicating a deformation induced transformation. It is therefore possible that heavy grinding followed by a light electropolish could result in high proportions of epsilon phase in the surface layers of a sample. This high level could be further exagerated by the use of copper radiation which penetrates only about $6\mu m$.

To complement the X-Ray technique and to further give evidence for the above theory, Mossbauer spectroscopy was used on alloys

181 and 273. Mossbauer electron backscatter penetrates $< 1\mu m$ whereas Mossbauer X-Ray backscatter penetrates $\sim 30\mu m$. These spectra could therefore be compared with cobalt and copper X-Ray radiations.

Unfortunately, Mossbauer studies cannot distinguish between epsilon and austenite phases as they are both non-magnetic. For this reason, $(\varepsilon+\gamma)$ have been grouped together, Table 12.

It is interesting to note the good correlation between X-Ray and Mossbauer analysis. For alloy 181 cobalt X-Ray diffraction (penetration distance, (p.d.) $\sim 30\mu m$) gave 27.3% $(\gamma+\varepsilon)$ and copper X-Ray diffraction (penetration distance, (p.d.) $\sim 6\mu m$) gave 28.3% $(\gamma+\varepsilon)$. Mossbauer electron spectra (p.d. $< 1\mu m$), however, gave 1.2% $(\gamma+\varepsilon)$ but after removing $\sim 5\mu m$ this rose to 25.5% $(\gamma+\varepsilon)$, in good agreement with the X-Ray studies. The only anomaly was the Mossbauer X-Ray spectra (p.d. $\sim 30\mu m$) which gave 15.6% $(\gamma+\varepsilon)$ compared to 27.3% $(\gamma+\varepsilon)$ using cobalt X-Ray (p.d. $\sim 30\mu m$). This may be explained by the fact that the sample after heat treatment was slightly oxidised. Also, the Mossbauer electron spectra (p.d. $< 1\mu m$) gave 1.2% $(\gamma+\varepsilon)$ which disagrees with previous X-Ray studies that epsilon phase is high in the surface layers, figures 37 and 38.

Further X-Ray and Mossbauer analysis of alloy 273 under the same heat-treated condition also gave good correlation, Table 12. X-Ray diffraction using cobalt (p.d. $\sim 30\mu m$) gave 22.0% $(\gamma+\varepsilon)$ which is in excellent agreement with Mossbauer X-Ray spectra (p.d. $\sim 30\mu m$) which gave 22.7% $(\gamma+\varepsilon)$. Again the Mossbauer electron spectra (p.d. $< 1\mu m$) gave a low $(\gamma+\varepsilon)$ of 7.8%. Analysis

of the bulk (centre of specimen plus a 2 minute polish) gave 18.0% $(\gamma+\varepsilon)$.

Thus, it is possible that at the very surface of the sample $(\gamma+\varepsilon)$ is very low, possibly due to oxidation/decarburisation. Below the surface, in the outermost surface layers ε is high, possibly due to deformation induced transformation through grinding of $\gamma \rightarrow \varepsilon$, as γ is relatively low. Over these few surface layers ε gradually reduces as γ increases, followed by a plateau of both phases at $\sim 30\mu m$. α' martensite is assumed to vary accordingly, being very high in the surface layers and reducing on increasing depth.

Bowkett and Harries (148) have done a similar analysis using X-Ray diffraction and Mossbauer analysis of a 321 stainless steel. They investigated α' martensite formation in their austenitic matrix and found it to be higher in the surface layers of their material . X-Ray analysis showed that ε content in the surface regions (up to a depth of $\sim 23\mu m$) increased progressively with deformation to 20% cold work, to a maximum of $\sim$ 22% and then decreased with further deformation to zero at 50% cold work.

Comparing the above with results in the present investigation it was also found that epsilon phase was higher in the surface layers, probably due to a deformation induced transformation of $\gamma \rightarrow \varepsilon$. α' martensite was also higher at the surface as found by Bowkett and Harries, but it must be remembered that their material was austenitic compared to ferritic in the present work.

As previously mentioned, austenitising temperature and cooling rate also affect the phase content. Table 9 gives a comparison of phase content for alloys 181 and 193 after air cooling and water quenching from 850°C. Air cooling in both alloys resulted in higher epsilon contents, e.g. for alloy 181 there was 5.5% ε after air cooling compared to 3.0% ε after water quenching. Similarly in Table 10 after air cooling from 1000°C alloy 181 produced 22.5% ε compared to 13.8% ε on water quenching after a 30 second polish. This Table also highlights the differences in phase content due to austenitisation temperature; the higher the austenitisation temperature the higher the epsilon content.

5.2 Optical and Electron Microscopy of Alloys 181 (Fe-7.89Mn) and 193 (Fe-8.54Mn-0.17Ti-0.18Al)

As detailed in Section 4.2 the structure of alloy 181 is lath martensite while that of alloy 193 contained "massive ferrite" as well as lath martensite. The only difference between the two alloys is the addition of 0.18% aluminium and 0.17% titanium to 193 to scavenge the interstitials. This also resulted in 193 having a finer grain size, Table 13, and lower hardness.

Lath or "massive" martensite has a body-centred cubic structure due to the low carbon content. The optical microstructure, figure 45 (a) and (b), consists of rectangular regions often with jagged edges. In three dimensions the massive or lath martensite grains would look like slabs rather than blocks. These slabs do not cross the parent austenite grain boundaries and the microstructural appearance is markedly different from the familiar acicular forms of high interstitial or high solute

ferrous martensite which consists of single or connected lenticular plates embedded in a matrix of retained austenite.

Transformations designated massive martensite appear to be true shear transformations as specimens of iron-based alloys, after transforming to massive martensite, exhibit tilts on pre-polished surfaces. These tilts correspond to shear plates formed in packets of parallel plates which usually completely cover the surface.

As can be seen in figures 47 (a) and (b) the transmission electron microscopy studies reveal the substructure to consist of 'bundles' or 'sheaves' of parallel sided ferrite plates, often called 'laths'. The plates in general contain a high density of random dislocations. The laths, which do not always have straight interfaces, dovetail together, completely filling space. The lengths of the laths is usually several microns and the width varies between 0.3 and 2.0 microns. In 181 they appear to be rather fine at about 0.3 to 0.5 microns.

It is well known that alpha iron plates formed by shear on $\{111\}$ austenite planes have the Kurdjumov-Sachs orientation relationship:

$$(111)_\gamma \,//\, (101)_{\alpha'}$$
$$\langle 110\rangle_\gamma \,//\, \langle 111\rangle_{\alpha'}$$

Massive ferrite is produced on quenching many dilute iron alloys including those with nickel, manganese, cobalt, silicon, carbon and nitrogen. The alpha grains tend to be large and irregular, not like those characteristic of an annealed material.

Figures 46, 48 and 49 show the optical and electron micrographs of 193 thought to contain massive ferrite. The massive ferrite can cross the original austenite grain boundaries and can be revealed by thermal etching of a pre-polished surface (36). There is no surface rumpling in this transformation and so it can be concluded that the reaction is non-martensite in nature. The substructure of massive ferrite consists of large irregular grains containing high angle boundaries and a fairly high dislocation density with dislocation tangles. Figures 48 and 49 reveal this sort of structure in alloy 193.

The transformation temperature is found to decrease with increasing substitutional alloy concentration. Swanson and Parr (149) showed this decrease for iron-nickel alloys from about 750°C for pure iron to 360°C for iron - 10% nickel. The addition of interstitial trace elements such as carbon or nitrogen have a similar but more pronounced effect.

In all binary substitutional solid-solution alloys the transformation temperature can be depressed to a temperature of maximum undercooling by increasing the cooling rate (149) indicating that the transformation is thermally activated. Typical C-curve behaviour is shown in TTT curves. By quenching past the nose of the C-curve the massive ferrite reaction can be completely suppressed in favour of massive martensite or bainitic ferrite.

Bearing these points in mind, the transformation of alloy 193 to massive ferrite may be due to the fact that titanium and aluminium have reduced the interstitials to a very low level

resulting in an increase in transformation temperature. The grain size being finer than alloy 181 gives a greater grain boundary area, and as massive ferrite is nucleated at the prior austenite grain boundaries there are many more nuclei available for transformation to massive ferrite.

The hardness of alloy 193 in all conditions, Table 13, is lower than alloy 181. Nasim (2) found a similar trend in his pure alloys of Fe-Mn. In the quenched condition his Fe-8Mn-0.1Ti-0.1Al alloy had a hardness of 253 Hv30 compared to 289 Hv 30 in his Fe-8Mn alloy (both alloys contained 0.03%N). He suggested that this was due to the titanium and aluminium scavenging the interstitials to very low levels in solid solution thereby making it softer. His alloys were found to be fully lath martensite. However, his austenitisations were much higher, 1000°C, compared to the present investigation, thereby producing a much coarser grain size and hence less nuclei for massive ferrite transformation.

Holden et al (28) and Roberts (49) both found massive martensite at manganese levels similar to the present investigation, but not massive ferrite unless the manganese level was much lower at 5% (49).

Further support for the presence of massive ferrite in the present investigation was found from the dilatometric studies, Tables 14, 15, 16 and figure 52. There is good agreement that the Ms for lath martensite is 355±10°C and for massive ferrite a higher arrest temperature of 390°C, particularly for alloy 273. However one sample of alloy 193, Table 14, did show

an Ms of 380°C indicating massive ferrite, although the average Ms was 345°C.

It is therefore suggested that a combination of low austenitisation temperature and low interstitial levels in solid solution produce a structure of massive ferrite.

5.3 Influence of Heat-Treatment on Toughness of Pure Alloys 273 (Fe-7.85Mn) and 275 (Fe-8Mn-0.13Ti-0.104Al)

5.3.1 Air Cooling and Water Quenching from 850°C

Figure 53 shows graphically the effect of water quenching from 850°C compared with air cooling for alloys 273 and 275.

The DBTT in alloy 273 (Fe-7.85Mn) was reduced by 144°C for water quenching rather than air cooling whereas for alloy 275 (Fe-8Mn-0.13Ti-0.1 04Al) the DBTT was reduced by only 31°C. In the water quenched condition alloy 273 exhibited a lower shelf fracture mode of intergranular +20% cleavage, whereas 275 was fully cleavage fracture. On air cooling both alloys exhibited intergranular plus cleavage fractures. The lower DBTT of alloy 275 in both the air cooled and water quenched conditions can be attributed to the 0.13Ti and 0.104Al additions to 275. This resulted in both a lower hardness and finer grain size in 275, Table 22.

The above results therefore indicate that embrittlement is occurring in alloy 273 which is reduced in 275 by the aluminium and titanium additions. Bolton (1) and later Freeman (150) found that Fe-Mn alloys containing between 4 and 10% manganese

in the lath martensite condition exhibited brittleness in the as-quenched condition due to a weakness at the prior austenite grain boundaries. Bolton (1) suggested that the segregation of some harmful impurities may have occurred during austenitisation leading to a potential weakening of grain boundaries in the subsequently quenched condition. Freeman (150) reported intergranular fracture in a 10% Mn alloy in the water quenched condition. In contrast, Roberts (49) did not find any intergranular brittleness in his alloys. Nasim (2) found agreement with both these investigators. He found intergranular fracture in his Fe-8Mn-0.003N and Fe-8Mn-0.03N alloys in the water quenched condition. His Fe-8Mn-03N-0.1Ti-0.1Al alloy exhibited cleavage fracture in agreement with Roberts (49). Alloys 273 and 275 are also in agreement with Nasim. Nasim found intergranular fracture on air cooling with brittle cleavage on iced-brine quenching. He found a rise in DBTT in his Fe-8Mn-0.003N alloy of 350°C on air cooling compared to iced-brine quenching. In his titanium and aluminium treated alloy a corresponding increase in DBTT of ~150°C was found.

Auger electron spectroscopy studies were undertaken on the intergranular areas of the fracture surfaces of both alloys 273 and 275 to look for any embrittling element that may be present. Alloy 275 in the water quenched condition gave a fully brittle cleavage fracture, figure 66, and so was not examined. Alloy 275, on air cooling, however, was predominantly intergranular, figure 65. AES studies revealed 2.6 ± 0.8 atomic % phosphorus at the fracture surface, Table 38 and figure 136. This P persisted until 25 monolayers were removed.

Manganese was not apparently segregated to the grain boundary. The C, O and Si is probably contamination from the argon used in sputtering, as they increased markedly upon argon-ion sputtering, reaching a peak at 20 monolayers.

Alloy 273 (Fe-7.85Mn) on air cooling was also predominantly intergranular in fracture mode, figure 62. AES studies again revealed phosphorus present on the intergranular facets which was removed after sputtering 10 monolayers. Nitrogen was also present at 3.2 ± 1.0 atomic % which increased slightly on sputtering before dropping off completely after 30 monolayers removed, figure 129 and Table 37. Again, C, O and Si were present and increased on sputtering. Nickel was also found on the fracture surface at 2.8 ± 0.1 atomic % which was removed after 10 monolayers. Conversely, manganese increased on sputtering.

Comparing these two alloys in the air cooled condition it appears that the titanium and aluminium additions have been successful in alloy 275 in scavenging nitrogen as it was only present on the fracture surface of 273. Phosphorus was present on both fracture surfaces. Hence, it is clear that the higher DBTT of 273, in the air cooled condition, of 210°C is due to P and N compared to alloy 275 with a DBTT of +26°C with only P present.

Alloy 273 in the water quenched condition also displayed intergranular fracture, although a higher proportion of cleavage fracture at 20% was exhibited. The AES results again revealed desegregation of carbon at the boundary with oxygen

contamination, figure 120 and Table 36. Manganese was slightly higher at the grain boundary at 12.9% peak height ratio which reduced on sputtering to 7.2% after 30 monolayers.

Nasim (2) also found P and N at the grain boundaries in his Fe-8Mn low N alloy after water quenching on one sample, with another sample having enrichment of Mn and N at the intergranular boundaries. During air cooling he postulated that Mn and N had cosegregated to the prior austenite grain boundaries but found no evidence of Mn segregation in the stable austenite field. Evidence to support this was obtained from Auger spectra on fractured surfaces in the water quenched condition (1000°C austenitisation). Manganese concentrations on the fracture surface approximated to that of the bulk. These results therefore indicated that no significant alloying element segregation had occurred during the austenitising treatment. Nasim (2) found, however, that manganese segregated to grain boundaries in the metastable austenite $(\alpha+\gamma)$ phase fields with enhanced concentrations of nitrogen at the austenite grain boundaries.

The possible driving forces for segregation of manganese could be as follows:

(a) There is a grain boundary segregation of nitrogen which because of its strong interaction with manganese (80) would attract manganese atoms to the grain boundaries, thus lowering the chemical potential of the system. Evidence for a strong Mn-N interaction was first reported

by Fuller and Garwood (151) who reported a strong secondary hardening peak due to precipitation of Mn_3N_2 on tempering at 450°C.

(b) The equilibrium segregation of manganese to the prior austenite grain boundaries in the $(\alpha+\gamma)$ phase field, while in the metastable austenitic condition. However, the bulk reaction γ (metastable) $\rightarrow (\alpha+\gamma)$ equilibrium is extremely slow in the Fe-Mn system (19).

(c) Segregation of N and Mn to prior austenite grain boundaries in the metastable ferrite or lath martensite condition below the Ms of 355°C. However, the diffusion of Mn at these temperatures is rather sluggish even in ferrite. Nitrogen, on the other hand, being an interstitial may well segregate at these temperatures.

The segregation of nitrogen to the prior austenite grain boundary is also given support by Krahe and Guttmann (152) in an Fe-1.92Mn-0.2C alloy. The driving force for segregation of nitrogen to prior austenite grain boundaries could be due to three factors:

(a) The misfit strain of interstitial nitrogen in the austenite lattice, which is more easily accommodated at grain boundaries.

(b) Reduced solid solubility of nitrogen during quenching, ie nitrogen comes out of solution during cooling due to its lower solubility.

(c) Chemical interaction with major alloying elements which have previously concentrated at the grain boundaries.

Nasim (2) suggested that since rapidly quenched alloys failed by cleavage it was unlikely that substitutional segregation of nitrogen to grain boundaries occurred during austenitising. Nasim also found that the level of manganese on brittle grain boundaries was characteristic of the bulk in water quenching and so (c) would not occur. It is, therefore, likely that (a) and (b) in combination is responsible for segregation of nitrogen to prior austenite grain boundaries. This will be particularly so when the $\gamma/\alpha+\gamma$ solvus is crossed and austenite is metastable. Segregation in metastable austenite will continue down to the Ms (~350°C). At the Ms many other sinks such as packet boundaries, dislocations and interlath boundaries would arise for impurities.

In summary, the Mn-N interaction found on air cooling by Nasim was not found in the present investigation. Only alloy 273 in the water quenched condition showed a slight increase in manganese at the grain boundary. Nitrogen was only present on intergranular facets in alloy 273 after air cooling from 850°C. It is clear that the titanium and aluminium additions have scavenged free nitrogen in alloy 275. Water quenching has been sufficiently fast to prevent segregation of nitrogen in both alloys. Nasim found nitrogen even after iced-brine quenching on intergranular facets. This may be due to the higher nitrogen content of his alloys compared to alloys 273 and 275. Nasim's low nitrogen alloy K1525 contained 0.003%N whereas 273 and 275

contained 0.0014 and 0.0017%N respectively. K1525 also exhibited a higher DBTT of +115°C after water quenching compared to +66°C in 273 after a water quench, probably due to the higher nitrogen level. Nasim also austenitised at 1000°C compared to 850°C in the present investigation. Quenching or air cooling from 1000°C compared to 850°C would give a larger driving force for segregation of Mn and N. Certainly, phosphorus can be held partly responsible for intergranular fracture in these alloys on air cooling as found in 273 and 275 at intergranular fracture surfaces. Nasim also found P on his intergranular facets.

Nasim also found carbon de-segregation at the grain boundary as in the present investigation. It is suggested that this is contamination due to sputtering, also suggested by Nasim.

However, Lee and Morris (67) carried out Auger analysis on an intergranular fracture in Fe-12%Mn after water quenching and found no impurity segregation. They deducted that the grain boundary is the "weak-link" in Fe-Mn alloys and the easiest path for fracture, due to a tough matrix. Nasim (2) however, has fouud that iced-brine quenching suppresses intergranular fracture, suggesting that grain boundary fracture is not microstructurally determined. It is possible that Lee and Morris may have slight segregation beyond the limits of detection.

5.3.2 Tempering at 600°C

Tempering at 600°C produces reverted austenite which gives a large improvement in impact toughness as shown by the reduction

in DBTT, Table 20 and figures 58 to 61. As expected, water quenching and tempering gave superior impact toughness compared to air cooling and tempering. However, alloy 273 gave a lower DBTT in the AC+T and WQ+T conditions when compared to 275, although alloy 275 had the finer grain size. As explained in Section 4.4.2 this must be due to the higher volume fraction of austenite present in the WQ+T condition of alloy 273, Table 21. However, this does not explain the lower transition temperature in the AC+T condition of 273 which had a slightly lower austenite level than 275; 2.5% γ in alloy 275 compared to 2.0% in alloy 273 at room temperature. This may be due to inaccuracies in measurement of austenite. Table 21 shows that on cooling to -196°C the 2.0% γ at room temperature rose to 3.1% γ in the same sample. It is highly unlikely that the austenite increased on cooling to -196°C and it is suggested that the room temperature austenite level may in fact have been slightly higher.

The levels of reverted austenite were in fact similar to those found by Charlesworth (4) in alloys 181 and 193 upon quenching and tempering of 1.5% and 4.4% respectively. However, he also found high levels of epsilon martensite of 20.2% and 26.6% in 181 and 193 respectively, whereas the present investigation found none. This may be due to the reasons discussed in Section 5.1.

On examination of the fracture surfaces the ductile areas on the lower shelf of the impact curves appeared as 'rough' areas at low magnification, figure 67. At higher magnifications these areas looked like ductile tearing, figure 68. It is suggested

that these areas are due to the presence of reverted austenite. This austenite, which precipitates at the prior austenite grain boundaries, as well as inter-packet and inter-lath boundaries, may have impeded the fracture path on impact testing. The austenite being tough at very low temperatures may have resisted the brittle fracture path and have experienced decohesion along its interface with the neighbouring ferritic matrix, as the main crack propagates through the structure.

Duchateau and Guttmann found similar 'rough' areas on their SEM fracture surfaces (69). Their fractures were, however, intergranular and they postulated that the rough areas were either ductile rupture or brittle decohesion of the austenite along the prior austenite grain boundaries. Stannard and Baker (88) also found that many grain boundary facets had dimpled surfaces characteristic of ductile failure on their intergranular fracture surfaces. This was after a heat treatment consisting of an 850°C oil quench and 650°C temper to produce reverted austenite. They deduced that reverted austenite was responsible as it formed a continuous grain boundary film making the boundary weaker than the matrix and thereby allowing a low energy ductile crack to propagate through the grain boundary region.

Schumann (48) and Charushnikova (64) have also reported the benefit of reverted austenite and epsilon martensite as ductile areas to arrest the propagation of brittle cracks and/or sinks for embrittling impurities such as nitrogen. Bolton (1) reported an improvement in impact toughness by treating his

alloy for one hour at 600°C, suggesting it to be due to de-segregation of impurity elements at prior austenite grain boundaries. It is now evident that although de-segregation may occur, the main de-embrittling effect is due to reverted austenite formation.

To take full benefit of reverted austenite effects it should be stable down to -196°C, achieved by adding appropriate alloying elements or by suitable heat treatment (91, 92). In the present investigation room temperature charpy samples with known amounts of reverted austenite were cooled to -78°C and -196°C, and results show in Table 21 that there was no transformation of the austenite at these temperatures, proving the reverted austenite to be thermally stable.

Stannard and Baker (88), however, found in their 6% manganese alloy that there was a decrease in stable austenite and a production of fresh α' martensite or epsilon phase when cooled to -196°C. This resulted in a reduction in impact values. It is, therefore, clear that the level of substitutional alloying element and its partitioning to austenite during heat treatment is important in the stability of austenite down to -196°C.

AES Studies

Auger electron spectroscopy was done on alloy 273 in the air cooled and tempered condition, Table 39, figures 145 and 146, in order to try to determine if any elements segregate preferentially to ductile areas (believed to be reverted austenite) compared to cleavage areas.

Results have shown that P was observed on both ductile and cleavage areas of similar proportions; 2.9 ± 0.9 atomic % on cleavage facets compared to 2.6 ± 0.8 atomic % on ductile areas. In both cases sputtering removed the P after 15 monolayers. C, O and Si were, as previously, detected on as-quenched and air cooled specimens, found to increase on sputtering, and are thought to be due to contamination. Sulphur was also found on both types of fracture area at a level of 1.8 ± 0.7 atomic % on cleavage and 1.2 ± 0.5 atomic % on ductile areas. This disappeared on sputtering and may be MnS inclusions on the fracture surface. The main differences between the two types of fracture were found with N and Mn. Nitrogen was quite high on the cleavage fracture surface at 7.0 ± 2.3 atomic % and decreased on sputtering. It is possible that the fracture path was inter-lath on cleavage fractures where P and N may have segregated during cooling. Motley (147) found evidence to support inter-lath fracture routes in his alloys due to segregation within the ferrite during ageing at 450°C. Fractographic studies showed that many of the prior austenite grain boundaries, along which the brittle fracture occurred, were faceted. The distance between the facets was the same as the width of martensite laths, suggesting a weak inter-lath boundary due to segregation.

The level of manganese was overall at a higher level in the ductile area compared to the cleavage areas. This may be explained by the segregation of manganese to reverted austenite on tempering.

5.4 Influence of Heat-Treatment and Higher Impurity Levels on Toughness of Commercially Impure Alloy 278 (Fe-8Mn - 0.19Ti-0.012N)

Alloy 278, made to commercial impurity levels but with sufficient titanium to tie-up free nitrogen, gave relatively poor impact properties, figure 104 and Table 34, for similar heat-treatments to alloys 273 and 275. Water quenching improved the DBTT in contrast to air cooling, and tempering at 600°C to produce reverted austenite further improved toughness. However, the lowest DBTT was -50°C after a 4 hour temper at 600°C which produced 17.4% γ and 3.6% ε. With this level of austenite it would have been expected that a significant improvement in properties compared to alloys 273 and 275 would have been obtained. The main difference between these alloys and 278 was the presence of epsilon martensite which may be embrittling (96, 116). However, Duchateau and Guttmann (69) found that epsilon martensite was not embrittling if it was in small amounts in an extremely dispersed morphology within small austenite islands.

Hardness was significantly higher, Table 35, when compared to alloy 275 which was also titanium treated; ~275Hv30 in 278 compared to 207Hv30 in 275 for 1h850°CWQ+2hr600°CWQ. Grain size was also significantly reduced in alloy 278 at 20 μm compared to 31 μm in the optimum heat treated condition, Table 35. The higher hardness and smaller grain size is probably due to the higher carbon and titanium levels in this alloy, producing a pinning dispersion of TiC for a finer grain size, and increasing hardness due to precipitation hardening, and solid solution hardening from carbon.

The low temperature fracture mode was quasi-cleavage with ~50% ductile tearing (due to the austenite) in the air cooled and tempered or water-quenched and tempered conditions, figure III. Upper shelf fracture surfaces exhibited ductile dimples which contained numerous particles thought to be Al_2O_3 , Ti(C,N) and AlN, identified by edax., figures 106 to 109. A high level of AlN and Ti(C,N) at the grain boundaries may explain the reduced upper shelf energies compared to the pure alloys 273 and 275 and the generally poorer DBTT.

Supporting evidence for this is provided by Nasim's work (2). He found a higher transition temperature in alloy 137, Fe-8Mn-0.1Ti-0.1Al, of -40°C after "thermal cycling" compared to his pure alloy K1525, Fe-8Mn,of -60°C. He suggested that this was due to grain boundary precipitation of AlN and Ti (C,N).

Quarrell (153) and Fukagawa (154) also reported that precipitation of AlN on primary austenite grain boundaries in low alloy steels resulted in embrittlement.

This higher level of AlN and Ti (C,N) in alloy 278 could also explain the presence of higher levels of austenite and epsilon martensite when compared to pure alloys 273 and 275. Nasim (2) found that on thermal cycling the precipitation of AlN and Ti(C,N) resulted in acceleration of the whole diffusion process, causing an increase in the volume fraction of γ , ε . Support for this is provided by Freeman (150) in Fe-10Mn-0.04C where austenite precipitation was observed after one hour at 570°C or 24 hours at 520°C. Austenite was found at the lath and prior austenite grain boundaries, growing into long narrow islands. The lath....

and prior austenite grain boundaries were also sites for precipitation of Fe_3C and it was suggested that the austenite was nucleated at these carbide particles. This process has also been observed in Fe-9% nickel steels (155) where austenite nucleates at the carbide particles which had precipitated during the quench at lath boundaries.

It is therefore suggested that larger amounts of reverted austenite and epsilon martensite are present in alloy 278 and are due to precipitation of AlN and Ti(C,N) particles at the grain boundaries.

Auger electron spectroscopy of the cleavage fractures, Table 40, and figure 150, revealed P and Mn at the fracture surface which both fell away during sputtering. Carbon and oxygen were also present on sputtering, as previously found in 273 and 275, which is probably due to contamination. The sample examined was air cooled from 850°C and it can only be assumed that P segregated to interlath and/or interpacket boundaries on air cooling, which may have been the route for a brittle cleavage crack.

In summary, the poor impact properties of this alloy may be due to the intrusion of epsilon martensite, the presence of AlN, Ti(C,N) or Al_2O_3 at the grain boundaries, and the increased hardness of this alloy compared to 273 and 275.

5.5 Microstructures of Alloys 273(Fe-7.85Mn), 275(Fe-8Mn-0.13Ti-0.104Al) and 278(Fe-8Mn-0.19Ti-0.012N)

Alloys 273 and 275 both exhibited mixed structures of lath

martensite and massive ferrite in the air cooled and water quenched conditions, as shown typically in figures 71 to 74. These mixed structures were also found in alloy 193 (Fe-8.54Mn-0.17Ti-0.18Al) as discussed in Section 5.2. Massive ferrite, it was suggested, is possible due to low levels of interstitial elements in solid solution, which raises the transformation temperature. So, for alloy 275 the additions of titanium and aluminium have reduced the interstitials, carbon and nitrogen to very low levels. However, alloy 273 did not contain aluminium and titanium, similar to alloy 181 (Fe-7.89Mn) which produced a lath martensite structure. But alloy 273 produced a mixed structure. Presumably, this is due to the low levels of carbon and nitrogen already in solution of 0.008%C and 0.0014%N, compared to 0.014%Cand 0.008%Nin alloy 181.

Conversely, alloy 278 (Fe-8Mn-0.19Ti) contains quite high levels of carbon and nitrogen of 0.028% and 0.012% respectively and so,as expected,this alloy produced a fully lath martensite structure, figures 112 to 116.

The reverted austenite produced in all three alloys had similar morphologies. Elongated islands of dimensions approximately 2μm by 0.1μm were produced at prior austenite grain boundaries and at interlath boundaries. Patwardhan (156) recently pinpointed plausible locations for austenite retention in powder samples of 0.02%C, 4.0%Mn, 1.0%Si alloys. The locations for austenite retention of decreasing probability were:

(a) grain boundaries and adjoining areas

(b) interpacket boundaries

(c) interlath boundaries

Patwardhan found that a thin layer of untransformed austenite found along interpacket boundaries in his lath structure explained the better toughness for a given strength level in the lath structure compared to lower bainites.

Duchateau and Guttmann (69) also found reverted austenite at inter-lath and prior austenite grain boundaries of thickness 0.05-0.1μm which compare well with 0.1μm thickness found in the present investigation.

Zackay (157) found that with multiple cycles the reverted austenite was retained in several unusual morphologies, particularly bead-like particles in the grain boundary.

Nasim (2) also found bead-like precipitated austenite at the grain boundaries in his thermally cycled material.

In the present investigation the orientation relationship between the austenite and the ferritic lath martensite was found to obey the Kurdjumov-Sachs orientation relationship:

$$\{111\}_\gamma \,//\, \{011\}_{\alpha'}$$

and $$\langle 110\rangle_\gamma \,//\, \langle 111\rangle_{\alpha'}$$

as shown in figures, 51, 78, 79, 86

Although many Ti(C,N) particles could be seen in the optical microstructures of 275 and 278, figures 80, 81, 112 and 113

only one carbide was found by transmission electron microscopy. Figure 87 shows the bright and dark field images of a particle thought to be TiC of orientation relationship:

$$(011)_{TiC} \;//\; (\bar{1}11)_{\alpha}$$

Epsilon martensite was not found in alloys 273 and 275 by either X-Ray diffraction or electron microscopy. However, alloy 278 did contain a small amount and was visible at inter-lath locations, figure 116. Nasim (2) found epsilon at similar locations in his alloys.

5.6 Resistance to Embrittlement at 450°C of Alloys 273 (Fe-7.85Mn) and 275 (Fe-8Mn-0.13Ti-0.104Al)

Results detailed in Section 4.4.7 indicate that both alloys are largely resistant to embrittlement at 450°C.

Bolton (1) first reported embrittlement when tempering Fe-Mn alloys in the range 250-450°C. Squires (66) also observed embrittlement on ageing between 300 and 500°C in Fe-Ni-Mn maraging alloys. This embrittlement was studied by tensile ductility tests and found to be a maximum at 450°C.

Nasim (2) found embrittlement was enhanced on ageing his Fe-Mn alloys at 450°C. K1525 (0.003N) embrittled very rapidly on ageing at 450°C, i.e. zero ductility after 5 minutes at 450°C. His higher nitrogen alloy 134 (0.03N) also embrittled rapidly on ageing at 450°C with a rise in DBTT from +40°C to +200°C in 6 minutes ageing time. In alloy 137 (0.03N) with titanium and aluminium additions, the rise in DBTT was less pronounced, from +10°C to +145°C in 6 minutes.

Alloy 181 (.008N) showed a considerable rise in DBTT on ageing from +650°C to +330°C in 6 minutes at 450°C. Alloy 193 (008N,0.1Ti,0.1Al) was comparable to that in alloy 137 of +30°C to +140°C in 6 minutes (see figure 15).

Nasim suggested that the embrittlement on ageing was a maximum at some intermediate level of 'free' nitrogen (alloy 181) and less for higher levels of nitrogen (alloy 134) or very low levels of nitrogen (alloys 137 and 193). The embrittlement was caused by Mn-N interaction on ageing at 450°C leading to grain boundary embrittlement.

The nitrogen levels in alloys 273 and 275 is at a very low level, and so from the above data it is not surprising that the alloys are resistant to embrittlement as there is very little free nitrogen in solution, particularly in 275 which was titanium and aluminium treated.

5.7 Tensile Properties of Alloys 273 (Fe-7.85Mn) and 275 (Fe-8Mn-0.13Ti-0.104Al)

Alloys 273 and 275 were tempered at 600°C and 650°C for times of 2 to 16 hours in order to produce structures of varying γ and ε phase content. Tensile tests at room temperature and -78°C were carried out for comparison with Nasim (2) who found unusual stress-strain curves attributed to deformation induced transformation of γ and/or ε to α during tensile testing at -78°C.

Results are detailed in Section 4.5. The unusual stress-strain curves of Nasim were not found in the above alloys, or in thermally cycled samples (Section 4.7). This may be due to the

higher levels of ε phase in Nasim's alloy of 28% in K1525 after thermally cycling compared to only 1.8% ε in alloy 273 for the same heat-treatment.

In the present investigation proof stresses tended to fall with a general increase in austenite and epsilon martensite levels. This generally led to an increase in impact energies of charpy samples.

In alloy 275 tempered at 600°C the room temperature proof stress fell with increasing tempering time, corresponding to an increase in γ and ε, figure 96.

However, the -78°C tensile tests showed a decrease in proof stress up to 8 hours at 600°C followed by a sharp increase after 16 hours at 600°C. This was also exhibited by the tensile stress at -78°C. A possible explanation is the fact that the γ and ε did not transform on testing for the 16 hr specimen, whereas the others did transform, i.e. $\gamma \rightarrow \alpha'$ and $\varepsilon \rightarrow \alpha'$, as shown by the X-Ray results in Table 26. This absence of transformation must be due to an increased stability of the γ and ε phases on tempering for a longer time at 600°C.

In alloy 273, figure 92, tempered at 600°C a fall in proof stress was noted after 8 and 16 hrs which corresponded to an increase in γ and ε levels. This also resulted in a decrease in hardness.

Tempering at 650°C tended to increase the tensile and proof strengths with a corresponding increase in hardness compared to 600°C.

In general, an increase in γ and ε levels led to a decrease in proof stress, but tensile stress was largely unaffected. This increase in γ and ε also led to an increase in corresponding impact energies at -78°C, figure 93.

Zackay's work (158) tends to support this as he found that with increasing amounts of ε in a primary α structure, the yield stress decreased. This was also found by Nasim (2) in K1525. Zackay also suggested that in a $(\alpha + \varepsilon)$ duplex structure the flow or strain tends to concentrate in the weaker ε phase and the yield stress is controlled by the strength of the ε phase.

Holden (28) also found that ε phase depresses the proof and tensile stresses in a ferritic structure. It is also worth noting from Holden's results that the presence of ε in an austenitic structure tends to increase the tensile and proof stresses, figure 17, and as the austenite level increases the strength falls.

5.8 Effect of Molybdenum on Toughness

Molybdenum was added to both pure and commercially impure Fe-Mn alloys as it is well known that it reduces the susceptibility of alloy steels to temper embrittlement (81). It has also been added to Fe-Mn alloys in the order of 2.5 and 5.0% (147) and 0.5% (69). However, it has been reported that it is not advantageous to add molybdenum in amounts greater than about 0.5% (70) and that higher concentrations can be detrimental (71, 147). For these reasons an addition of 0.5% was made to the base composition of Fe-8Mn.

5.8.1 Pure Alloys 325A (Fe-7.57Mn-0.5Mo) and 325B (Fe-7.59Mn-0.5Mo-0.1Al-0.085Ti)

The as-quenched grain size of alloy 325A was finer and the hardness lower than 325B, which explains the lower DBTT of +18°C of 325A compared to +52°C in alloy 325B, Table 46. Comparing this with the pure alloys 273 (Fe-7.85Mn) and 275 (Fe-8Mn-0.13Ti-0.104Al), alloy 275 gave the lower DBTT of -5°C compared to +66°C in 273. Again, alloy 275 had the finer grain size and lower hardness compared to 273, which supports the above findings. However, it seems somewhat anomalous why alloy 325B with the titanium and aluminium additions, had a larger grain size and higher hardness than 325A when the converse was expected.

The as-quenched fracture appearance in both alloys was a mixture of cleavage and intergranular, suggesting that the molybdenum addition was not completely effective in reducing embrittlement. Motley (147) found in his Fe-8Mn alloys containing 2.5% molybdenum that in the as-quenched condition the molybdenum improved toughness by changing the fracture mode from intergranular to cleavage. Duchateau and Guttmann (69) in their Fe-9Mn-0.5Mo alloy found that embrittlement was suppressed by the molybdenum addition due to the reduction in phosphorus at the prior austenite grain boundary. In Motley's alloy the molybdenum level was sufficient to improve toughness whereas the lower level of 0.5% in the present investigation clearly was not. In Duchateau and Guttman's alloy 0.5% molybdenum was sufficient to reduce phosphorus segregation but their alloy had very low nitrogen 0.0009% compared to 0.006% in alloys

325A and B. Auger analysis of fracture surfaces has not been done on the 0.5% molybdenum alloys in the present investigation, but it is proposed that the molybdenum addition may have been sufficient to give some reduction in phosphorus levels at grain boundaries but not enough to suppress nitrogen levels. The phosphorus level in Duchateau and Guttman's alloy was 0.007% compared to 0.006% in the present investigation.

In the quenched and tempered condition, Table 46, alloy 325A (Fe-7.57Mn-0.5Mo) had a DBTT of -64°C compared to -86°C in 325B (with Ti and Al additions). This can be explained by the higher amount of reverted austenite in 325B of 5.8% compared to 3.3% in 325A. This compares well with alloys 273 and 275 where the higher austenite level of 3.6% in 273 in the same heat-treatment condition gave a lower DBTT than 275 which had only 1.9% austenite. No epsilon martensite was present in either alloy 325A or 325B, consistent with none present in 273 and 275.

5.8.2 Commercially Impure Alloys 317 and 318 Containing 0.5%Mo and Various Levels of Titanium

These alloys were only investigated in the optimum heat-treated condition of 1h850°CWQ+2hr600°CWQ. Results are detailed in Section 4.12 and Table 48, figures 182 and 183. With the higher nitrogen level of this set of alloys at ~0.011%, similar to alloy 278 (commercially impure alloy with 0.19%Ti and 0.012%N) it was expected that the higher the level of titanium present, the lower the DBTT as the amount of free nitrogen

present would be lower. Also, increasing titanium levels were expected to give a reduction in grain size, thereby improving impact properties.

Alloy 318A (0.05Ti) gave the lowest DBTT of -100°C which corresponded to the highest level of reverted austenite, 36.6%. However, the amount of austenite and/or epsilon martensite did not in general correlate well with DBTT. Duchateau and Guttmann (69) found that as $(\gamma+\varepsilon)$ increased the DBTT decreased. This anomaly may be explained by other factors affecting toughness.

As already mentioned, increasing titanium levels were expected to give finer grain sizes. In fact, the alloy with the finest grain size was 318B which contained 0.16% titanium. This may be explained by the stoichiometry of TiC, TiN and AlN. In 318B for the carbon level of 0.037%, 0.148% titanium would be necessary for stoichiometry of TiC. For the nitrogen level of 0.011% a level of 0.021% aluminium or 0.038% titanium would be necessary for stoichiometry of TiN or AlN. The alloy actually contained 0.05% Al and 0.16%Ti and so this alloy was very close to the required stoichiometric levels, being slightly above. It therefore appears that there is an optimum reduction in grain size when stoichiometric proportions of TiC, TiN and AlN are produced.

Hardness tended to decrease with increasing titanium levels, as found in 325A and B and in 273 and 275. This is probably due to interstitials being taken out of solution. The hardness was high, in general, at ~360-450 Hv30, compared to alloy 278

(Fe-8Mn-0.19Ti) which was 275 Hv30. This is probably due to the molybdenum which may produce solid solution hardening.

Austenite levels were quite high which is surprising as molybdenum is a ferrite former. Comparing 318B (0.16Ti) with 278 (Fe-8Mn-0.19Ti) both had a DBTT of -40°C. However, 278 had 10% γ and 3.5% ε compared to 318B which had 14.3% γ and 7.9% ε. The molybdenum does not therefore appear to have affected γ and ε levels. It seems that austenite levels tend to decrease with increasing titanium level.

5.8.3 Summary

The molybdenum addition of 0.5% does not seem to have improved toughness levels in the quenched or quenched and tempered conditions. It may show an improvement on embrittlement in the air cooled condition, which requires further work. Titanium level, however, does seem to affect toughness through its effects on grain size, austenite level and free nitrogen. There is an optimum level which seems to be about 0.05% in these alloys.

5.9 Grain Refinement of Commercially Impure Alloy 277 (Fe-8Mn-0.23v)

5.9.1 Solution Treated Toughness

Iced brine quenched samples (from 1160°C) gave a poor DBTT of +170°C with a grain size of 55μm and a hardness of 358 Hv30. The large grain size and the presence of quench cracks (figure 165) explains the high DBTT. Re-austenitising at 850°C resulted in a

finer grain size of 31μm and a lower hardness of 345 Hv30. The DBTT was correspondingly lower at + 140°C. The absence of precipitates at these temperatures to pin the grain boundaries has allowed excessive grain growth, particularly at 1160°C. These results formed the base for comparison of refinement of grain size through particle pinning of boundaries by vanadium carbide.

Scanning electron microscopy revealed an intergranular fracture mode for IBQ samples and quasi-cleavage/intergranular for IBQ+850°CWQ. The intergranular fracture, figure 156, is probably due to the quench cracks arising from the initial IBQ. Auger electron spectroscopy of the intergranular facets, Table 41, and figure 154, failed to reveal any intergranular segregation of P, Mn or N. Carbon was present on the fracture surface. This may be due to contamination, although previous samples examined (Section 4.9) had only shown carbon contamination on sputtering.

5.9.2 Grain Refinement Heat-Treatment

From the age-hardening curves, figure 160 and 161, an ageing temperature of 550°C was chosen with ageing times of 3, 10, 18 and 30 hours. Resultant re-austenitisation transition curves, figure 155, showed a reduction in DBTT with time at temperature and a corresponding decrease in grain size, Table 43.

The temperature of 550°C was chosen to give precipitation of vanadium carbide in a reasonable time. However, at 550°C precipitation of reverted austenite occurs which has an effect

on grain size and possibly carbide formation. Figure 171 shows the amount of austenite produced on ageing; increasing with ageing time at 550°C. Figure 171 also shows the decrease in grain size due to the precipitation of vanadium carbide pinning grain boundaries. The grain size is reduced to 3.8μm after 30 hours at 550°C and re-austenitisation. It is suggested that the reverted austenite produced on ageing, together with the vanadium carbide precipitates help to refine the grain size. Figure 168 shows carbides on a boundary.

In the above results, even overageing of carbides, above the hardening peak, figure 171, of ~18 hours at 550°C resulted in a reduction of grain size. In theory, as the carbides overage and coarsen the grain-pinning effect of the carbides should decrease resulting in an increase in grain size. The continued decrease in grain size on overageing must therefore be due to the reverted austenite produced on tempering. This in effect breaks up the structure as found in thermal cycling treatments (2).

5.9.3 Predicted Grain Size

Section 2.3.6 describes the theory of grain refinement due to pinning of grain boundaries by precipitates. Using the Zener equation (104) and the Gladman equation (106) an attempt has been made to predict the grain size of alloy 277 after the grain refinement heat treatment, using the 3 hr at 550°C temper. Appendix I details the calculations.

From Zener's equation the smallest grain size should be 17.2μm, whereas for the 3 hr at 550°C treatment it was reduced to 12.5μm.

This was an overestimate from Zener's equation as expected. Gladman's equation, however, underestimates the grain refinement of 0.56 - 1.69 μm.

To account for these differences the following points should be noted:

(i) The volume fraction of carbide was theoretically determined as it is very difficult to obtain from carbon replica photomicrographs.

(ii) The value of Z (ratio of the radii of growing grain and its neighbour) is not an easily calculated value and is assumed to lie between 2 and $\sqrt{2}$ (107).

(iii) The mean precipitate size was taken to be 0.027 μm. (diameter) calculated from 790 measurements. However, the 'median' precipitate size was 0.016 μm. (diameter)

(iv) Grain refinement due to austenite has not been accounted for in the calculations.

Clearly, further work is necessary to accurately quantify the above parameters. Assessment of particle sizes at the other ageing of times of 10, 18 and 30 hours would help in this respect. However, it is clear that the grain refinement heat treatment has worked and provided the 'quench crack' problem is overcome, alloys could be produced with ultra-fine grain sizes with improved low temperature toughness.

5.10 The Effect of Epsilon and Austenite Phases on Strength and Toughness

As discussed in Section 2.3.6 the precise mechanism by which reverted austenite improves toughness is not clear. It has been suggested that:

(i) The austenite islands act as a sink for impurity atoms, thereby reducing temper embrittlement.

(ii) The austenite islands act as shock absorbers as FCC alloys have excellent toughness at low temperatures.

(iii) Grain refinement of the ferrite matrix takes place by formation of finely dispersed austenite islands during tempering.

(iv) Transformation of the austenite to α-martensite and/or ε-martensite may occur during impact testing and thereby improve the toughness.

In the present investigation the presence of reverted austenite at prior austenite grain boundaries and inter-lath boundaries has produced significant improvements in toughness of iron-manganese alloys. SEM fractographs have revealed that the presence of reverted austenite results in areas of 'ductile tearing', figure 68, at the lower shelf energies. However, it is not clear whether the crack propogates through the ductile austenite phase or along the interface between the austenite and lath martensite. Motley (147) showed on an optical micrograph

of a fractured charpy sample, that an intergranular crack went through the reverted austenite, as it could be seen either side of the crack. He suggested that toughness was improved in his Fe-Mn-Mo alloys due to the crack blunting mechanism of austenite at prior austenite grain boundaries. Duchateau and Guttmann (69) suggested that the reverted austenite suffered brittle decohesion along the prior austenite grain boundaries. Fultz and Morris (87), however, found that when good fracture toughness was exhibited in their Fe-6%Ni alloy the austenite had transformed before it could interact directly with a propagating crack.

In the present investigation, tensile tests were performed on specimens with various levels of γ and ε to study the effects of transformation on testing (Section 5.7). In general, it was found that increasing levels of $(\gamma+\varepsilon)$ led to a decrease in proof strength and an increase in impact energy. Transformation of the γ and ε had taken place on testing through the transformations $\gamma \rightarrow \alpha'$ martensite and $\varepsilon \rightarrow \alpha'$ martensite. No direct evidence of $\gamma \rightarrow \varepsilon$ was found which would have resulted in an increase in ε from a corresponding decrease in γ. However, one sample, alloy 275, tempered for 16 hr at 600°C did not transform on tensile testing, due to stability of γ and ε through the long tempering treatment. This specimen showed an increase in proof strength. A corresponding decrease in impact energy was not evident, but tests were carried out at -78°C, close to the DBTT of this alloy. So, from the above evidence it is possible that transformation of $\gamma+\varepsilon$ on testing leads to an increase in impact energy. This agrees with Fultz and Morris (87) in that they encountered good fracture toughness when the austenite had transformed before it could interfere directly with a crack.

Haga (92) suggested that austenite did directly interfere with crack propagation as the transformation of austenite in his specimens occurred no further than 10μm from the fracture surface. However, Haga observed poor impact energies corresponding to a shallow depth of plastic deformation below the fracture surface. Fultz and Morris deduced that greater depths of plastic deformation below a fracture surface and corresponding transformation of austenite resulted in greater toughness.

It is therefore suggested that (iv) above does occur in that γ and ε transforms during impact testing, thereby improving toughness. For point (ii) the austenite islands may act as shock absorbers but they do transform to α' martensite ahead of the crack tip. De-cohesion may occur along the austenite/lath martensite boundary.

Auger studies of ductile areas and cleavage areas failed to reveal P and N segregation to the ductile areas, thought to be austenite, Section 5.3.2. However, an increase in Mn was found compared to the cleavage areas suggested partitioning of manganese to the reverted austenite. The fact that the reverted austenite precipitates at the grain boundaries means that it may reduce temper embrittlement and so point (i) may be correct.

Point (iii) suggests that grain refinement may occur during tempering by the formation of finely dispersed austenite islands. This appears to hold true for alloy 277 which was

grain refined by both vanadium carbide particles pinning the grain boundaries, and by the presence of reverted austenite. After overageing, grain refinement still occurred and this must have been due to the presence of reverted austenite after tempering at 550°C, which helped to refine the structure upon re-austenitising at 850°C. (This point is discussed in Section 5.9.)

No evidence has been found to suggest that epsilon is embrittling. Duchateau and Guttmann (69) deduced that its effect was beneficial and not distinguishable from that of austenite.

5.11 Impact Toughness of 5% Nickel and 9% Nickel Steels

Two nickel steels were impact tested for comparison of properties with the Fe-Mn alloys investigated. From the results, Table 50 and figure 187, it is clear that the 9% nickel steels are still superior to Fe-Mn alloys, even though the 9% nickel steel was made to commercial impurities. The DBTT of 9% nickel was $<$ -160°C whereas the best Fe-Mn alloy in the present investigation was alloy 273 with a DBTT of -125°C. However, the 5% nickel steel had a DBTT of -70°C so it would appear that with careful control of P and N levels for a commercially viable cryogenic steel the Fe-8Mn alloys may have a future, particularly if the price of nickel continues to rise.

heat-treated conditions has revealed that the phase analysis varies from the surface of samples into the bulk. Epsilon martensite was found to be greater in the surface layers, reducing to a constant level after ~ 2 minutes electropolish. Austenite was found to be low at the surface compared to the bulk. Deformation, through grinding leads to an increase in epsilon phase through a deformation-induced transformation.

Good correlation of phase analysis was found by both X-Ray diffraction and Mossbauer techniques.

2. Pure alloy 193 (Fe-8Mn-0.1Al-0.1Ti), in the air cooled condition, exhibited a structure of massive ferrite compared to alloy 181 (Fe-8Mn) which was fully lath martensite. This is suggested to be due to the titanium and aluminium additions reducing interstitials to very low levels, resulting in reduced hardenability and transformation at a higher temperature to massive ferrite.

3. Alloys 273 (Fe-8Mn) and 275 (Fe-8Mn-0.1Al-0.1Ti) exhibited mixed structures of lath martensite and massive ferrite as found in alloy 193 due to low interstitial levels. Alloy 278 (Fe-8Mn-0.2Ti) was fully lath martensite, presumably due to the higher levels of carbon and nitrogen.

4. Alloy 193 (Fe-8Mn-0.1Al-0.1Ti) in the air cooled or water-quenched conditions had a lower hardness compared to alloy 181 (Fe-8Mn) due to titanium and aluminium scavenging interstitials to low levels.

5. Alloy 275 (Fe-8Mn-0.1Al-0.1Ti) gave improved impact properties after water quenching (cleavage fracture) compared to air cooling (intergranular fracture) from austenitisation temperature. Also, the ductile-brittle transition temperature was lower than alloy 273 (Fe-8Mn), and the grain size finer and hardness lower. The titanium and aluminium additions were successful in scavenging nitrogen, as it was only present on the intergranular fracture surface of alloy 273.

6. Phosphorus and nitrogen were found on intergranular fracture surfaces after air cooling of alloy 273, which explains the high DBTT of +210°C. Only phosphorus was found on the intergranular fracture surface of alloy 275 after air cooling, resulting in a lower DBTT of +26°C compared to 273. The Mn-N interaction found after air cooling by Nasim (1) was not found in the present investigation.

7. A large improvement in toughness was found on tempering at 600°C due to the formation of reverted austenite at prior austenite and inter-lath boundaries.

8. Alloy 273 had a lower DBTT in the air cooled and tempered condition (1h850°CAC+2h600°CWQ) and the water-quenched and tempered condition (1h850°CWQ+2h600°CWQ) compared to alloy 275. This was thought to be due to the higher volume fraction of reverted austenite in alloy 273.

9. Evidence to support segregation of manganese to reverted austenite on tempering was found by AES studies on cleavage

and ductile fracture surfaces. The ductile areas of the fracture surface, thought to correspond to areas of reverted austenite, were higher in concentrations of manganese than cleavage areas.

10. Alloy 278 (Fe-8Mn-0.2Ti), made to commercial impurity levels, resulted in poor impact properties compared to pure alloys 273 and 275. This may be due to the intrusion of epsilon martensite and/or the presence of AlN, Ti(C,N) or Al_2O_3 at the grain boundaries, as well as the increased hardness of this alloy compared to 273 and 275. It is suggested that the higher levels of austenite and presence of epsilon in this alloy is due to nucleation of these phases at AlN and Ti(C,N) particles at grain boundaries.

11. In the optimum heat-treated condition (1h850°CWQ+2h600°CWQ) alloys 273 and 275 were largely resistant to embrittlement at 450°C, presumably due to the low levels of free nitrogen in solution.

12. Tensile testing at room temperature and -78°C on alloys 273 and 275 showed that, in general, an increase in $(\gamma+\varepsilon)$ levels led to a decrease in proof stress, with tensile stress largely unaffected. When γ and ε were stable after deformation this led to an increase in proof stress, whereas transformations of $\gamma \rightarrow \alpha'$ and $\varepsilon \rightarrow \alpha'$ led to a decrease in proof stress. After long tempering times (16 hr) at 600°C deformation-induced transformations did not occur.

13. A 0.5%Mo addition to pure alloys was not completely effective in reducing embrittlement, as a mixture of cleavage and intergranular fractures were found in the optimum heat-treated condition (1h850°CWQ+2h600°CWQ). This may be due to the level of nitrogen which was high compared to other investigators who made additions of 0.5%Mo.

14. In commercially impure alloys an addition of 0.5%Mo did not improve toughness in the optimum heat-treated condition. Titanium levels did seem to improve toughness through its effects on refining grain size, reducing free nitrogen and austenite levels. The optimum level of titanium was found to be at the stoichiometric level for TiC and TiN.

15. The novel grain refining heat treatment was quite effective for alloy 277 (Fe-8Mn0.2V) in reducing the grain size. The reduction was found to be due to the combined effects of vanadium carbide particle pinning and the production of reverted austenite on tempering. However, the initial IBQ from 1160°C led to quench cracks which gave very poor impact toughness.

    The theoretically predicted pinned grain size was over-estimated using the Zener equation and underestimated using the Gladman equation.

16. A comparison of 5% nickel and 9% nickel steels showed that 9% nickel gives superior properties to 8%Mn, but 8%Mn has similar properties to 5%Ni steels. Careful control of phosphorus and nitrogen in Fe-8Mn alloys could lead to a viable alloy for cryogenic applications at -100°C.

7.0 FURTHER WORK

The present work indicates that a steel based on 8%Mn would not form a commercially viable alternative steel to 9% nickel steel for cryogenic applications unless low levels of impurities could be achieved.

However, alloys based on $\gamma+\varepsilon$ or γ may have suitable cryogenic properties if the strength level can be increased.

From an academic point of view the following points need clarification:

1. X-Ray and Mossbauer analysis of alloy 273 by removal of surface layers, with analysis between removal of each successive layer. This would clarify the change in phase content from surface to bulk.

2. Room temperature and sub-zero tensile tests of alloys containing high levels of ε and γ to investigate the deformation-induced transformations of these phases on tensile properties.

3. Further TEM, AES studies and X-Ray mapping of fracture surfaces, containing high levels of γ and ε to determine partitioning of manganese and segregation of impurities to these phases.

4. Investigation of air-cooling on 0.5%Mo containing alloys by impact testing and AES studies.

5. Determination of vanadium carbide precipitate sizes in alloy 277 (Fe-8MnO.2V) aged for 10, 18 and 30 hours at 550°C to compare results with those found for 3 hr at 550°C.

REFERENCES

1. J. D. Bolton, E. R. Petty and G. B. Allen. Met. Trans., 1972, 2, pp2915-23.

2. M. Nasim, Ph.D Thesis, CNAA, 1979, Sheffield City Polytechnic.

3. B. C. Edwards, M. Nasim and E. A. Wilson, Scripta Met., 1978, 12, pp377-380.

4. H. R. Charlesworth, Unpublished Work, 1976-1979, Sheffield City Polytechnic.

5. J. Witowski, "Storage of Liquid Gases - Recent Developments", B.P. Co. Ltd., Cranfield I. T., Course on storage of oil and gas, 14th - 18th April, 1980.

6. K. J. Irvine, I.S.I./B.I.S.R.A. Conference, "Strong, Tough, Structural Steels", April 1967, ppl-11.

7. S. K. Banerji, C. J. McMahon Jr., H. C. Feng, Met. Trans., 9A, 1978, pp237-247.

8. W. P. Rees and B. E. Hopkins, JISI, 1952, pp403-409.

9. C. Pickard, J. Rieu and C. Goux, Met. Trans., vol 7A, Dec. 1976, ppl811-1815.

10. B. E. Hopkins and H. R. Tipler, JISI, May 1954, ppll0-117.

11. J. M. Hodge, R. D. Manning and H. M. Reichbold, Trans. AIME, 1949, 185, pp233-40.

12. M. Gensamer, Trans. TMS-AIME, 1959, 215 pp2-18.

13. J. Manenc, Rev. Met., 1970, 67, pp443-50.

14. N. J. Petch, Fracture, Wiley, New York, 1959.

15. G. Tither and J. W. Morrow, Metals Eng. Quarterly, Aug. 1975, pp42-45.

16. H. Ohtani, F. Terasaki, T. Kunitake, Trans. ISlJ, 12, 1972, pp718-127.

17. Materials for Cryogenic Service, Publication 4262/108, International Nickel Ltd.

18. G. P. Sanderson and D. T. Llewellyn, JlSl, August 1969, ppl-12.

19. M. Hansen and K. Anderko, "Constitution of Binary Alloys", McGraw-Hill Book Co., 1958, 1st supplement: R. P. Elliot 1965, 2nd supplement: F. A. Shunk 1969.

20. E. A. Wilson, Scripta Met., 4, 1970, p309.

21. E. A. Wilson, S. M. Vickers, C. Quixall and A. Bradshaw. Institute of Metallurgists Conference - "Phase Transformations", York, April 1979.

22. E. A. Wilson, Metal Science, 18, Oct., 1984, pp471-483.

23. M. J. Bibby and J. Gordon Parr, JlSl, 1964, 202, pl00.

24. M. Izumiyama, M. Tsuchiya and Y. Imai, J. Jpn. Inst. Met., 1970, 34, p286.

25. F. Duflos and B. Cantor, Acta Met., 1982, 30, p323.

26. Y. Inokuti and B. Cantor, Acta Met., 1982, 30, p343.

27. A. Gilbert and W. S. Owen, Acta Met., 1962, 10, p45.

28. A. Holden, J. D. Bolton and E. R. Pelty, JlSl, Sept. 1971, pp721-728.

29. H. I. Aaronson, C. Laird and K. R. Kinsman, "Phase Transformations", 1970, 313, Metals Park, Ohio, American Society for Metals.

30. "Martensite: Fundamentals and Technology", Edited by E. R. Petty, Longman, London, 1970, chapter 4.

31. "Theory of Structural Transformations in Solids", Armen G. Khachaturyua,

32. K. Wakasa and C. M. Wayman, Acta Met., 1981, 29, pp973 to 990.

33. B. P. Sandvik and C. M. Wayman, Met. Trans., vol 14A, May 1983, pp809-822.

34. P. M. Kelly and J. Nutting, JlSl, March 1961, pp 199-211.

35. A. R. Marder & G. Krauss, Trans ASM, 1967, 60, pp651.

36. W. S. Owen, E. A. Wilson & T. Bell, High Strength Materials, Edited by V. F. Zackay, Published by J. Wiley & Sons, New York (1965) p67.

37. T. Bell & W. S. Owen, JISI, April 1967, pp428-434.

38. J. A. Venables, Phil Mag., 1962, 7, p35.

39. A. Holden, J. D. Bolton & E. R. Petty, JISI, Sept. 1971, pp721-728.

40. H. Schumann, Neue Hutte, March 1974, No. 3, pp166-170.

41. I. N. Bogachev, M. S. Khadyev and Y. U. R. Nemirovskiy, Phys. Met. Metalloved, 1975, 40, No. 4, pp764-772.

42. L. N. Andryushchenko and I. Ya. Georgiyeva, Phys. Met. Metalloved, 1972, 33, No. 6, pp1285-1296.

43. I. N. Bogachev, Phys. Met. Metalloved, Vol. 44, No. 3, 1977, pp65-70.

44. A. P. Gulyaev, T. F. Volynova and I. Ya. Georgieva, Metalloved. I. Termicheskaya Obrabotka Metallov, No. 3, March 1978, pp2-6.

45. P. M. Giles and A. R. Marder, Met. Trans., May 1971, Vol 2, pp1371-1378.

46. S. D. Antolovich and B. Singh, Met. Trans, 1971, 2, pp2135-2141.

47. G. Y. Lai, W. E. Wood, V. F. Zackay and E. R. Parker, Met. Trans., 1974, 5, p1663.

48. H. Schumann, Arch. Eisen, 1967, 38, p743.

49. M. J. Roberts, Met. Trans., Dec. 1970, Vol 11, pp3287-94.

50. P. M. Kelly, Acta. Met., 1965, 13, p635.

51. R. Lagneborg, Acta. Met., 1964, 12, p823.

52. J. D. Bolton, PhD Thesis, 1970, Sheffield City Polytechnic.

53. L. D. Jaffe and D. C. Buffum, Trans. ASM, Vol. 42, 1950, pp604-618.

54. W. Steven and K. Balaiva, JISI, Vol. 193, 1959, pp141-147.

55. A. Preece and R. D. Carter, JISI, 1953, Vol. 173, 387-398.

56. B. C. Woodfine, JISI, Vol. 173, 1953, pp229-255.

57. B. C. Edwards, H. E. Bishop, J. C. Riviere, B. L. Eyre, Acta. Met., 24, 1976, pp957-67.

58. B. C. Edwards, B. L. Eyre, G. Gage, Acta. Met., Vol. 28, 1980, pp335-356.

59. A. S. Nikonenko, Phys. Met. Metalloved, 1964, 18, No1, pp126-129.

60. T. Boniszewski, British Welding Journal, 1965, 12, pp349.

61. F. G. Wilson, United Steels (Swinden Labs.), Report No. PM 5055/12/66, 1966.

62. J. M. Capus, Metallurgia, Vol. 62, 1960, pp133-138.

63. G. C. Gould, ASTM, Special Technical Publication, 1968, 407, p90.

64. G. A. Charushnikova, Ya. E. Goldstein and Ya. G. Razumov, Metal Science and Heat Treatment, 1969, No. 7, pp539-542.

65. F. Nikbakht, MSc Thesis, Sheffield City Polytechnic, 1977.

66. D. R. Squires and E. A. Wilson, Met. Trans., Vol 3, Feb. 1972, pp575-581.

67. H. J. Lee and J. W. Morris Jr., Met. Trans., 1983, Vol. 14A, pp913-920.

68. S. K. Hwang and J. W. Morris Jr., Met. Trans., Vol. 11A, 1980, pp1197-1206.

69. D. Duchateau and M. Guttmann, Metal Science, Vol. 17, 1983, pp229-240.

70. R. H. Greaves and J. A. Jones, JISI, 1925, III, pp231-255.

71. A. E. Powers, JISI, 1957, 186, pp323-328.

72. G. W. Austin, A. R. Entwisle, G. C. Smith, JISI, 1953, 173, pp376-386.

73. J. M. Capus, Temper Embrittlement in Steel, ASTM, STP407, 1968, pp3-19.

74. P. A. Restaino and C. J. McMahon, Trans. ASM, 1967, 60, pp699-706.

75. J. R. Rellick and C. J. McMahon Jr., Met. Trans., 1974, pp2439-2450.

76. A. Joshi and D. F. Stein, Temper Embrittlement of Alloy Steel, ASTM, STP499, 1972, pp59-89.

77. R. Viswanathan and T. P. Sherlock, Met. Trans., 1972, 3, pp459-468.

78. T. Inoue, Proceeding of 4th Bolton Landing Conference, 1974, pp553-559.

79. C. J. McMahon, A. K. Cianelli and H. C. Feng, Met. Trans., 8A, 1977, ppl055-57.

80. M. Guttmann, Metal Science, 1976, 10, pp337-341.

81. M. Wayman, M. Guttmann, P. Dumoulin, Met. Soc. CIM, Annual Volume, 1977, pp57-60, Edited by J. M. Togini and G. C. Weatherly.

82. W. Jolley, Trans. TMS-AIME, 1968, Vol. 242, pp306-314.

83. N. P. Allen, JISI, 1950, 166, p281.

84. S. D. Antolovich, A. Saxena, G. R. Chanini, Met. Trans., Vol. 5, 1974, p623.

85. K. J. Kim and L. H. Schwartz, Mat. Sci. & Eng., Vol. 33, 1978, p5.

86. C. K. Syn, B. Fultz, J. W. Morris Jr., Met. Trans., Vol. 16A, Feb. 1985, ppl73-177.

87. B. Fultz and J. W. Morris Jr., Met. Trans., Vol. 16A, Feb. 1985, ppl73-177.

88. D. M. Stannard and A. J. Baker, "Strengths of Metals and Alloys", Vol. 2, 5th International Conference on Strength of Metals and Alloys, Aug. 1979.

89. D. Duchateau and M. Guttmann, Acta. Met., Vol. 29, 1981, ppl291-1297.

90. S. Nagashima, T. Ooka, S. Sekino, H. Mimura, K. Aoki, Trans. ISI Japan, 1971, Vol. 11, p402.

91. S. Yano, Trans. ISI Japan, 1973, Vol. 13, ppl33-140.

92. H. Haga, Trans. ISI Japan, 1973, Vol. 13, ppl41-144.

93. J. I. Kim and J. W. Morris, Jr., Met. Trans., 1981, Vol. 12A, ppl957.

94. Y. Tomota, M. Strum and J. W. Morris, Jr., Met. Trans., Vol. 17A, March 1986, pp537-547.

95. C. W. Marshall, R. F. Heheman, A. R. Troiano, Trans. ASM, 1962, 55, pl35.

96. S. K. Hwang and J. W. Morris, Jr., Met. Trans., Vol. 11A, 1980, ppl197-1206.

97. M. Niikura and J. W. Morris, Jr., Met. Trans., Vol. 11A, 1980, ppl531-1540.

98. N. J. Petch and Hall, Phil. Mag., 1956, 1, pl86.

99. R. L. Reuben and T. N. Baker, Met. Tech., 1984, Vol. 11, pp-6-13.

100. S. Jin, J. W. Morris, Jr., V. F. Zackay, Met. Trans., Vol. 6A, 1975, ppl41-149.

101. S. Jin, S. K. Hwang & J. W. Morris, Jr., Met. Trans., Vol. 6A, 1975, ppl721-1726.

102. N. Nasim and E. A. Wilson, "Phase Transformations", April 1979, No. 11, Vol. 21.

103. M. J. Schanfein, "Properties of Materials for Liquified Natural Gas Storage", ASTM, STP579, 1975, p361.

104. Private Communication by Zener to C. S. Smith, Trans. AIMME, 175, 15, 1949.

105. M. Hillert, Acta. Met., 1965, Vol. 13, p227.

106. T. Gladman, Proc. Roy. Soc. , 1966, A294, p298.

107. T. Gladman, F. B. Pickering, JISI, June 1967, p653.

108. S. K. Hwang, J. W. Morris, Jr., Vol. 10A, May 1979, pp545-555.

109. R. L. Miller, Met. Trans., Vol. 3, April 1972, pp905-912.

110. F. J. Moratrag and T. E. Norman, Revue de Metallurgie, June 1961, Vol. 58, pp489-506.

111. M. Takahashi, Trans. ISI Japan, 1980, 20, (5), B191.

112. R. Miura, Proc. Int. Cryo. Mat. Conference, Jan. 1982, pp409-412.

113. T. Sasaki, Trans. ISI Japan, 1982, Vol. 22, ppl011-1020.

114. K. Sipos, L. Remy, A. Pineau, Met. Trans., Vol. 7A, June 1976, pp857-864.

115. I. N. Bogachev, Phys. Met. Metallog., Vol. 41, 1976, No. 4, pp875-877.

116. Y. Tomota and J. W. Morris., Jr., Trans. ISI Japan, 1984, 24, B273.

117. Y. Tomota and J. W. Morris, Jr., Trans. ISI Japan, 1984, 24, B274.

118. I. N. Bogachev, Phys. Met. Metallog., Vol. 44, 1978, No. 1. pp65-70.

119. T. Ohno, The Sumitomo Search, May 1979, No. 21, pp34-41.

120. C. Ouchi, Nippon Technical Report, Overseas No. 32, 1981, ppl2-22.

121. C. H. White and R. W. K. Honeycombe, JISI, June 1962, pp457-466.

122. J. Charles, A. Lutts, A. Berghezan, 4th Int. Cryog. Mat. Conf., 1981, San Diego, ppl05-115.

123. J. Charles, A. Berghezan, A. Lutts, P. L. Dancoisne, Met. Progress, May 1981, pp72-74.

124. J. Charles, A. Berghezan, Cryogenics, May 1981, pp-278-281.

125. J. Charles, A. Berghezan, A. Lutts, Proc. Int. Cryog. Mat. Conf., Japan, 1982, ppl20-123.

127. K. M. Chang and J. W. Morris, Jr., Met. Trans., Sept. 1979, Vol. 10A, ppl377-87.

128. G. T. Haddick, Met. Progress, Nov. 1978, pp37-40.

129. H. Yoshimora, Trans. ISI Japan, Vol. 16, 1976, pp98-105.

130. T. Horiuchi, 4th ICMC, San Diego, 1981, pp93-103.

131. R. Ogawa, J. W. Morris, Jr., Proc. ICMC, Japan, 1982, ppl24-128.

132. K. Ishikawa, Proc. ICMC, Japan 1982, pp364-367.

133. I. N. Bogachev, V. F. Yegolayev, T. L. Frolova, Phys. Met. Metalloved, 1972, 33, No. 4, pp808-813.

134. B. Aronsson, "Steel-Strengthening Mechanisms", Climax Moly. Co., 1969, pp77-89.

135. F. B. Pickering, "The Basis of Quantitative Metallography", Institute of Metals, Monograph No. 1, 1976.

136. J. A. Durnin and K. A. Ridal, JISI, January 1968, pp60-67.

137. B. L. Averbach, M. Cohen, Met. Tech., February 1948, 15.

138. B. D. Cullity, "Elements of X-Ray Diffraction", 2nd Edition, 1978, Addison-Wesley Publishers.

139. M. W. Bowkett and D. R. Harries, UKAEA Harwell Report No. AERE R9093, 1978.

140. R. E. Weber and A. L. Johnson, J. App. Phys., 1969, 40, p314.

141. "Handbook of Auger Electron Spectroscopy", Edited by L. E. Davis, N. C. McDonald, P. W. Palmbery, G. E. Riach, R. E. Weber, 2nd Edition, Published by Physical Electronics Division, Perkin-Elmer Corporation, 1976.

142. S. Thorpe, Private Communication.

143. F. W. Jones and W. I. Pumphrey, JISI, 1949, 163, pp121-131.

144. D. W. Gomersall and J. Parr, JISI, 1965, 203, pp275-279.

145. A. P. Gulyaev, T. F. Volynova and I.Ya.Georgieva, Metalloved, No. 3, March 1978, pp2-6.

146. A. R. Troiano and F. T. McGuire, Trans ASM, 1943, 31, pp340-359.

147. M. Motley, Ph.D. Thesis, CNAA, 1984, Sheffield City Polytechnic.

148. M. W. Bowkett and D. R. Harries, UKAEA Harwell Report No. AERE R9093, 1978.

149. W. D. Swanson and J. G. Parr, JISI, 202, 1964, pp119.

150. B. Freeman, Ph.D Thesis, University of Cambridge, 1973.

151. B. A. Fuller, R. D. Garwood, JISI, March 1972, pp206-208.

152. P. R. Krahe, M. Guttmann, Scripta Met., 7, 1973, pp387-394.

153. A. G. Quarrell and J. A. Wright, JISI, Ap 1962, pp299-307.

154. M. Fukagawa, Proc.ICSTIC, Suppl. Trans ISI Japan, 1971, vol 11, pp1092-1096.

155. G. R. Brophy and A. J. Miller, Trans.Am.Soc. of Met., 41, 1949, p185.

156. A. K. Patwardhan, Arch Eisen, 54, No. 4, April 1983, p167.

157. V. F. Zackay, 3rd Int. Conf. on Strength of Metals and Alloys, Cambridge, August 1973, p591.

158. M. J. Yokota, J. W. Morris Jr, V. F. Zackay, ASTM, STP579, 1975, pp361-377.

TABLE 1 Compositions of Stainless Steels
(AISI specifications)

AISI Number	C	Si	Mn	P max	S max	Cr	Mo	Ni	Others
304	0.08 max	1.00 max	2.00 max	0.045 max	0.030 max	18.00/ 20.00	---	8.00/ 10.50	---
316	0.08 max	1.00 max	2.00 max	0.045 max	0.030 max	16.00/ 18.00	2.00/ 3.00	10.00/ 14.00	---
321	0.08 max	1.00 max	2.00 max	0.045 max	0.030 max	17.00/ 19.00	---	9.00/ 12.00	Ti 5xC min
347	0.08 max	1.00 max	2.00 max	0.045 max	0.030 max	17.00/ 19.00	---	9.00/ 13.00	Nb + Ta 10xC min

TABLE 2 Chemical Analyses of Laboratory Casts

LAB	Chemical Composition (%)													
CAST	C	Si	Mn	P	S	Cr	Mo	Ni	Cu	Sn	Al	V	Ti	N
181	0.014	0.037	7.89	0.004	0.009	0.04	0.02	0.06	Nil	Nil	0.004	---	<.01	0.008
193	0.018	0.05	8.54	0.004	0.01	0.07	0.02	0.06	Nil	Nil	0.18	---	0.17	0.008
M176	0.08	0.12	0.33	0.010	0.010	0.11	0.07	9.50	0.17	0.024	0.014	---	---	---
H5405	0.10	0.27	0.77	0.007	0.006	0.52	0.41	4.96	---	---	0.038	0.072	---	---
K1525	0.004	0.011	8.10	0.006	0.010	0.002	---	0.003	---	0.005	---	---	---	0.003
273	0.008	0.02	7.85	0.011	0.011	0.068	0.02	0.096	Nil	0.006	0.01	0.05	0.005	0.0014
275	0.005	0.05	8.00	0.004	0.014	0.12	0.025	0.13	Nil	0.008	0.104	0.06	0.13	0.0017
277	0.031	0.25	8.08	0.017	0.027	0.086	0.043	0.11	0.09	0.018	0.013	0.23	Nil	0.012
278	0.028	0.25	8.07	0.017	0.025	0.092	0.047	0.11	0.095	0.018	0.019	0.048	0.19	0.012
317A	0.045	0.32	7.9	0.022	0.026	0.13	0.46	0.16	0.11	0.016	0.05	0.05	<.01	0.011
317B	0.052	0.38	8.0	0.025	0.032	0.16	0.47	0.20	0.14	0.020	0.06	0.07	0.30	0.010
318A	0.037	0.32	8.0	0.021	0.030	0.14	0.45	0.16	0.12	0.018	0.06	0.05	0.05	0.011
318B	0.037	0.31	8.1	0.020	0.030	0.15	0.45	0.16	0.12	0.018	0.05	0.06	0.16	0.011
325A	<.01	0.018	7.57	0.006	0.013	0.13	0.48	0.11	<.01	0.009	0.005	0.055	0.01	0.006
325B	<.01	0.037	7.59	0.006	0.013	0.15	0.48	0.12	<.01	0.009	0.10	0.055	0.085	0.006

TABLE 3 CuKα Radiation λ = 1.7902 Å Theoretical Intensity for (hkl) 'R' Factor

Phase	hkl	θ	Sinθ	'd' spacing	Sinθ/λ	m	L.P.	e^{-2m}	V	f	F	R
	(110)	26.21	0.442	2.027	0.247	12	7.85	0.957		14.1	28.20	131.15
	(200)	38.66	0.625	1.433	0.349	6	3.43	0.916		11.2	22.40	17.30
α	(211)	49.91	0.765	1.170	0.427	24	2.73	0.877	23.38	9.0	18.00	34.06
	(220)	62.08	0.884	1.013	0.494	12	3.60	0.838		8.1	16.20	17.38
	(310)	81.10	0.988	0.906	0.552	24	12.63	0.803		7.4	14.80	97.54
	(111)	25.62	0.432	2.070	0.241	8	8.27	0.959		14.0	56.00	94.03
	(200)	29.95	0.499	1.793	0.279	6	5.80	0.945		13.0	52.00	42.02
γ	(220)	44.90	0.706	1.268	0.394	12	2.83	0.894	46.0	10.0	40.00	25.27
	(311)	55.90	0.828	1.081	0.463	24	2.96	0.857		9.0	36.00	37.29
	(222)	59.86	0.865	1.035	0.483	8	3.32	0.845		8.0	32.00	10.86
	(10.0)	23.78	0.403	2.220	0.225	6	9.76	0.964		14.9	14.90	23.69
	(00.2)	26.16	0.441	2.030	0.246	2	7.85	0.957		14.0	28.00	22.27
ε	(10.1)	27.32	0.459	1.950	0.256	12	7.15	0.954	23.0	13.8	27.60	117.86
	(10.2)	36.64	0.597	1.500	0.333	12	3.80	0.923		11.6	23.20	42.82
	(11.0)	44.37	0.699	1.280	0.390	6	2.86	0.896		10.0	20.00	11.63

TABLE 4 CuKα Radiation $\lambda = 1.542$ Å Theoretical Intensity for (hkl) 'R' Factor

Phase	hkl	θ	Sinθ	'd' spacing	Sinθ/λ	m	L.P.	e^{-2m}	V	f	F	R
	(110)	22.41	0.382	2.027	0.25	12	4.41	0.976		13.14	26.28	66.909
	(200)	32.30	0.535	1.433	0.346	6	2.17	0.955	23.38	10.35	20.70	10.39
α	(211)	41.20	0.659	1.170	0.427	24	1.53	0.929	$(KX)^3$	9.25	18.50	21.35
	(220)	49.50	0.740	1.013	0.48	12	0.504	0.912		7.09	14.18	2.02
	(310)	58.30	0.581	0.906	0.552	24	0.55	0.886		6.85	13.70	4.03
	(111)	21.85	0.372	2.07	0.251	8	4.64	0.975		13.14	52.56	47.25
	(200)	24.45	0.430	1.793	0.28	6	3.56	0.969		11.54	46.16	20.78
γ	(220)	37.40	0.607	1.268	0.394	12	1.75	0.941	46.0	9.25	37.00	12.78
	(311)	45.48	0.712	1.081	0.461	24	1.40	0.919		8.36	33.44	16.31
	(222)	48.15	0.745	1.035	0.482	8		0.912		7.56	30.24	
	(10.0)	20.30	0.347	2.22	0.225	6	5.12	0.980		12.34	12.34	8.66
	(00.2)	22.32	0.38	2.03	0.246	2	4.45	0.976		13.14	26.28	11.34
ϵ	(10.1)	23.28	0.395	1.95	0.256	12	4.07	0.974	23.0	12.92	22.37	44.98
	(10.2)	30.95	0.514	1.50	0.334	12	2.4	0.955		10.35	10.35	5.56
	(11.0)	37.0	0.602	1.28	0.390	6	1.78	0.941		9.25	18.50	6.50

TABLE 5 X-Ray Penetration Distances

Reflection (hkl)	2 θ^{o}			Penetration, x μm		
	MoKα	CuKα	CoKα	MoKα	CuKα	CoKα
(200)α	28.8	64.6	77.3	19.0	4.8	32.5
(211)α	35.4	82.4	99.8	23.0	6.0	39.8
(200)γ	22.9	50.9	59.9	15.0	3.9	25.9
(220)γ	32.6	74.9	89.8	21.0	5.5	36.7
(311)γ	38.4	91.0	111.8	25.0	6.4	43.0
(101)ϵ	21.1	47.0	54.6	14.0	3.6	23.9

TABLE 6 X-Ray Diffraction Phase Analysis of Alloy 181 (Fe-7.89 Mn)

Heat Treatment	% Phase			Electropolishing Time
	ϵ	γ	α	
1 hour 850°C WQ	0	0	100	2 minutes
1 hour 850°C WQ + 2 hour 600°C WQ	2.5	17.5	80.0	10 seconds
1 hour 850°C WQ + 2 hour 600°C WQ	0	21.8	78.2	2 minutes
1 hour 850°C WQ + 2 hour 600°C WQ	0.3	12.3	87.4	10 minutes
1 hour 850°C WQ + 2 hour 600°C AC	0	15.3	84.7	10 seconds
1 hour 850°C WQ + 2 hour 600°C AC	0	27.6	72.4	2 minutes
1 hour 850°C WQ + 2 hour 600°C AC	2.6	13.7	83.6	10 minutes
1 hour 850°C WQ + 2 hour 600°C AC	(20.2)	(1.5)	(78.3)	-
1 hour 850°C WQ+ 2 hour 600°C WQ + 0.1 hour 450°C AC	0 (0)	11.1 (12.2)	88.9 (87.8)	10 seconds -
1 hour 850°C WQ + 1 hour 450°C AC	0 (21.3)	9.8 (7.2)	90.2 (71.6)	10 seconds -
1 hour 850°C WQ + 10 hour 450°C AC	0 (28.8)	13.7 (1.9)	86.3 (69.3)	10 seconds -

( ) Results of H R Charlesworth Ref:4

TABLE 7 X-Ray Diffraction Phase Analysis of Alloy 193
(Fe-8.54Mn-0.17Al-0.18Al)

Heat Treatment	% Phase			Electropolishing Time
	ϵ	γ	α	
1 hour 850°C WQ	0	0	100	2 minutes
1 hour 850°C WQ + 2 hour 600°C WQ	3.5	6.4	90.1	10 seconds
"	1.9	4.7	93.4	2 minutes
"	1.4	3.9	94.7	10 minutes
1 hour 850°C WQ + 2 hour 600°C AC	3.1	2.6	94.3	10 seconds
"	3.1	4.5	92.4	2 minutes
"	3.6	4.9	91.5	10 minutes
"	(26.6)	(5.1)	(79.6)	-
1 hour 850°C WQ + 2 hour 600°C WQ + 0.1 hour 450°C AC	4.2	5.5	90.3	10 seconds
	(27.6)	(4.4)	(68.0)	-
1 hour 850°C WQ + 2 hour 600°C WQ + 1 hour 450°C AC	1.4	5.6	93.0	10 seconds
	(41.1)	(2.6)	(56.3)	-
1 hour 850°C WQ + 2 hour 600°C WQ + 10 hour 450°C AC	1.5	5.7	92.8	10 seconds
	(51.6)	(3.5)	(44.9)	_

( ) Results of H R Charlesworth, Ref:4

TABLE 8

X-Ray Diffraction-Phase Analysis Comparing Swinden Laboratories and Sheffield City Polytechnic

Alloy 181 : Fe - 7.89Mn
Alloy 193 : Fe - 8.54Mn - 0.117Ti - 0.18Al

Heat Treatment = 1 hour 850°C WQ + 2 hour 650°C AC
X-ray Source = Cobalt Kα radiation

Alloy	% Phase			Comments
	ϵ	γ	α	
181	3.2	5.4	91.3	X-Ray and electropolish at Swinden Laboratories
	3.7	4.2	92.1	X-Ray at Sheffield Poly
	1.4	3.1	95.5	Re-electropolish(10mins) and X-Ray at Sheff Poly
	39.4	2.5	58.7	Original results from H Charlesworth (Ref 4) using Cu Kα radiation
193	0.5	1.1	98.4	X-Ray and electropolish at Swinden Laboratories
	0	0	100	X-Ray at Sheffield Poly
	0	0	100	Re-electropolish(10mins) and X-Ray at Sheff Poly
	26.4	1.5	72.0	Original results from H Charlesworth (Ref 4) using Cu Kα radiation

TABLE 9 Comparison of Phase Analysis after Air Cooling and Water Quenching from 850°C

Alloy 181 : Fe - 7.89Mn
Alloy 193 : Fe - 8.54Mn - 0.117Ti - 0.18Al

Samples electropolished for 10 minutes
Cobalt radiation

Alloy	Heat Treatment	% Phase		
		ϵ	γ	α
181	1 hr 850°C AC + 2 hr 650°C AC	5.5	6.6	87.9
	1 hr 850°C WQ + 2 hr 650°C AC	3.0	4.6	92.4
193	1 hr 850°C AC + 2 hr 650°C AC	1.0	0	99.0
	1 hr 850°C WQ + 2 hr 650°C AC	0	0	100

TABLE 10 Comparison of Phases Present After Air Cooling and Water Quenching from 1000°C For Various Electropolishing Times (CoKα radiation)

Alloy	Heat Treatment	Electropolishing Time	% Phase		
			ε	γ	α
181	1 hour 1000°C AC + 2 hour 650°C AC	30 seconds	22.5	6.3	71.2
	1 hour 1000°C WQ + 2 hour 650°C AC		13.8	11.6	74.6
193	1 hour 1000°C AC + 2 hour 650°C AC		11.3	6.8	81.9
	1 hour 1000°C WQ + 2 hour 650°C AC		1.9	5.0	93.1
181	1 hour 1000°C AC + 2 hour 650°C AC	2 minutes	11.9	11.4	76.7
	1 hour 1000°C WQ + 2 hour 650°C AC		7.3	9.8	82.9
193	1 hour 1000°C AC + 2 hour 650°C AC		2.7	6.8	90.5
	1 hour 1000°C WQ + 2 hour 650°C AC		1.4	3.9	94.7
181	1 hour 1000°C AC + 2 hour 650°C AC	5 minutes	11.9	12.1	76.0
	1 hour 1000°C WQ + 2 hour 650°C AC		7.5	8.6	83.9
193	1 hour 1000°C AC + 2 hour 650°C AC		2.6	7.0	90.4
	1 hour 1000°C WQ + 2 hour 650°C AC		0.7	3.7	95.6
181	1 hour 1000°C AC + 2 hour 650°C AC	Re-ground plus 30 second polish	10.1	8.6	81.3
	1 hour 1000°C WQ + 2 hour 650°C AC		9.3	10.6	80.1
193	1 hour 1000°C AC + 2 hour 650°C AC		2.9	7.4	89.6
	1 hour 1000°C WQ + 2 hour 650°C AC		1.6	3.5	94.9

TABLE 11 X-Ray Diffraction Phase Analysis Comparing Cu and Co Radiation For Various Heat-Treatments and Polishing Times

Alloy	Heat Treatment	Electropolishing Time	% Phase					
			Co Kα			Cu Kα		
			ε	γ	α	ε	γ	α
181	1 hr 850°C AC + 2 hr 600°C WQ	10 Seconds	-	-	-	2.6	11.2	86.2
	1 hr 850°C WQ + 2 hr 600°C WQ		-	-	-	2.0	6.3	91.8
193	1 hr 850°C AC + 2 hr 600°C WQ		-	-	-	2.9	8.1	89.0
	1 hr 850°C WQ + 2 hr 600°C WQ		-	-	-	1.9	4.9	93.2
181	1 hr 850°C AC + 2 hr 600°C WQ	30 Seconds	0	9.6	90.4	1.4	11.0	87.6
	1 hr 850°C WQ + 2 hr 600°C WQ		0	5.7	94.3	1.2	7.5	91.3
193	1 hr 850°C AC + 2 hr 600°C WQ		0.6	16.9	82.5	1.9	8.0	90.1
	1 hr 850°C WQ + 2 hr 600°C WQ		0.8	6.4	92.8	2.4	6.2	91.4
181	1 hr 850°C WQ + 2 hr 600°C WQ	10 Minutes	0	21.8	78.2	0	24.6	75.4
	1 hr 850°C WQ + 2 hr 600°C AC		2.6	13.7	83.6	4.1	14.8	81.1
193	1 hr 850°C WQ + 2 hr 600°C WQ		1.4	3.9	94.7	2.4	0	97.6
	1 hr 850°C WQ + 2 hr 600°C AC		3.6	4.9	91.5	3.9	0	96.1
181	1 hr 1000°C AC + 2 hr 650°C AC	5 minute polish + re-ground + 30 second polish	10.1	8.6	81.3	11.0	9.1	79.9
	1 hr 1000°C WQ + 2 hr 650°C AC		9.3	10.6	80.1	12.6	12.1	75.3
193	1 hr 1000°C AC + 2 hr 650°C AC		2.9	7.4	89.7	4.0	9.7	86.2
	1 hr 1000°C WQ + 2 hr 650°C AC		1.6	3.5	94.9	0	0	100

TABLE 12 X-Ray and Mossbauer Analysis of Alloys 181 and 273
Heat-treated condition: One hour 1000°C AC + Two hour 650°C AC

Alloy	Electropolish Condition	Phase Analysis % X-Ray - Co Kα			Phase Analysis % X-Ray - Cu Kα			Phase Analysis % Mossbauer-Electron		Phase Analysis % Mossbauer-X-Ray	
		ε	γ	α	ε	γ	α	ε + γ	α	ε + γ	α
181	10 seconds to remove oxide	20.8	6.5 (27.3)	72.7	16.4	11.9 (28.3)	71.7	1.2	98.8	15.6	84.4
	5 μm removed	-	-	-	-	-	-	25.5	74.5	37.3	62.7
273	As heat-treated	4.8	17.2 (22.0)	78.0	-	-	-	7.8	92.2	22.7	77.3
	Centre of sample + 2 minute polish	7.2	10.8 (18.0)	82.0	-	-	-	-	-	-	-

TABLE 13 Grain Size (Prior γ) and Hardness Measurements Of Alloys 181 and 193

Alloy 181 - Fe - 7.89Mn
Alloy 193 - Fe - 8.54Mn - 0.17Ti - 0.18Al

Alloy	Heat Treatment	Mean Prior γ Grain Size-μm	Hardness Hv30
181	1h 850°C WQ	45, 50	262/268 (260)
	1h 850°C AC	33, 48	255/286
	1h 900°C WQ	69	269/271
	1h 900°C AC	76	275/274
193	1h 850°C WQ	28, 32	220/228 (220)
	1h 850°C AC	31, 44	215/226
	1h 900°C WQ	57	240/238
	1h 900°C AC	70	236/243

( ) Results of H R Charlesworth (Ref: 4)

TABLE 14 Dilatometric analysis of alloys 181 and 193

Alloy	Cooling	Sample Number	Transformation Temperatures, °C			
			As	Af	Ms	Mf
181	Air*	1	570	730	280	170
		2	620	730	310	210
		3	590	710	280	220
		Mean	593	723	290	200
	Water Quench	1	-	-	85	61
		2	-	-	97	64
		Mean	-	-	91	62.5
193	Air*	1	570	770	295	210
		2	545	760	360	270
		3	570	770	380	250
		Mean	562	767	345	243

* Heating rate 20°C/minute

TABLE 15 Dilatometric analysis of alloys 273 and 275 carried out at Swinden Laboratories

Alloy	Heating Rate °C/Min	Cooling Rate °C/Min	Transformation Temperatures, °C			
			As	Af	Ms	Mf
273	50	500	675	700	390	260
	50	13,200 (220°C/S)	658	685	335	90
275	50	500	660	715	355	265
	50	13,200 (220°C/S)			315	215

TABLE 16 Comparison of Transformation Temperatures in Fe-Mn ALlloys in the vicinity of 8%Mn

Composition Mass %	Alloy No	Heating Rate °C/Min	Cooling Rate °C/Min	As °C	Af °C	Ms °C	Mf °C	References
Fe - 8.5Mn	-	10	10	660*	666*	322*	268*	Jones & Pumphrey(143)
Fe - 6.9Mn	-	-	12×10^5	-	-	375	-	Gomersall & Parr (144)
Fe - 9.85Mn	-	-	(20000°C/S)	-	-	250	-	
Fe - 3.65Mn	-	10	10	695	780	590	445	Gulyaev et al (145)
Fe - 9.0Mn	-	10	10	590	665	310	180	
Fe - 7.8Mn	-	440	420	660	700	460	334	Hwang & Morris (108)
Fe - 8.61Mn -0.045C	-	50	200	554	689	264	-	Duchateau & Guttmann (69)
Fe - 8.72Mn -0.052C -0.047Ti	-	50	200	582	751	256	-	
Fe - 8.1Mn	K1525	50	50	677	723	360	336	Nasim (2)
Fe - 7.95Mn -0.03N	134	50	50	670	710	357	330	
Fe - 7.78Mn -0.03N -0.128Ti -0.071Al	137	50	50	678	721	355	325	
Fe - 7.89Mn	181	20	450	593	723	290	200	This investigation
Fe - 8.54Mn -0.17Ti 0.18Al	193	20	450	562	767	345	243	Sheffield City Polytechnic
Fe - 7.85Mn	273	50	500	675	700	390	260	This investigation
	273	50	13200(220°C/S)	658	685	335	90	
Fe-8Mn-0.13Ti	275	50	500	660	715	355	265	Swinden Laboratory
0.104Al	275	50	13200(220°C/S)	-	-	315	215	

* 10% transformation

TABLE 17 Charpy Impact Data for Alloys 273 (Fe-7.85 Mn) and 275 (Fe-8.0 Mn-0.13 Ti-0.104 Al) Air Cooled and Water Quenched

Alloy	Heat Treatment	Test Temperature °C														
		+300	+250	+225	+200	+150	+100	+80	+70	+60	+40	+30	+18	0	-10	-43
273	1 hr 850°C AC	78	72	75	18	8	5	-	-	-	-	-	2	-	-	-
	1 hr 850°C WQ	-	-	-	91	-	87	73	79	11	6	-	7	-	-	-
275	1 hr 850°C AC	-	-	-	106	-	111	110	-	121	112	76	5	6	-	-
	1 hr 850°C WQ	-	-	-	-	-	-	-	-	-	111	-	111	108	4	5

TABLE 18 Charpy Impact Data for Alloy 273 (Fe07.85 Mn)
Air Cooled and Tempered and Water Quenched and Tempered

Heat Treatment	Impact Energy - Joules Test Temperature °C													
	+40	+18	0	-20	-43	-60	-78	-90	-100	-110	-120	-130	-140	-160
1 hr 850°C AC + 2 hr 600°C WQ	94	107	96	81	68	70	54	46	79 14	20 11	58 9	5	15	7
1 hr 850°C WQ + 2 hr 600°C WQ	98	107	-	-	98	-	68 77	-	84	-	75	-	32	11

TABLE 19 Charpy Impact Data for Alloy 275 (Fe-8 Mn - 0.13 Ti - 0.104 Al) Air Cooled and Tempered and Water Quenched and Tempered

Heat Treatment	Impact Energy - Joules															
	Test Temperature °C															
	+20	+18	0	-20	-43	-45	-60	-65	-70	-78	-90	-100	-110	-120	-140	-160
1 hr 850°C AC + 2 hr 600°C WQ	-	132	-	125	106	110	92	-	106	98	6	107	4	15	5	9
1 hr 850°C WQ + 2 hr 600°C WQ	127 125	-	136	-	170	-	-	100	-	72	-	6 107	-	16	20	9

TABLE 20 Fractographic and Impact Transition Data - 273, 275

Alloy 273 Fe - 7.85Mn
Alloy 275 Fe - 8.0Mn -0.13Ti -0.104Al

Alloy No	Heat Treatment	Fracture Mode		Impact Transition Temperature, °C
		Lower Shelf	Upper Shelf	
273	1hr 850°C AC	Intergranular + 10% Cleavage	Ductile Dimples	+210
	1hr 850°C WQ	Intergranular + 20% Cleavage	Ductile Dimples	+ 66
	1hr 850°C AC + 2hr 600°C WQ	Cleavage + 35% Ductile	Ductile Dimples	-96
	1hr 850°C WQ + 2hr 600°C WQ	Cleavage + 35% Ductile	Ductile Dimples	-125
275	1hr 850°C AC	Intergranular + 10-15%Quasi-Cleavage	Ductile Dimples	+ 26
	1hr 850°C WQ	Cleavage	Ductile Dimples	- 5
	1hr 850°C AC + 2hr 600°C WQ	Cleavage	Ductile Dimples	- 70
	1hr 850°C WQ + 2hr 600°C WQ	Cleavage + 5% Ductile	Ductile Dimples	- 82

TABLE 21

X-Ray Diffraction Analysis of Alloys 273 and 275
Cobalt Radiation

Alloy 273 Fe - 7.85Mn
Alloy 275 Fe - 8.0Mn - 0.13Ti - 0.104Al

Alloy No	Heat-Treatment	% Austenite		
		R.T.	-78°C	-196°C
273	1hr 850°C WQ + 2hr 600°C WQ	3.6 (4.6)	4.3	5.1
273	1hr 850°C AC + 2hr 600°C WQ	2.0 (4.1)	2.7	3.1
275	1hr 850°C WQ + 2hr 600°C WQ	1.9 (1.7)	2.0	2.0
275	1hr 850°C AC + 2hr 600°C WQ	2.0 (3.1)	2.7	3.1

( ) Copper Radiation

TABLE 22 Grain Size and Hardness of VM 273 and 275

Alloy 273 Fe - 7.85Mn
Alloy 275 Fe - 8.0Mn - 0.13Ti - 0.104Al

Alloy No	Heat Treatment	Grain Size(um)	Hardness HV30+
273	1hr 850°C WQ + 2hr 600°C WQ	39±4	205
	1hr 850°C WQ		251
	1hr 850°C AC + 2hr 600°C WQ	39±4	208
	1hr 850°C AC		246
275	1hr 850°C WQ + 2hr 600°C WQ	31±3	207
	1hr 850°C WQ		239
	1hr 850°C AC + 2hr 600°C WQ	27±3	200
	1hr 850°C AC		229

+ mean of 5 impressions

TABLE 23 Effect of Ageing at 450°C on Impact Toughness and Hardness After Optimum Heat Treatment
(1 Hour 850°C WQ plus 2 hour 600°C WQ)

Alloy 273 Fe - 7.85 Mn
Alloy 275 Fe - 8.0 Mn - 0.13 Ti - 0.104Al

Ageing Time at 450°C (hours)	ALLOY 273 Impact Energy-(Joules) -40°C	-78°C	Hv30	ALLOY 275 Impact Energy-(Joules) -40°C	-78°C	Hv30
0	96.0	68.0	205	134.0	8.0	207
0.1	79.0	61.0	208	92.0	10.0	210
1.0	81.0	15.0, 52.0	209	104.0	83.0	210
10.0	79.0	70.0	210	92.0	75.0	209
100.0	71.0	75.0	210	58.0	65.0	212

TABLE 24 Effect of Ageing at 450°C on Phase Content After Optimum Heat Treatment

Alloy 273 Fe - 7.85 Mn
Alloy 275 Fe - 8.0 Mn - 0.13 Ti - 0.104Al

Alloy No	Heat Treatment	% Phase		
		ϵ	γ	α
273	1 hr 850°C WQ + 2 hr 600°C WQ + 6 min 450°C	0	3.6	96.4
		0	3.1	96.9
	1 hr 850°C WQ + 2 hr 600°C WQ + 1 hr 450°C	0	3.5	96.5
	1 hr 850°C WQ + 2 hr 600°C WQ + 10 hr 450°C	0	2.7	97.3
	1 hr 850°C WQ + 2 hr 600°C WQ + 100 hr 450°C	0	3.1	96.9
275	1 hr 850°C WQ + 2 hr 600°C WQ + 6 min 450°C	0	1.9	98.1
		0	4.1	95.9
	1 hr 850°C WQ + 2 hr 600°C WQ + 1 hr 450°C	0	3.3	96.7
	1 hr 850°C WQ + 2 hr 600°C WQ + 10 hr 450°C	0	3.6	96.4
	1 hr 850°C WQ + 2 hr 600°C WQ + 100 hr 450°C	0	3.8	96.2

TABLE 25 Tensile Properties at Room Temperature and -78°C of Alloys 273 and 275 after 1h 850°C WQ and Tempered at 600°C

Alloy 273 : Fe - 7.85 Mn
Alloy 275 : Fe - 8.0 Mn - 0.13 Ti - 0.104 Al

Alloy No	Heat Treatment Time at 600°C h	Tensile Properties at Room Temperature			Tensile Properties at -78°C		
		0.2% Proof Stress N/mm²	Tensile Stress N/mm²	% El	0.2% Proof Stress	Tensile Stress	% El
273	2	506±6	597 ± 6	32	583± 6	708±6	34
	4	492±6	597 ± 6	31	598± 6	718±6	34
	8	463±6	601 ± 6	33	540± 6	703±6	36
	16	450±6	592 ± 6	32	545± 6	719±6	35
275	2	526±6	614 ± 6	36	614± 6	729±6	32
	4	519±6	619 ± 6	36	597± 6	736±6	33
	8	507±6	620 ± 6	41	575± 6	728±6	35
	16	491±6	628 ± 6	36	602± 6	756±6	35

TABLE 26

X-Ray Diffraction Phase Analysis of Tensile Samples to show the Effect of Deforamtion on Phase Content for Various Tempering Times at 600°C after 1 hr 850°C WQ for Alloys 273 and 275

Alloy No	Heat Treatment Time at 600°C	% Phase								
		As Heat-Treated			RT Tensile			-78°C Tensile		
		ϵ	γ	α	ϵ	γ	α	ϵ	γ	α
273	2	0	5.4	94.6	0	0	100	0	5.1	94.9
	4	1.3	5.7	93.0	0	0	100	0	6.2	93.8
	8	1.7	10.0	88.3	0	0	100	0	0	100
	16	2.5	11.8	85.7	0	0	100	0	0	100
275	2	1.6	6.1	92.3	0	0	100	0	0	100
	4	2.4	7.9	89.7	0	0	100	0	0	100
	8	1.2	7.7	91.1	0	6.1	93.9	0	0	100
	16	2.8	7.8	89.4	4.4	12.9	82.6	2.4	6.2	91.4

TABLE 27

Effect of Tempering Time at 600°C after 1 hr 850°C WQ
On Impact Properties and HarnessS for Alloys 273 and 275

Alloy No	Heat Treatment Time at 600°C WQ	Impact Energy at -78°C (Joules)	Hardness Hv30	Fracture Appearance
273	2	39	198±5	Cleavage + ~ 15% Ductile tearing
	4	69	202±4	Cleavage + ~ 20% Ductile tearing
	8	66	208±4	Cleavage + ~ 40% Ductile tearing
	16	72	203±5	Cleavage + ~ 50% Ductile tearing
275	2	78.0	208±4	Cleavage + ~ 5% Ductile dimples
	4	106	208±3	Cleavage + ~ 10% Ductile dimples
	8	80.0	211±4	Cleavage + ~ 20% Ductile dimples
	16	89	209±5	Cleavage + ~ 15% Ductile dimples

TABLE 28 Tensile Properties at Room Temperature and -78°C of alloys, 273 and 275 after 1 hr 850°C WQ and tempered at 650°C

Alloy 273 Fe-7.85 Mn
Alloy 275 Fe-8.0 Mn - 0.13 Ti - 0.104 Al

Alloy	Heat Treatment Time at 650°C (h)	Tensile Properties at room temperature			Tensile Properties at -78°C		
		0.2% Proof Stress N/mm²	Tensile Stress N/mm²	% El	0.2% Proof Stress N/mm²	Tensile Stress N/mm²	% El
273	2	618 ± 6	655 ± 6	23	655 ± 6	741 ± 6	32
	4	628 ± 6	659 ± 6	26	708 ± 6	774 ± 6	26
	8	584 ± 6	642 ± 6	28	660 ± 6	771 ± 6	31
	16	560 ± 6	623 ± 6	29	670 ± 6	760 ± 6	27
275	2	521 ± 6	622 ± 6	25	684 ± 6	785 ± 6	27
	4	579 ± 6	658 ± 6	27	683 ± 6	769 ± 6	29
	8	589 ± 6	647 ± 6	26	699 ± 6	780 ± 6	31
	16	579 ± 6	628 ± 6	29	742 ± 6	800 ± 6	29

TABLE 29

X-Ray Diffraction Phase Analysis of Tensile Samples to Show the Effect of Deformation on Phase Content for Various Tempering Times at 650°C after 1 hr 850°C WQ for Alloys 273 and 275

Alloy	Heat Treatment Time at 600°C	% Phase								
		As Heat-Treated			RT Tensile			-78°C Tensile		
		ϵ	γ	α	ϵ	γ	α	ϵ	γ	α
273	2	0.9	5.9	93.2	2.0	0	98.0	0	2.1	97.9
	4	0.7	6.7	92.6	1.3	0	98.7	0	0	100
	8	4.3	9.4	86.3	0	0	98.0	3.5	0	96.5
	16	0.7	5.0	94.3	1.0	0	99.0	1.4	0	98.6
275	2	0.8	3.6	95.6	0	0	100	0	0	100
	4	1.0	9.6	89.4	0	0	100	1.3	0	98.7
	8	2.6	4.1	93.3	2.0	0	98.0	0	0	100
	16	2.8	5.3	89.9	1.0	0	99.0	0	0	100

TABLE 30 Effect of Tempering Time at 650°C after 1 hr 850°C WQ on Impact Properties and Hardness for Alloys 273 and 275

Alloy No	Heat Treatment Time at 650°C WQ	Impact Energy at -78°C (Joules)	Hardness Hv30	Fracture Appearance
273	2	42.0	258±4	Cleavage + ~ 5% Ductile tearing
	4	35.0	249±5	Cleavage + ~ 5% Ductile tearing
	8	54.0	246±5	Cleavage + ~ 10% Ductile tearing
	16	58.0	256±4	Cleavage + ~ 10% Ductile tearing
275	2	3.4 3.5	223±4	Cleavage
	4	12.0	235±4	Quasi-Cleavage
	8	5.0	234±5	Cleavage + ~ 10% Ductile dimples
	16	84.0	241±4	Cleavage + ~ 80% Ductile dimples

TABLE 31 Tensile Properties of Alloy 273 after Thermal Cycling Treatments
(Alloy 273 Fe-7.85 Mn)

Heat Treatment	Room Temperature Tensile			-78°C Tensile		
	0.2% Proof Stress N/mm $^{-2}$	Tensile Stress N/mm $^{-2}$	% El	0.2% Proof Stress N/mm $^{-2}$	Tensile Stress N/mm $^{-2}$	% El
1 hr 1000°C WQ + 2hr 740°C AC + 2hr 655°C AC (IA + IB)	579	719	26	732	825	23
1 hr 1000°C WQ + 2hr 740°C AC + 2hr 655°C AC + 2hr 740°C AC + 2hr 655°C AC (IB + IB + IIA + IIB)	657	720	23	810	920	27

TABLE 32 X-Ray Phase Analysis of Alloy 273 after Thermal Cycling Treatments

Heat Treatment	% Phase Analysis								
	As Heat Treated			R T Tensile			-78°C Tensile		
	ϵ	γ	α	ϵ	γ	α	ϵ	γ	α
1 hr 1000°C WQ + 2hr 740°C AC + 2hr 655°C AC (IA + IB)	1.8	5.3	92.9	0	0	100	0.8	0	98.2
1 hr 1000°C WQ + 2hr 740°C AC + 2hr 655°C AC + 2hr 740°C AC + 2hr 655°C AC (IB + IB + IIA + IIB)	0	8.9	91.1	1.2	0	98.8	1.5	0	98.5

TABLE 33 Charpy Impact Test Data for Alloy 278
(Fe - 8 Mn - 0.2 Ti)

Heat Treatment	Impact Energy - Joules Test Temperature - °C																
	+250	+200	+150	+130	+100	+60	+40	+20	0	-20	-25	-40	-60	-78	-100	-110	-120
1 hr 850°C AC	54	47	39	8	5	-	-	3	-	-	-	-	-	-	-	-	-
1 hr 850°C WQ	51	47	43	-	37	9	-	5	4	-	-	-	-	-	-	-	-
1 hr 850°C AC + 2 hr 600°C WQ	-	56	-	-	51	-	47	42	27	19	-	-		11	-	9	-
1 hr 850°C WQ + 2 hr 600°C WQ	-	-	-	-	-	-	-	50	49	40	-	30	28	12	10	-	-
1 hr 850°C WQ + 4 hr 600°C WQ	-	-	-	-	-	-	-	54	53	-	37	35	-	20	7	-	7

TABLE 34 Fractographic and Impact Transition Data for Alloy 278

Heat Treatment	Lower Shelf Fracture Mode	Impact Transition Temperature (°C)
1 hr 850°C WQ	Quasi-cleavage	+ 80
1 hr 850°C AC	Quasi-cleavage	+140
1 hr 850°C AC + 2 hr 600°C WQ	Quasi-cleavage + ~50% Ductile	0
1 hr 850°C WQ + 2 hr 600°C WQ	Quasi-cleavage + ~50% Ductile	-40
1 hr 850°C WQ + 4 hr 600°C WQ	Quasi-cleavage + ~60% Ductile	-50

TABLE 35 Grain Size, Hardness and Phase Content of Alloy 278 in Various Heat-treated Conditions

( ) Results for stabilised 'pure' alloy 275 taken from Tables 21 and 22

Heat Treatment	Hardness Hv30	Prior Austenite Grain Size, μm	% Phase		
			ε	γ	α
1 hr 850°C AC	265, 265, 267 (229)	-	0	0	100
1 hr 850°C AC + 2 hr 600°C WQ	239, 246, 250 (200)	18 (27)	2.0	11.5 (2.5)	86.5
1 hr 850°C WQ	292, 298, 301 (239)	-	0	0	100
1 hr 850°C WQ + 2 hr 600°C WQ	270, 274, 288 (207)	20 (31)	3.5	10.0 (1.9)	86.5
1 hr 850°C WQ + 4 hr 600°C WQ	347, 350, 352	17	3.6	17.4	79.0

TABLE 36 Quantification of AES Spectra
Alloy 273 1 hour 850°C WQ

Condition	Fracture Area	% of Fe(703eV) Peak				Atomic %		
		C	O	Mn	Si	C	O	Si
As Fractured	Intergranular	-	-	12.9	8.9	-	-	8.4 ± 2.2
1 min. Argon Sputter (~ 15 monolayers)	Intergranular	14.0	29.8	10.5	-	26.3 ± 11.2	12.2 ± 3.3	-
2 min.Argon Sputter (~30 monolayers)	Intergranular	12.3	13.0	7.2	-	23.1 ± 9.8	5.3 ± 1.4	-

TABLE 37 Quantification of AES spectra
Alloy 273 - 1hr 850°C AC

Condition	Fracture Area	% of Fe (703eV) Peak								Atomic %						
		P	C	O	N	Mn	Si	S	Ni	P	C	O	N	Si	S	Ni
As Fractured	Intergranular	5.1	6.5	10.9	3.6	8.3	4.0	-	4.3	2.6 ± 0.8	12.2 ± 5.2	4.5 ± 1.2	3.2 ± 1.0	3.8 - 1.3	-	2.8 ± 0.1
20 sec Argon Sputter (~ 5 monolayers)	Intergranular	4.4	13.9	19.7	4.4	8.0	3.6	-	6.6	2.2 ± 0.7	26.1 ± 11.1	8.1 ± 2.2	3.9 ± 1.3	3.4 ± 0.9	-	4.3 ± 0.2
40 sec Argon Sputter (~10 monolayers)	Intergranular	-	17.5	16.8	5.8	10.6	5.1	-	4.4		32.9 ± 14.0	6.9 ± 1.8	5.1 ± 1.7	4.8 ± 1.3		2.9 ± 0.1
60 sec Argon Sputter (~15 monolayers)	Intergranular	-	18.4	19.9	9.2	8.1	6.6	7.4	-	-	34.6 ± 14.8	8.2 ± 2.2	8.1 ± 2.7	6.2 ± 1.7	1.9 ± 0.7	-
60 sec Argon Sputter (~15 monolayers)	Precipitate	-	13.8	23.2	-	5.1	-	-	-	-	25.9 ± 11.0	9.5 ± 2.6	-	-	-	-
80 sec Argon Sputter (~20 monolayers)	Intergranular	-	19.0	30.7	8.4	10.2	10.0	-	-	-	35.7 ± 15.2	12.6 ± 3.4	7.4 ± 2.4	9.6 ± 2.6	-	
100 sec Argon Sputter (~25 monolayers)	Intergranular	-	18.7	18.0	7.2	11.1	7.2	-	-	-	35.2 ± 15.0	7.4 ± 2.0	6.3 ± 2.1	6.8 ± 1.8	-	-
120 sec Argon Sputter (~30 monolayers)	Intergranular	-	14.2	18.7	-	11.9	4.5	8.2	-	-	26.7 ± 11.4	7.7 ± 2.1	-	4.2 ± 1.1	2.1 ± 0.8	-

TABLE 38 Quantification of AES spectra
Alloy 275 - 1hr 850°C AC

Condition	Fracture Area	% of Fe (703eV) Peak							Atomic %					
		P	C	O	N	Mn	Si	Sn	P	C	O	N	Si	Sn
As Fractured	Intergranular	5.1	-	-	-	7.2	3.6	-	2.6 ± 0.8	-	-	-	3.4 ± 0.9	-
20 sec Argon Sputter (~5 monolayers)	Intergranular	-	6.2	8.0	-	5.1	4.7	-	-	11.7 ± 5.0	3.3 ± 0.9	-	4.4 ± 1.2	-
40 sec Argon Sputter (~10 monolayers)	Intergranular	3.7	12.6	17.8	-	5.9	3.7	7.4	1.9 ± 0.6	23.7 ± 10.1	7.3 ± 2.0	-	3.5 ± 0.9	2.0 ± 0.9
60 sec Argon Sputter (~15 monolayers)	Intergranular	5.0	13.7	16.5	5.4	5.0	3.6	5.0	2.5 ± 0.8	25.8 ± 11.0	6.8 ± 1.8	4.8 ± 1.6	3.4 ± 0.9	1.4 ± 0.6
80 sec Argon Sputter (~20 monolayers)	Intergranular	7.1	20.0	18.6	5.7	7.1	7.5	-	3.6 ± 1.1	37.6 ± 16.0	7.6 ± 2.0	5.0 ± 1.7	7.1 ± 1.9	-
100 sec Argon Sputter (~25 monolayers)	Intergranular	-	18.3	13.5	4.4	6.3	-	-	-	34.4 ± 14.6	5.5 ± 1.5	3.9 ± 1.3	-	-

TABLE 39 Quantification of AES spectra
Alloy 273 - 1hr 850°C AC + 2hr 600°C WQ

Condition	Fracture Area	% of Fe (703eV) Peak										Atomic %								
		P	C	O	N	Mn	Si	S	Ni	Sn	Ca	P	C	O	N	Si	S	Ni	Sn	Ca
As Fractured	Cleavage	5.8	-	-	8.0	7.3	5.1	7.3	-	-	5.5	2.9 ± 0.9	-	-	7.0 ± 2.3	4.8 ± 1.3	1.8 ± 0.7	-	-	3.7 ± 0.6
20 sec Argon Sputter (~5 monolayers)	Cleavage	3.7	8.2	14.6	5.2	3.0	6.3	-	-	6.3	-	1.9 ± 0.6	15.4 ± 6.6	6.0 ± 1.6	4.6 ± 1.5	5.9 - 1.6	-	-	1.7 % 0.8	-
40 sec Argon Sputter (~10 monolayers)	Cleavage	5.9	11.0	16.2	4.4	7.4	10.3	-	6.3	-	-	3.0 ± 0.9	20.7 ± 8.8	6.6 ± 1.8	3.9 ± 1.3	9.7 ± 2.6	-	4.1 ± 0.2	-	-
60 sec Argon Sputter (~15 monolayers)	Cleavage	-	10.1	13.8	5.8	7.2	4.3	-	-	-	-	-	19.0 ± 8.1	5.7 ± 1.5	5.1 ± 1.7	4.0 ± 1.1	-	-	-	-

Condition	Fracture Area	% of Fe (703eV) Peak										Atomic %								
		P	C	O	N	Mn	Si	S	Ni	Sn	Ca	P	C	O	N	Si	S	Ni	Sn	Ca
As Fractured	Ductile	5.1	-	-	-	8.1	10.3	4.8	-	-	-	2.6 ± 0.8	-	-	-	9.7 ± 2.6	1.2 ± 0.5	-	-	-
20 sec Argon Sputter (~5 monolayers)	Ductile	3.7	8.8	14.0	5.1	7.0	2.9	-	-	-	-	1.9 ± 0.6	16.5 ± 7.0	5.7 ± 1.5	4.5 ± 1.5	2.7 ± 0.7	-	-	-	-
40 sec Argon Sputter (~10 monolayers)	Ductile	6.2	9.4	17.4	-	8.7	2.9	-	-	-	-	3.1 ± 0.9	17.7 ± 7.5	7.1 ± 1.9	-	2.7 ± 0.7	-	-	-	-
60 sec Argon Sputter (~15 monolayers)	Ductile	-	12.0	15.9	-	8.0	4.3	5.1	-	-	-	-	22.6 ± 9.6	6.5 ± 1.7	-	4.0 ± 1.1	1.3 ± 0.5	-	-	-

TABLE 40 Quantification of AES Spectra
Alloy 278 1 hour 850°C AC

Condition	Fracture Area	% of Fe(703eV) Peak					Atomic %			
		P	C	O	Mn	Si	P	C	O	Si
As Fractured	Cleavage	9.0	-	-	13.4	9.0	4.5 ± 1.4	-	-	8.5 ± 2.3
1 min. Argon Sputter (~ 15 monolayers)	Cleavage	7.0	12.7	11.3	7.0	7.0	3.5 ± 1.1	23.9 ± 10.2	4.6 ± 1.2	6.6 ± 1.8
2 min.Argon Sputter (~30 monolayers)	Cleavage	-	12.0	16.2	8.5	9.9	-	22.6 ± 9.6	6.6 ± 1.8	9.3 ± 2.5

TABLE 41 Quantification of AES Spectra
Alloy 277 1 hour 1160°C IBQ

Condition	Fracture Area	% of Fe(703eV) Peak			Atomic %	
		C	O	Mn	C	O
As Fractured	Intergranular	10.3	-	8.1	19.8 ± 8.3	-
1 min. Argon Sputter (~ 15 monolayers)	Intergranular	12.9	12.1	15.0	24.3 ± 10.3	5.0 ± 1.3
2 min.Argon Sputter (~30 monolayers)	Intergranular	16.4	14.8	9.4	30.8 ± 13.0	6.1 ± 1.6

TABLE 42 Charpy Impact Data for Alloy 277 for Various Heat-treated Conditions (Fe-8 Mn-0.2 V)

Heat Treatment	Impact Energy - Joules, Test Temperature - °C								
	+300	+200	+170	+160	+150	+130	+100	+60	+20
1 hr 1160°C AC	30	34	-	-	14	-	15	-	3
1 hr 1160°C AC + 1 hr 850°C WQ	31	37	40	-	19	31	11	8	3
1 hr 11600C WQ + 3 hr 550°C WQ + 1 hr 850°C WQ	-	39	-	48	-	46	14	-	3
1 hr 1160°C WQ + 10 hr 550°C WQ + 1 hr 850°C WQ	-	43	-	-	-	-	-	-	3
1 hr 1160°C IBQ + 18 hr 550°C WQ + 1 hr 850°C WQ	-	-	-	-	-	-	30	-	-
1 hr 1160°C IBQ + 30 hr 550°C WQ + 1 hr 850°C WQ	-	39	-	-	-	-	-	-	4

TABLE 43 Grain Size, Hardness and Impact Transition Temperature for Alloy 277
(Fe-8 Mn-0.2 V)

Heat Treatment	Hardness* Hv30	Grain Size μm	Impact Transition Temperature (°C)
1 hr 1160°C IBQ	358 ± 4	55.0	+170
1 hr 1160°C IBQ + 1 hr 850°C WQ	345 ± 7	31.0	+140
1 hr 1160°C IBQ + 3 hr 550°C WQ + 1 hr 850°C WQ	335 ± 4	12.5	+115
1 hr 1160°C IBQ + 10 hr 550°C WQ + 1 hr 850°C WQ	349 ± 4	10.6	-
1 hr 1160°C IBQ + 18 hr 550°C WQ + 1 hr 850°C WQ	350 ± 3	8.2	~+100
1 hr 1160°C IBQ + 30 hr 550°C WQ + 1 hr 850°C WQ	337 ± 4	3.8	-

* 10 impressions, mean figure given ± standard deviation

TABLE 44 Phase Analysis by X-Ray diffraction after Ageing at 450°C to 600°C for Alloy 277
(Fe-8 Mn - 0.2 V)

Ageing Temperature (°C)	Ageing Time (min)	Phase Analysis (%)		
		ϵ	γ	α
450	94,410	0	8.0	92.0
450	30,000	0	5.0	95.0
450	60,000	0	6.6	93.4
450	0 to 10,000	0	0	100.0
500	22,340	0	12.7	87.3
550	10,500	5.8	20.6	73.6
600	37,235	5.0	35.3	59.7

TABLE 45 Charpy Impact Data for Pure Alloys
325A (Fe-7.57-0.5 Mo) and
325B (Fe-7.59 Mn-0.5 Mo-0.1 Al-0.1 Ti)

Alloy	Heat Treatment	Impact Energy - Joules, Test Temperature - °C										
		+100	+80	+60	+40	+20	+10	0	-50	-78	-120	-145
325A	1 hr 850°C WQ	81	79	81	64	57	7	7	-	-	-	-
	1 hr 850°C WQ + 2 hr 600°C WQ	102	-	-	-	-	-	108	77	30	5	4
325B	1 hr 850°C WQ	56	60	46	12	3	-	3	-	-	-	-
	1 hr 850°C WQ + 2 hr 600°C WQ	-	-	-	79	81	-	79	72	54	37	12

TABLE 46 Fracture Mode, Phase Analysis, Grain Size and Hardness of Alloys
325A (Fe-7.57 Mn-0.5 Mo) and
325B (Fe-7.59 Mn-0.5 Mo-0.01 Al-0.1 Ti)

Alloy	Heat Treatment	Lower Shelf Fracture Mode	DBTT °C	Phase Analysis (%) ε	γ	α	Hardness Hv30	Grain Size μm
325A	1 hr 850°C WQ	Cleavage + ~20% I.G.	+18	0	0	100	333, 338, 341	-
	1 hr 850°C WQ + 2 hr 600°C WQ	Cleavage + ~5% Ductile	-64	0	3.3	96.7	270, 274, 277	17
325B	1 hr 850°C WQ	Cleavage + ~30% I.G.	+52	0	0	100	388, 392, 396	-
	1 hr 850°C WQ + 2 hr 600°C WQ	Cleavage + ~10% Ductile	-86	0	5.8	94.2	291, 298, 298	33

TABLE 47 Charpy Impact Data for Alloys 317 and 318 after 1 hr 859°C WQ + 2 hr 600°C WQ

Alloy	Composition	Impact Energy - Joules Test Temperature - °C										
		+100	+20	0	-50	-78	-110	-114	-116	-143	-145	-196
317A	Fe-8Mn-0.5Mo(0 Ti)	45	46	46	34	24	-	21	-	20	-	7
317B	Fe-8Mn-0.5Mo-0.3 Ti	43	43	42	41	-	-	16	-	-	8	-
318A	Fe-8Mn-0.5Mo-0.05Ti	43	42	48	43	35	30	-	-	-	23	12
318B	Fe-8Mn-0.5Mo-0.16Ti	46	46	48	38	31	-	-	20	-	16	10

TABLE 48 Fracture Mode, Phase Analysis, Grain Size and Hardness of Alloys 317 and 318 after 1 hr 850°C WQ + 2 hr 600°C WQ

Alloy	Composition	Lower Shelf Fracture Mode	DBTT °C	Phase Analysis (%)			Hardness Hv30	Grain Size μm
				ε	γ	α		
317A	Fe-8Mn-0.5Mo(0 Ti)	Quasi-Cleavage + ~30% Ductile	-30	0	26.5	73.5	423, 418, 417	32
317B	Fe-8Mn-0.5Mn-0.30Ti	Quasi-Cleavage + ~20% Ductile	-75	2.9	11.4	85.7	367, 362, 358	24
318A	Fe-8Mn-0.5Mo-0.05Ti	Quasi-Cleavage + ~50% Ductile	-100	1.0	36.6	62.4	450, 438, 437	15
318B	Fe-8Mn-0.5Mo-0.16Ti	Quasi-Cleavage + ~20% Ductile	-40	7.9	14.3	77.8	386, 379, 370	12

TABLE 49 Charpy Impact Data for 9%Ni and 5% Ni Steels

Alloy	Heat Treatment	Impact Energy - Joules, Test Temperature - °C							
		+20	-45	-78	-100	-120	-140	-160	-196
Fe-9% Ni	1 hr 850°C WQ + 2 hr 600°C WQ (WQ + T)	64	54	54	53	48	45	47	40
(M176)	1 hr 900°C WQ + 1 hr 790°C WQ + 2 hr 600°C WQ (N NT)	61	52	52	46	45	45	44	34
Fe-5% Ni (H5405)	1 hr 800°C WQ + 2 hr 600°C WQ (WQ+T)	46	45	23	16	-	14	-	6

TABLE 50 Fracture Mode, Phase Analysis, Grain Size and Hardness of 9% Ni and 5% Ni Steels

Alloy	Heat Treatment	Lower Shelf Fracture Mode	DBTT °C	% Phase γ	% Phase α	Hardness Hv30	Grain Size μm
9% Ni	1 hr 850°C WQ + 2 hr 600°C WQ (WQ + T)	Ductile Dimples	<-160	9.4	90.6	260	16
(M176)	1 hr 900°C WQ + 1 hr 790°C WQ + 2 hr 600°C WQ (N NT)	Ductile Dimples	<-160	11.5	88.5	264	18
5% Ni (H5405)	1 hr 800°C WQ + 2 hr 600°C WQ (WQ+T)	Quasi-Cleavage	-70	0	100	358	30

FIGURE 1

LOWEST OPERATING TEMPERATURES OF CRYOGENIC STEELS

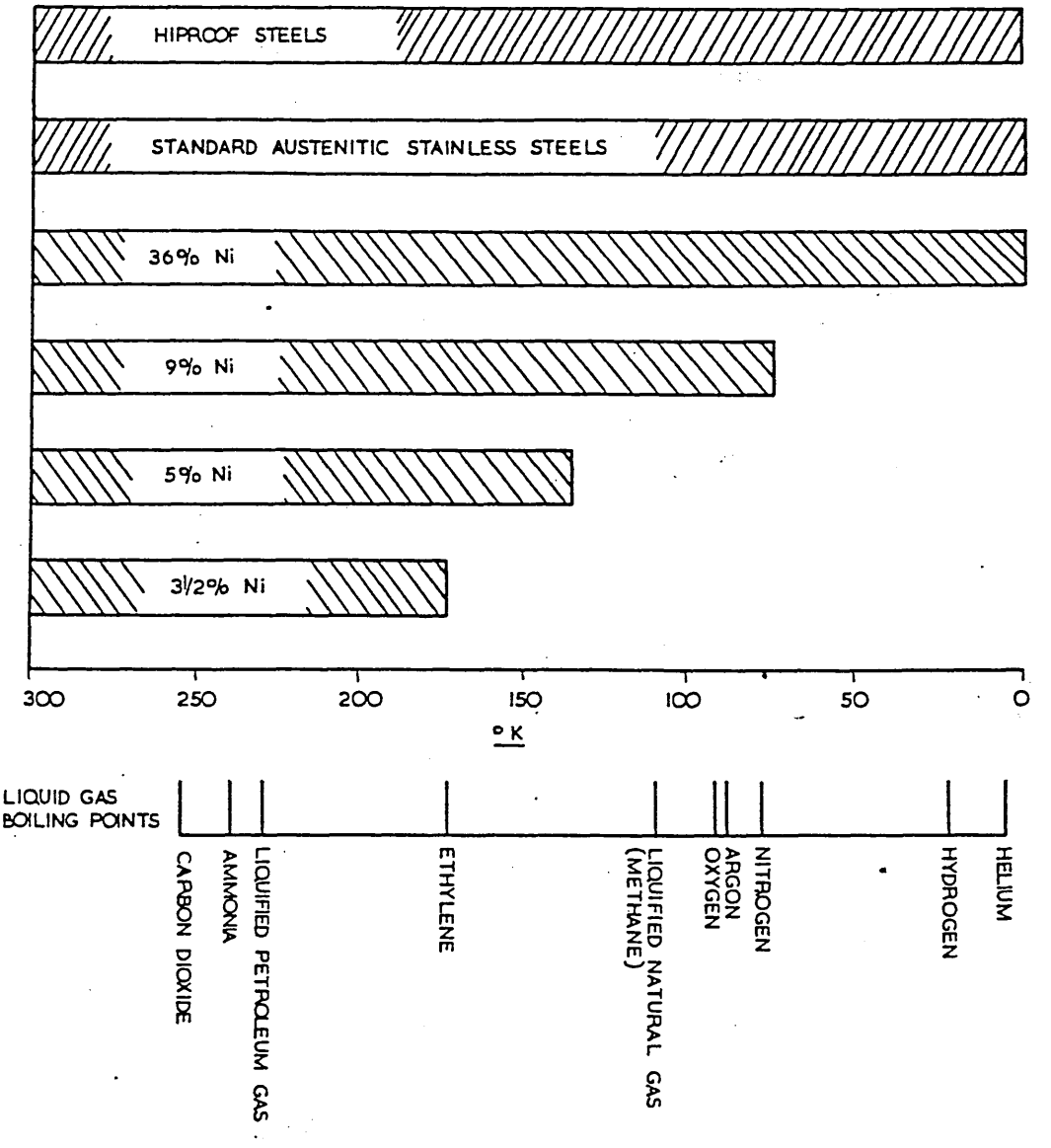

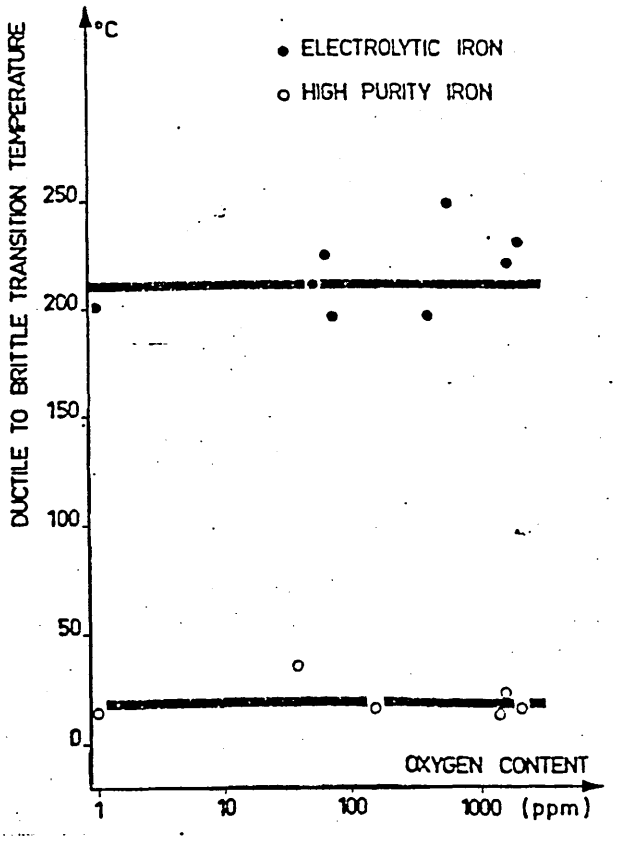

Fig2 . Influence of oxygen concentration on the transition temperature of a decarburized electrolytic iron and high purity iron (C:I0ppm) (9)

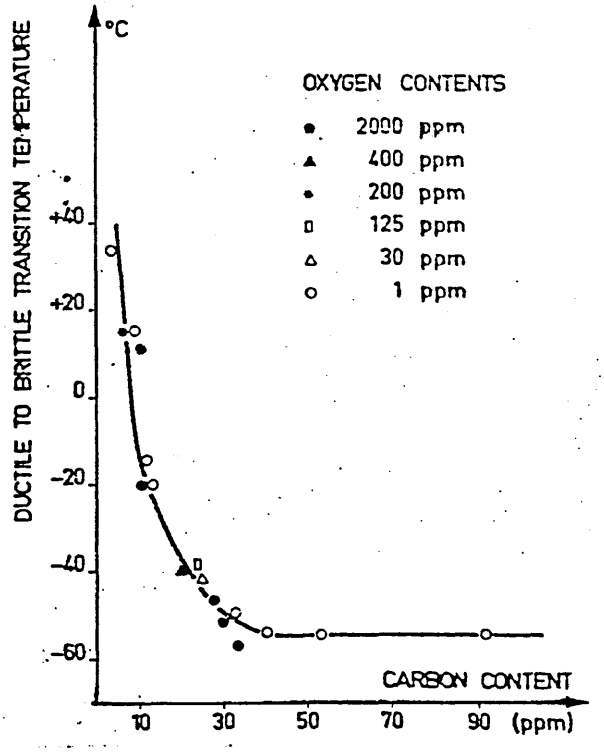

Fig 3 . Influence of oxygen concentration on the variation of transition temperature with the carbon content in high purity iron. (9)

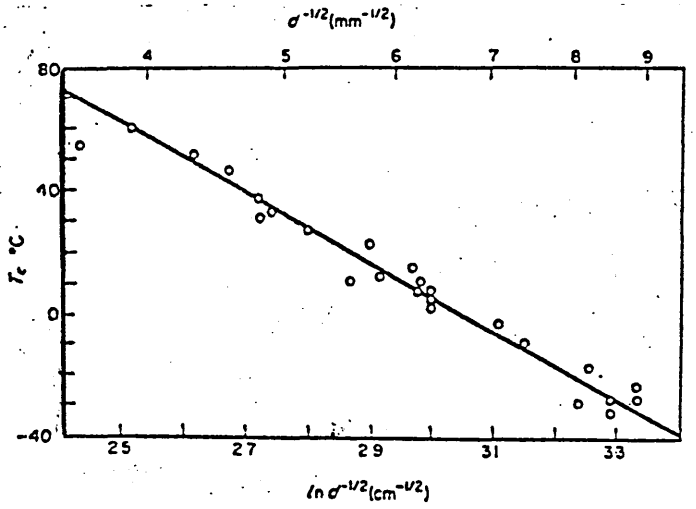

Fig 4 . The dependence of the transition temperature of mild steel on the grain size.(14)

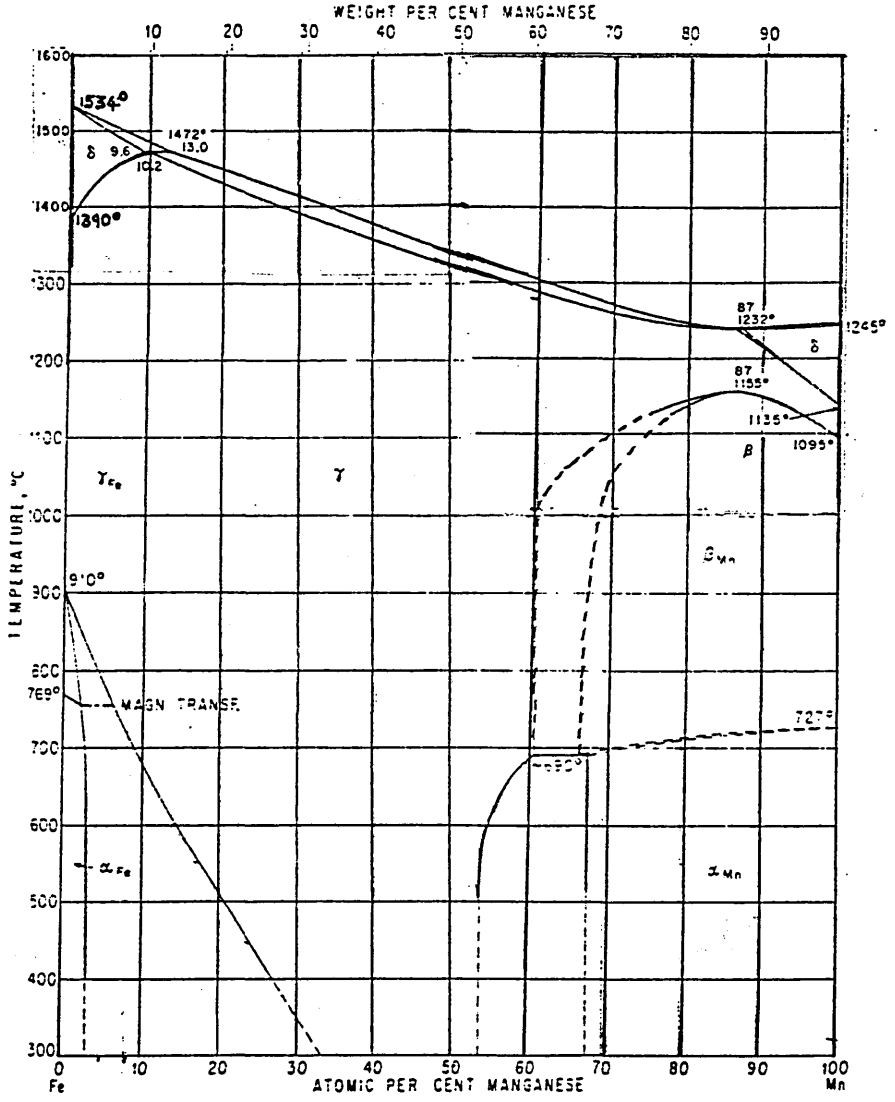

Figure 5 Fe-Mn Equilibrium Diagram (Ref:19)

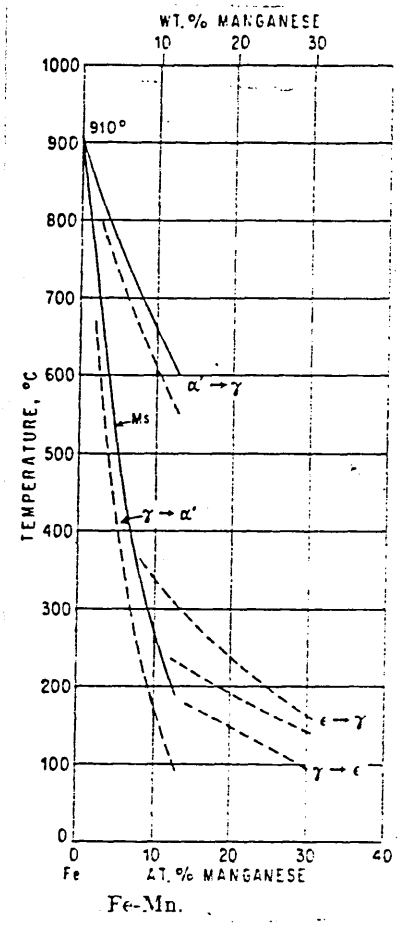

Figure 6 Fe-Mn Metastable Diagram(Ref:19)

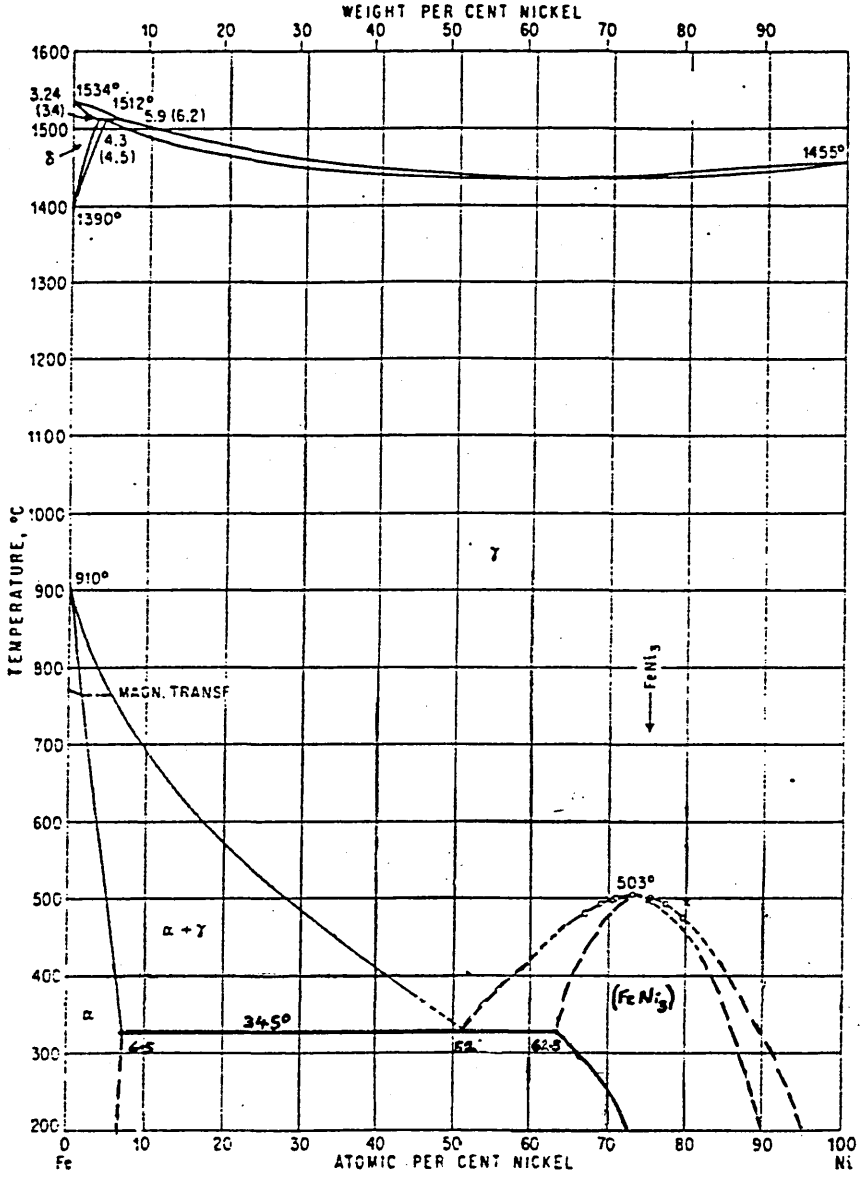

Figure 7 Fe-Ni Equilibrium Diagram (Ref:19)

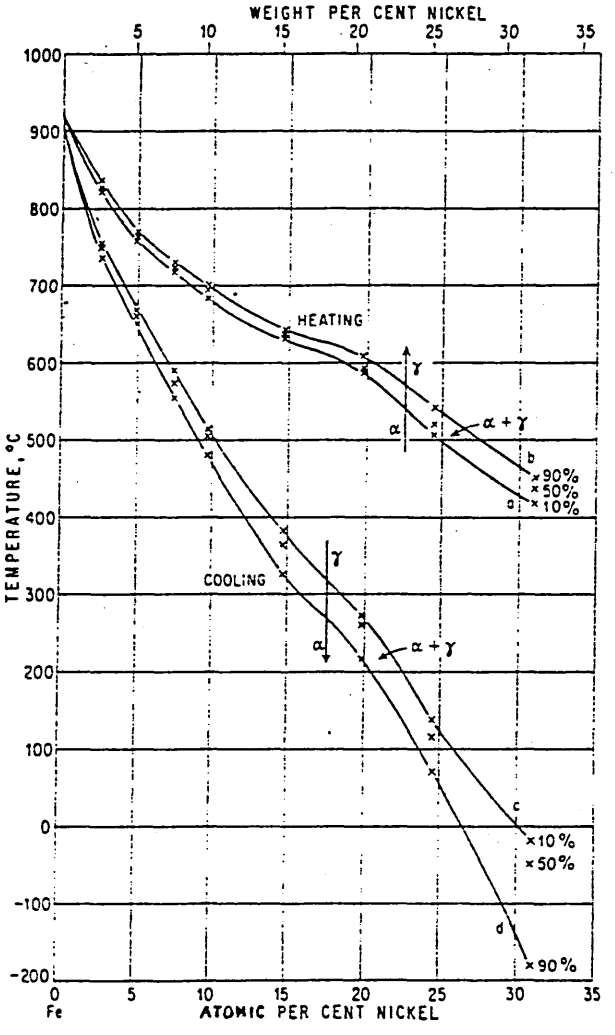

Figure 8 Fe-Ni Metastable Diagram(Ref:19)

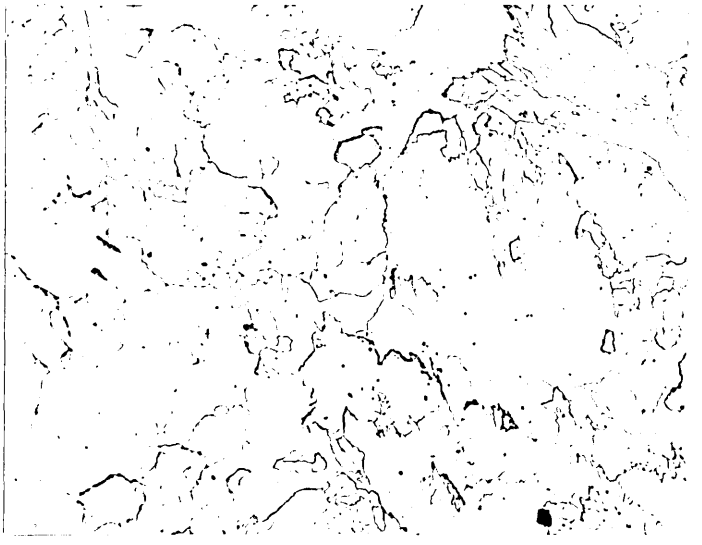

X100

Figure 9 Massive ferrite in Fe-3.9Cu,quenched into ice brine;etched in nital. After Wilson(Ref:22).

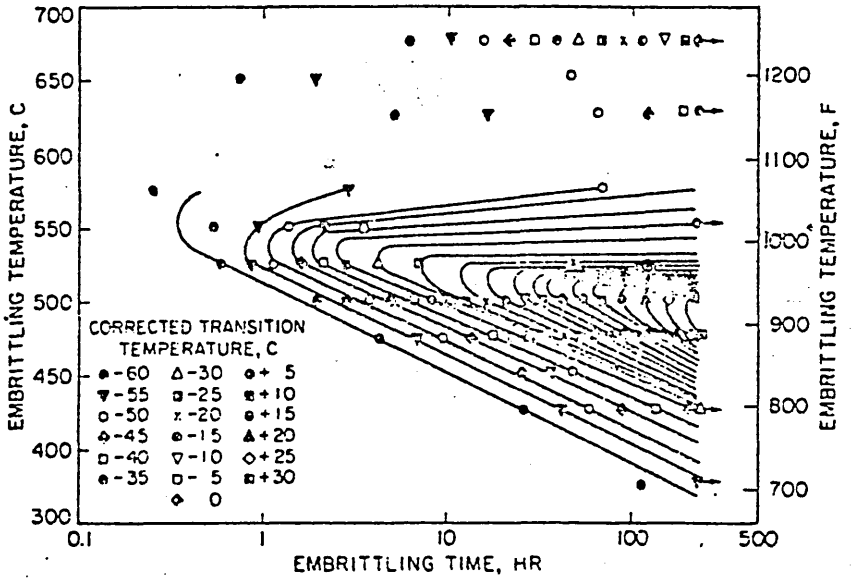

Fig 10 Isoembrittlement curves of Jaffe and Buffum (53) plotted as a time-temperature diagram, for a Ni-Cr steel (0.39 percent carbon, 0.79 percent manganese, 0.77 percent chromium, 1.26 percent nickel, 0.015 per cent phosphorus)

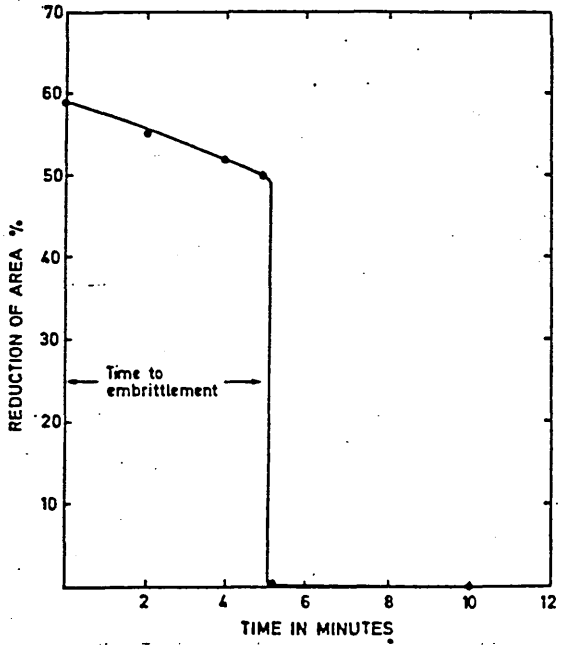

Fig.11 Variation of tensile ductility with ageing time at 450°C in K1525. Tensile tested at -78°C at a strain rate of 0.5 min^{-1}. (2).

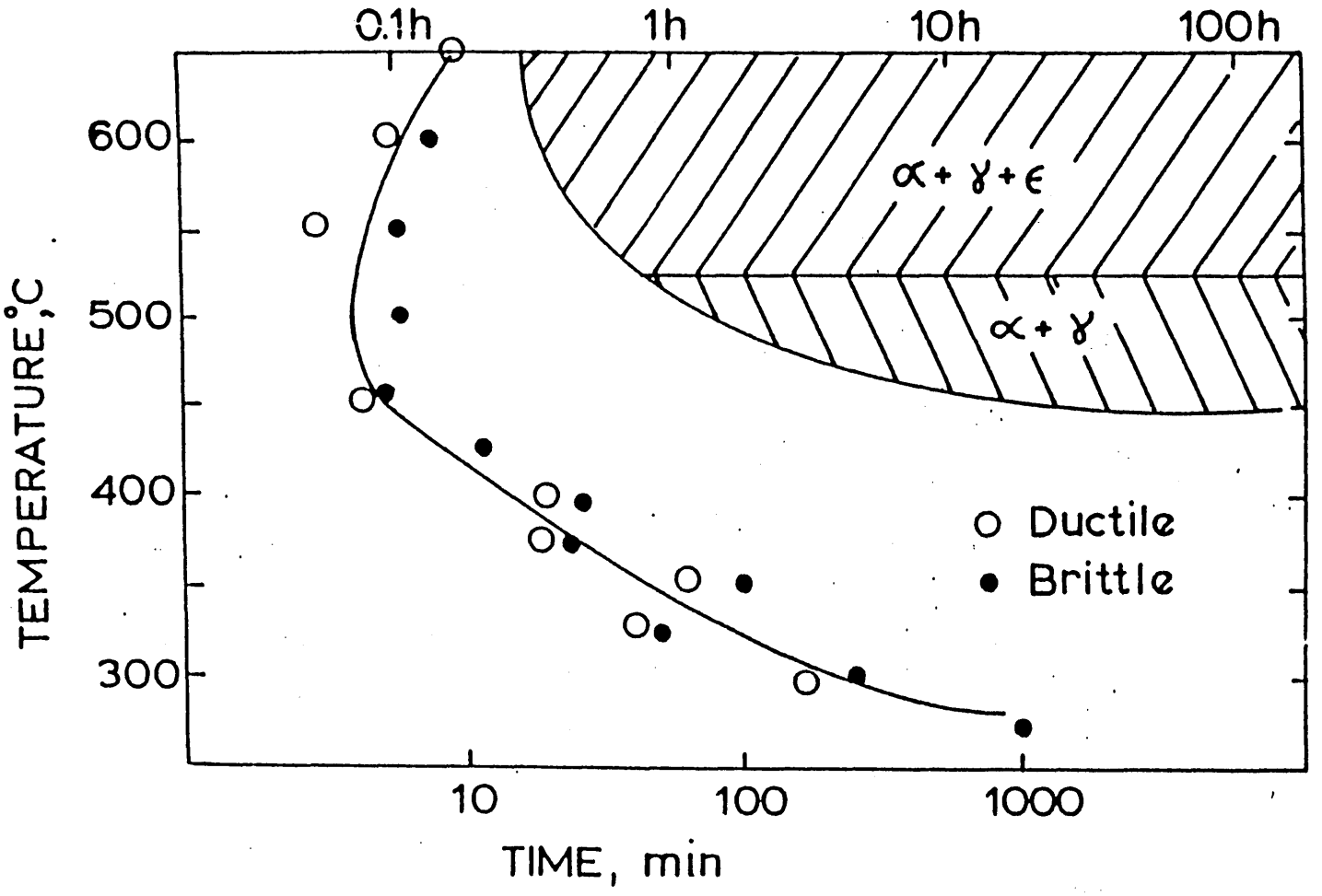

Figure 12 Embrittlement Kinetics curve determined from tensile ductility transition. Shaded portion shows the region during which phase-transformations occur on isothermal holding in alloy K1525 (reference 2)

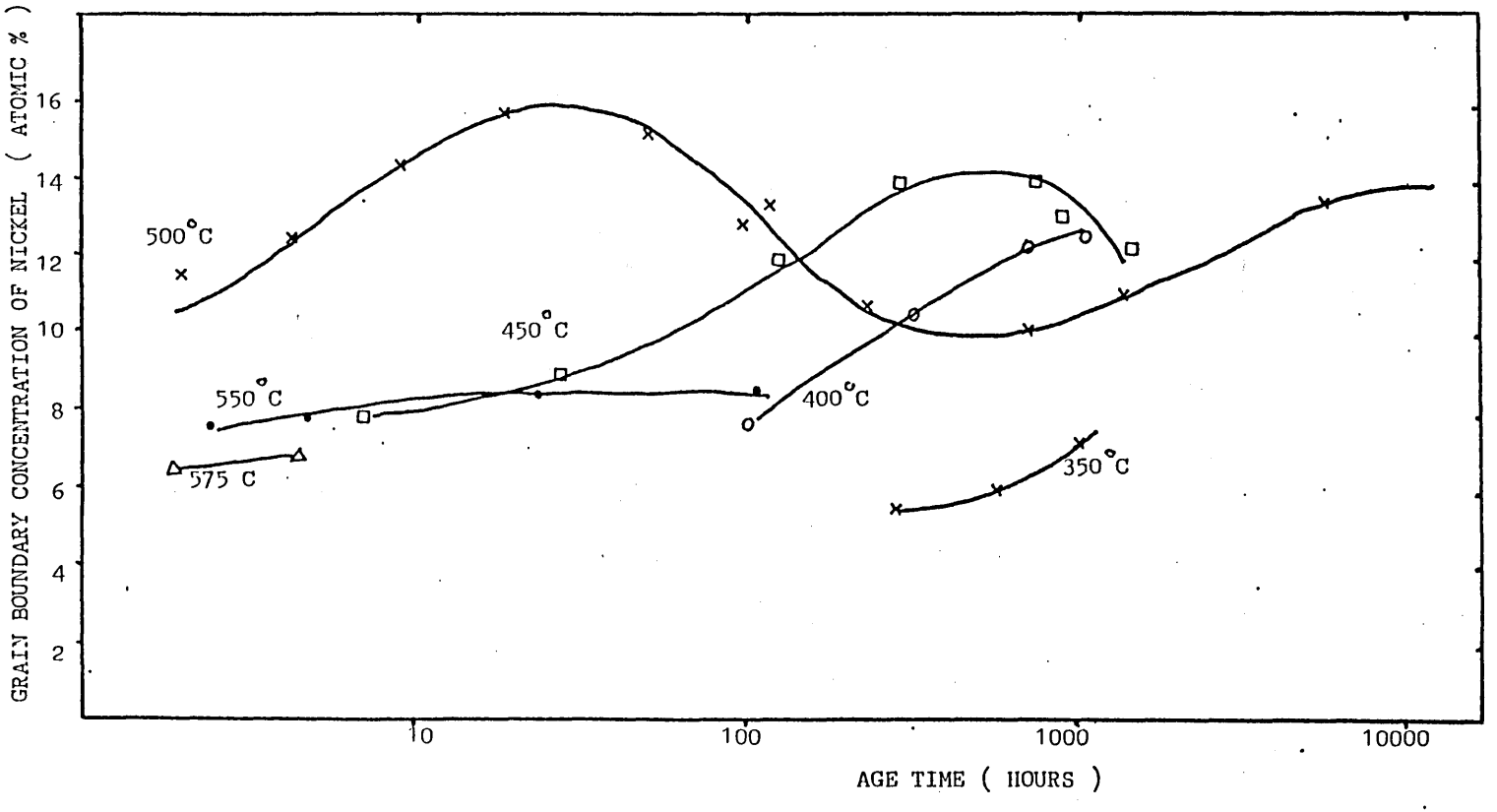

Figure 13 Variation in the grain boundary Nickel concentration as a function of ageing temperature and time.(58).

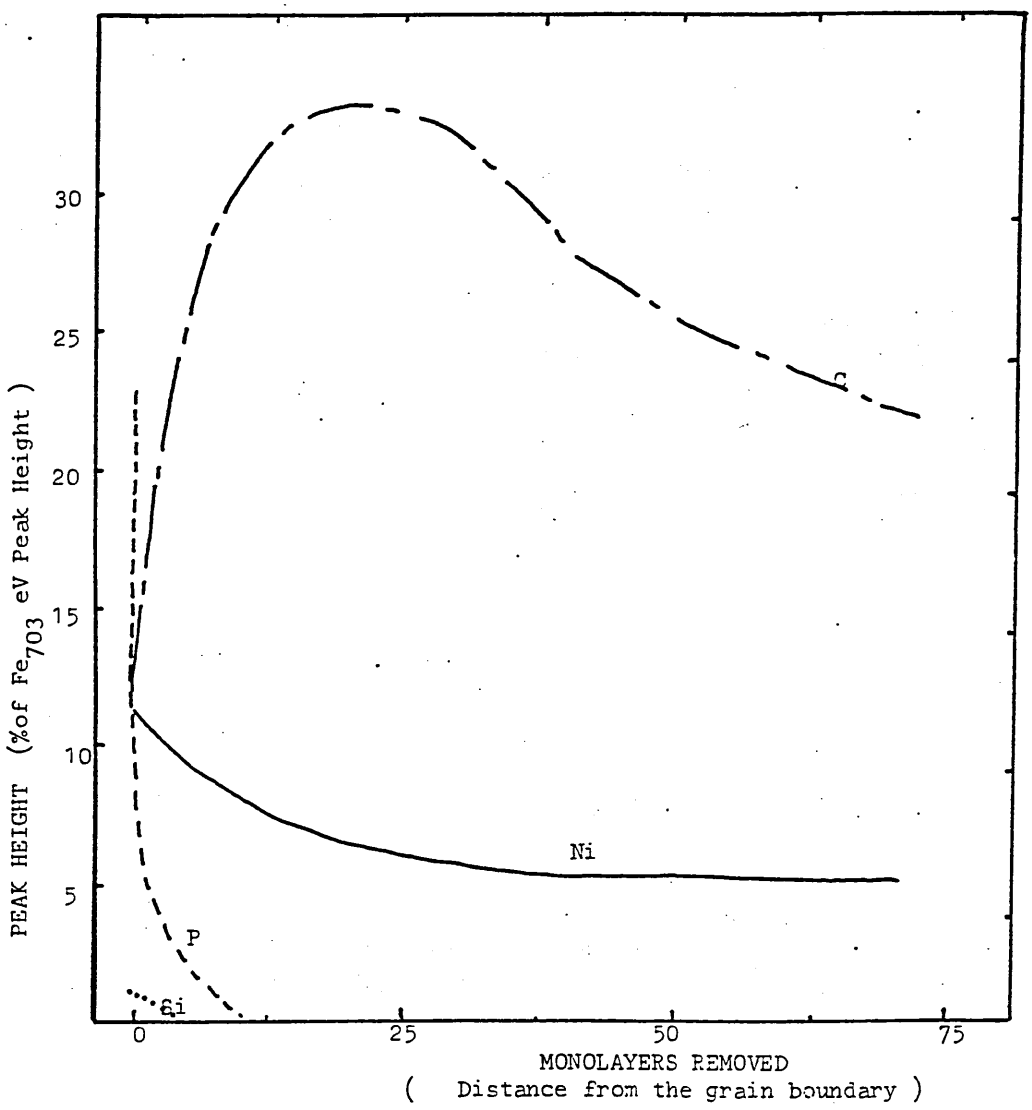

Figure 14 Ion bombardment concentration profiles.(58).

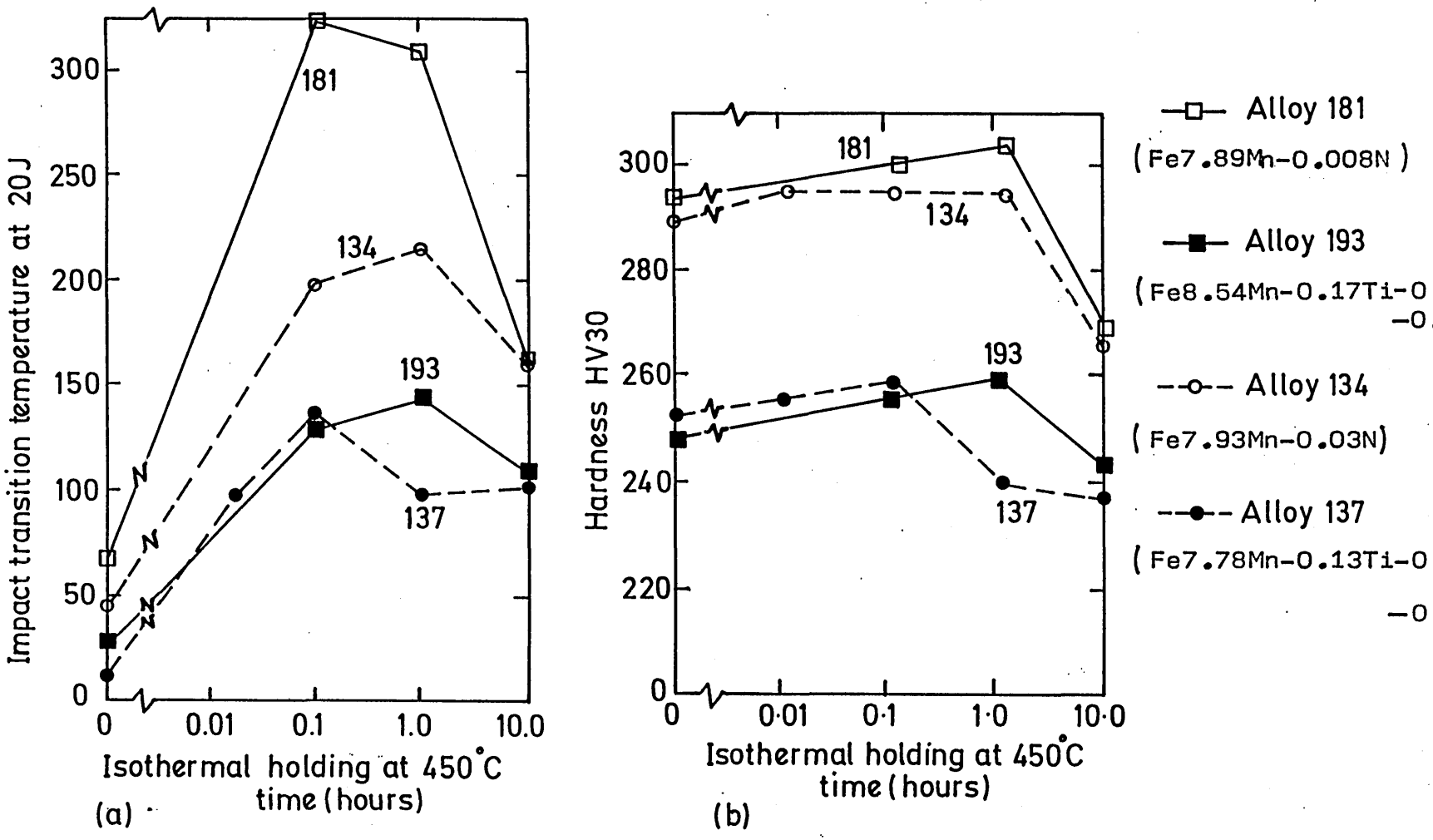

FIG.15 Effect of holding at 450°C on impact transition temperature and hardness of various alloys based on Fe-8Mn (After Nasim)[2]
Initial heat treatment 1/2 h 900°C Ice-brine quench.

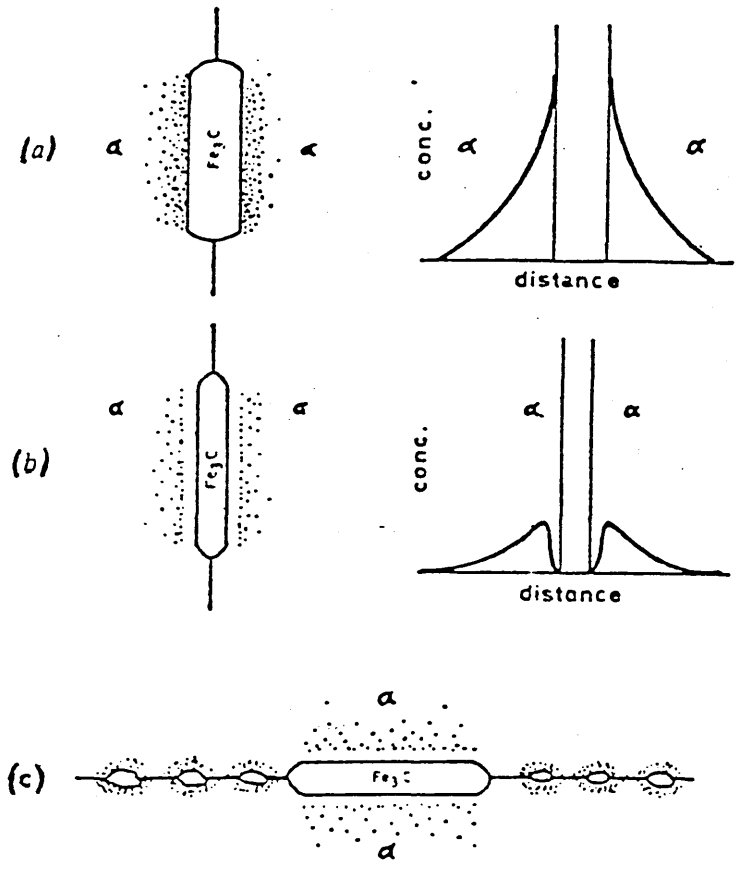

Fig.16 Schematic Representation of Embrittlement by Rejection of Embrittling Elements from Carbides.

(a) Initial Embrittlement by Slow Cooling from Austenite;

(b) Reversal by Heating to 650°C and Quenching;

(c) Re-Embrittlement by Reheating at 480°C.

Ref: E.Hondros , ' Interfaces', Proc. conf. Melbourne, 1969, Butterworth, London.

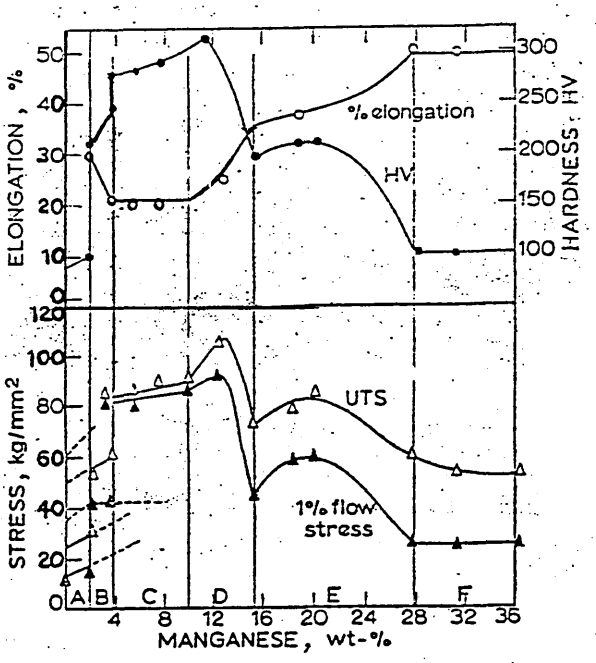

A equiaxed ferrite, *B* bainite, *C* lath martensite, *D* α'-martensite+ε, *E* ε+α, *F* austenite

Fig.17 The variation in mechanical properties with both composition and structure in Fe–Mn alloys (39)

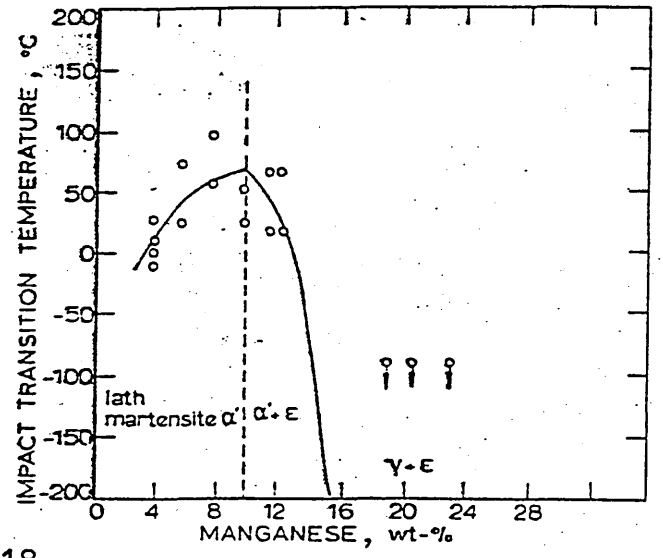

Fig18 The variation in impact transition temperature with manganese concentration (39)

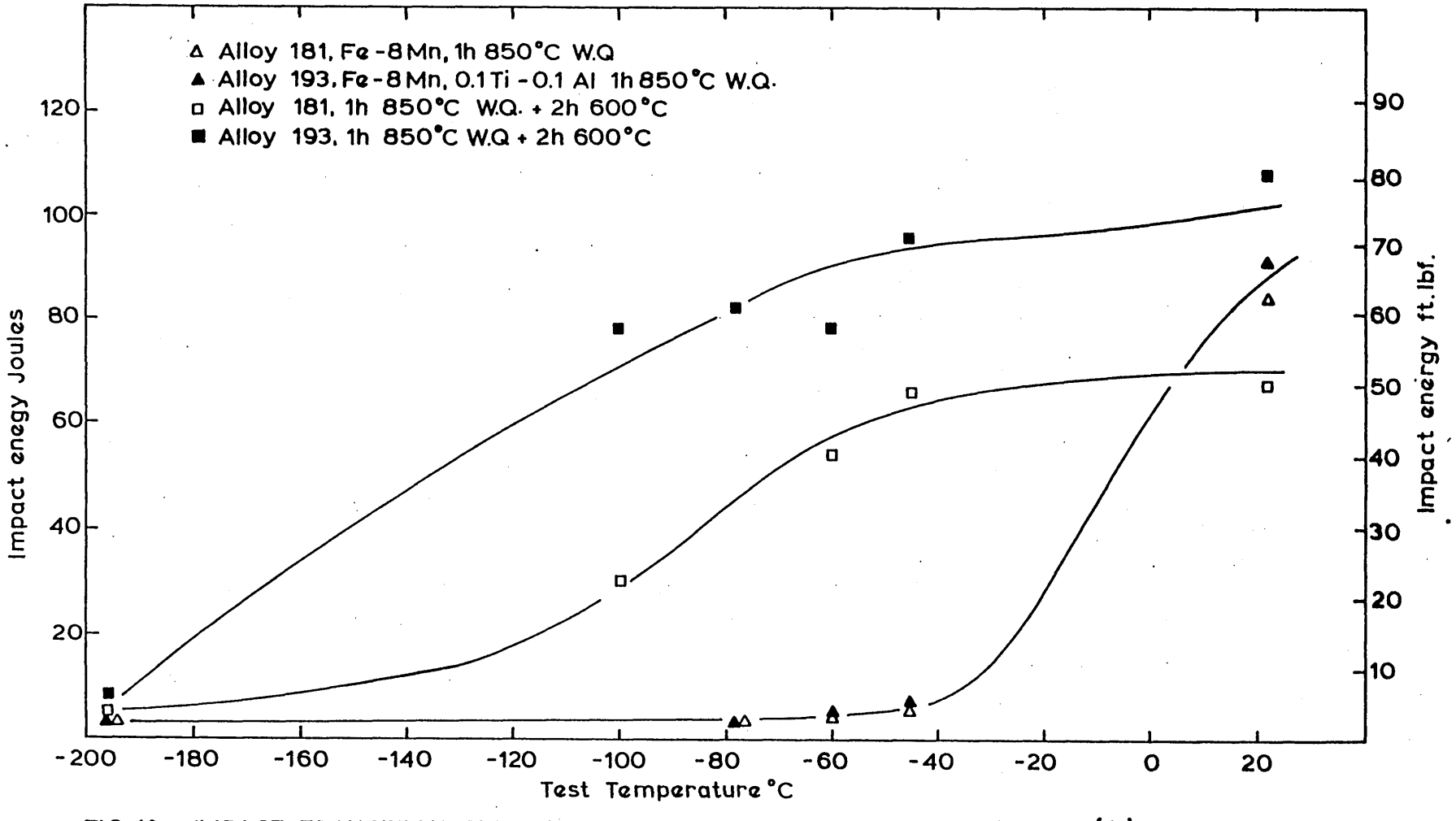

FIG. 19 IMPACT TRANSITION CURVES FOR ALLOYS 181 AND 193; 1h 850°C W.Q. (4)

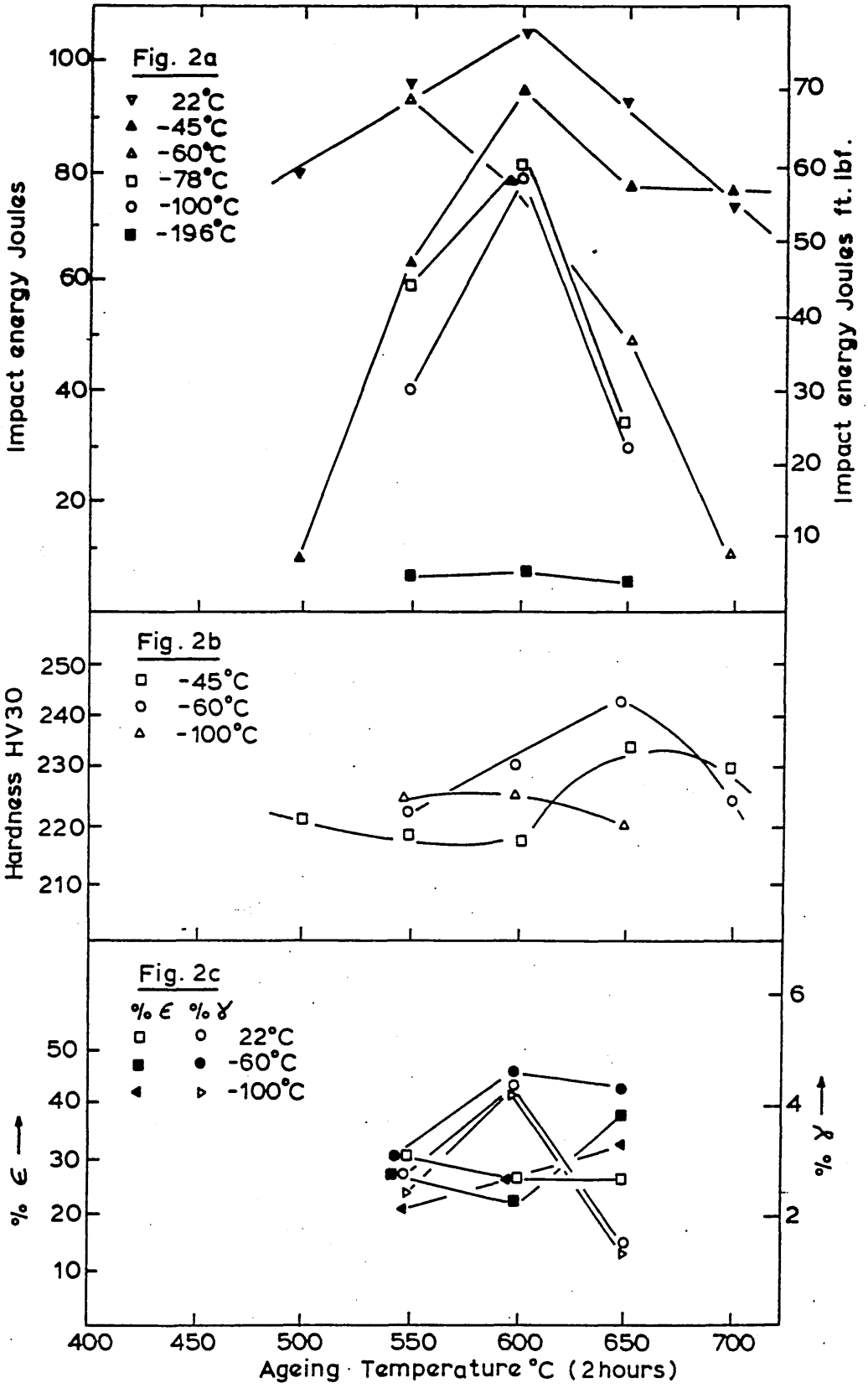

FIG. 20 ALLOY 193. Fe-8 Mn-0.1 Ti-0.1 Al VARIATION OF IMPACT ENERGY, HARDNESS, AND CONSTITUTION WITH AGEING TEMPERATURE. (Ref 4)

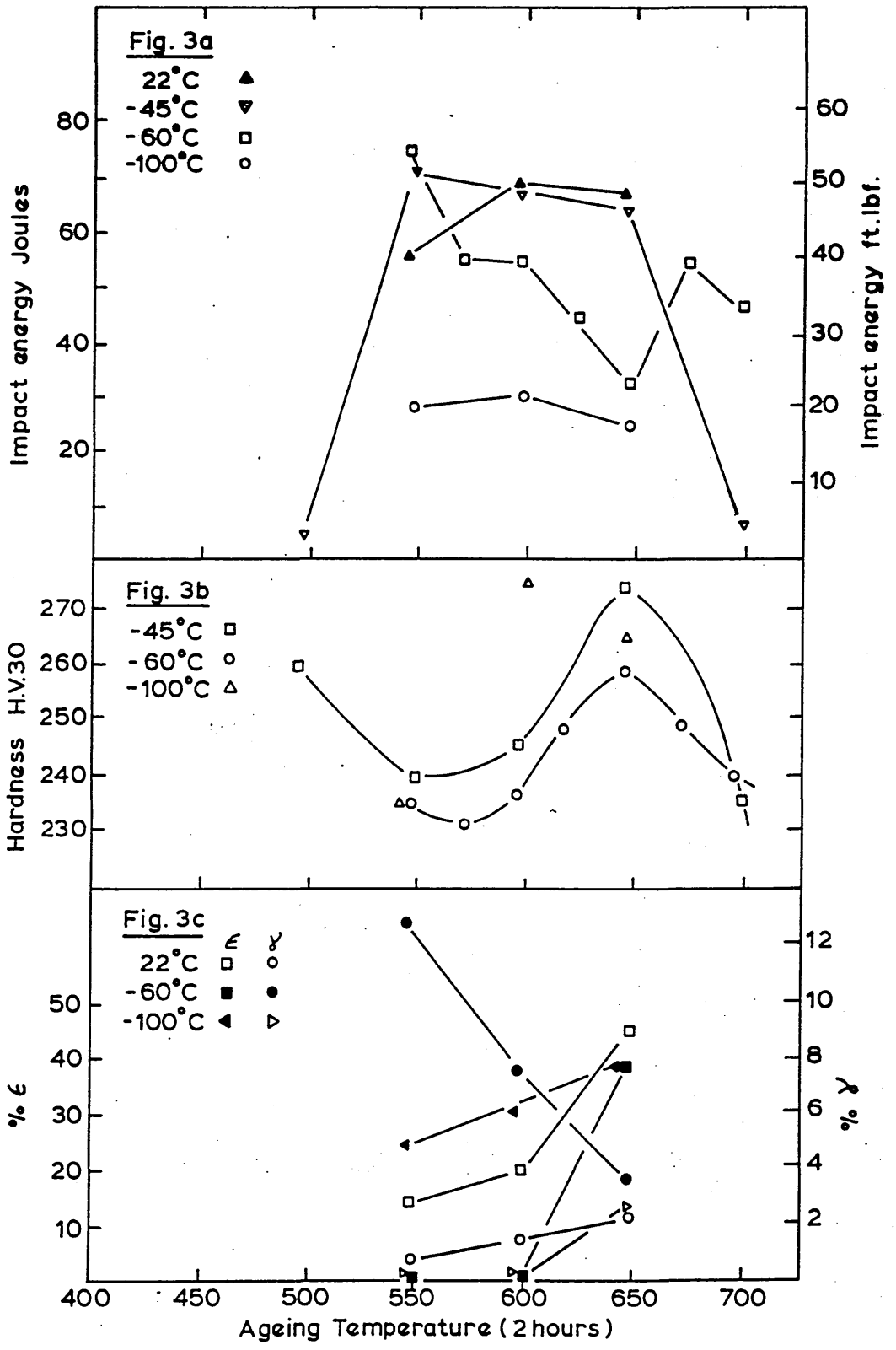

FIG. 21 ALLOY 181, Fe-8 Mn, 1h. 850°C W.Q. + AGED VARIATION OF IMPACT ENERGY, HARDNESS AND CONSTITUTION WITH AGEING TEMPERATURES. (Ref 4)

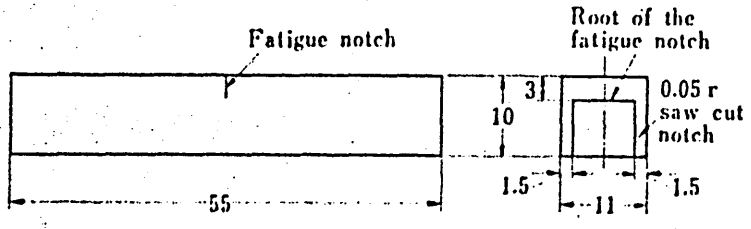

Fig.22 Geometry of the constrained-fatigue-notched specimen (ref:92)

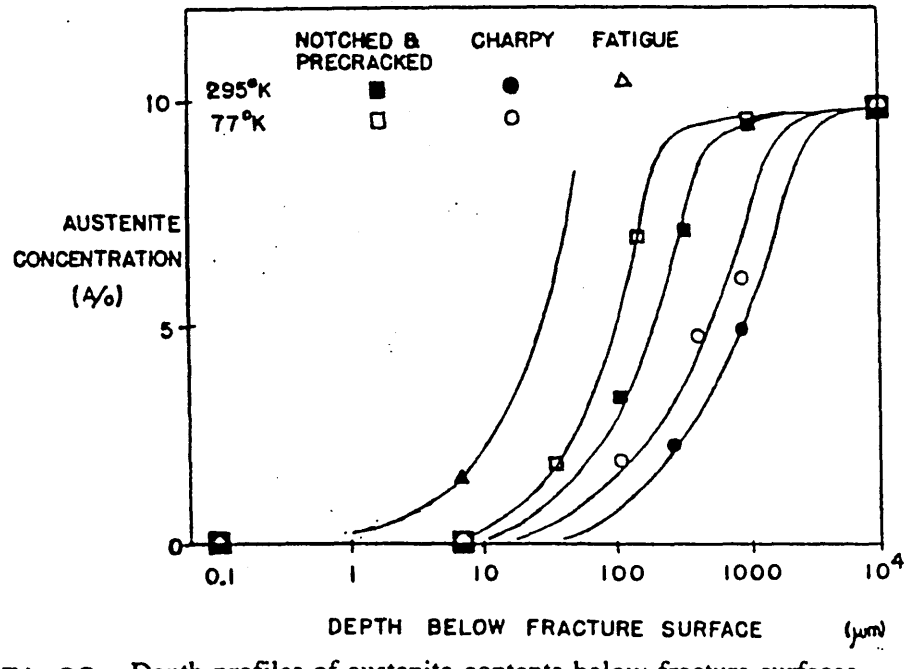

Fig23—Depth profiles of austenite contents below fracture surfaces.
(Ref: 87)

(a) SCHEMATIC REPRESENTATION OF THERMAL CYCLING TREATMENT CARRIED OUT IN ALLOY K1525 Fe.8 C Mn

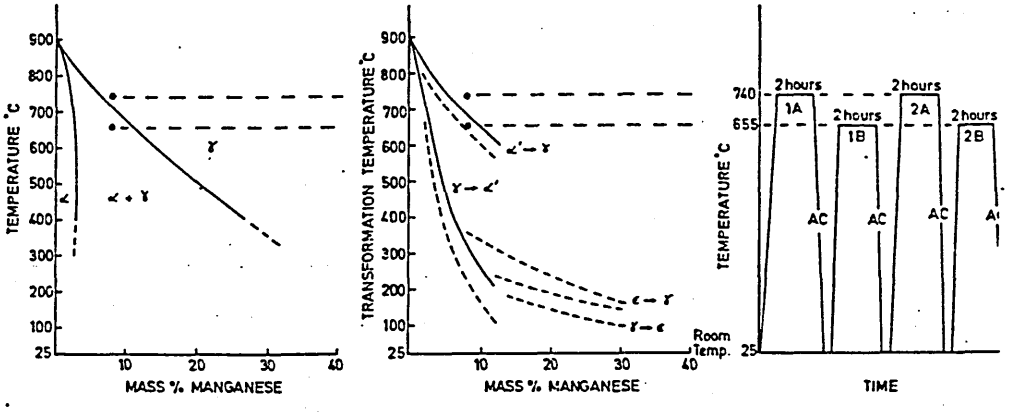

(b) SCHEMATIC ILLUSTRATION OF THE DEVELOPMENT OF MICRO-STRUCTURE ON THERMAL CYCLING TREATMENT

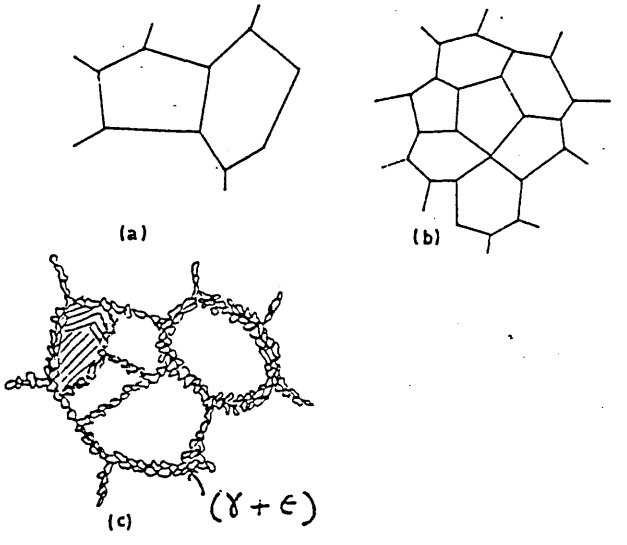

Figure 24 (a) and (b), Schematic representation of thermal cycling treatments. (After Nasim (2)).

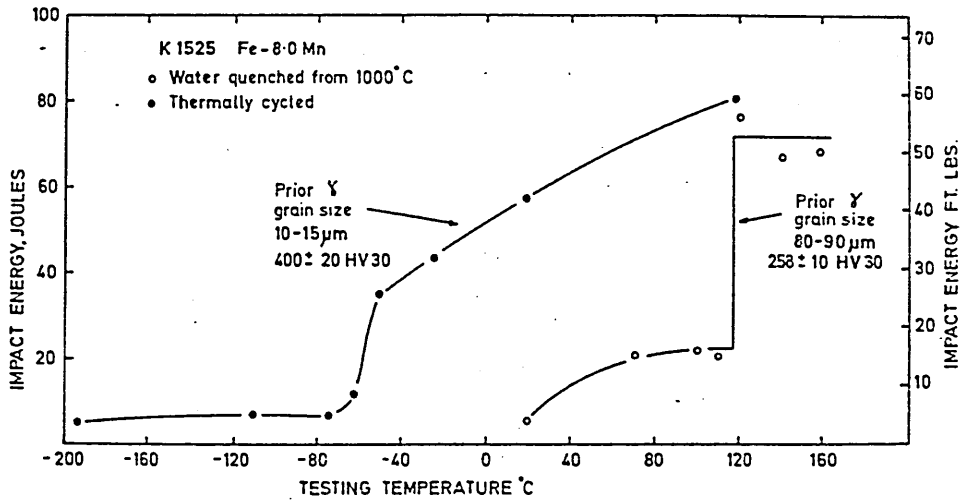

Figure 25 Effect of thermal cycling treatment on impact transition temperature in alloy K1525. After Nasim(2).

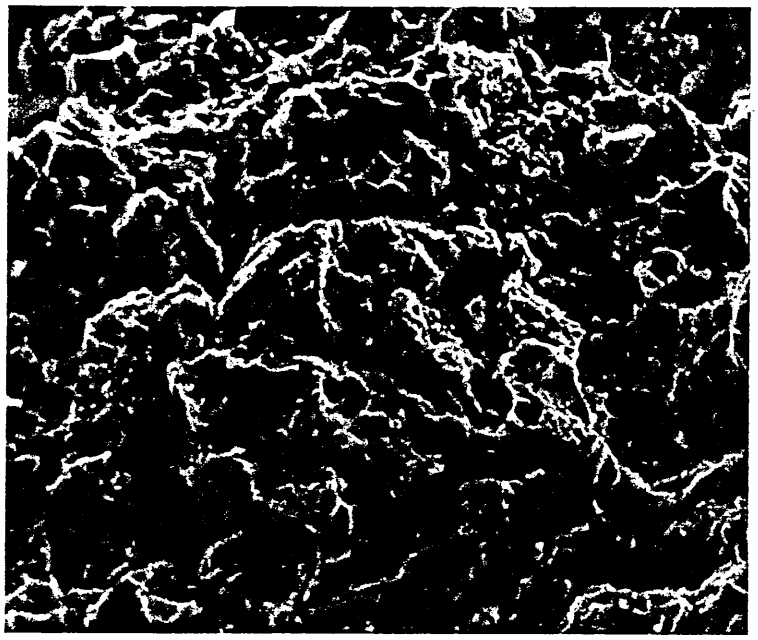

X520

Figure 26 S.E.M. micrograph of alloy K1525 after thermal cycling treatment, impact tested at -110°C. Ductile-cleavage fracture mode. After Nasim(2).

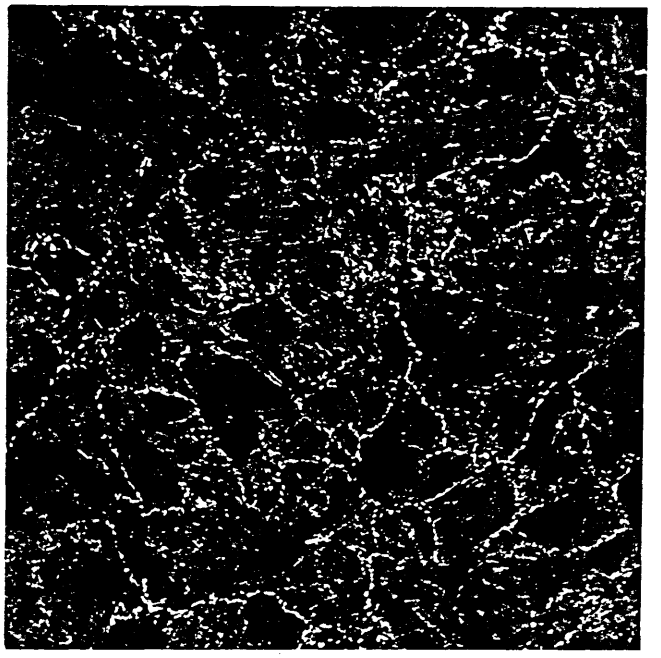

X500

Figure 27 Optical micrograph of alloy K1525 in the thermally cycled condition, showing white bead-like nucleation of austenite along the grain boundaries. After Nasim (2).

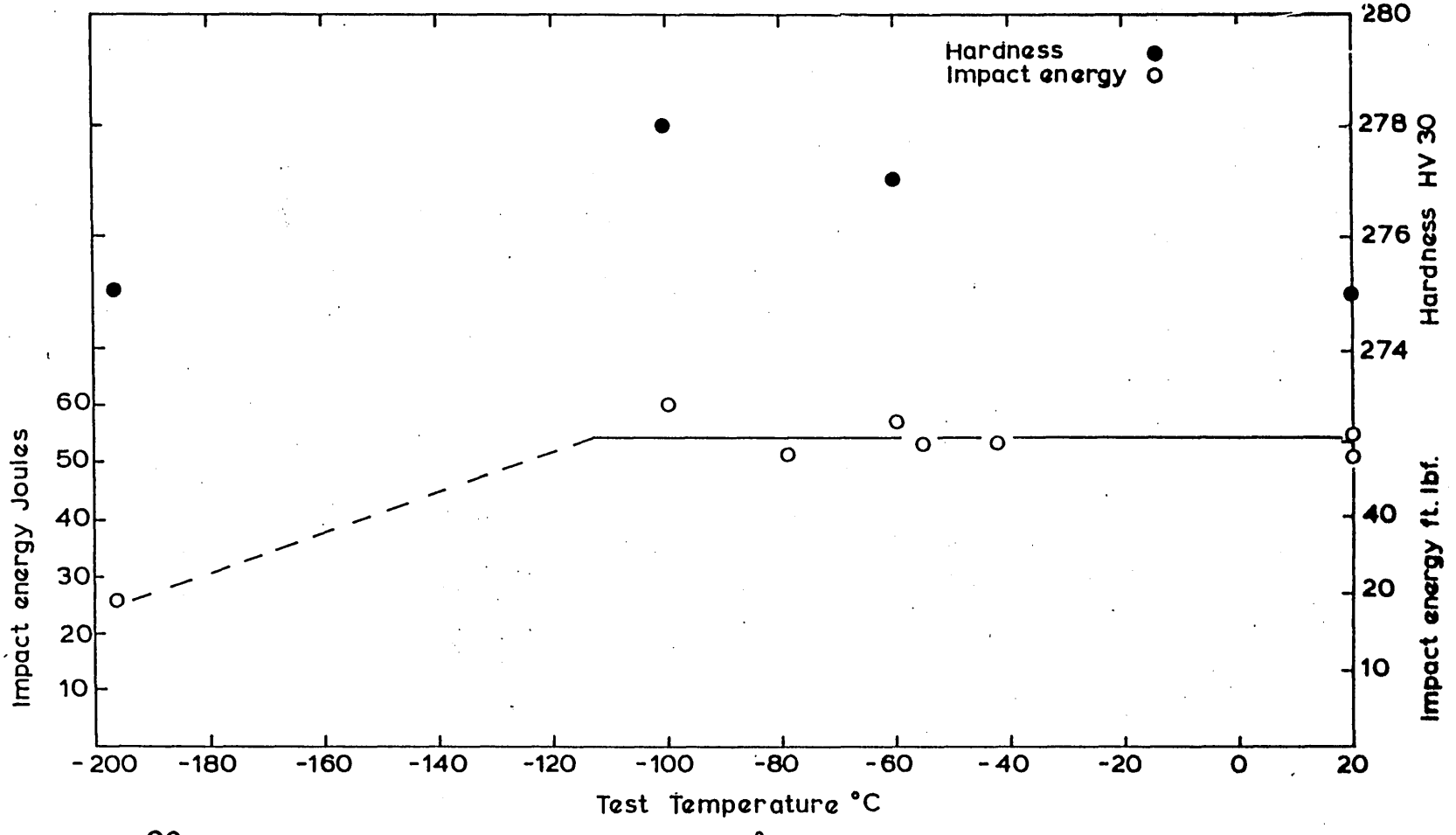

FIG.28 ALLOY K3337 Fe-20 % Mn, 1h 850°C W.Q. VARIATION OF IMPACT TOUGHNESS AND HARDNESS WITH TEST TEMPERATURE. (Ref 4)

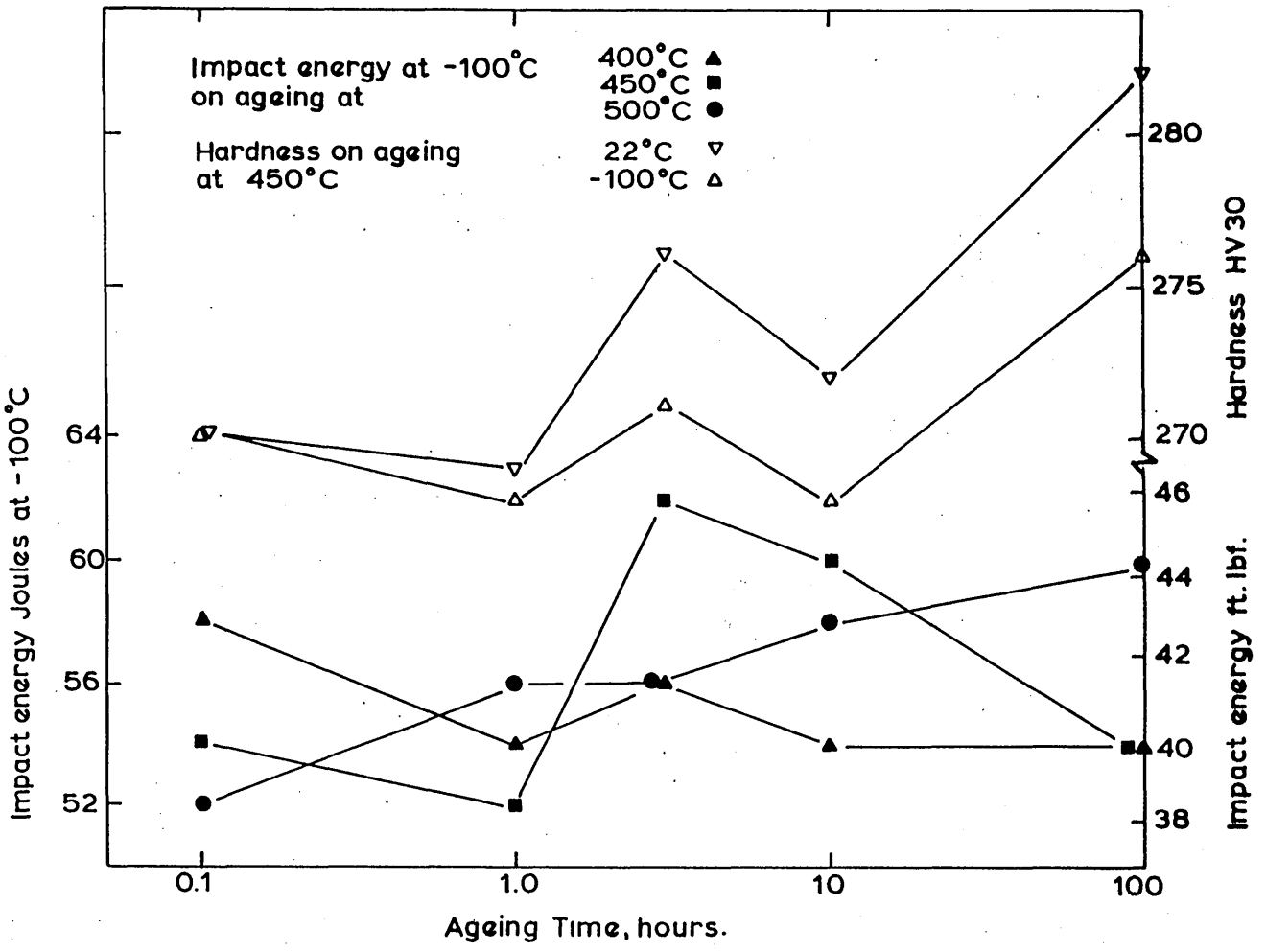

FIG.29 ALLOY K3337 Fe - 20% Mn 1h 850°C, W.Q. EFFECT OF AGEING TIME AT 400°C, 450°C AND 500°C ON HARDNESS AND IMPACT ENERGY AT -100°C. (Ref. 4)

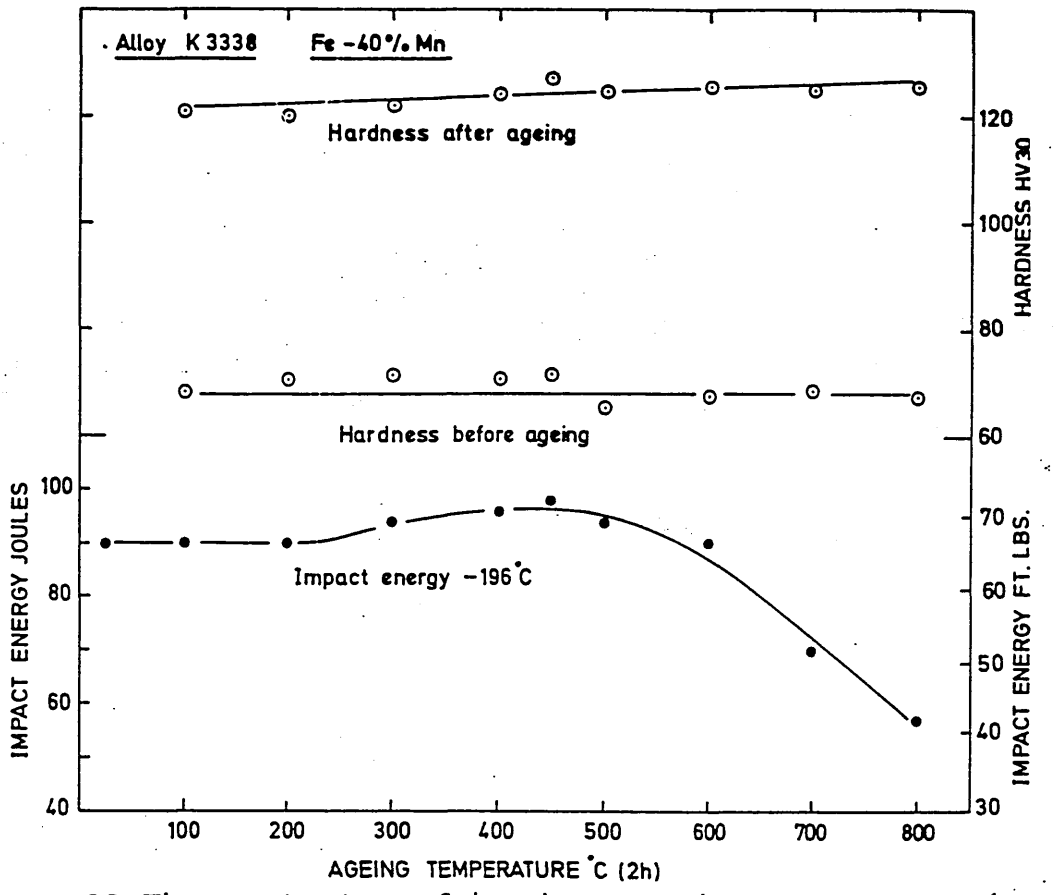

Figure 30 The variation of hardness and impact energy(-196°C) with ageing temperature, for alloy K3338(after Charlesworth, reference 4).

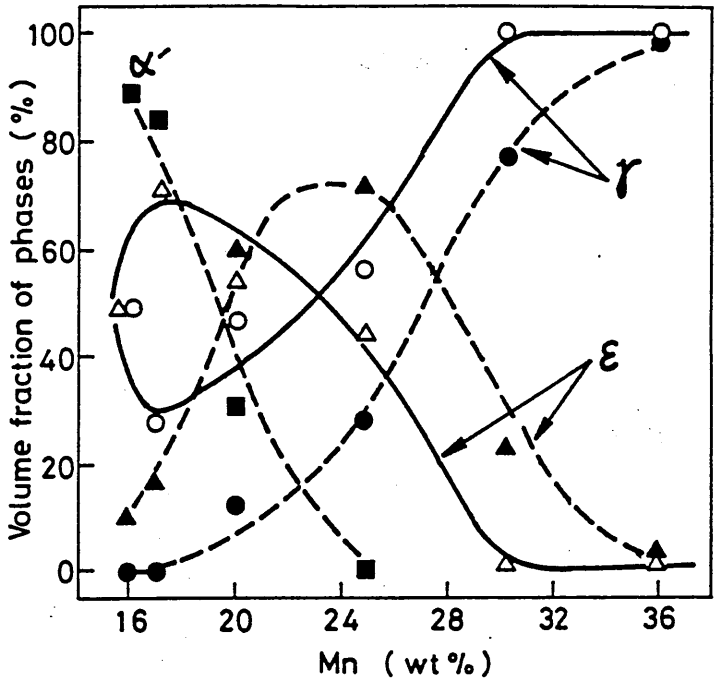

Fig.31—Distribution of constituent phases as a function of Mn content. The phase contents of as-quenched specimens (solid lines) and tensile specimens fractured at 77 K (dashed lines) were determined by X-ray diffraction. (Ref. 116)

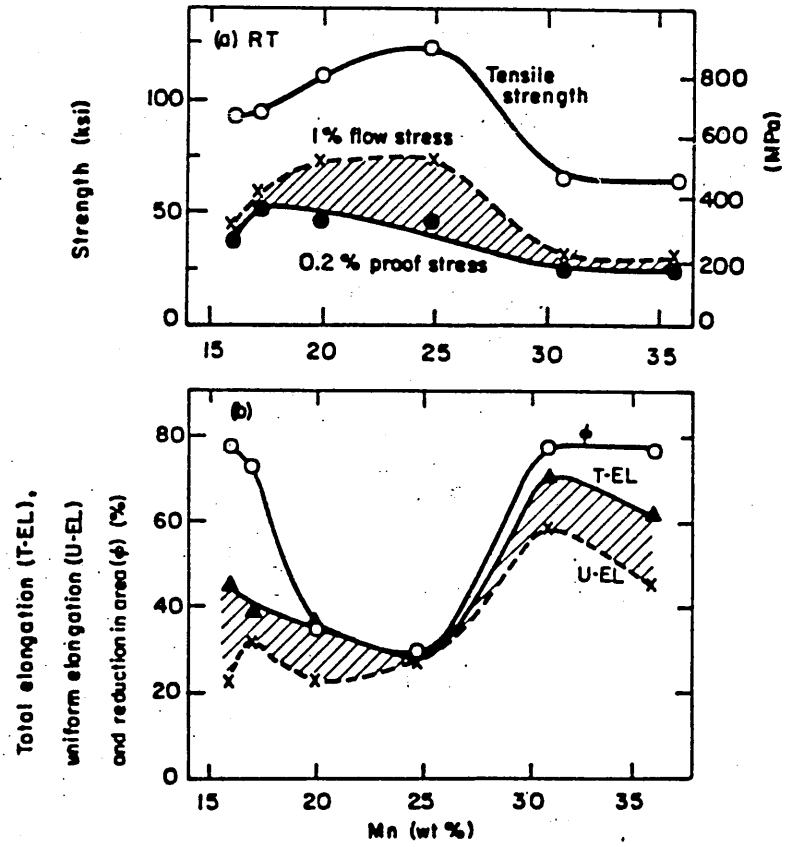

Fig.32 Effect of Mn content on 0.2 % proof stress, 1% flow stress, and tensile strength(a) and uniform elongation(U.EL), total elongation (T.EL), and reduction in area(φ) (b).(Ref.116)

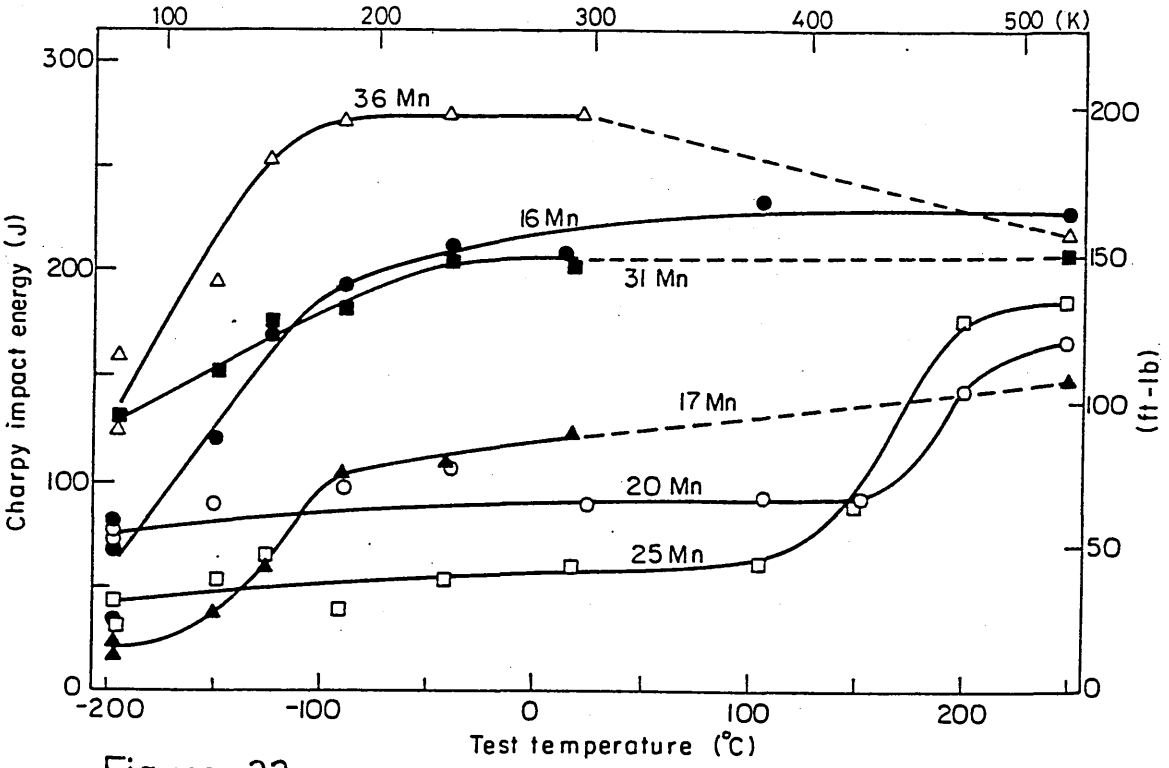

Figure 33 —Ductile-to-brittle transition (DBT) curves. (Ref 117)

Modified Hounsfield 'A' Type specimen

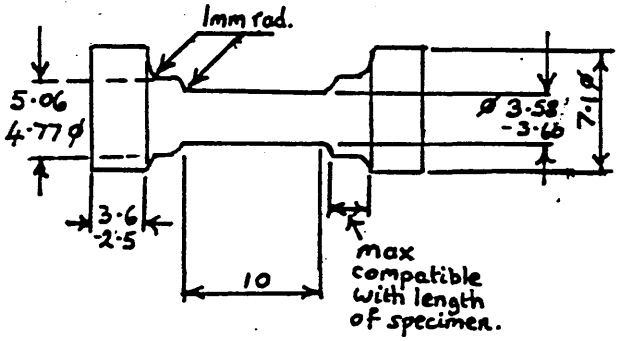

Dimensions in mm.

Figure 34

FIGURE 35 In conversion-electron Mössbauer spectroscopy, the electrons emitted after absorption of a 14.4 keV X-ray are observed by placing the sample inside a special counter. Because of the low penetration of these electrons (500 nanometres) this provides a means of studying the surface composition of samples.

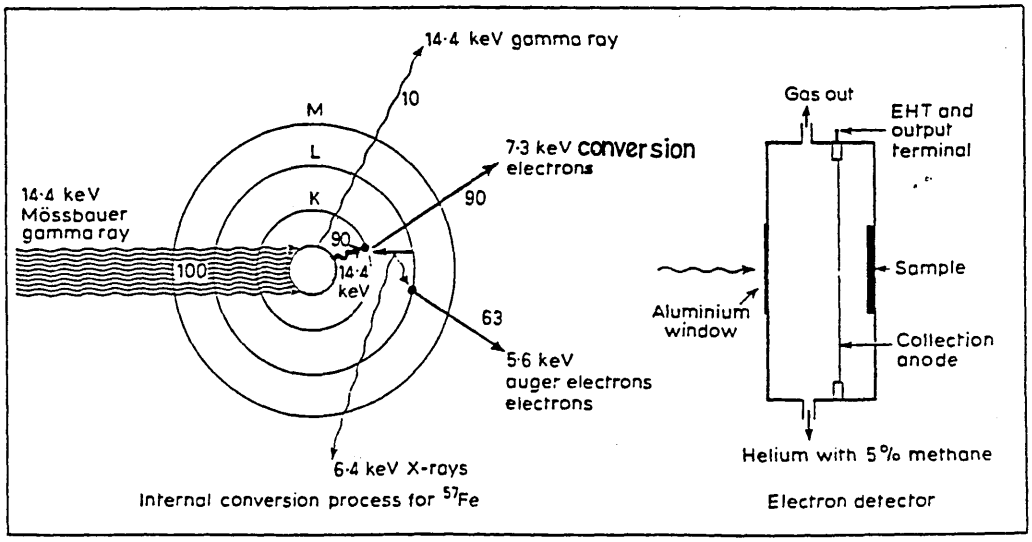

Reference: G.C.Allen and R.A.Mascall,C.E.G.B. Research, June 1982,pp32-44.

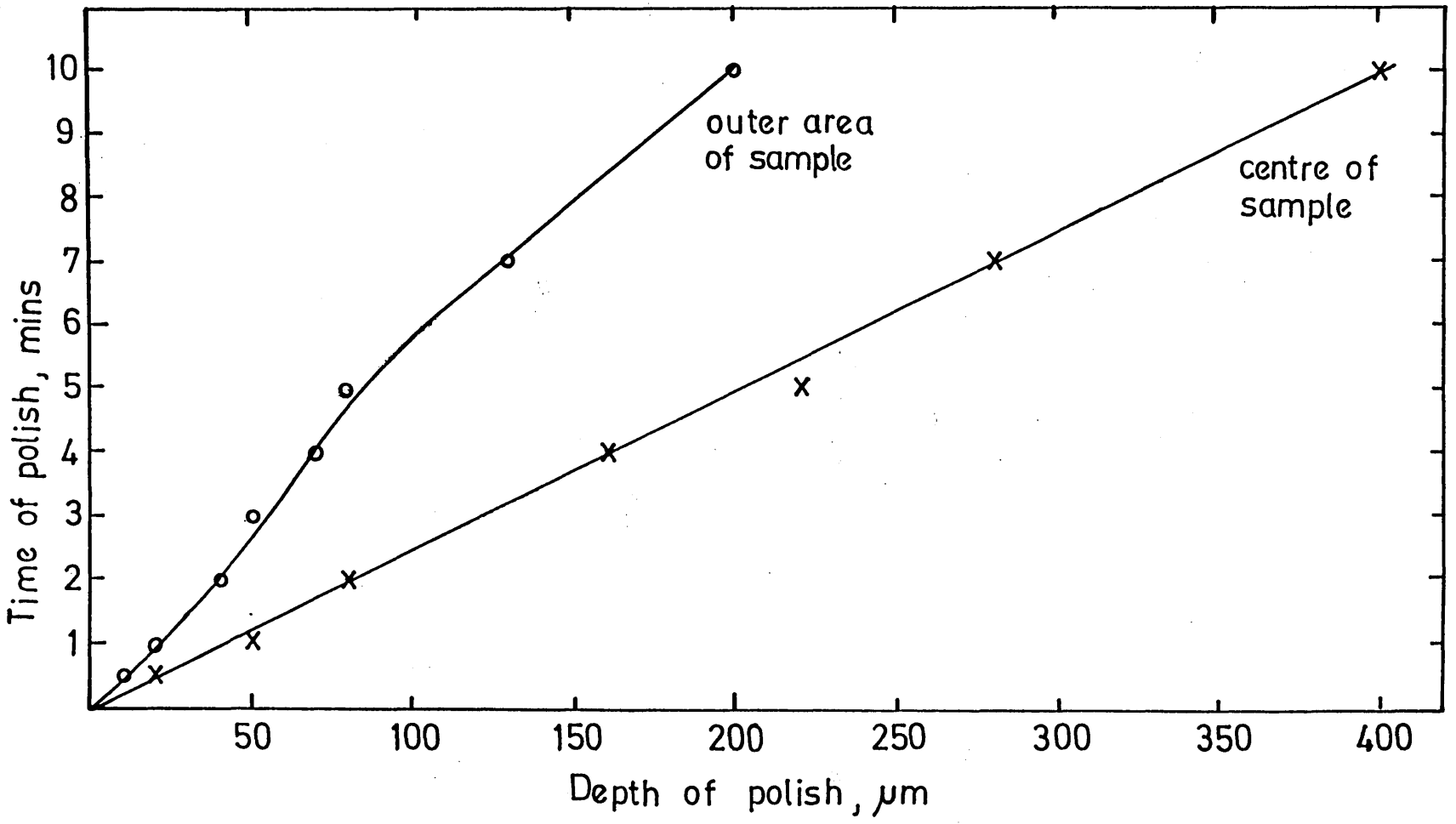

Figure 36 Electropolishing time at 35 volts v Depth of polish

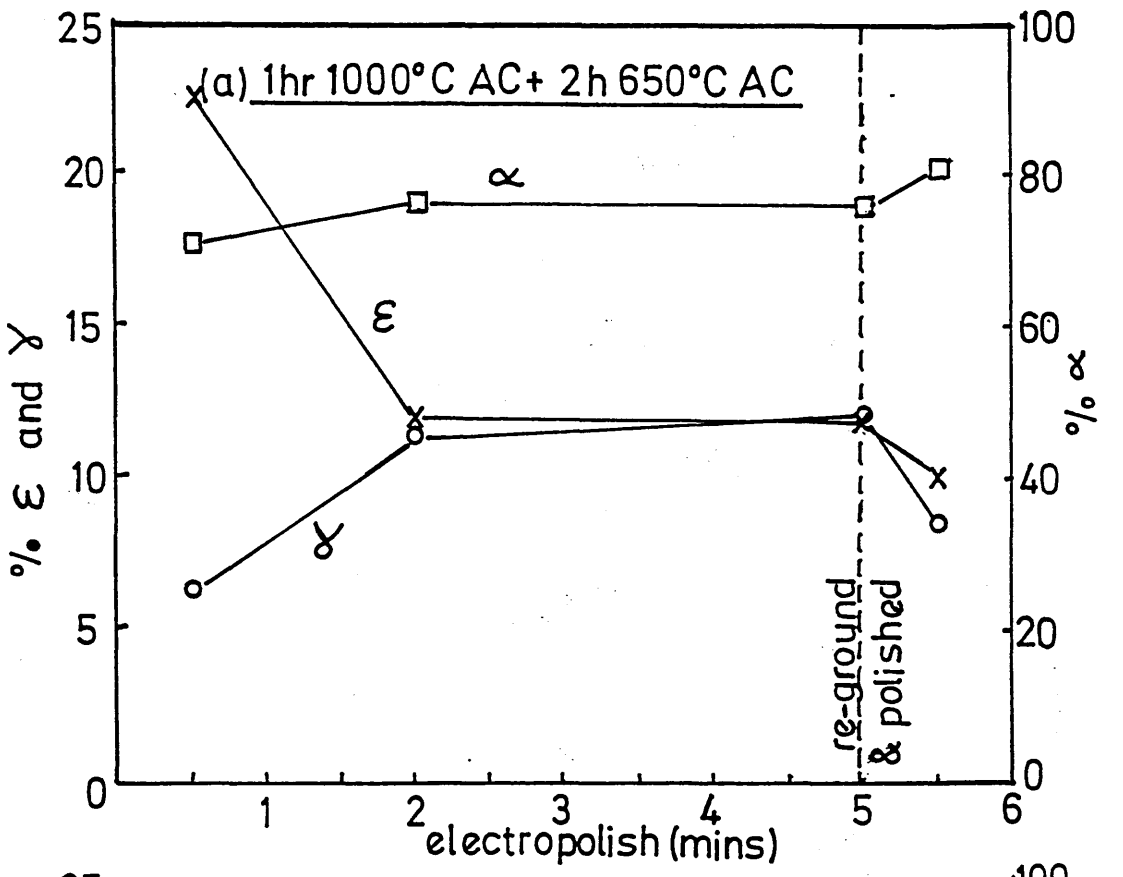

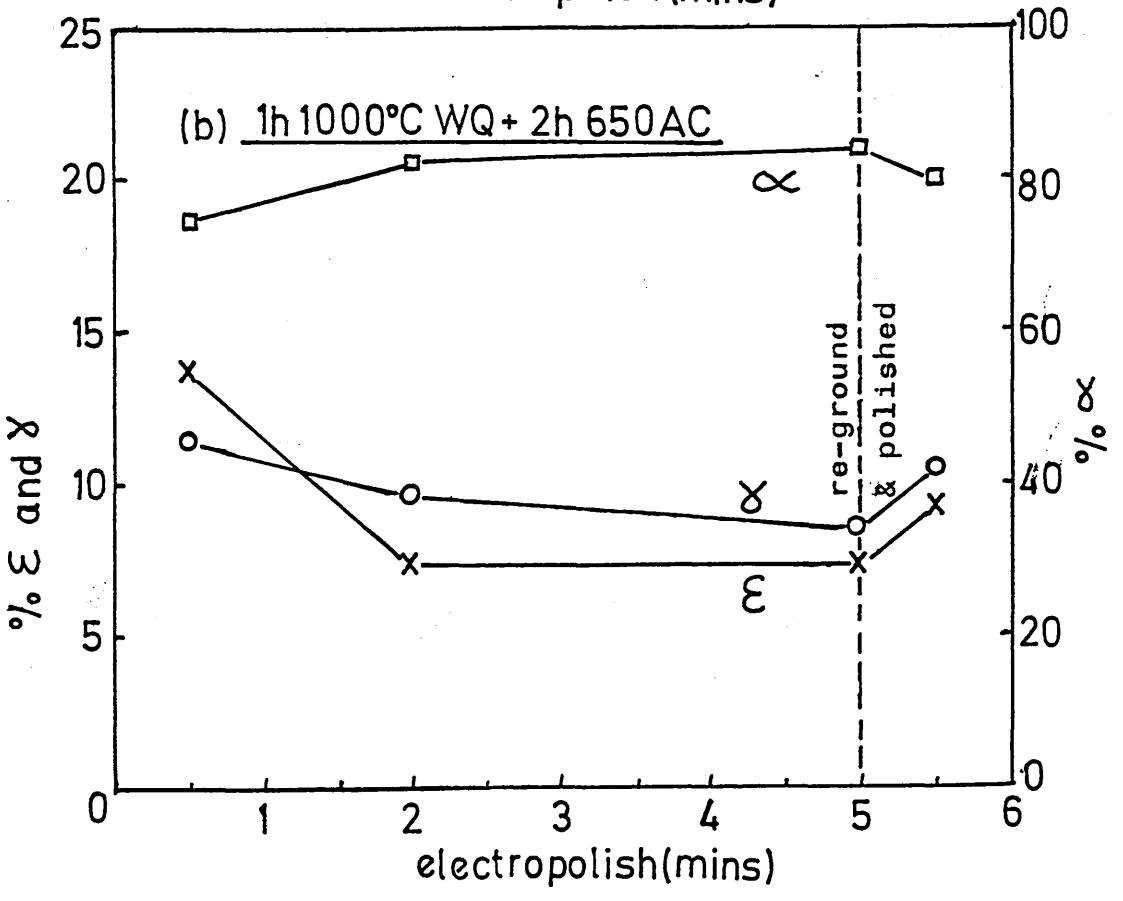

Figure 37(a) & (b) Variation of phase content with electropolishing time for alloy 181(Fe-7.89Mn) Heat treatments given on each graph.

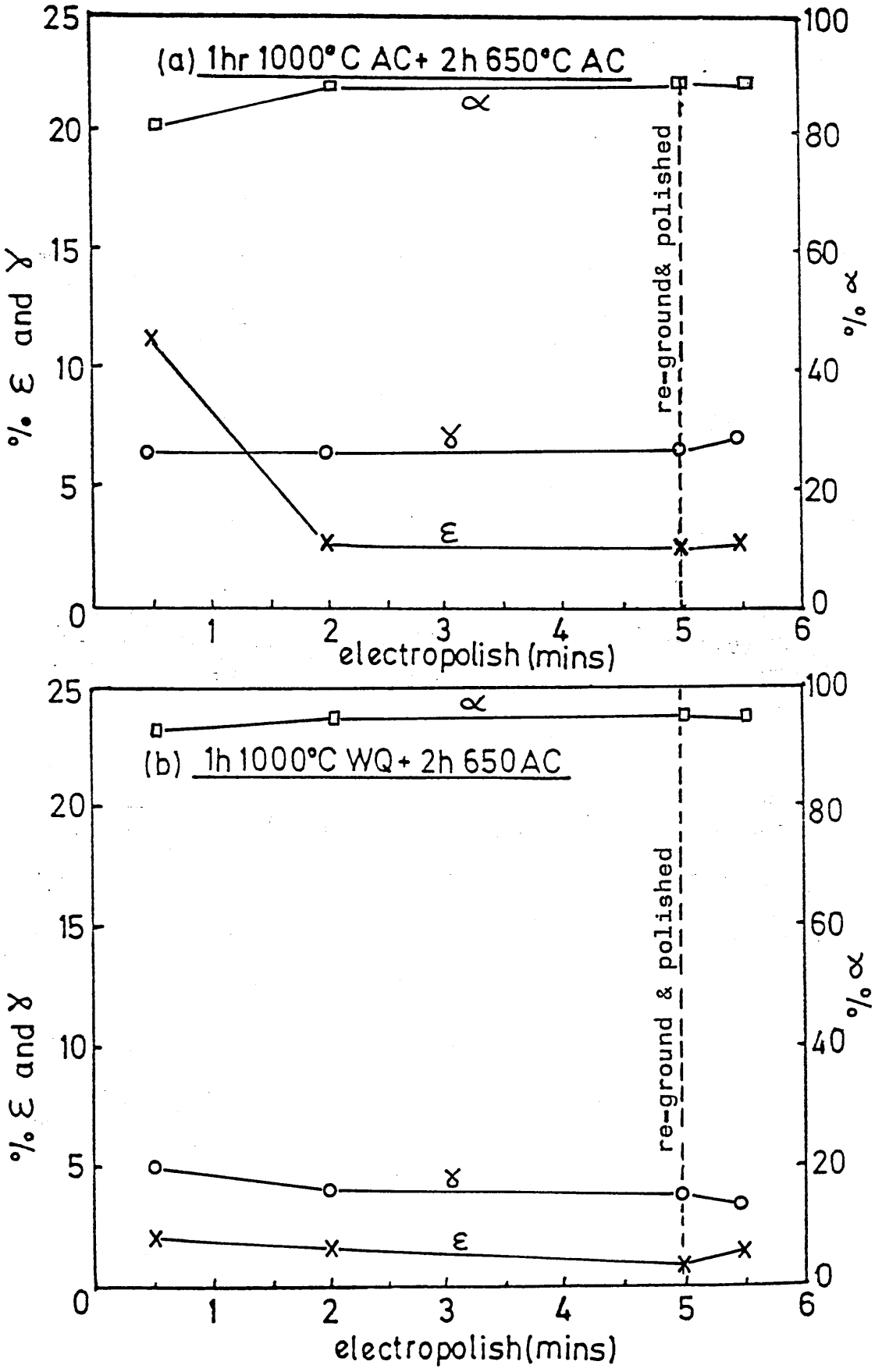

Figure 38(a) &(b) Variation of phase content with electropolishing time for alloy193 (Fe-8.54Mn-0.17Ti-0.18Al)
Heat treatment given on each graph.

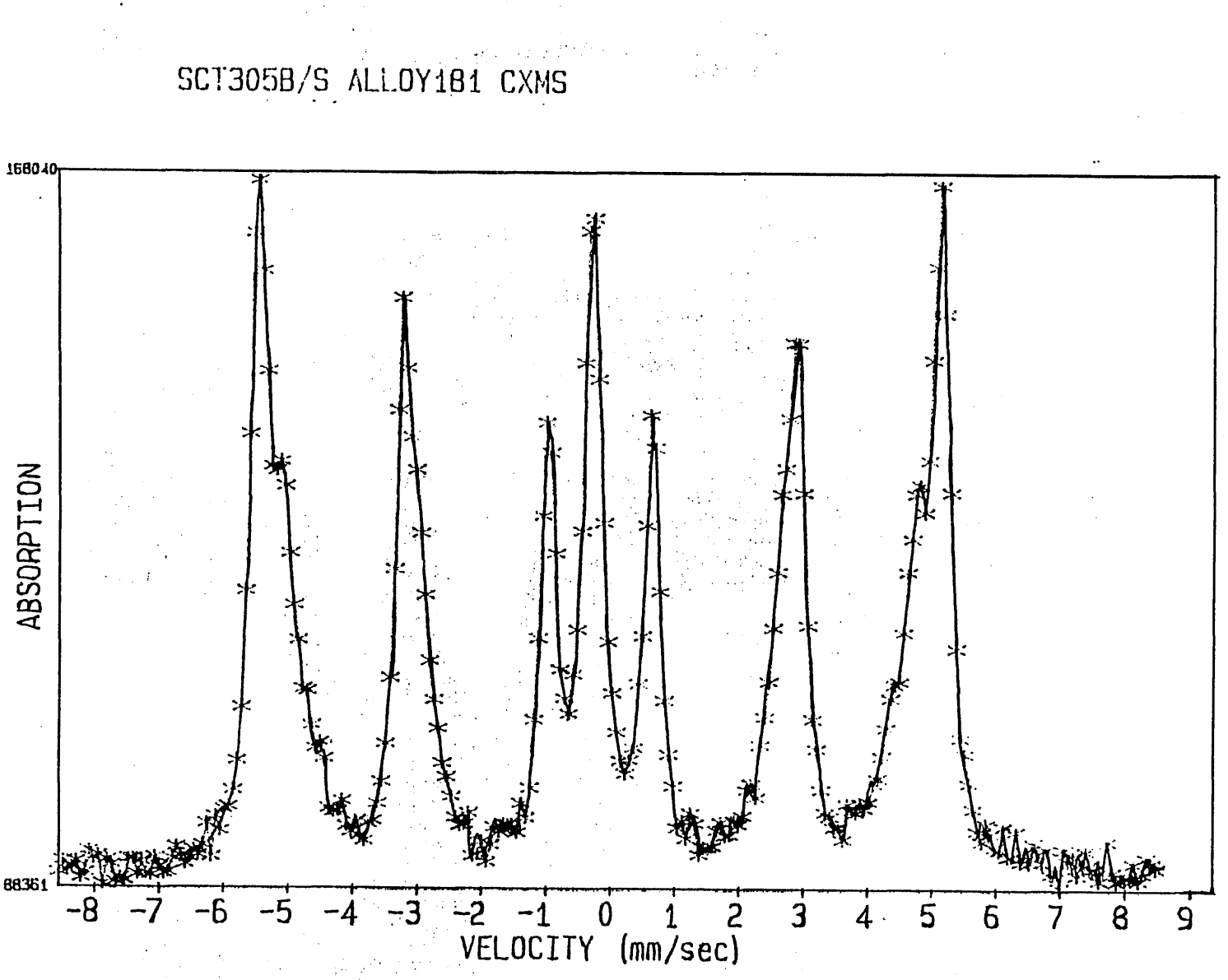

FIGURE 39 MÖSSBAUER X-RAY SPECTRA (alloy 181)

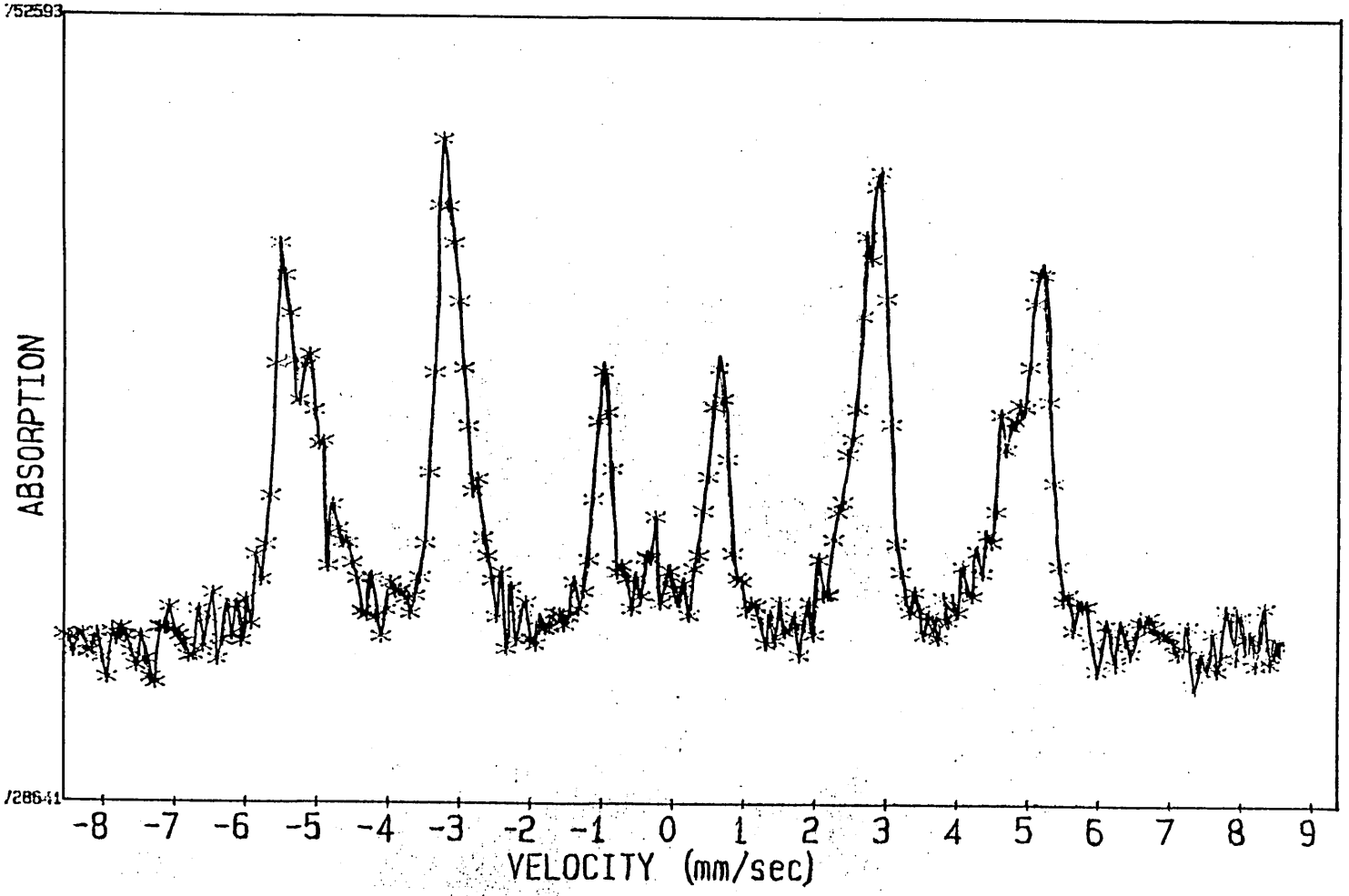

FIGURE 40 MÖSSBAUER ELECTRON SPECTRA (alloy 181)

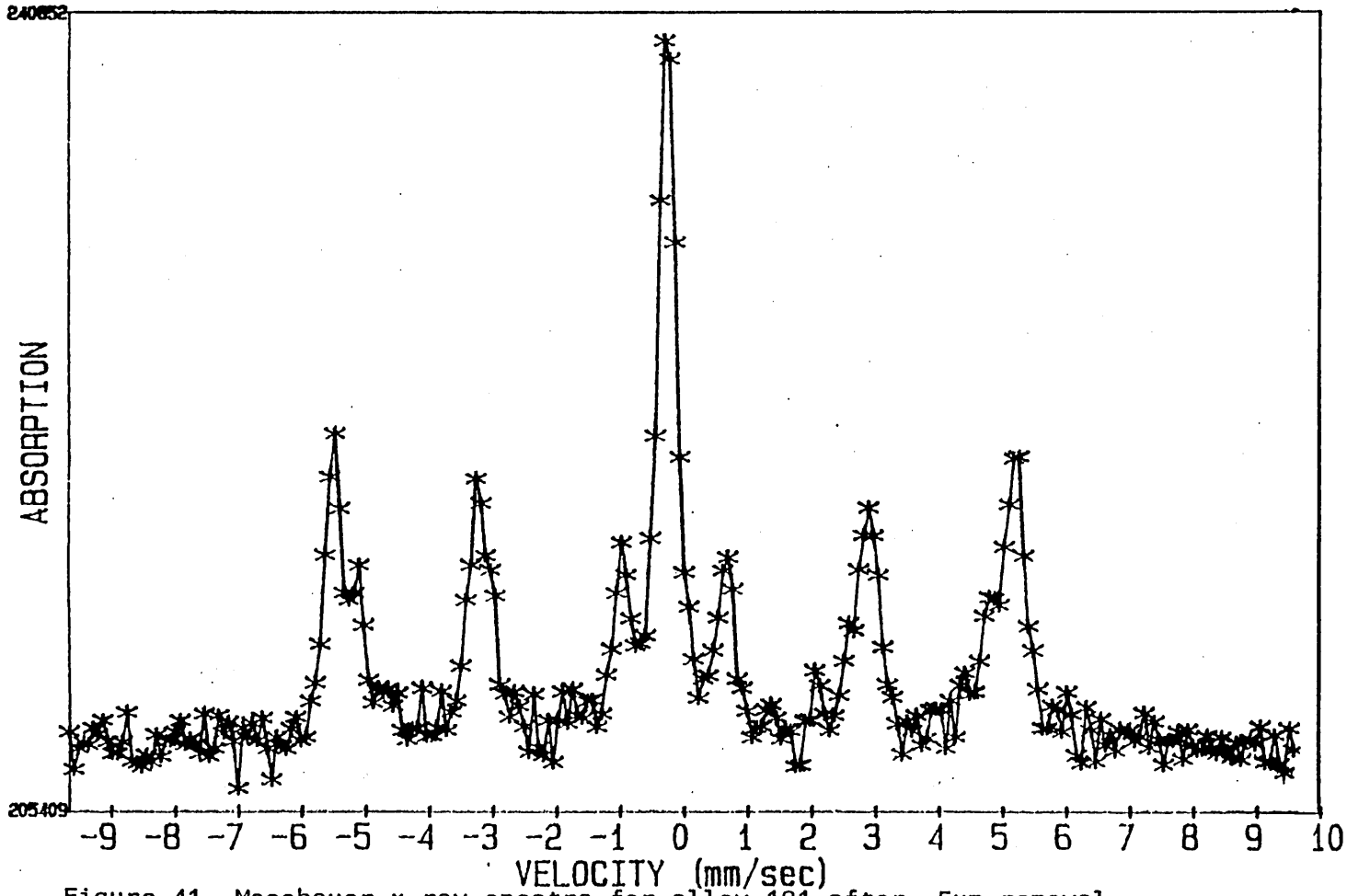

Figure 41 Mossbauer x-ray spectra for alloy 181 after ~ 5μm removal

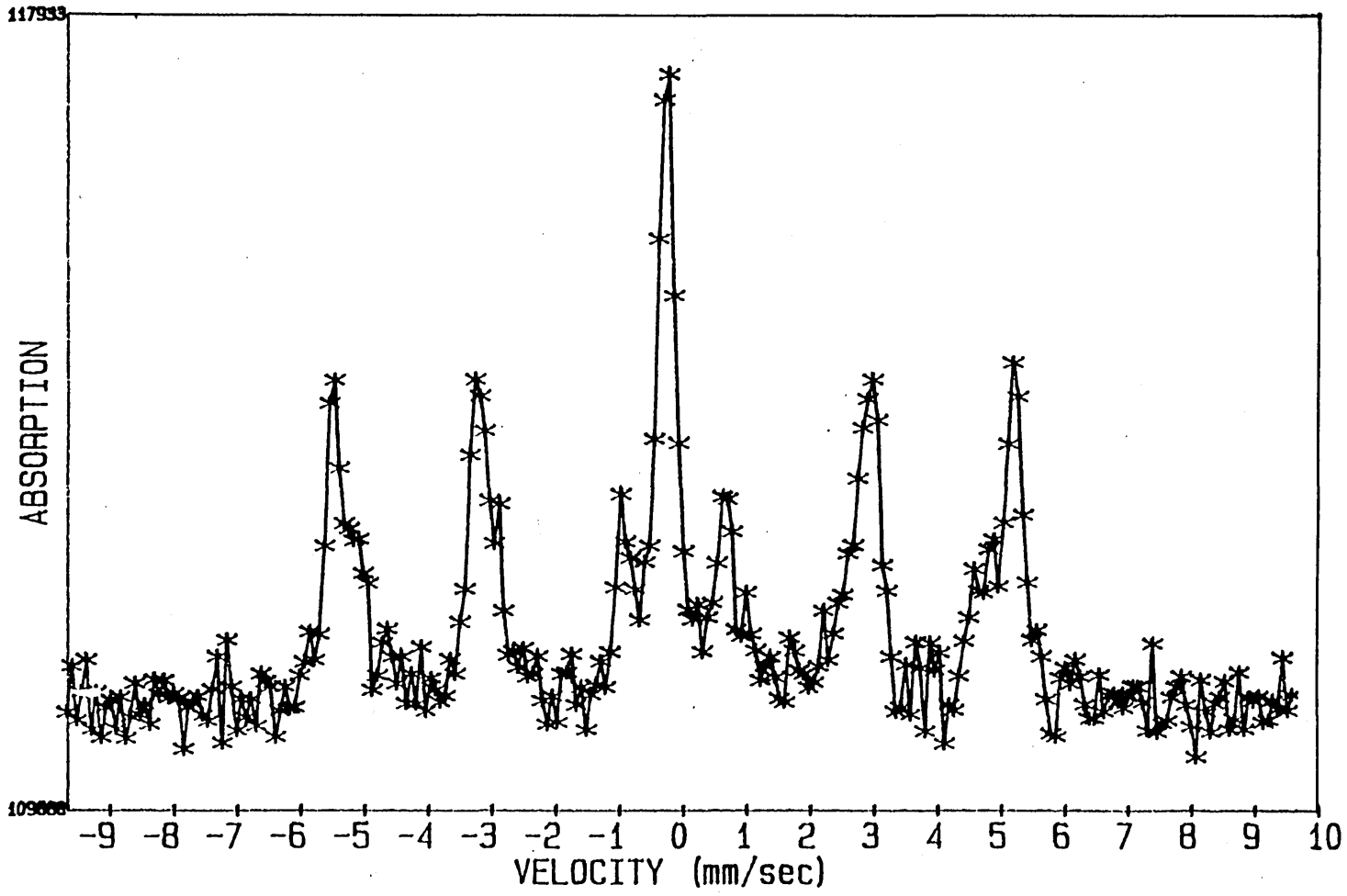

Figure 42 Mossbauer electron spectra for alloy 181 after ~ 5μm removal

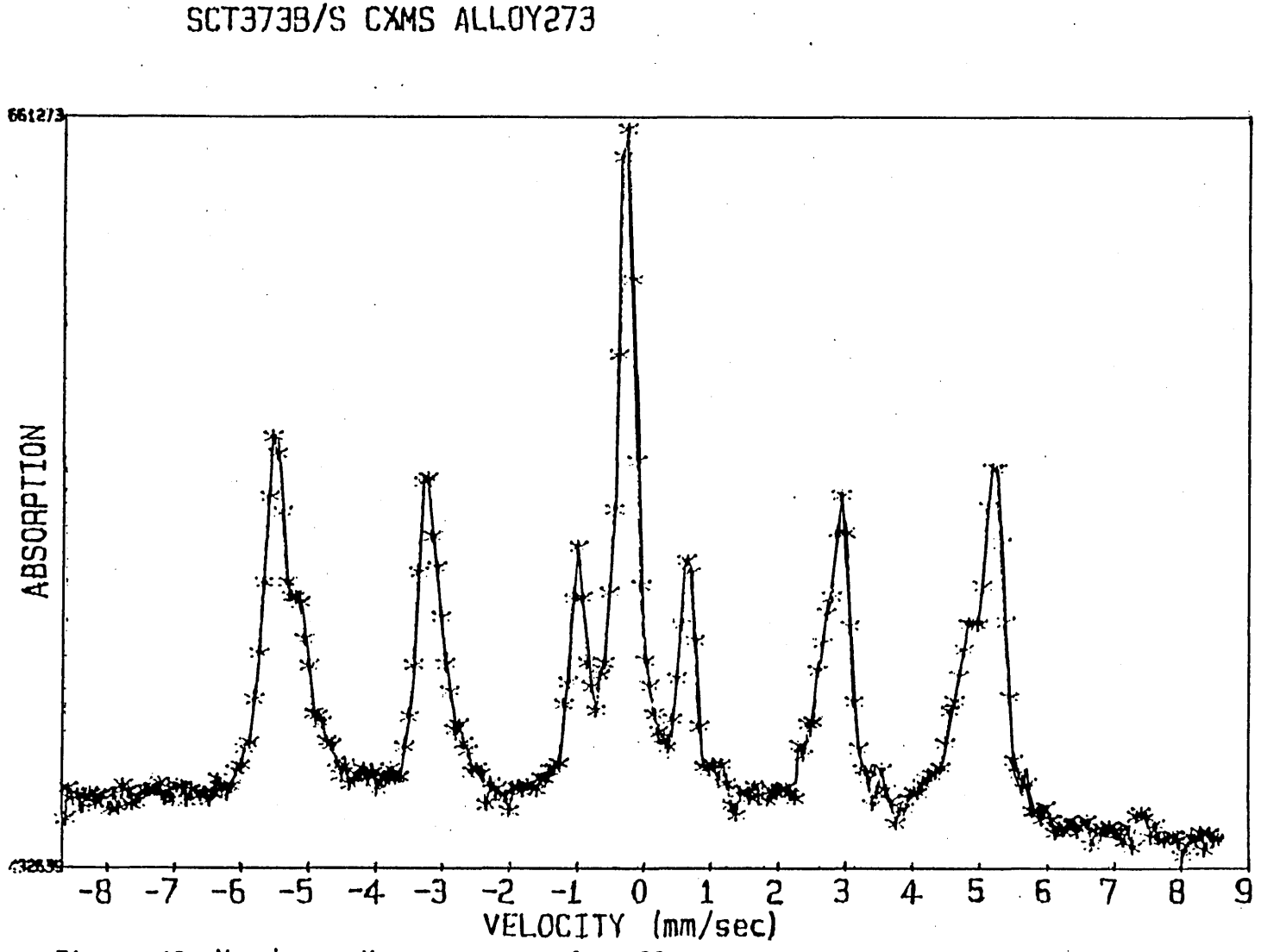

Figure 43 Mossbauer X-ray spectra for alloy 273

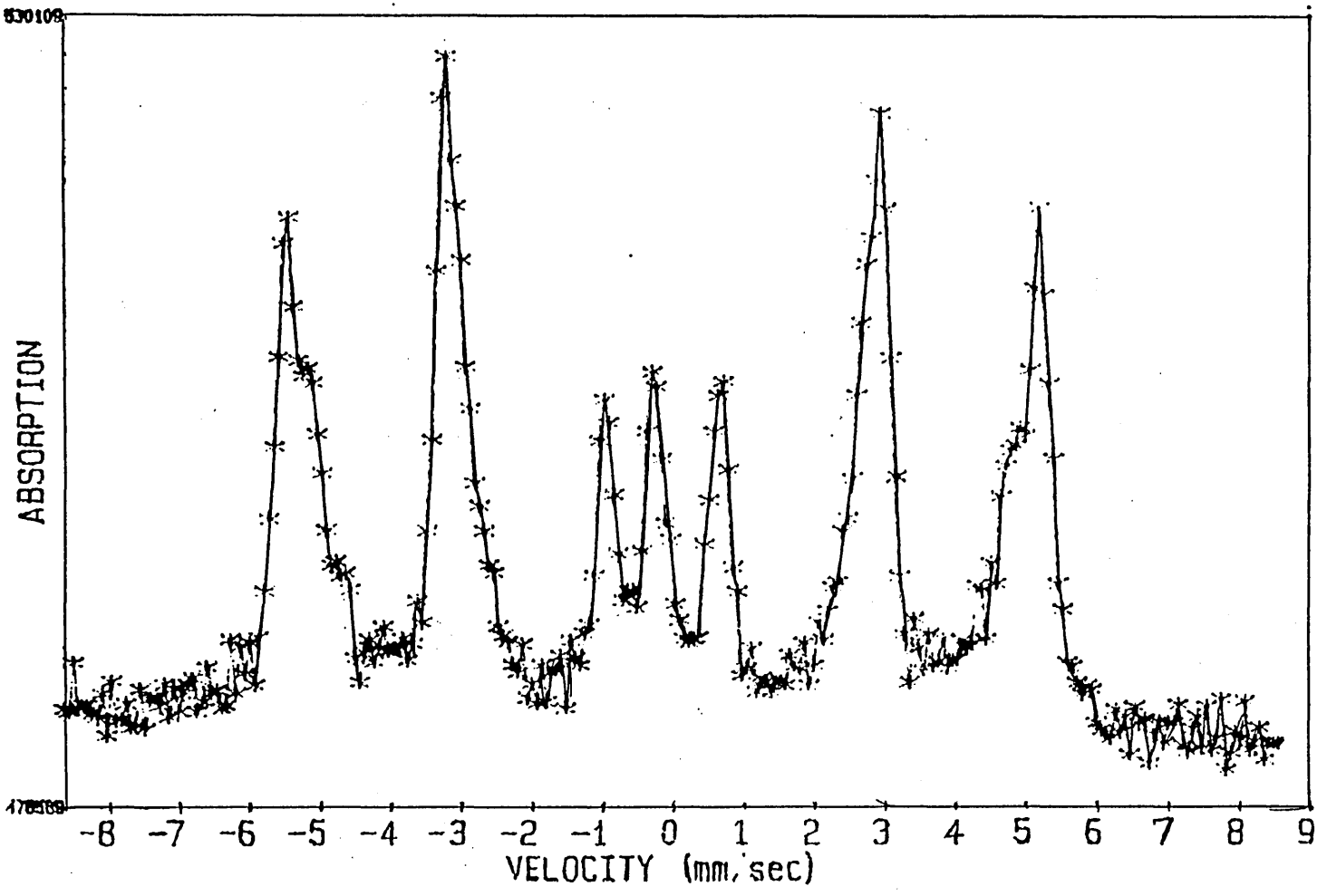

Figure 44 Mossbauer electron spectra for alloy 273

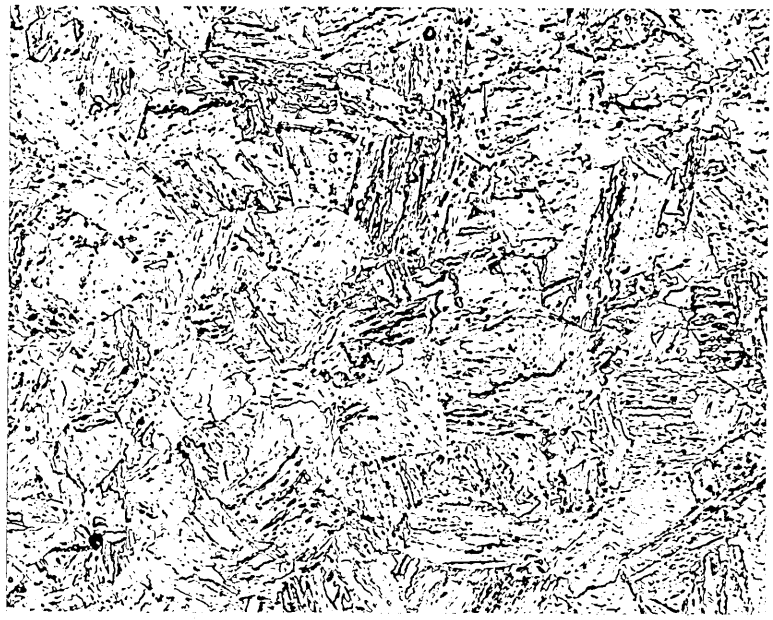

Figure 45(a) X400

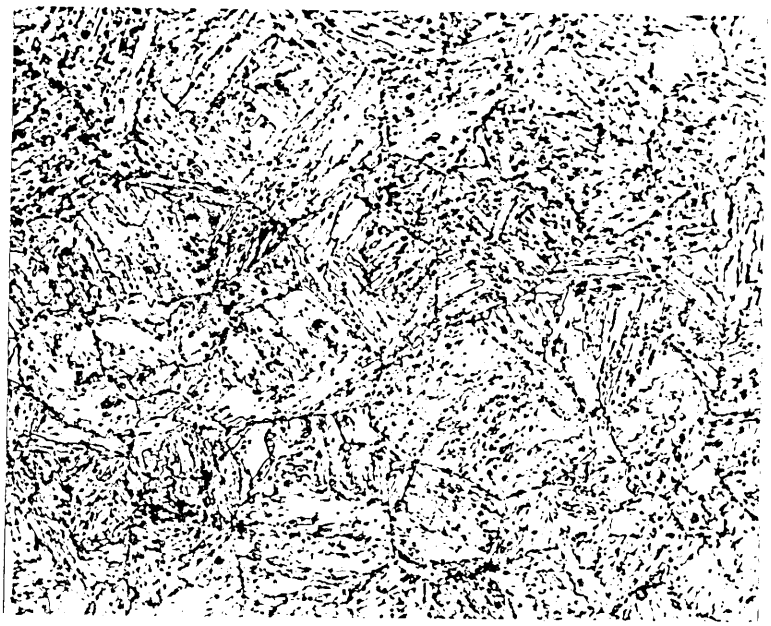

Figure 45(b) X400

Optical micrographs of alloy 181 (Fe-7.89%Mn)
Heat treated 1h 850°C (a) air cooled,(b)water quenched.

Figure 46(a) X400

Figure 46(b) X400

Optical micrographs of alloy 193(Fe-8.54Mn-0.17Ti-0.17Al) Heat treated 1h 850°C (a)air cooled ,(b)water quenched.

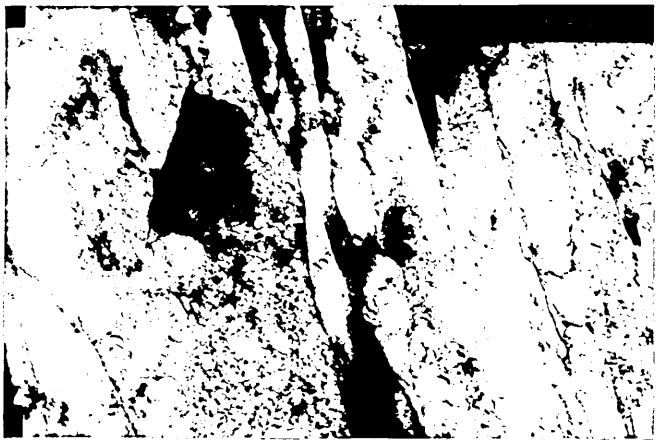

Figure 47(a) X20K

Figure 47(b) X33K

Thin film electron micrographs of alloy 181 showing a lath martensite structure.
Heat treatments: (a) 1h 850°C air cooled,
(b)1h 850°C water quenched.

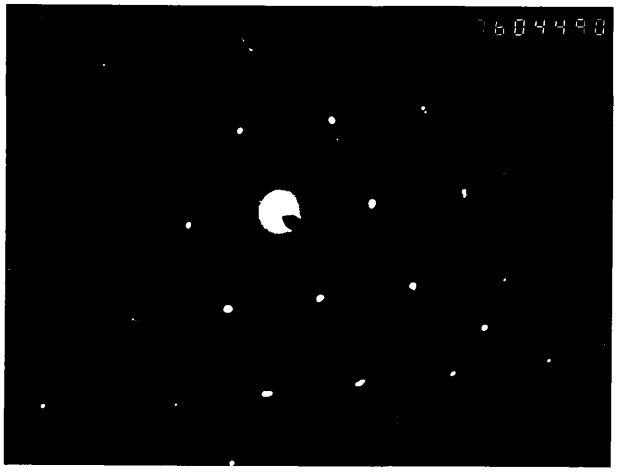

Figure 51(c) $\langle 111 \rangle \gamma$

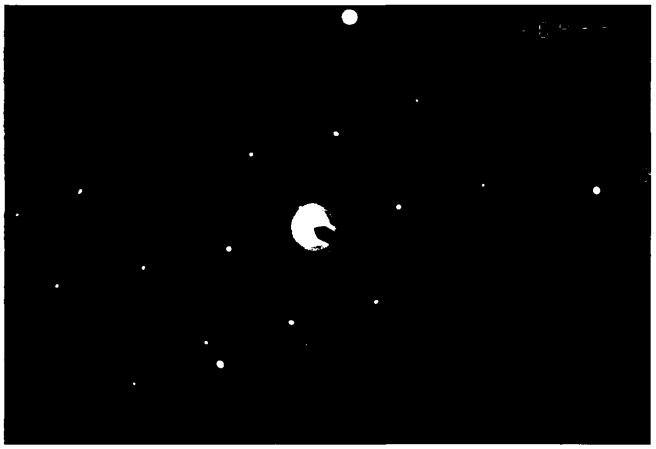

Figure 51(d) $\langle 110 \rangle \alpha'$

T.E.M. Diffraction patterns for alloy 193 showing (c) $\langle 111 \rangle$ reverted austenite and (d) $\langle 110 \rangle$ lath martensite.

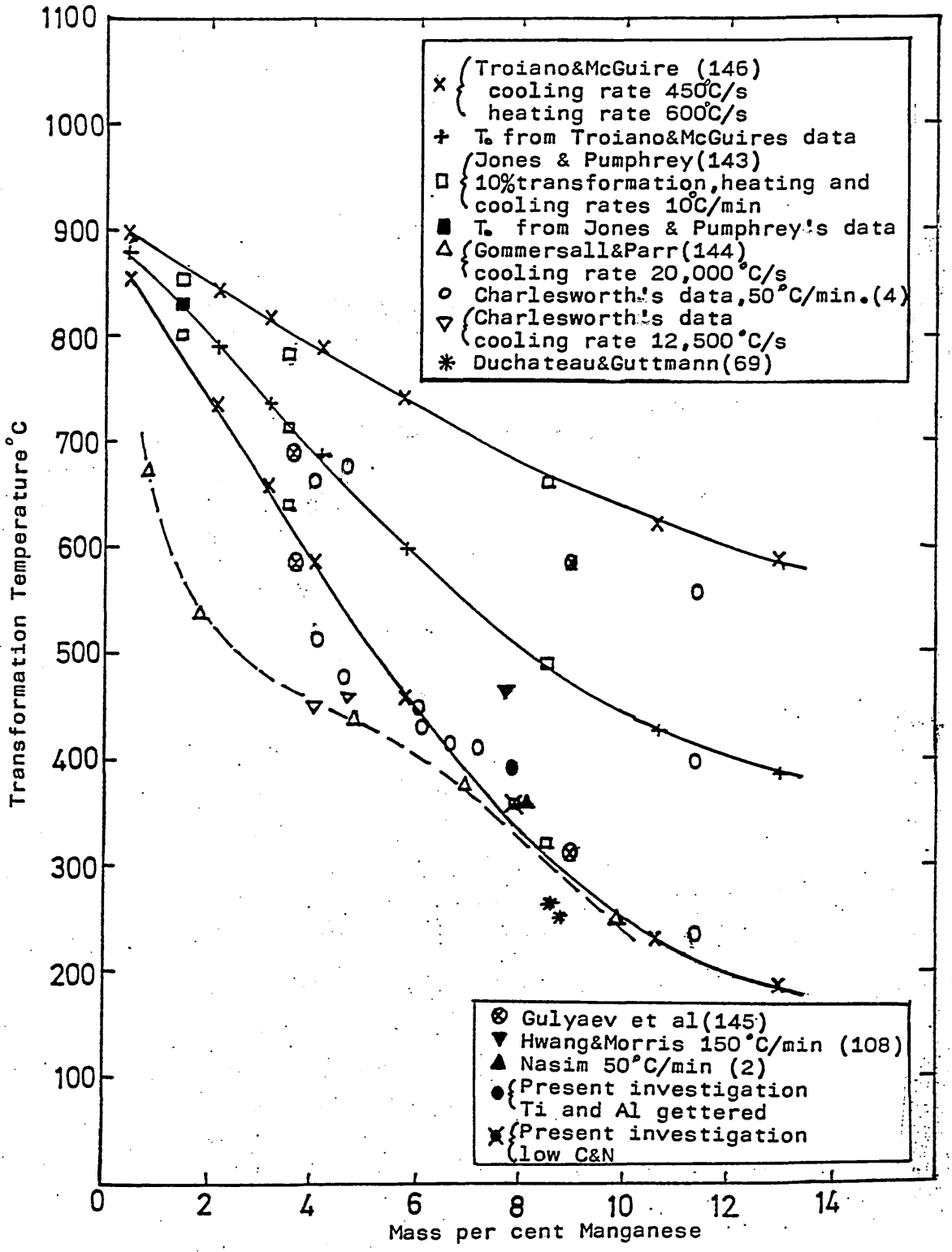

Figure 52 The $\gamma \rightleftharpoons \alpha$ Transformation in Fe-Mn alloys

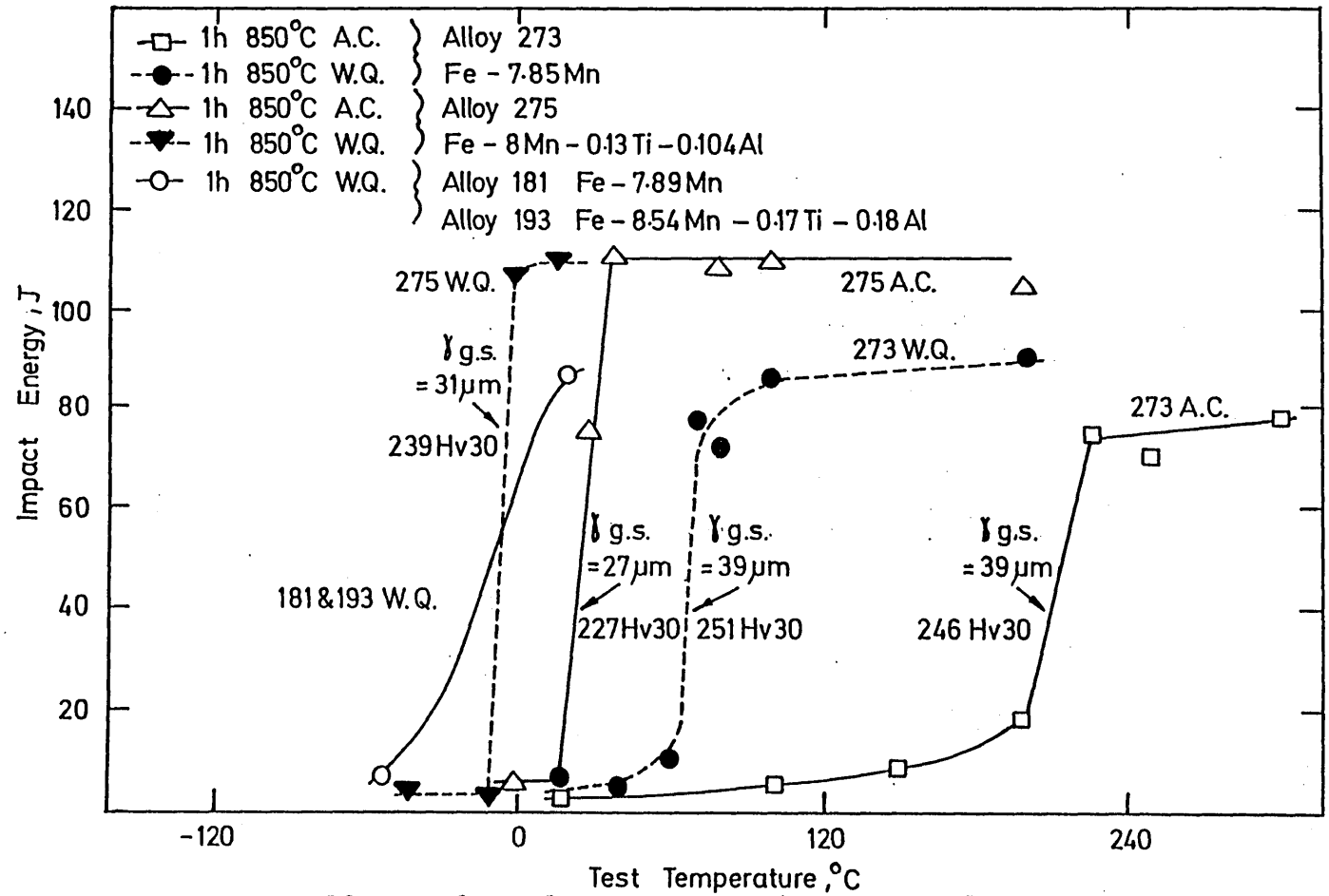

Figure 53 Effect of cooling rate and grain refinement on DBTT after 1 hour at 850°C

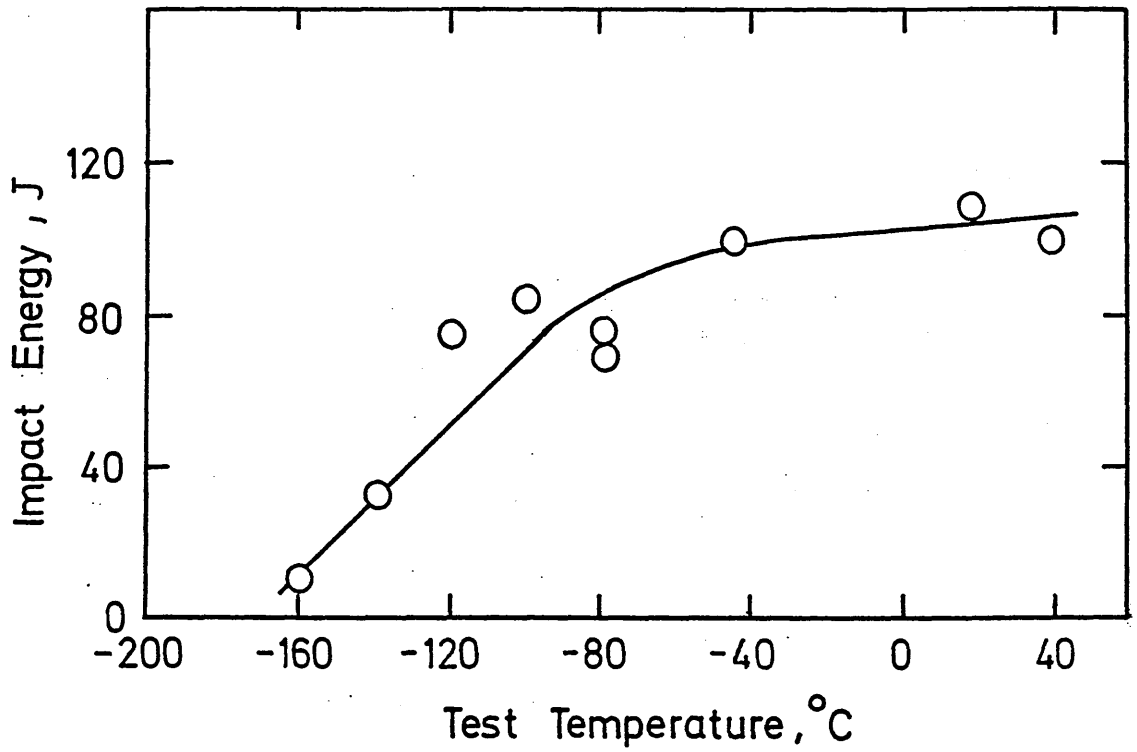

(b) Fracture appearance transition curve

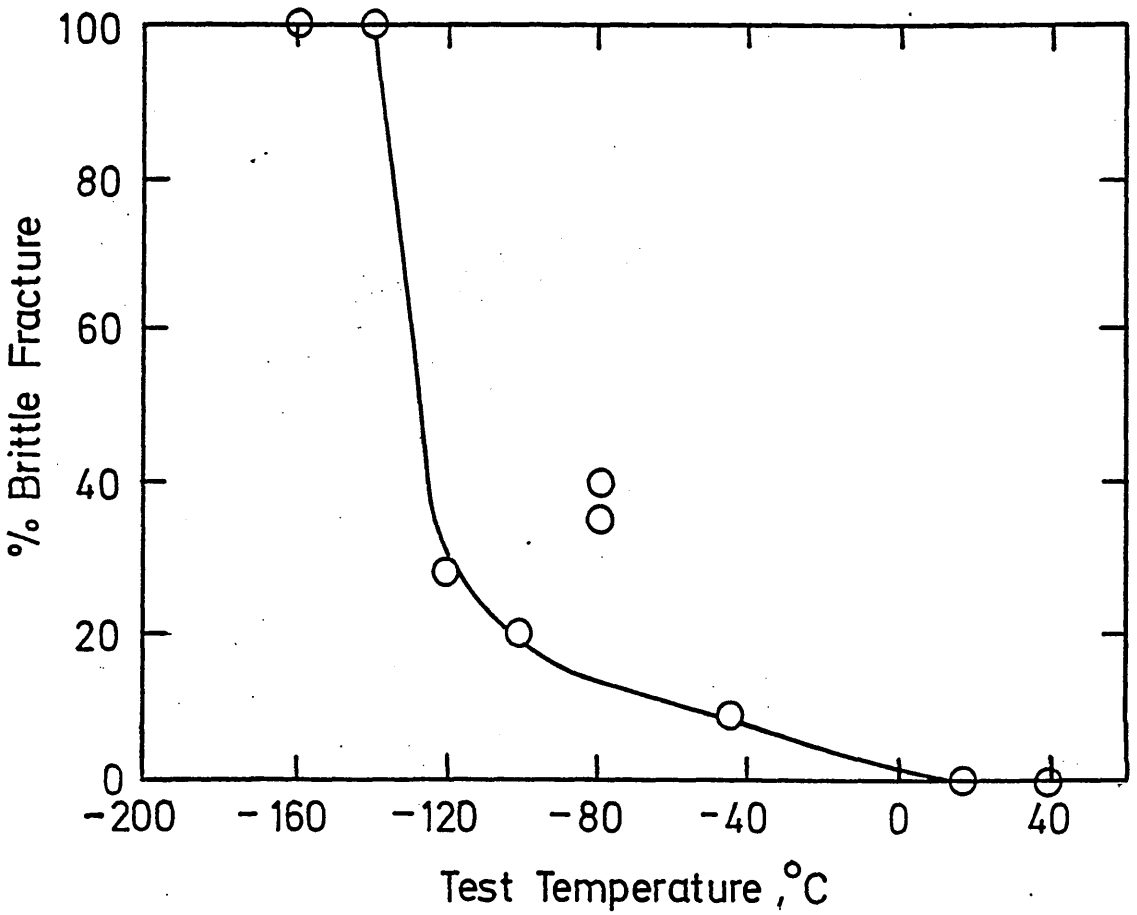

Figure54 Alloy 273 Fe-7.85 Mn
1h.850°C W.Q.+2h.600°C W.Q.

(a)Impact transition curve

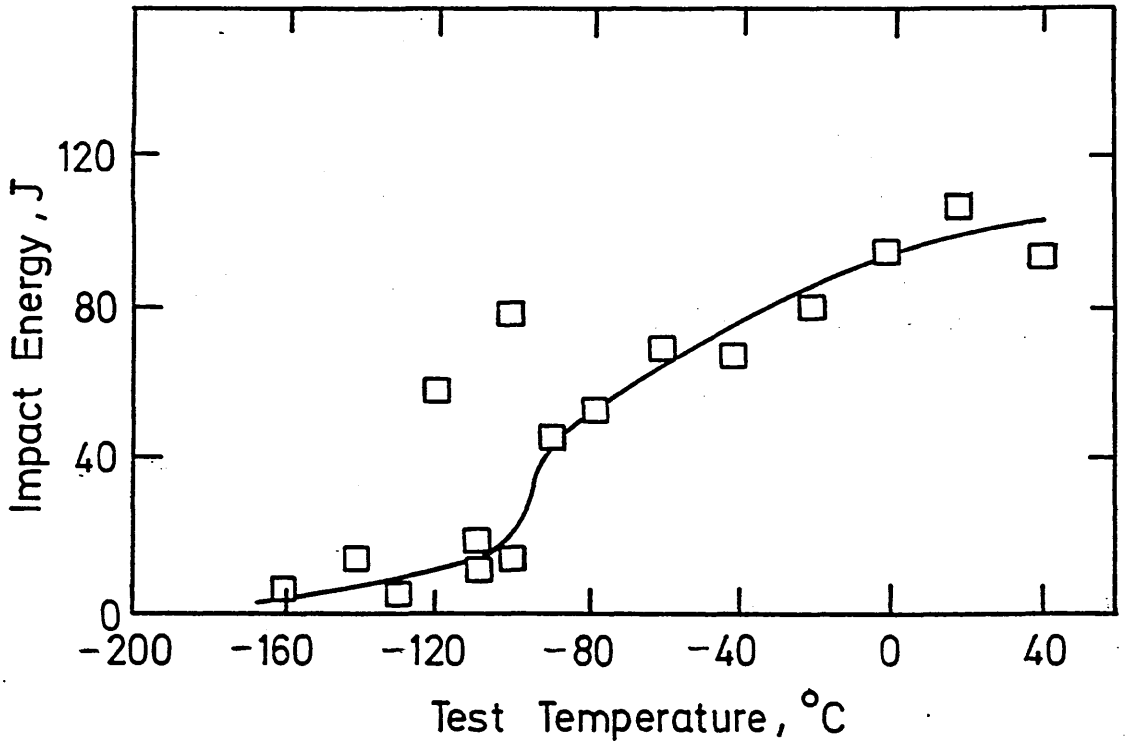

(b) Fracture appearance transition curve

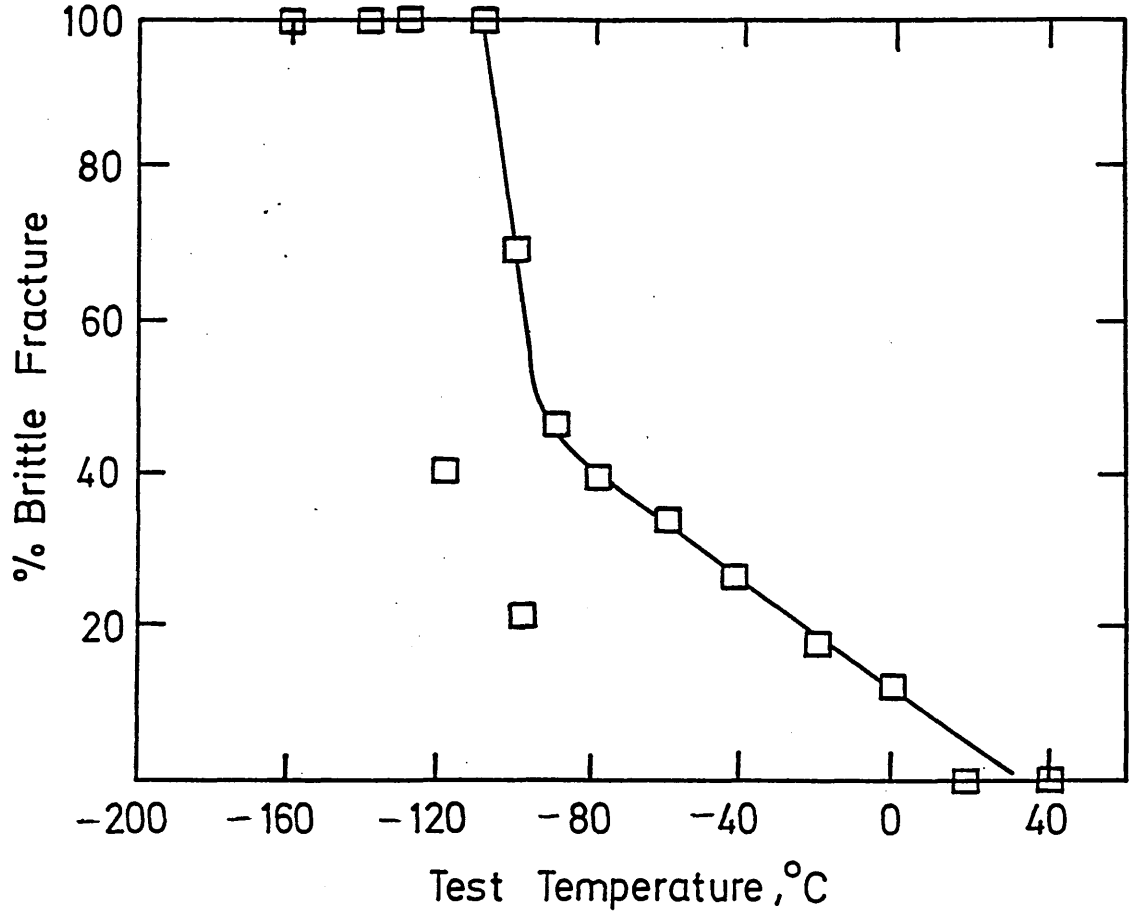

Figure 55 Alloy 273 Fe-7.85 Mn
1h.850°C A.C.+2h.600°C W.Q.

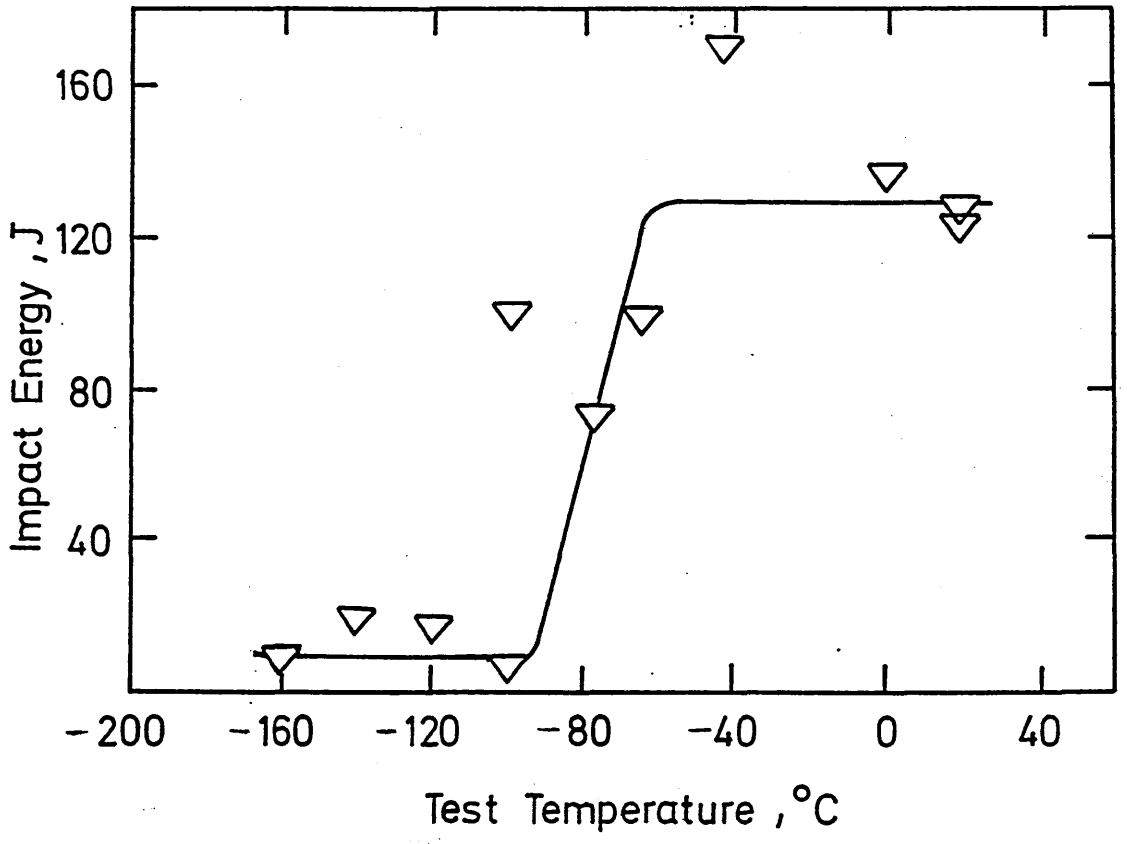

(b)Fracture appearance transition curve.

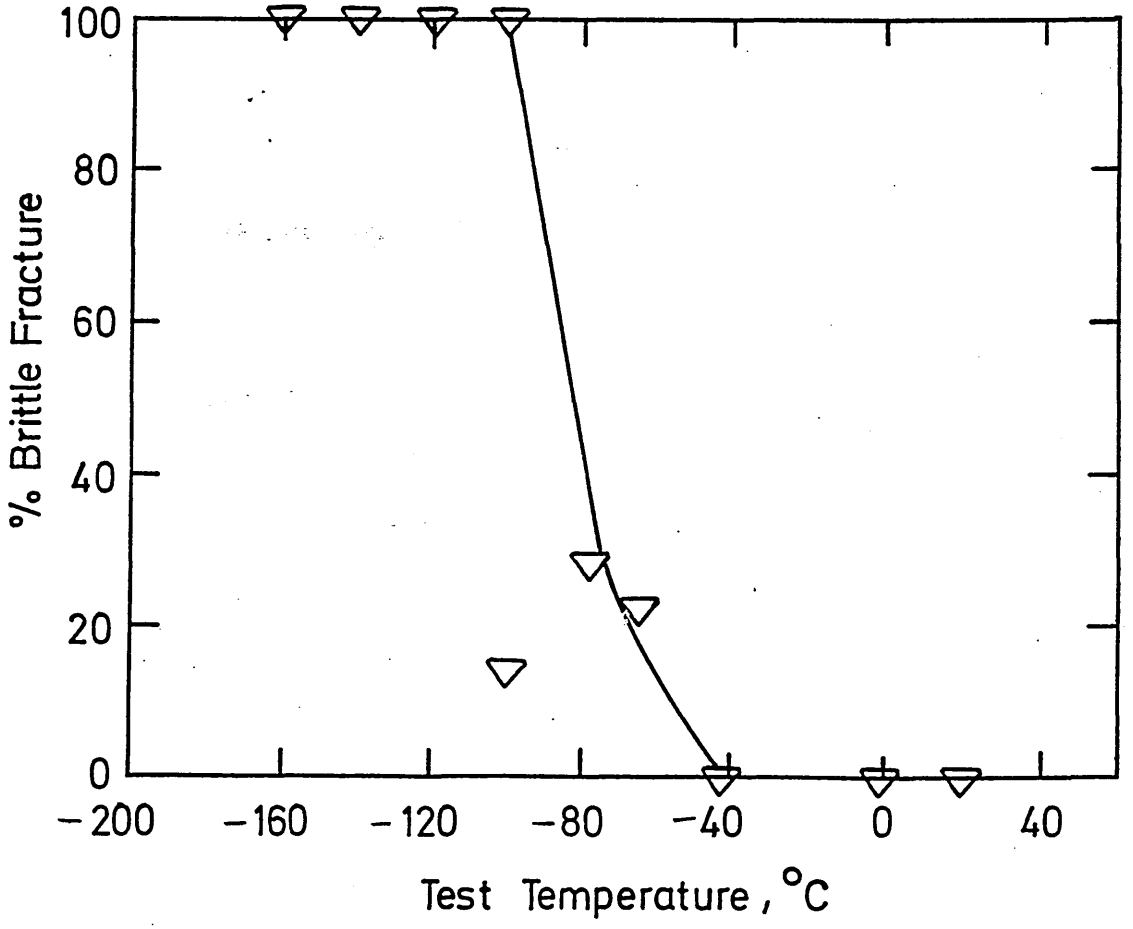

Figure 56 Alloy 275 Fe-8Mn-0.13Ti-0.104Al
1h.850°C WQ+2h.600°CWQ.

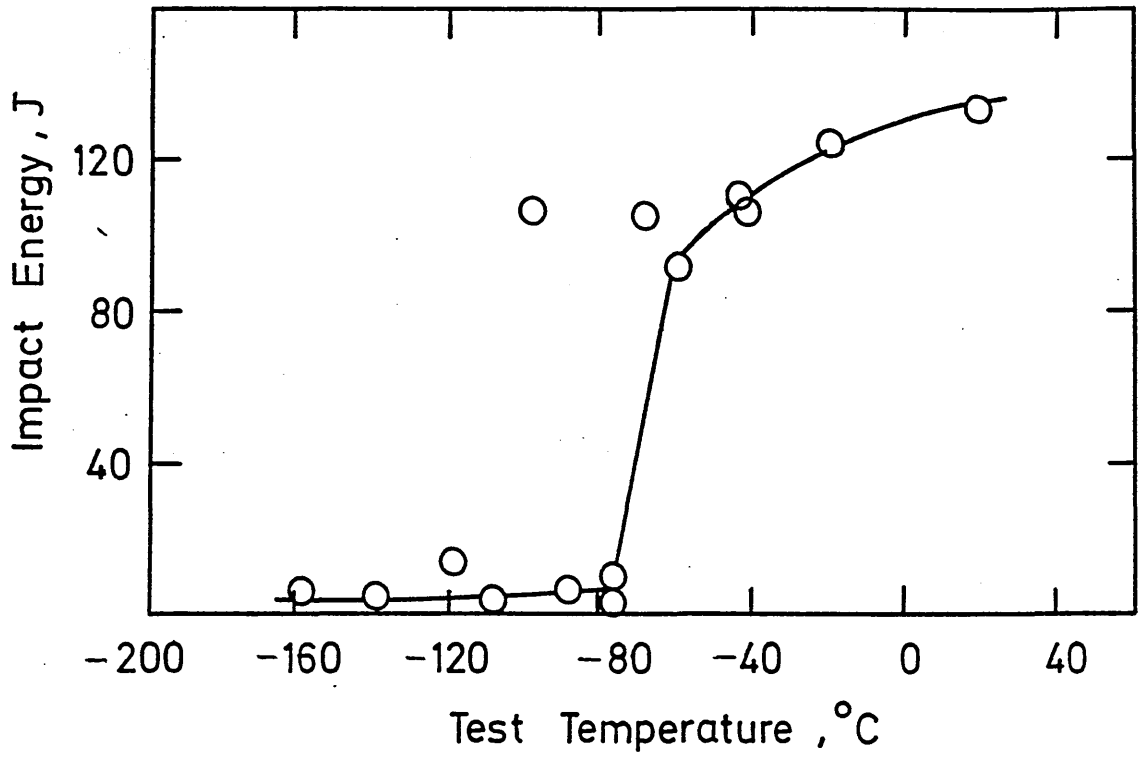

(b) Fracture appearance transition curve.

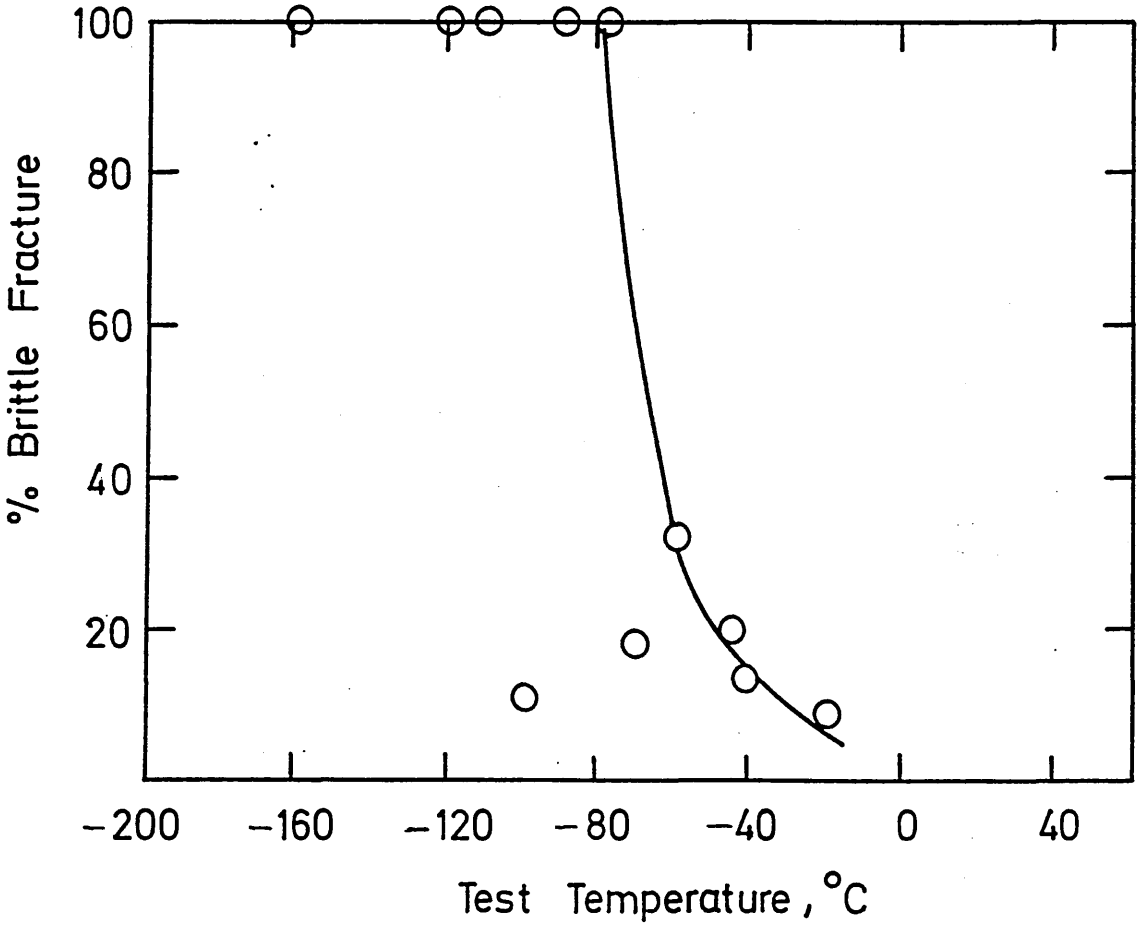

Figure57 Alloy 275 Fe-8Mn-0.13Ti-0.0104Al
1h.850°C A.C.+2h.600°C WQ.

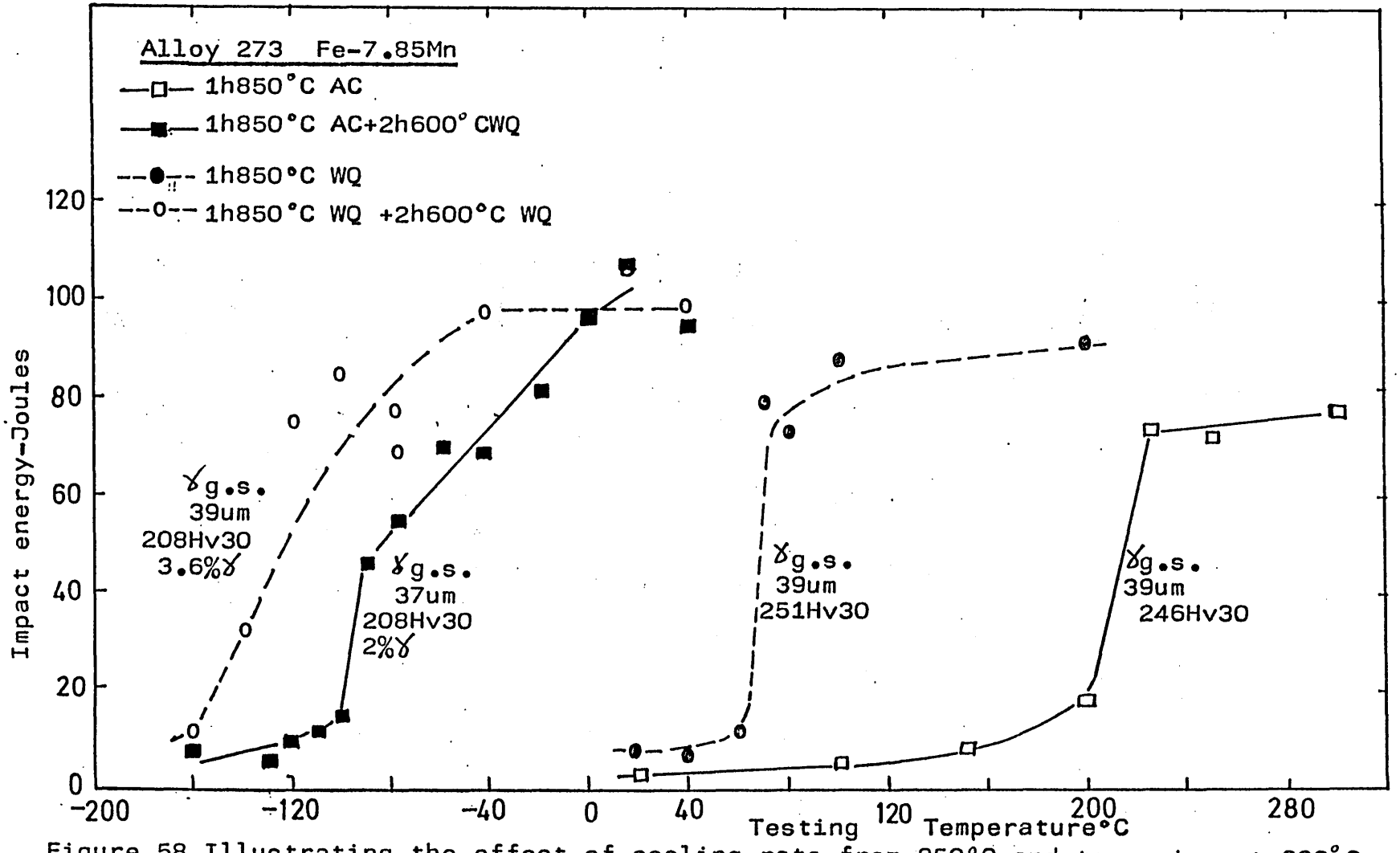

Figure 58 Illustrating the effect of cooling rate from 850°C and tempering at 600°C on DBTT of alloy273.

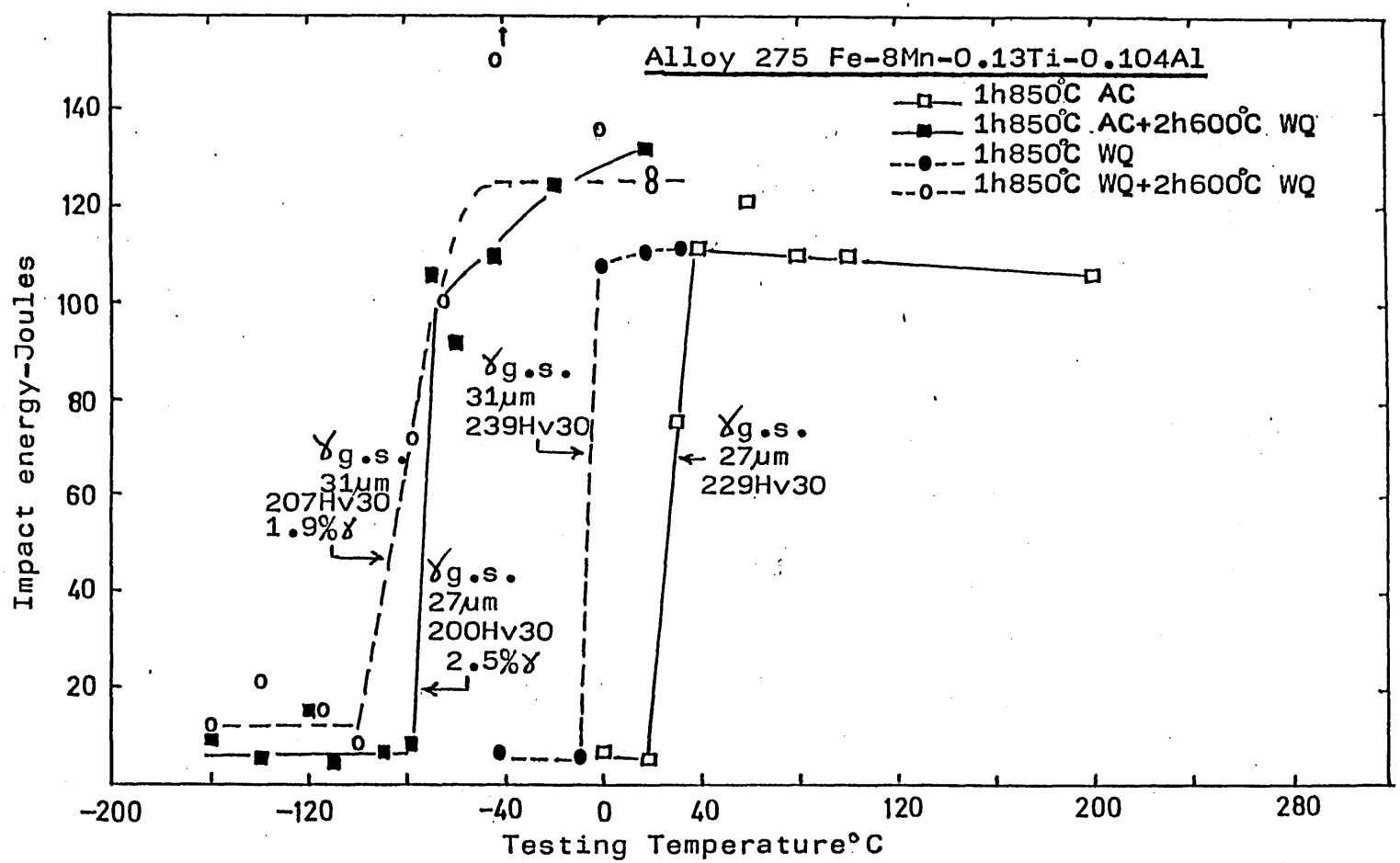

Figure 59 Illustrating the effect of cooling rate from 850°C and tempering at 600°C on DBTT of alloy 275.

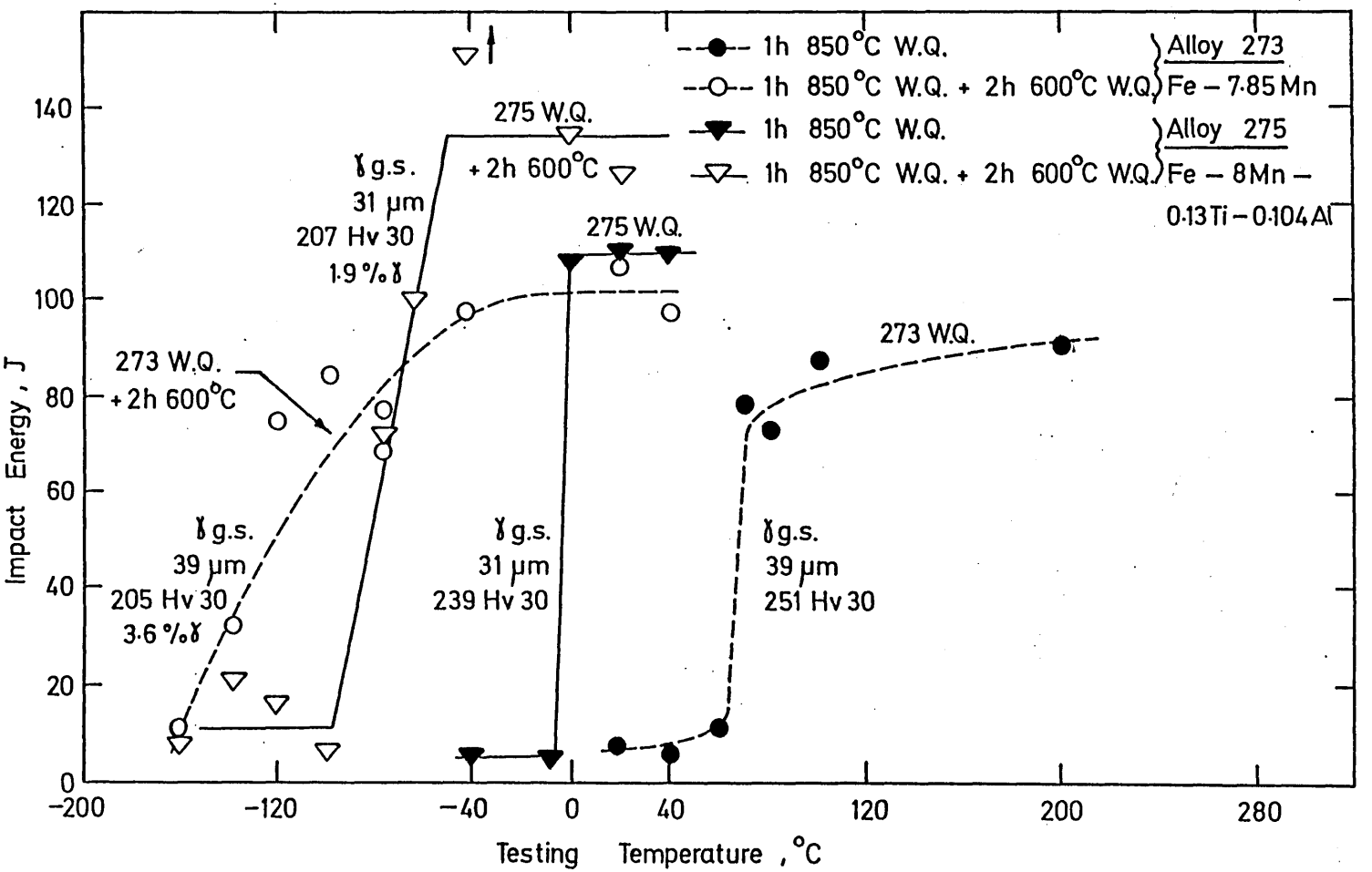

Figure60 Effect of grain refinement on DBTT after water quenching from 850° C and after tempering for 2h.@600° C.

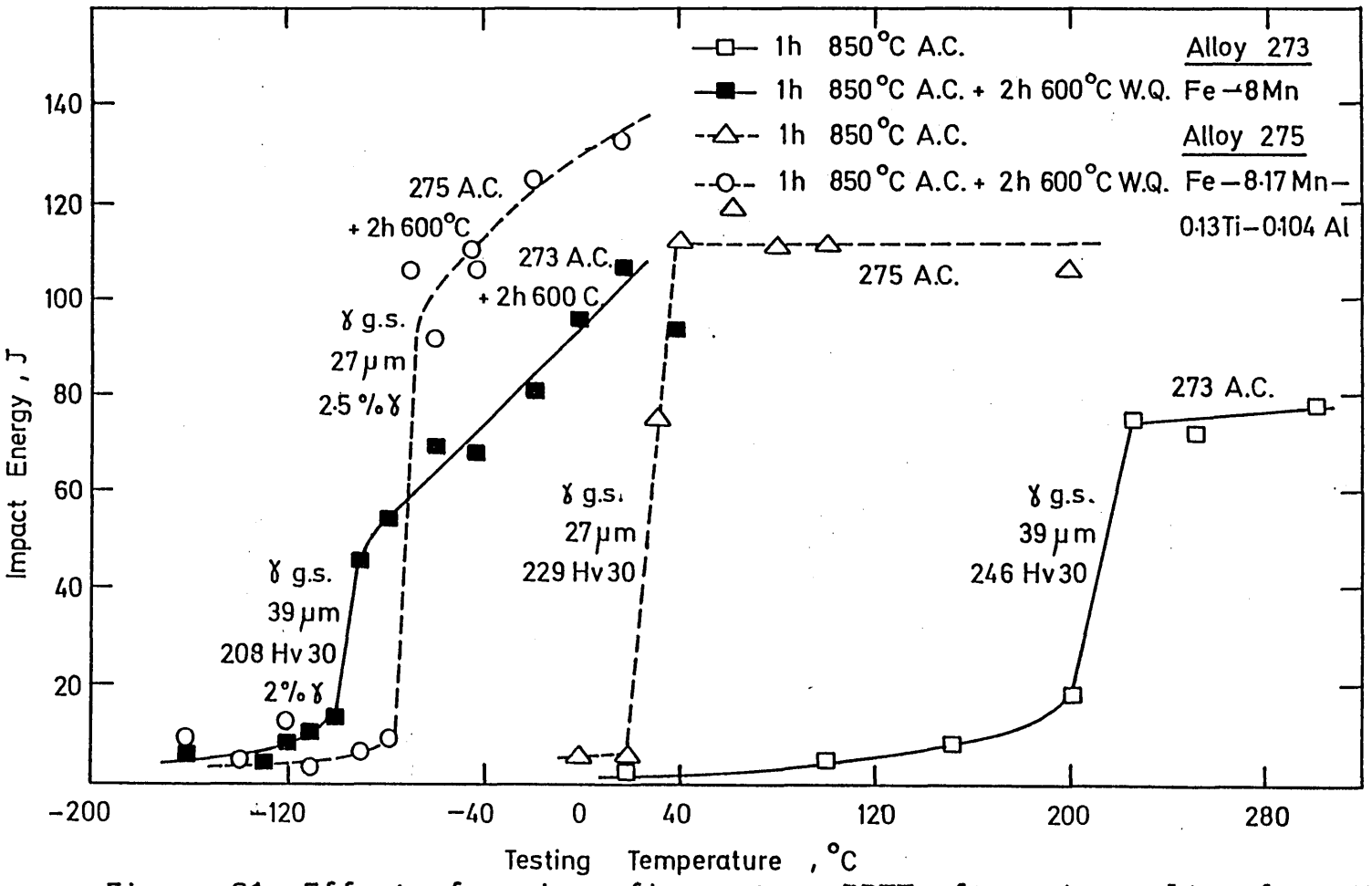

Figure 61 Effect of grain refinement on DBTT after air cooling from 850°C and after tempering for 2h.@600°C.

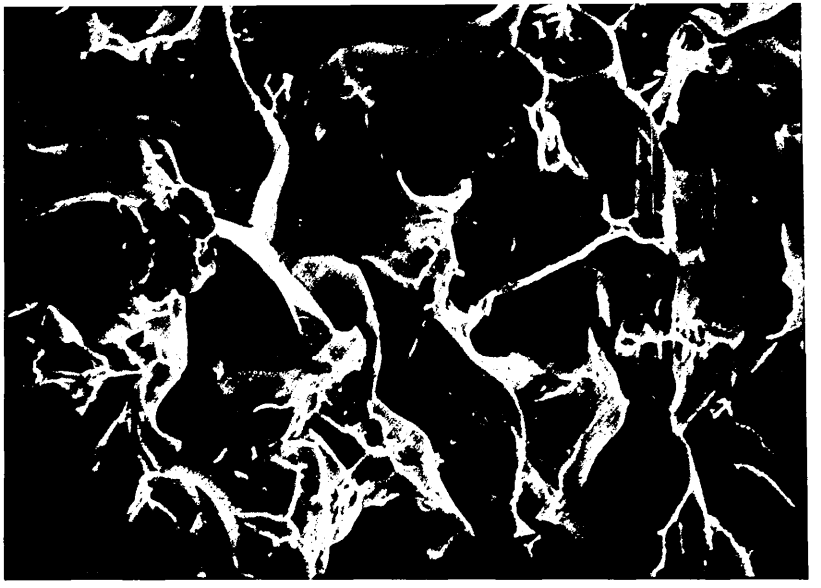

Figure 62 S.E.M. micrograph of alloy 273 after 1h.850°C A.C.,taken from a room temperature charpy, exhibiting intergranular fracture.

X800

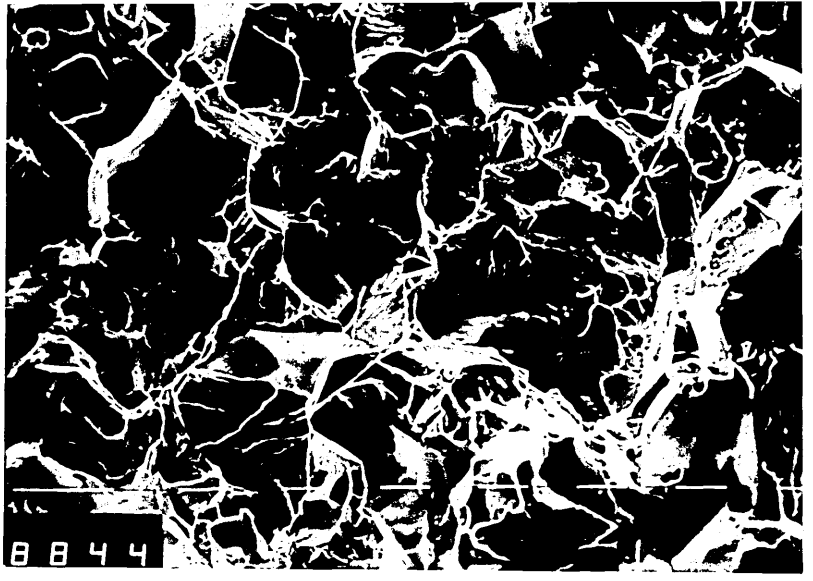

Figure 63 X600
S.E.M. micrograph of room temperature fracture surface of alloy 275,after 1h.850°C W.Q.,showing a cleavage fracture mode.

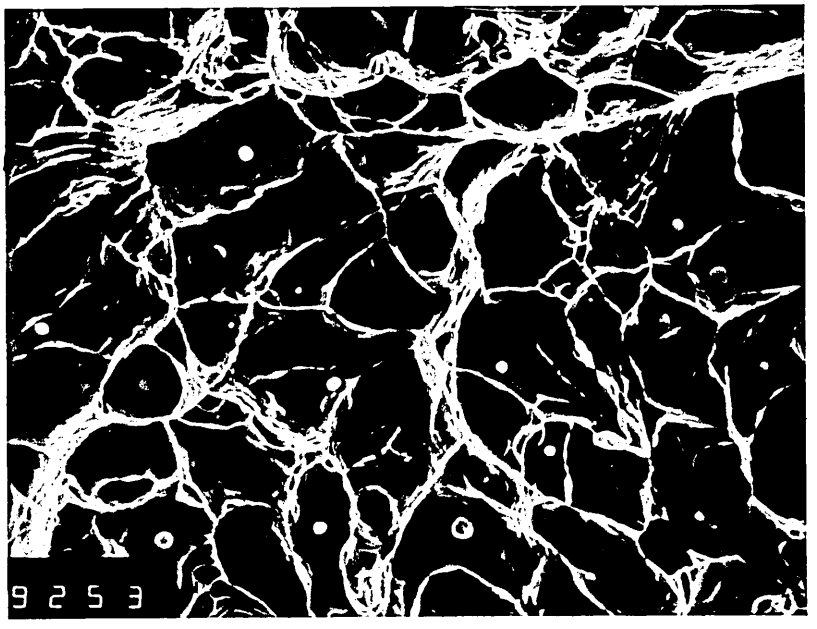

Figure 64 X720
S.E.M. micrograph as above but taken from a +100°C charpy sample showing ductile dimples.

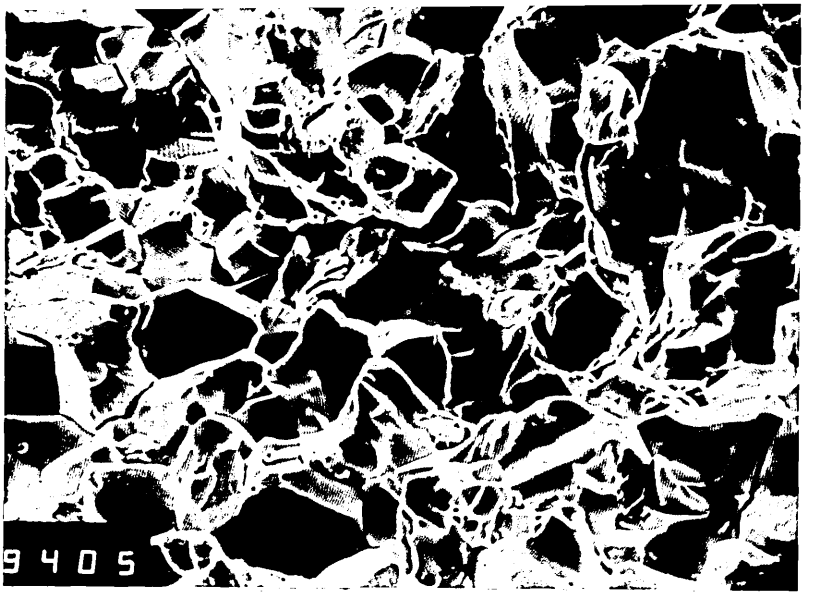

Figure 65 X720
S.E.M. micrograph of room temperature charpy fracture surface of alloy 275,after 1h.850°C A.C. showing an intergranular fracture mode.

Figure 66 X700
S.E.M. micrograph of -10°C charpy fracture surface of alloy 275,after 1h.850°C W.Q.,showing a cleavage fracture mode.

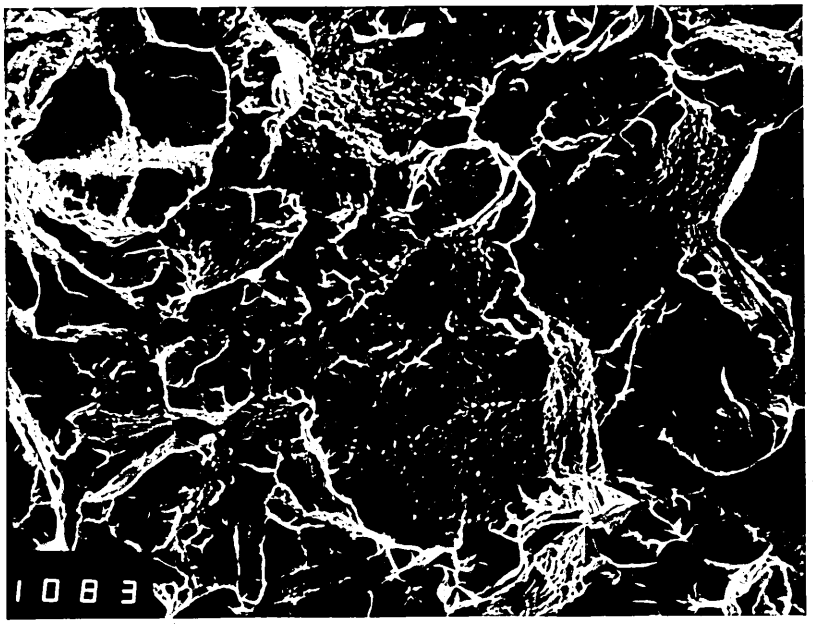

Figure 67 -100°C X720

Figure 68 -80°C X3200

Above two figures show S.E.M. micrographs of sub zero charpy fracture surfaces of alloy 273, after 1h.850°C A.C.+2h.600°C W.Q.,showing ductile tearing at low and high magnifications.

Figure 69 X500
Optical micrograph of alloy 273 in the 1h.850°C W.Q. condition.

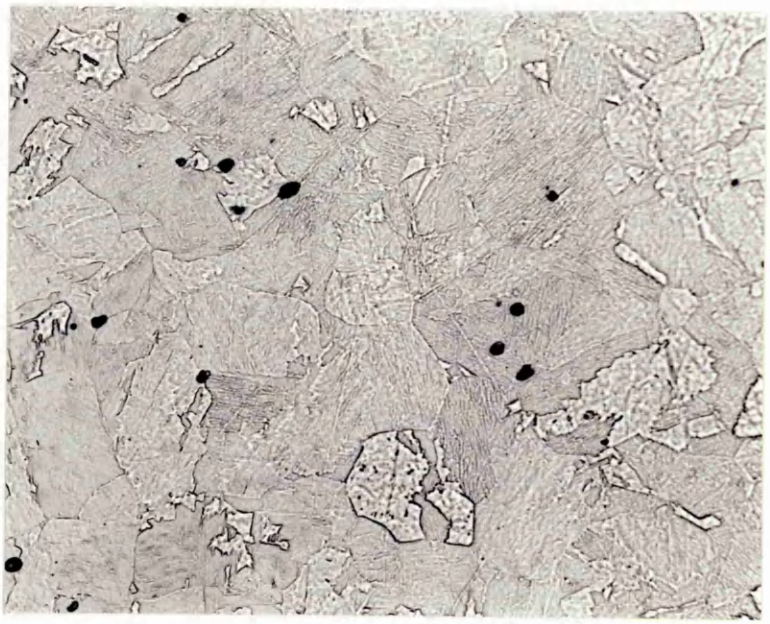

Figure 70 X500
Optical micrograph of alloy 273 in the 1h.850°C A.C. condition.

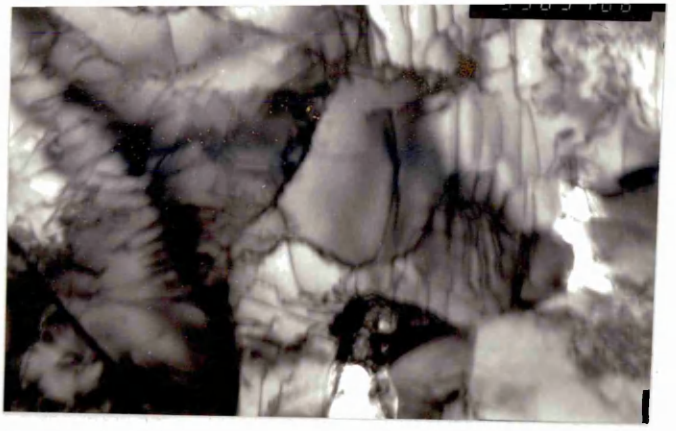

Figure 74 X33K

Figure 75 X20K

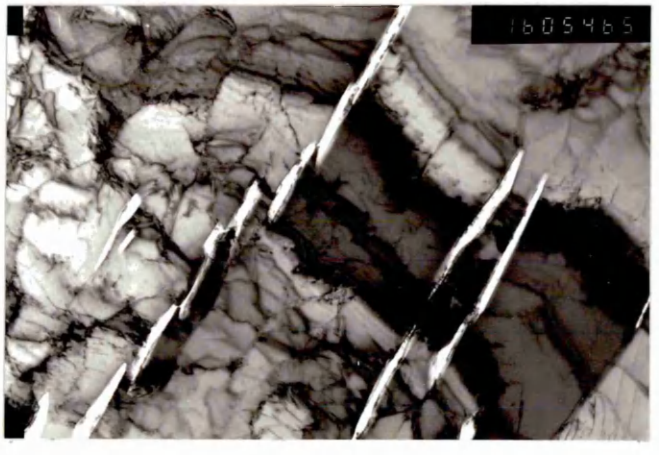

Figure 76 X16K

T.E.M. micrographs of alloy 273 in the 1h.850°C W.Q.+2h.600°C W.Q. condition showing the massive ferrite structure and reverted austenite.

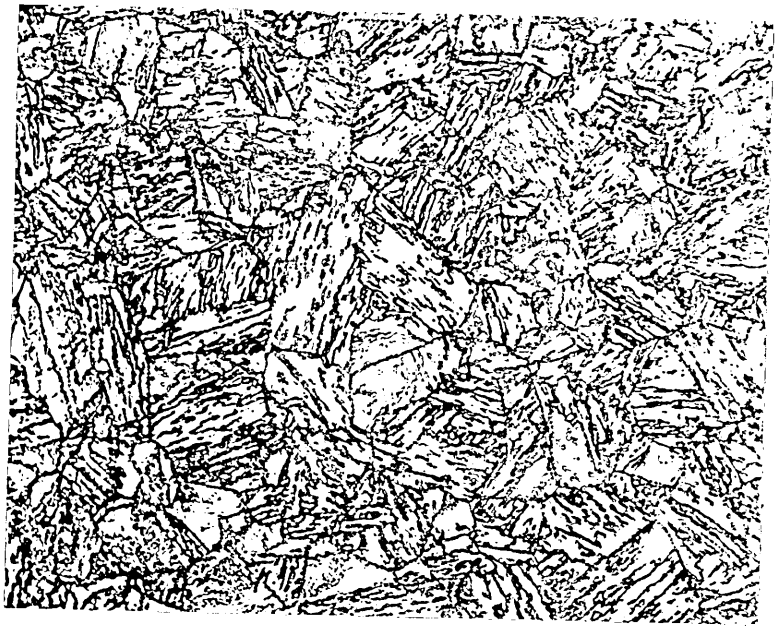

Figure 77 X500

Optical micrograph of alloy 273 in the 1h.850°C W.Q.+2h.600°C W.Q. condition showing the prior austenite grain boundaries.

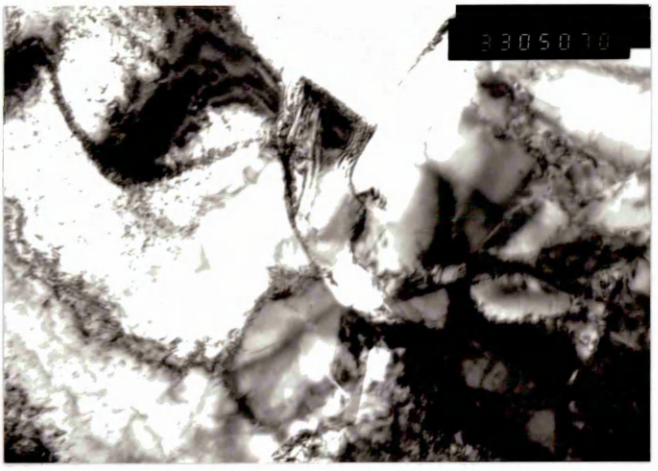

Figure 78(a) Bright field X33K

Figure 78(b) Dark field X33K

T.E.M. micrographs of alloy 273 in the 1h.850°C W.Q.+2h.600°C W.Q. condition, showing bright and dark field reverted austenite.

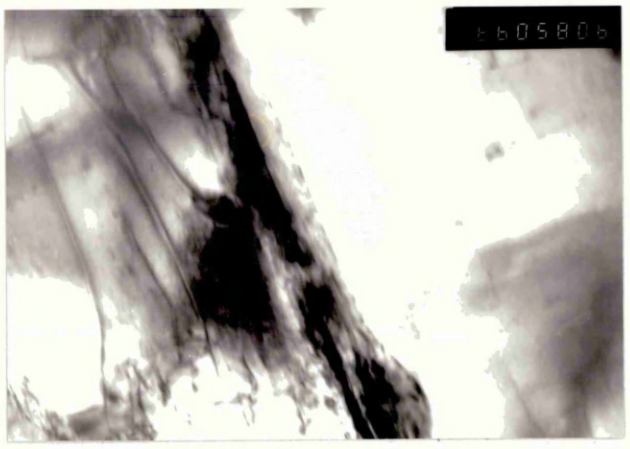

Figure 79(a) Bright field X66K

Figure 79(b) Dark field X66K

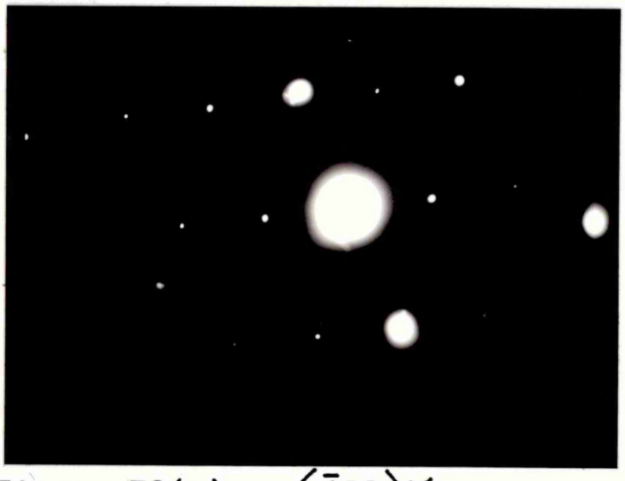

Figure 79(c) $\langle \bar{1}22 \rangle_\gamma$

T.E.M. micrographs of alloy 273 in the 1h.850°C A,C.+2h.600°C W.Q. condition, showing (a) bright field,(b) dark field, (c) diffraction pattern of reverted austenite.

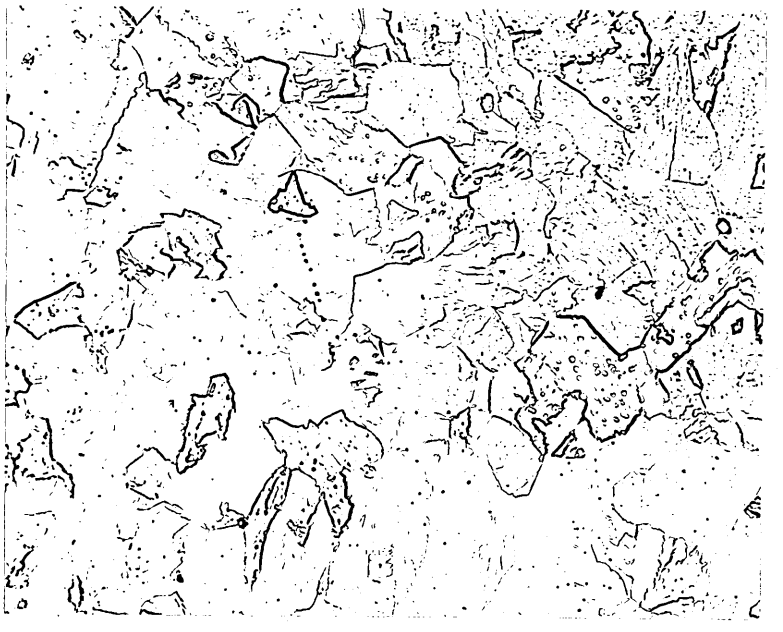

Figure 80 X500
Optical microstructure of alloy 275 in the 1h.850°C W.Q. condition showing the as quenched structure.

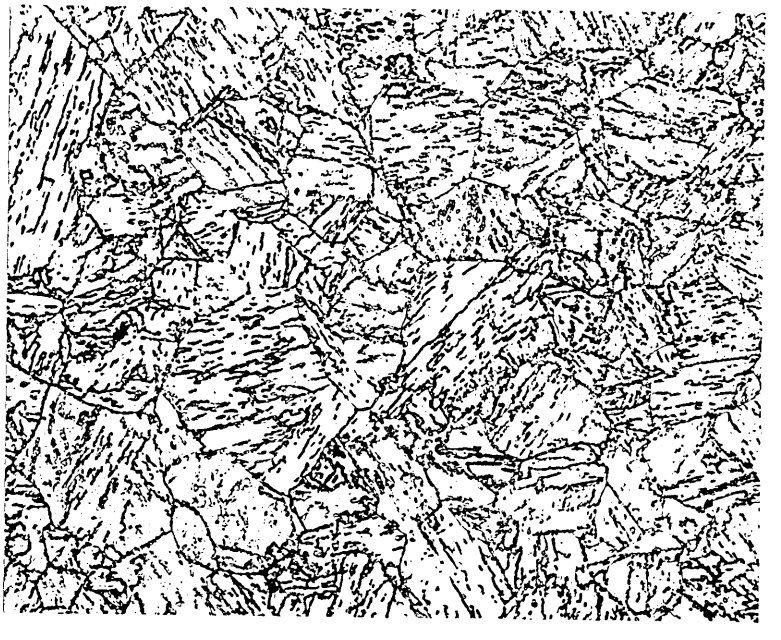

Figure 81 X500
Optical microstructure of alloy 275 in the 1h.850°C W.Q. +2h.600°C W.Q. condition showing the ferritic structure and prior austenite grain boundaries.

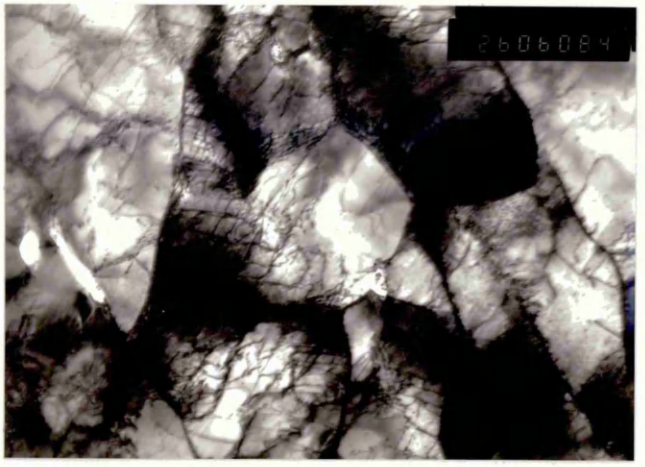

Figure 82 1h.850°C A.C.+2h600°C W.Q. X26K

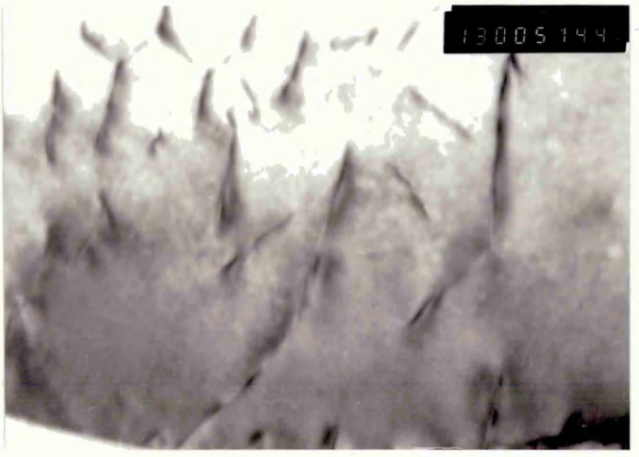

Figure 83 1h850°C W.Q.+2h600°C W.Q. X130K

Figure 84 1h850°C W,Q,+2h600°C W.Q. X100K

T.E.M. microstructures of alloy 275 showing the dislocation sub-structures.

Figure 85 X13K

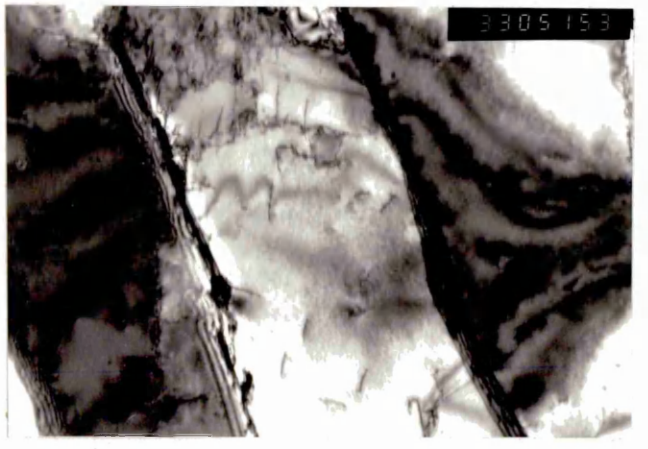

Figure 86(a) Bright field X33K

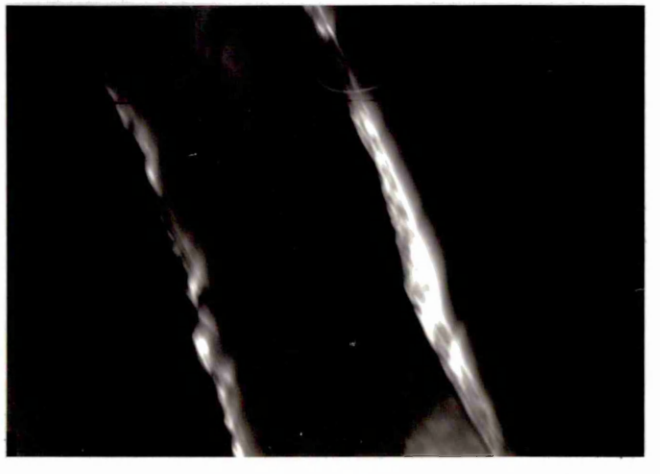

Figure 86(b) Dark field Rev.$\bar{8}$ X33K

T.E.M. microstructuresof alloy 275 in the 1h850°C W.Q.+2h600°C W.Q. condition showing (85)reverted austenite in the structure and (a) bright field and (b)dark field of reverted austenite.

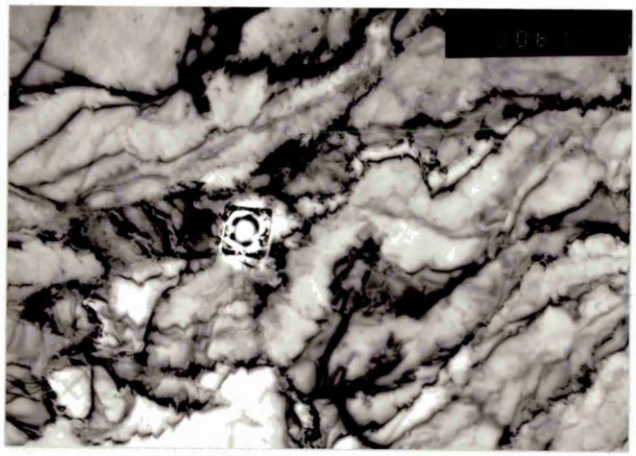

Figure 87(a) Bright field X50K

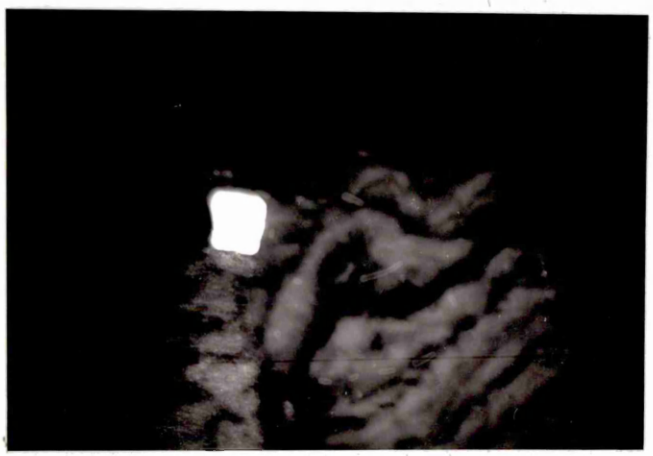

Figure 87(b) Dark field TiC/N X50K

T.E.M. microstructures showing bright and dark field of a TiC/N particle in alloy 275 in the 1h850°C W.Q. condition.

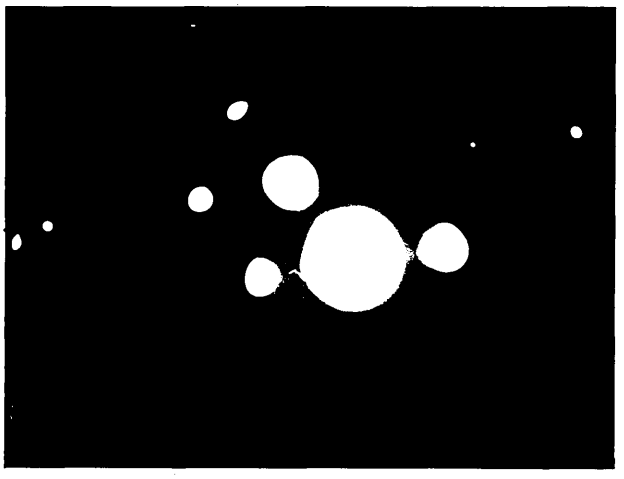

Figure 87(c) Diff.Patt. Ferrite $\langle \bar{1}11 \rangle$

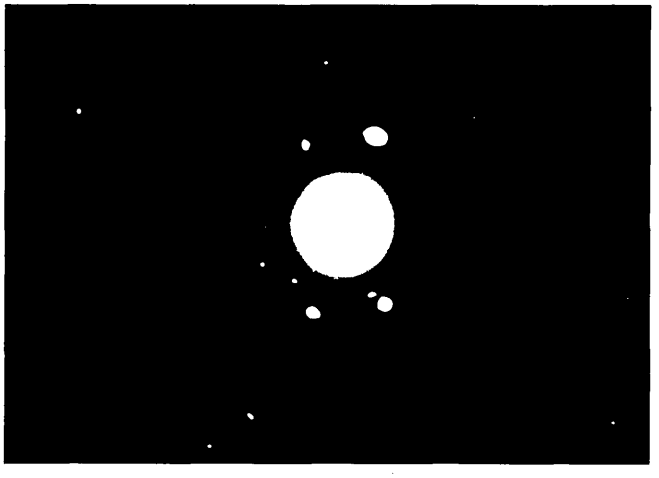

Figure 87(d) Diff.Patt. TiC/N $\langle 011 \rangle$

T.E.M. Diffraction patterns for alloy 275 in the 1h850°C W.Q. condition, showing the patterns for the ferritic matrix and the TiC/N particle.

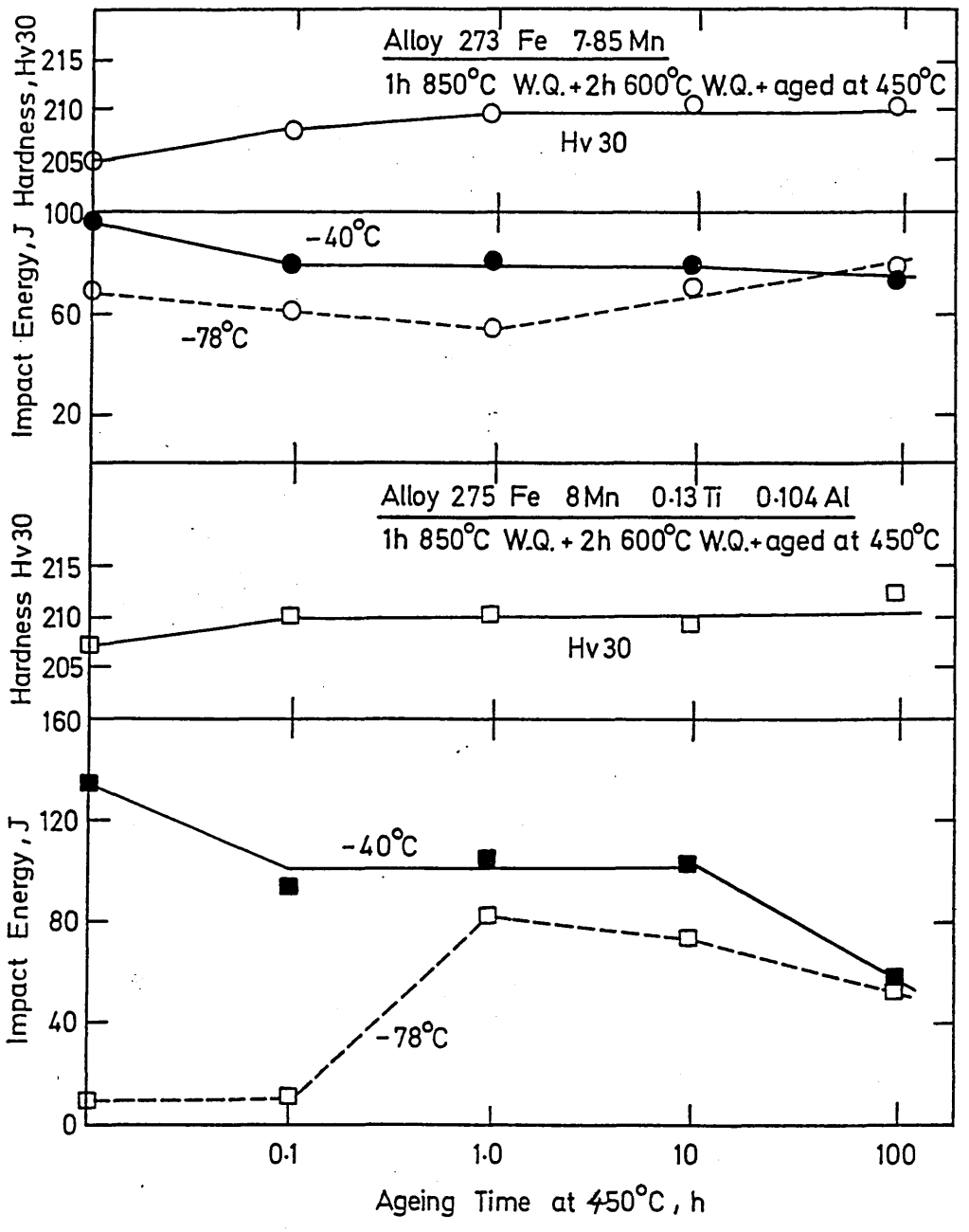

Figure 88 Effect of ageing at 450°C on impact toughness in the optimum heat treated condition.

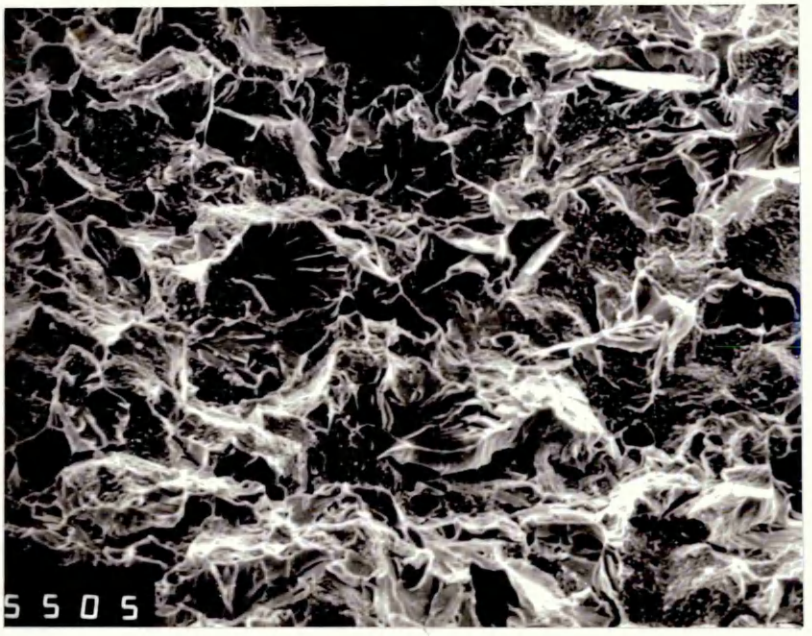

X400

Figure 89 S.E.M. micrograph of fracture surface of alloy 273 after optimum heat treatment and aged at 450°C for 6 minutes; tested at-40°C.

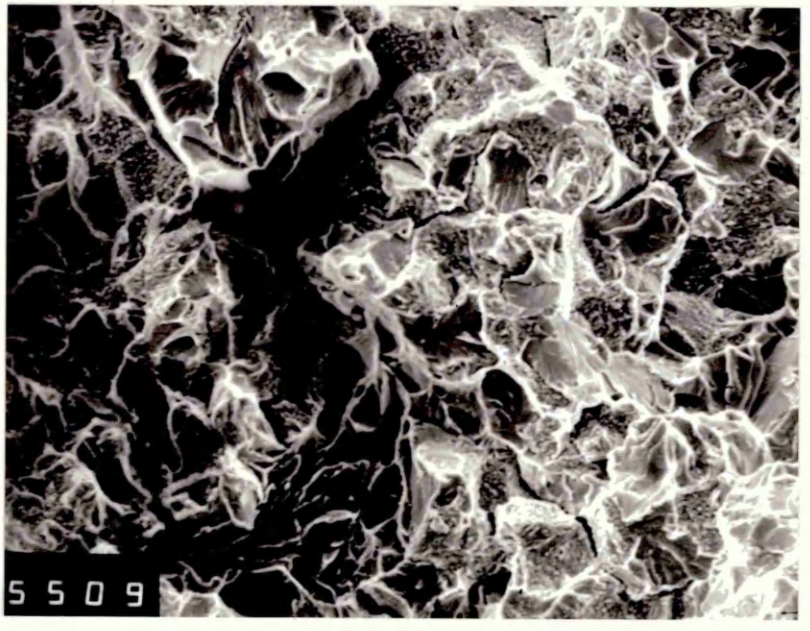

X400

Figure 90 S.E.M. as above but aged for 100h at 450°C.

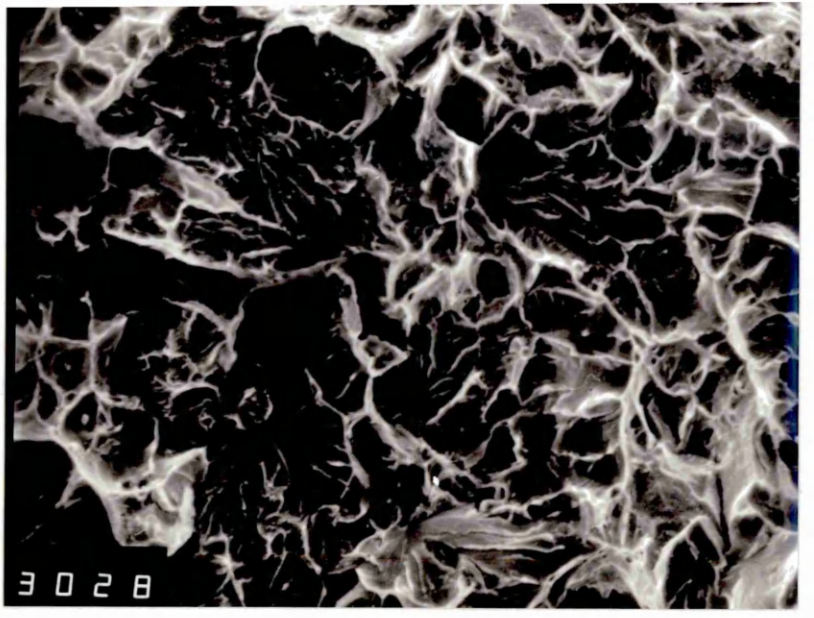

X400

Figure 91 S.E.M. micrograph of the fracture surface of alloy 275 after optimum heat treatment and aged at 450°C for 100h; tested at -78°C Quasi-cleavage fracture mode.

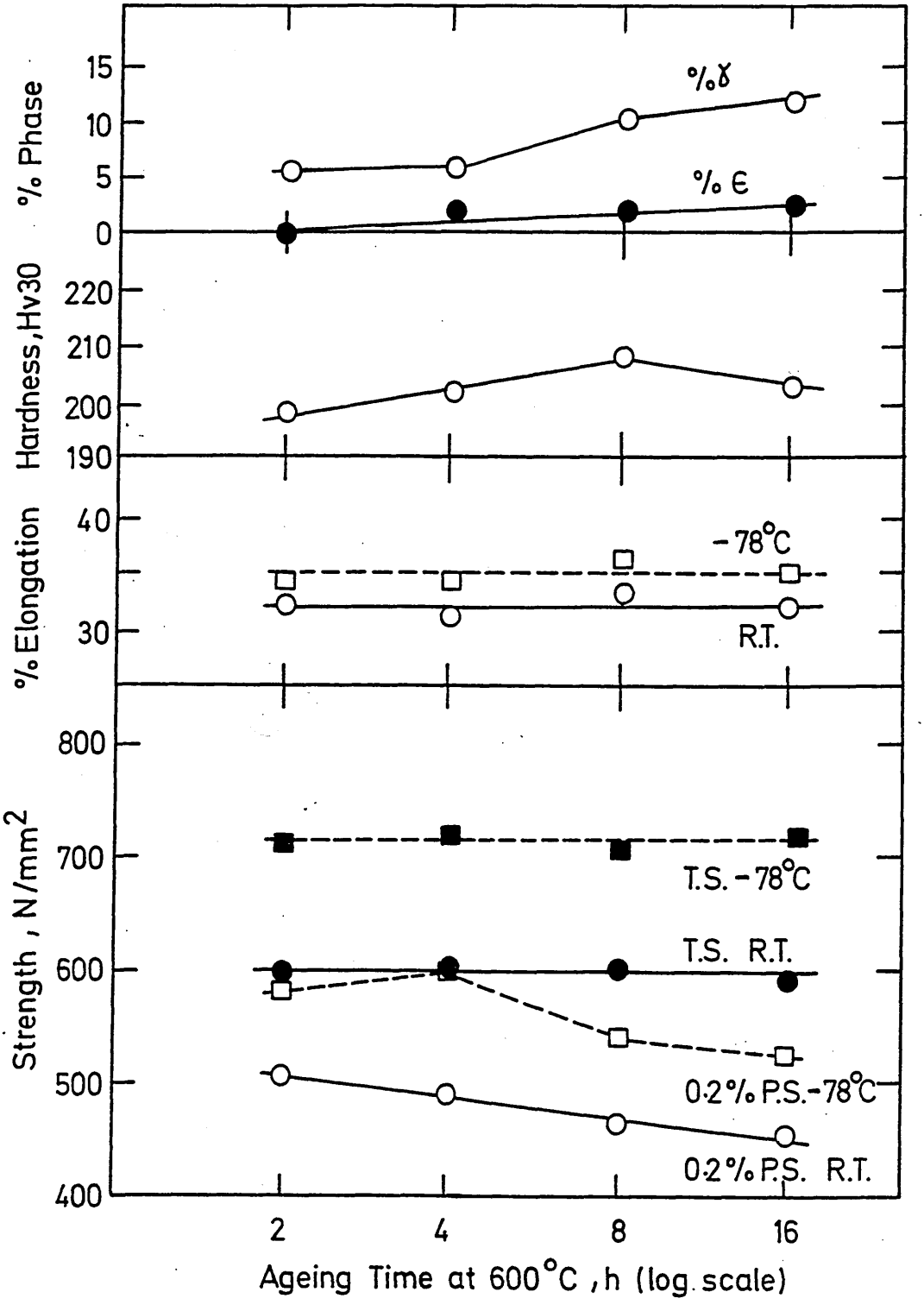

Figure92 Variation of mechanical properties determined at room temperature(R.T.) and-78°C,and phase content with ageing time at 600°C
Prior heat treatment:1h. 850°C WQ.
Alloy : 273

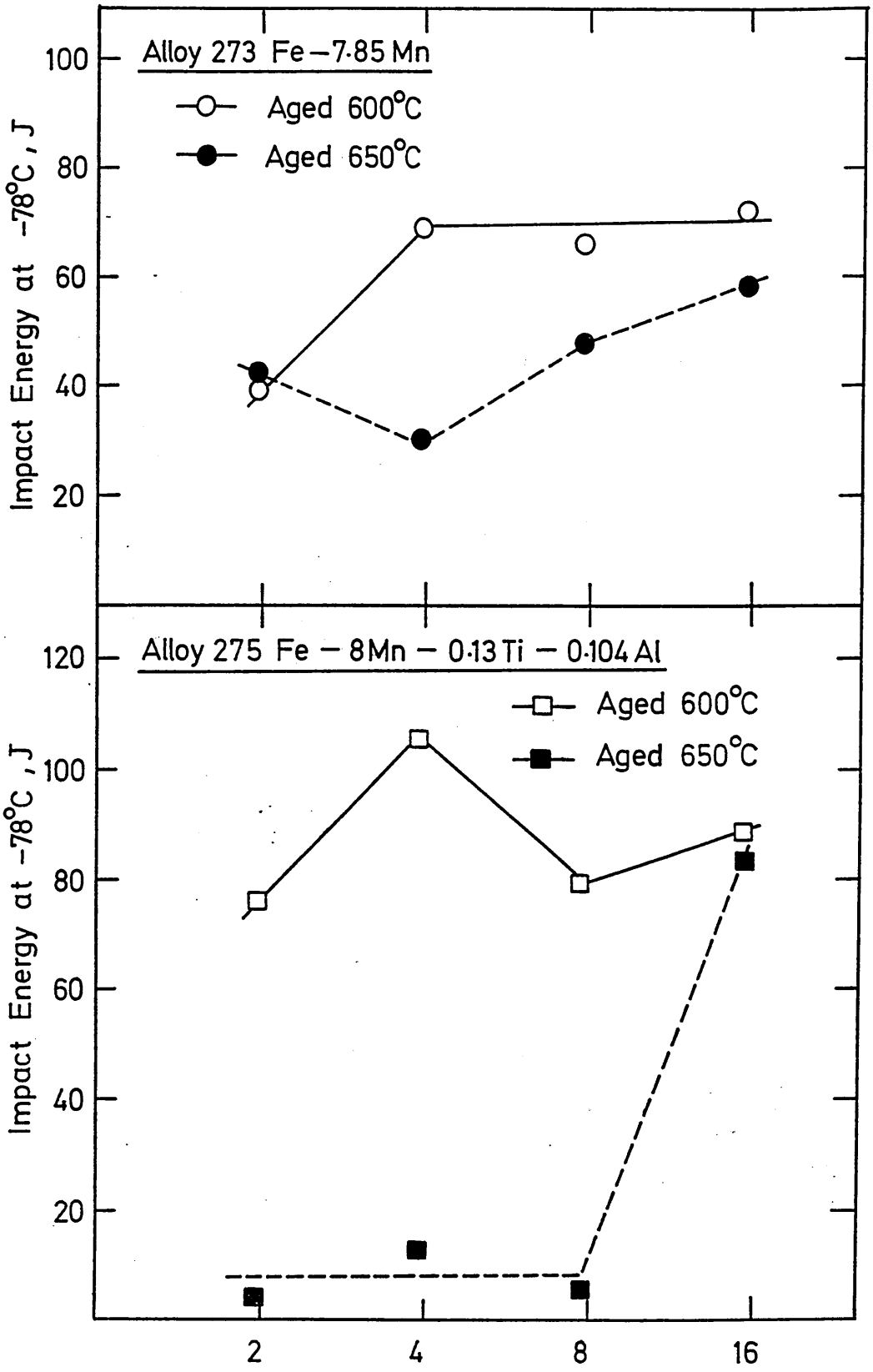

Figure 93 Impact tests at -78°C on alloy 273 and 275 aged at 600°C, (Prior heat treatment: 1h.850°C WQ.) and 650°C.

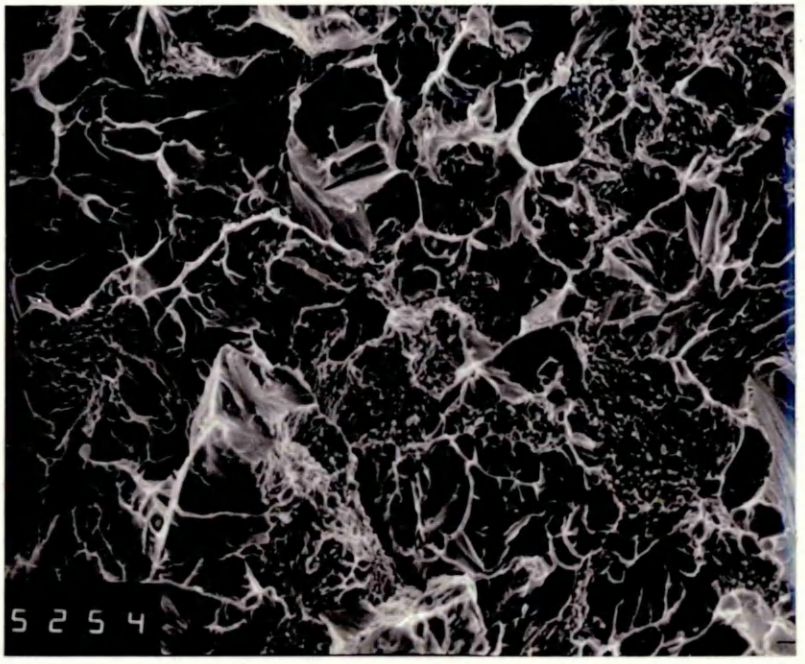

X400

Figure 94 S.E.M. micrograph of the fracture surface of alloy 273 after 1h850°C WQ+16h.600°C WQ tested at -78°C. Cleavage and ductile fracture.

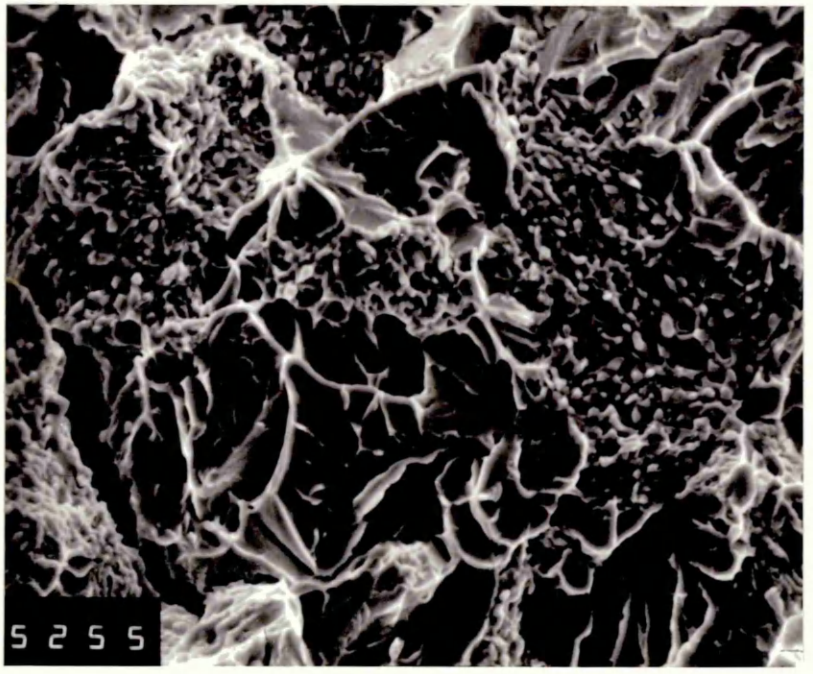

X800

Figure 95 S.E.M. micrograph as above but higher mag.

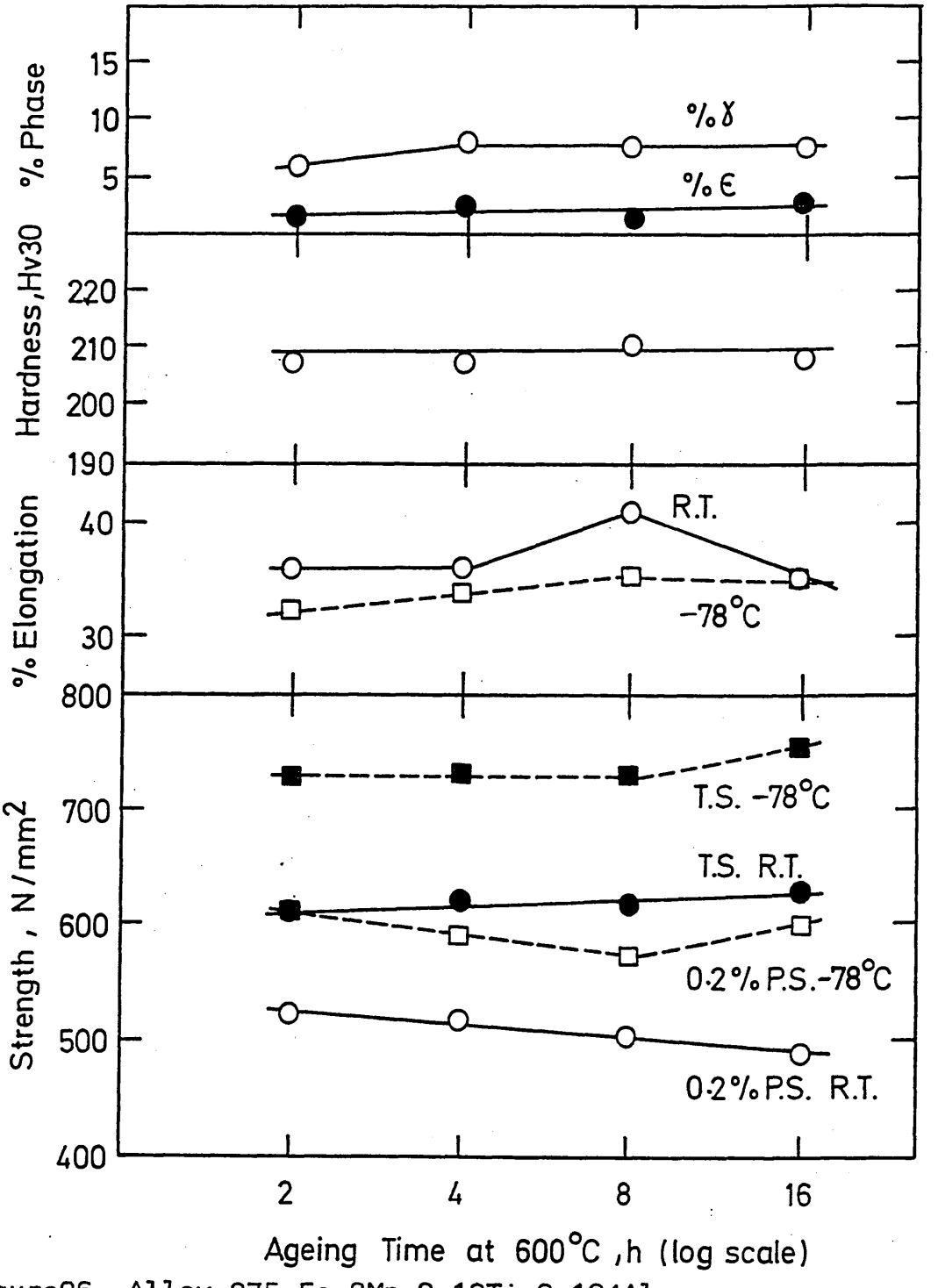

Figure96 Alloy 275 Fe-8Mn-0.13Ti-0.104Al
Variation of mechanical properties determined at room temperature (R.T.) and-78°C, and phase content with ageing time at 600°C.
Prior heat treatment:1h.@850°C WQ.

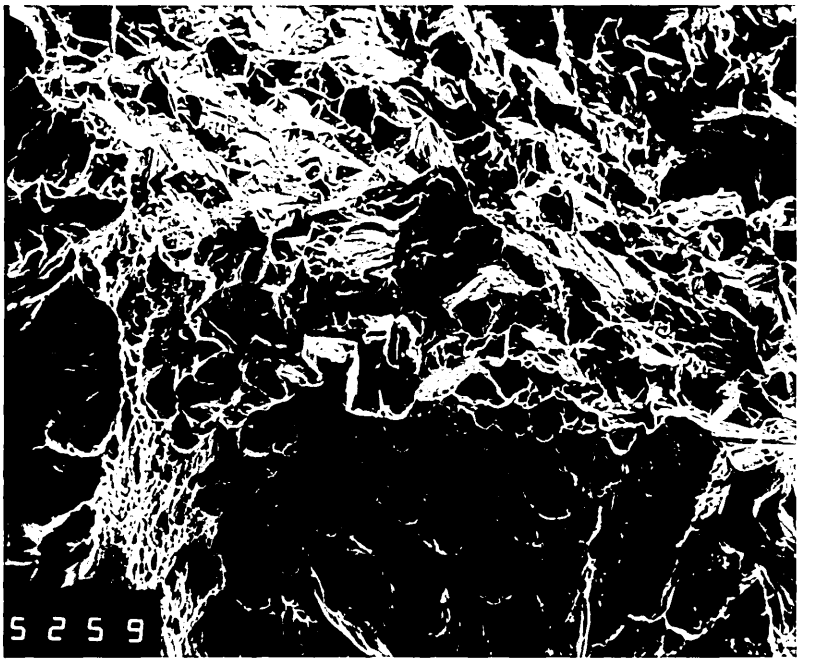

X200

Figure 97 S.E.M. micrograph of fracture surface of alloy 275 after 1h850°C WQ+8h600°C WQ; tested at -78°C,showing ductile and cleavage areas.

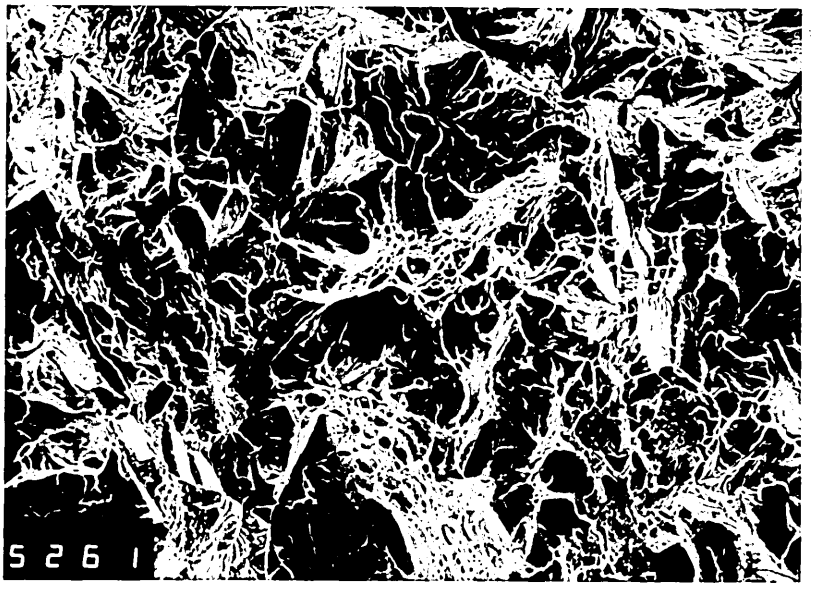

X200

Figure 98 S.E.M. micrograph as above but after 16h at 600°C.

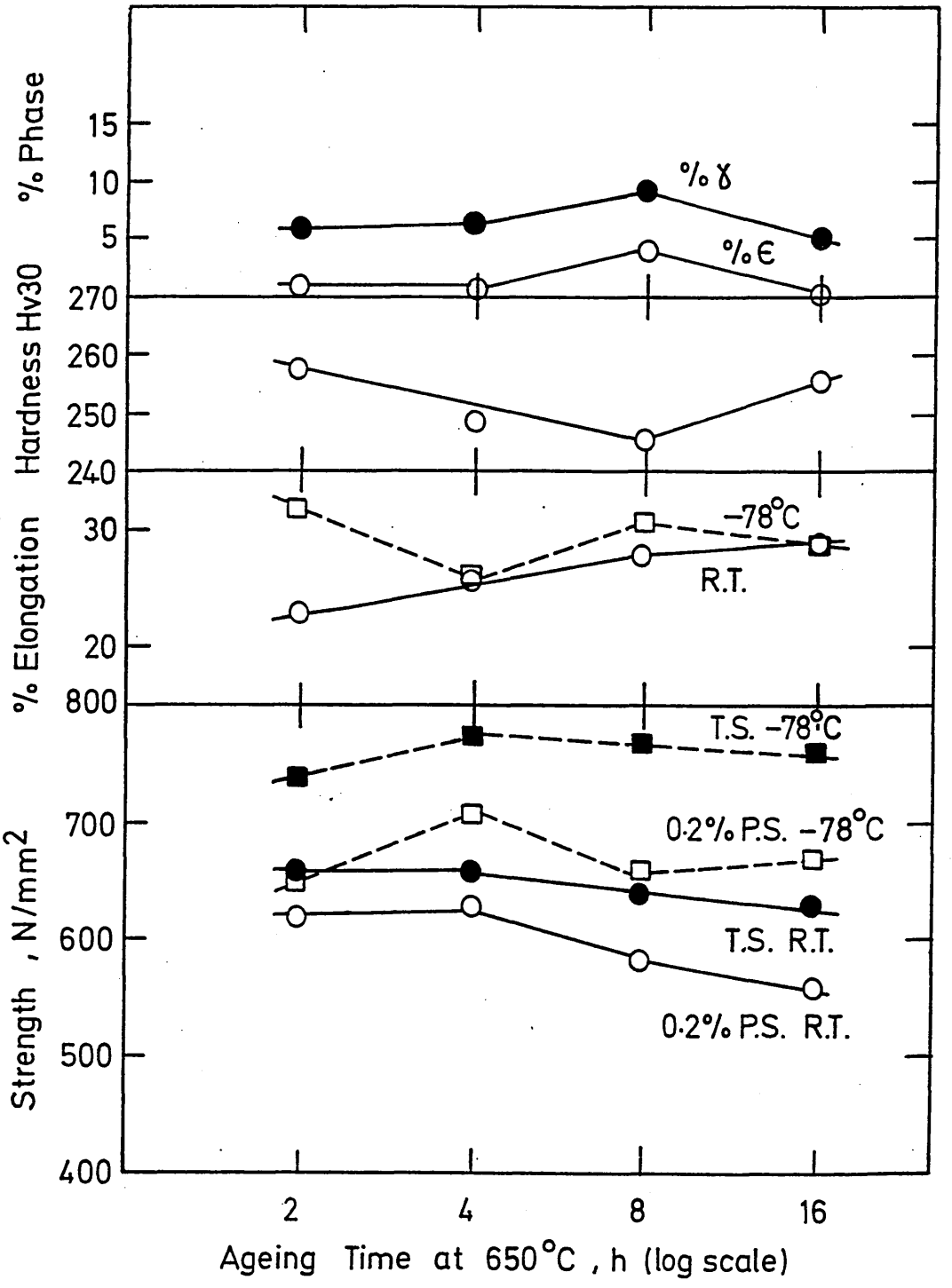

Figure 99 Alloy 273, Fe-7.85Mn
Variation of mechanical properties determined at room temperature (R.T.) and -78°C and phase content with ageing time at 650°C.
Prior heat treatment: 1h@850°C WQ.

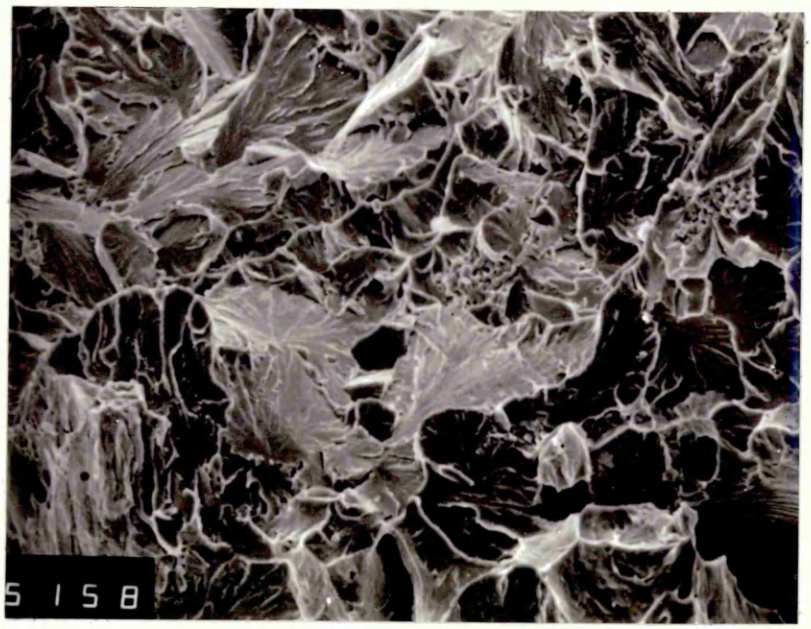

X400

Figure 100 S.E.M. micrograph of the fracture surface of alloy 273 after 1h850°C WQ+2h650°C WQ; tested at -78°C, showing predominantly cleavage fracture.

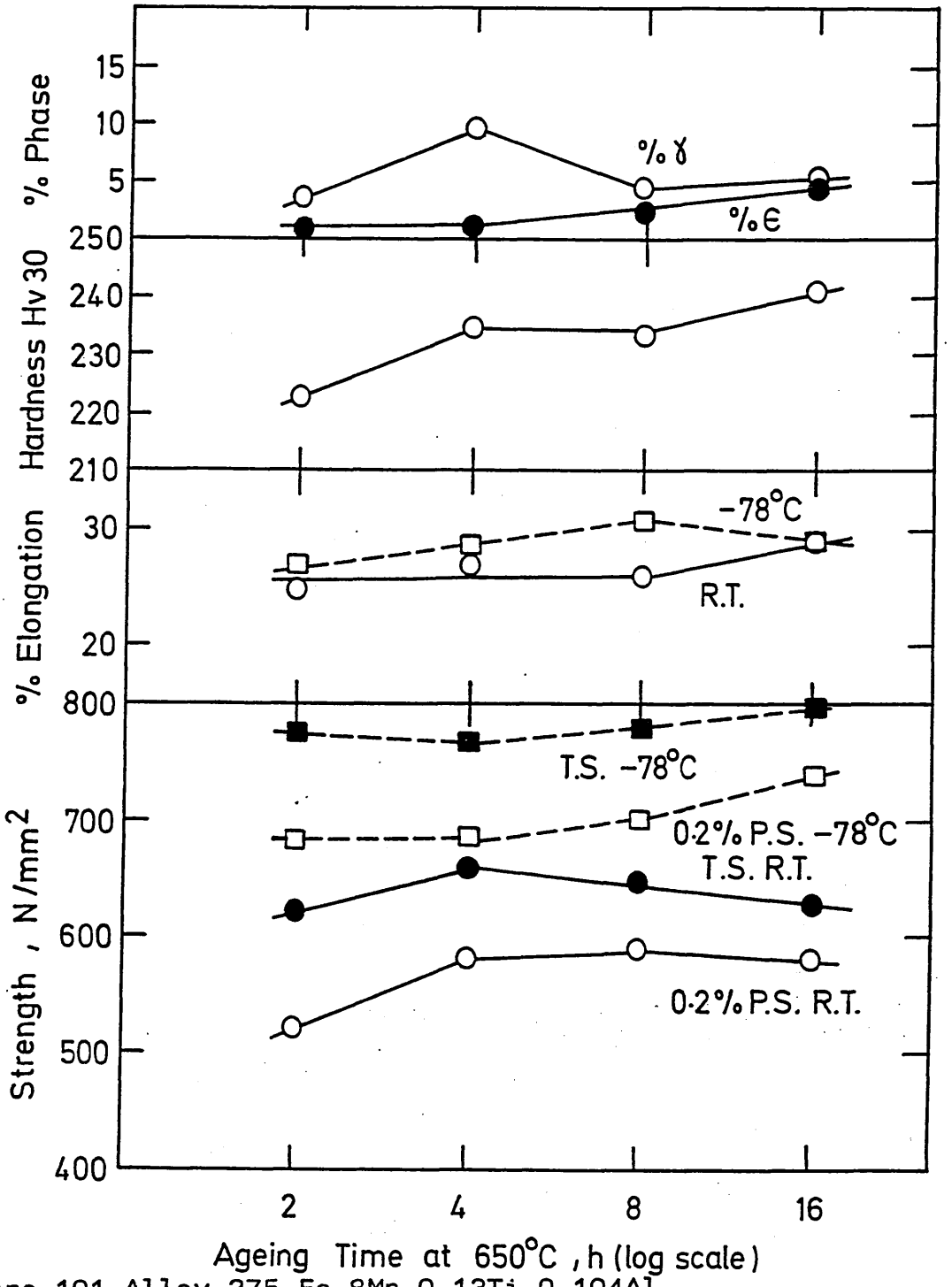

Figure 101 Alloy 275, Fe-8Mn-0.13Ti-0.104Al

Variation of mechanical properties determined at room temperature(R.T.) and-78°C and phase content with ageing time at 650°C.
Prior heat treatment:1h@850°C WQ.

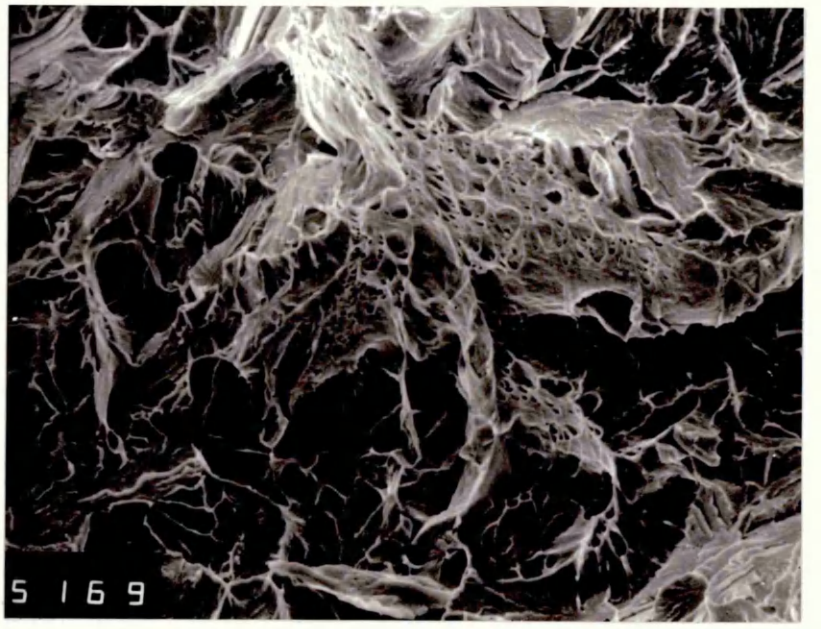

X400

Figure 102 S.E.M. micrograph of the fracture surface of alloy 275 after 1h850°C WQ+8h650°C WQ and tested at -78°C, showing cleavage and ductile fracture.

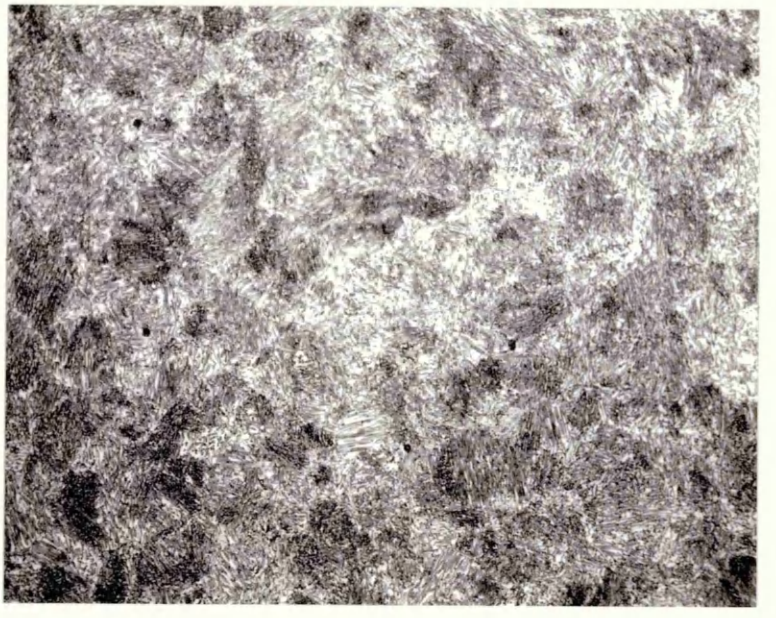

X500

Figure 103 Optical micrograph of alloy 273 in the thermally cycled condition.

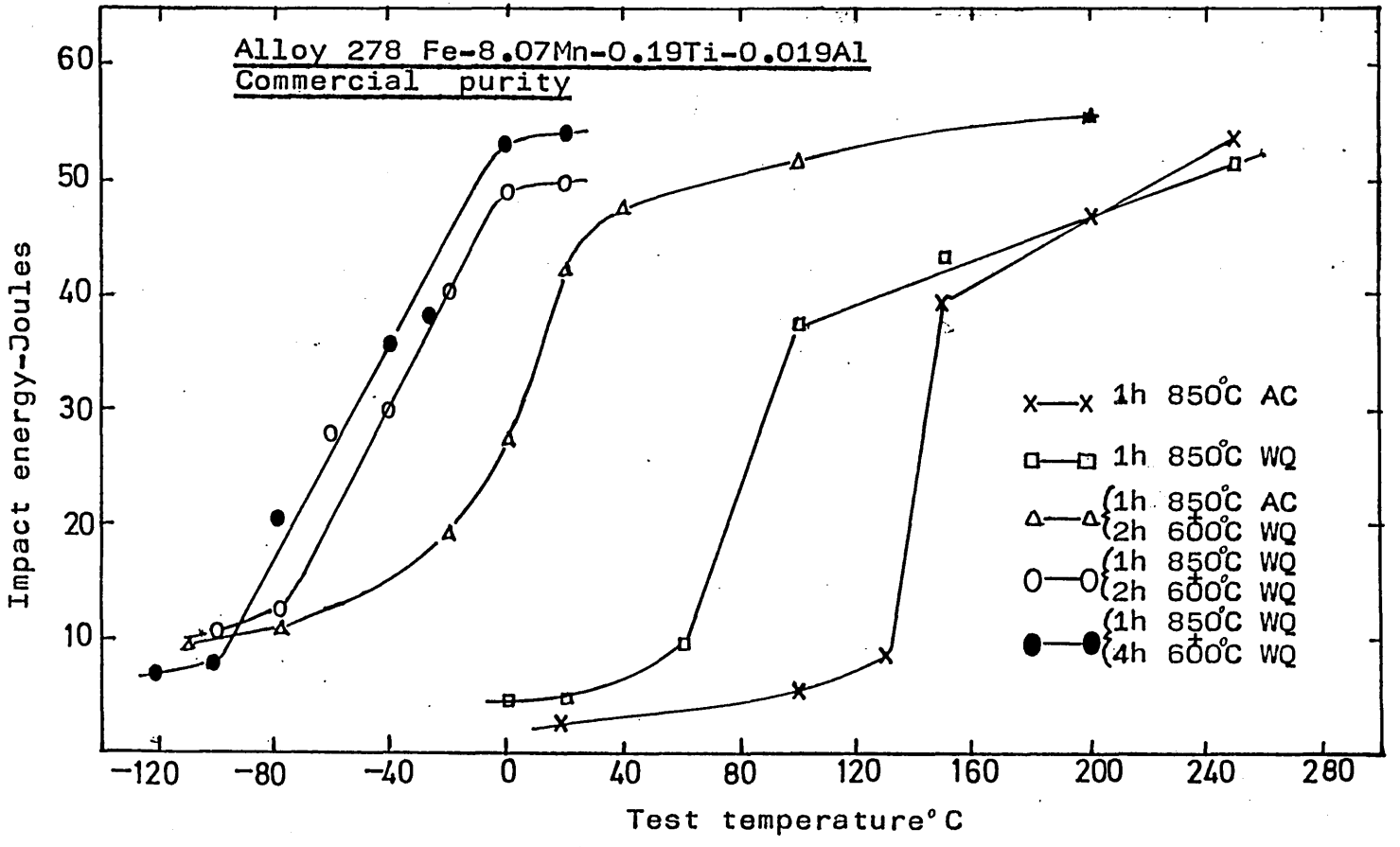

Figure 104 Charpy impact transition curves for alloy 278.

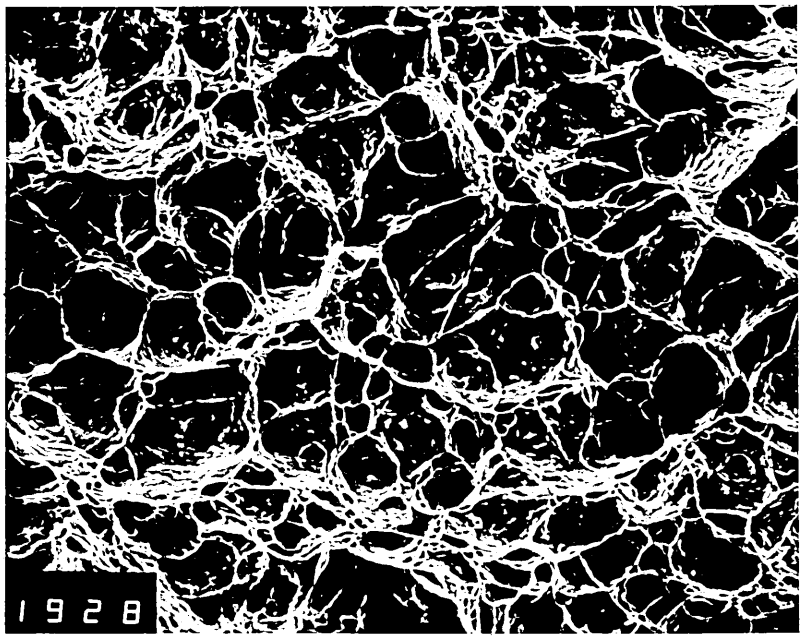

X400

Figure 105 S.E.M. micrograph of the fracture surface of alloy 278 in the 1h850°C AC+2h600°C WQ condition;tested at +200°C,showing a ductile dimple fracture mode.

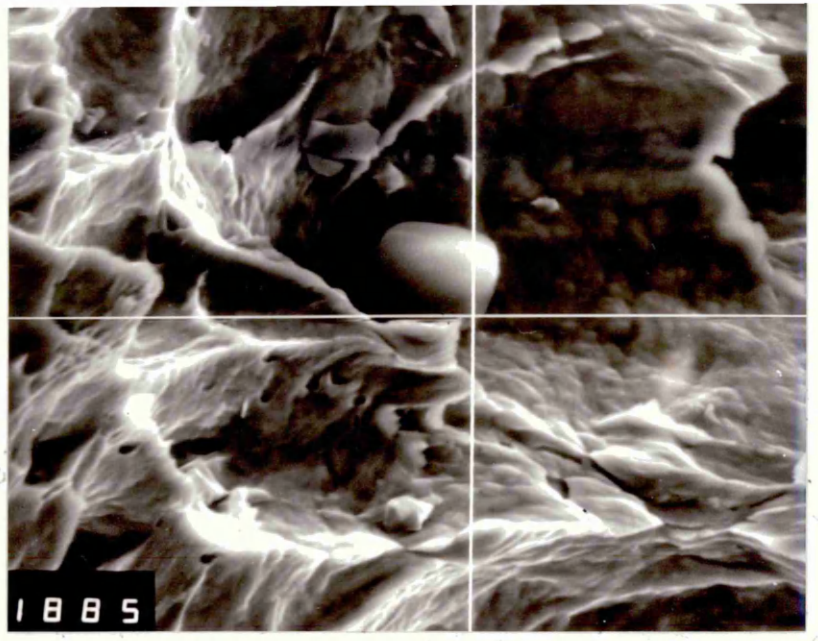

X1600

Figure 106 S.E.M. micrograph of an Al_2O_3 particle in alloy 278 after a WQ+T. Tested at +200°C

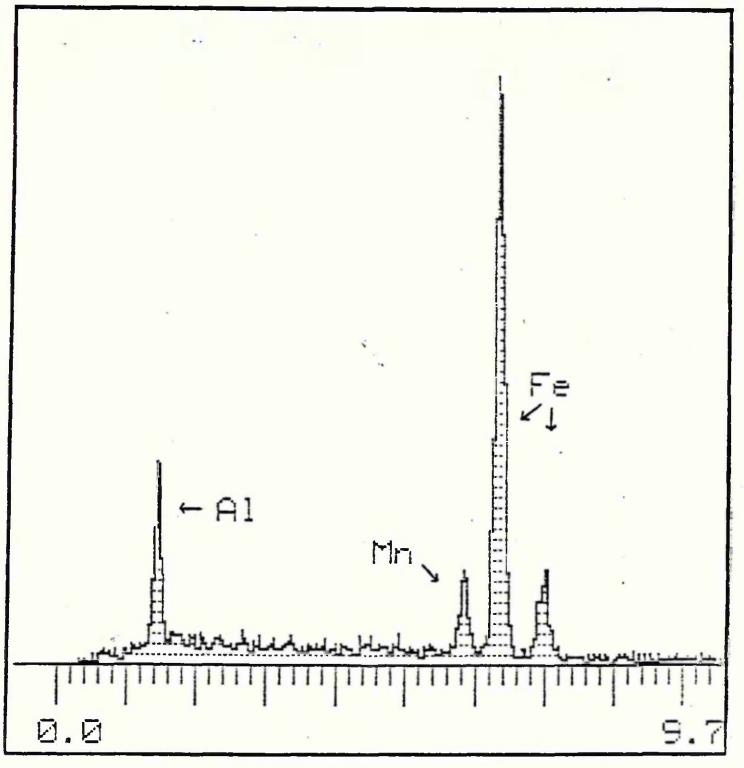

Figure 107 EDAX analysis of above particle confirming an aluminium-rich precipitate.

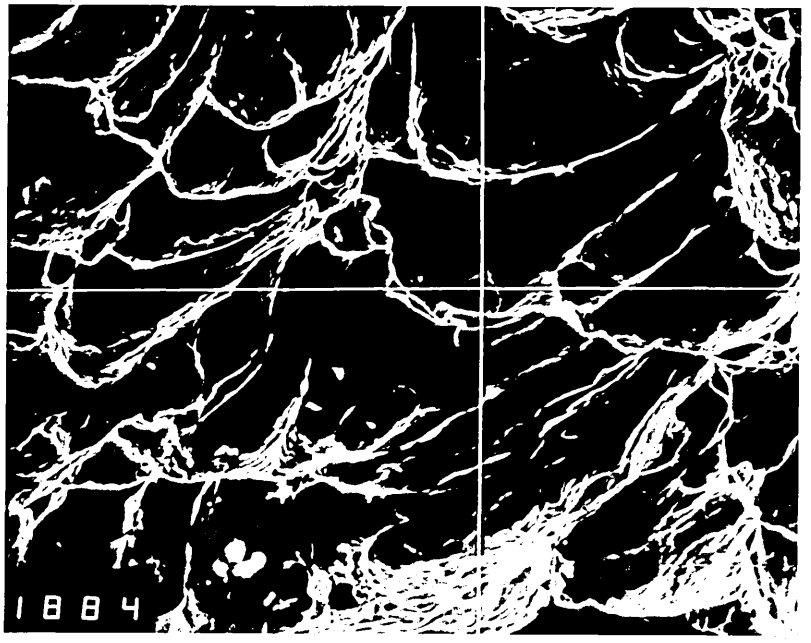

Figure 108 S.E.M. micrograph of a TiC/N particle in alloy 278 after a WQ+T. Impact tested at+200°C.

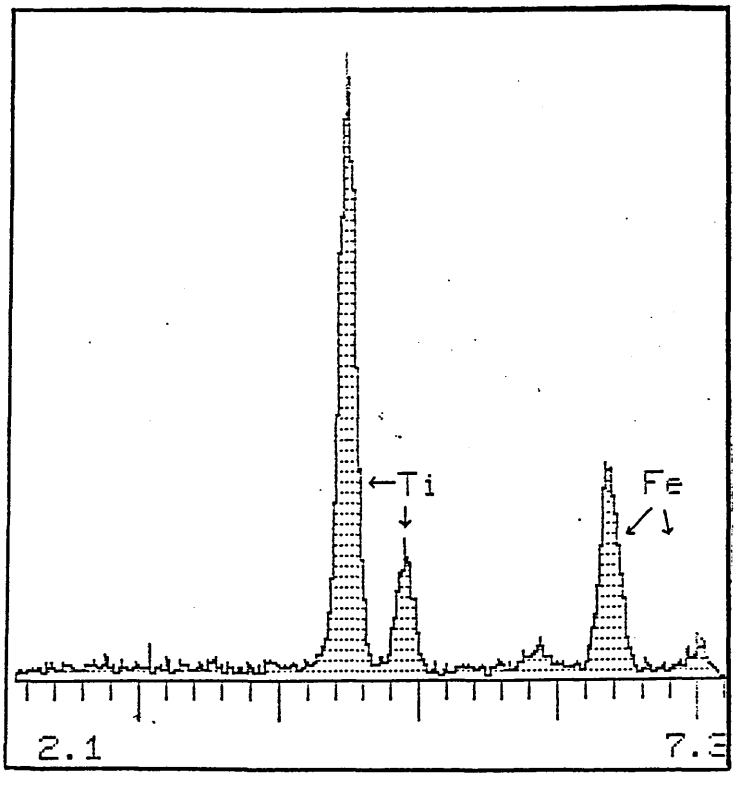

Figure 109 EDAX analysis of above particle confirming a titanium-rich precipitate.

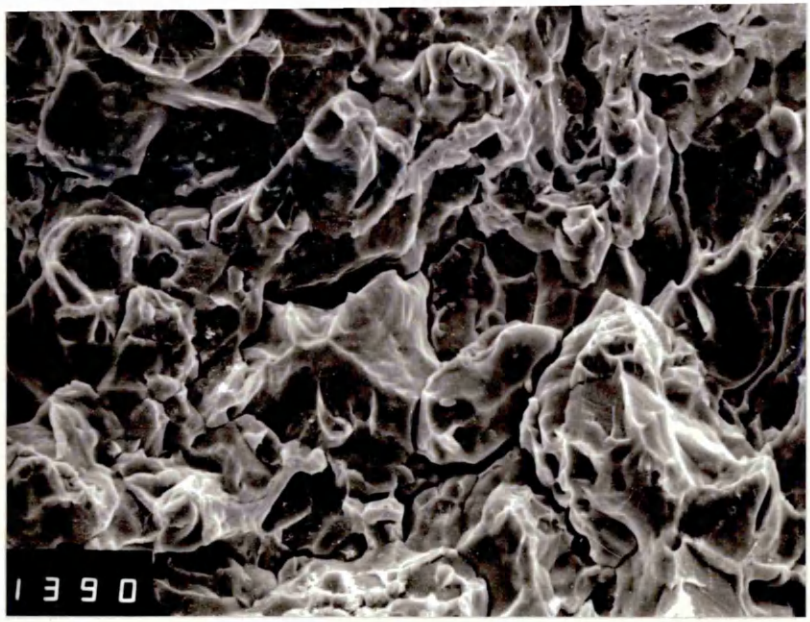

X880

Figure 110 S.E.M. micrograph of alloy 278 in the 1h850°C AC condition showing a quasi--cleavage fracture mode;tested at R.T.

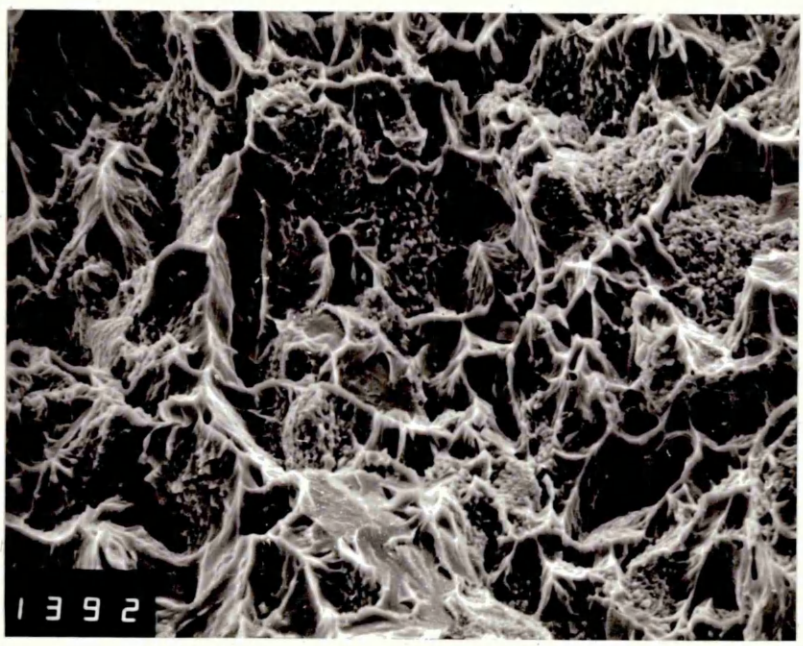

X880

Figure 111 S.E.M. micrograph of alloy 278 in the 1h850°C WQ+ 2h600°C WQ condition showing a cleavage/ductile-tearing fracture mode. Impact tested at -100°C.

X500

Figure 112 Optical micrograph of alloy 278 in the 1h850°C AC condition.

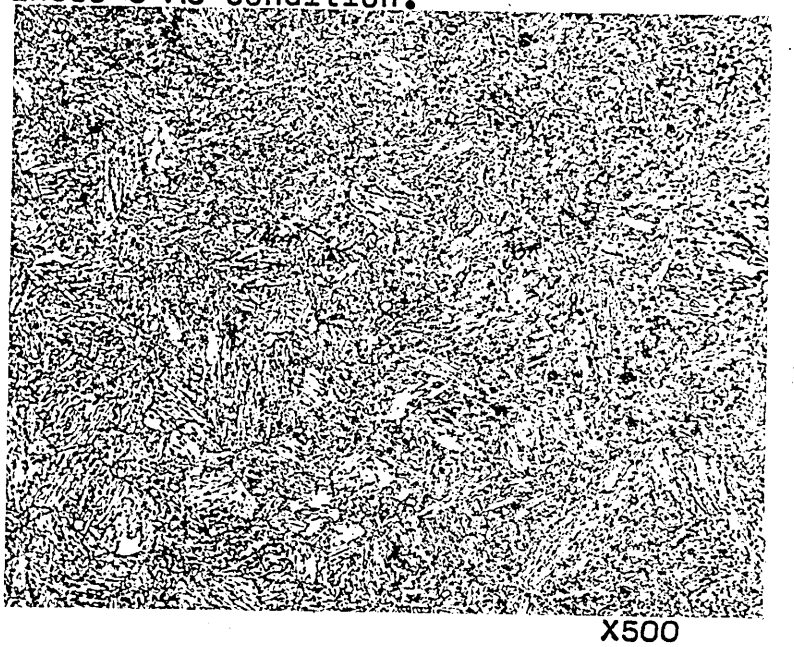

X500

Figure 113 Optical micrograph of alloy 278 in the 1h850°C WQ+2h600°CWQ condition.

X50K

Figure 114 T.E.M. micrograph showing the lath martensite structure in alloy 278 after a 1h850°C WQ+2h600°C WQ

X33K

Figure 115 As above but tempered for 4h@600°C, showing reverted austenite.

X50K

Figure 116 As above,showing a band of epsilon martensite between the laths.

Step Size = 0.25 eV. 3 Scans of 4000 channels at 20 ms per chan

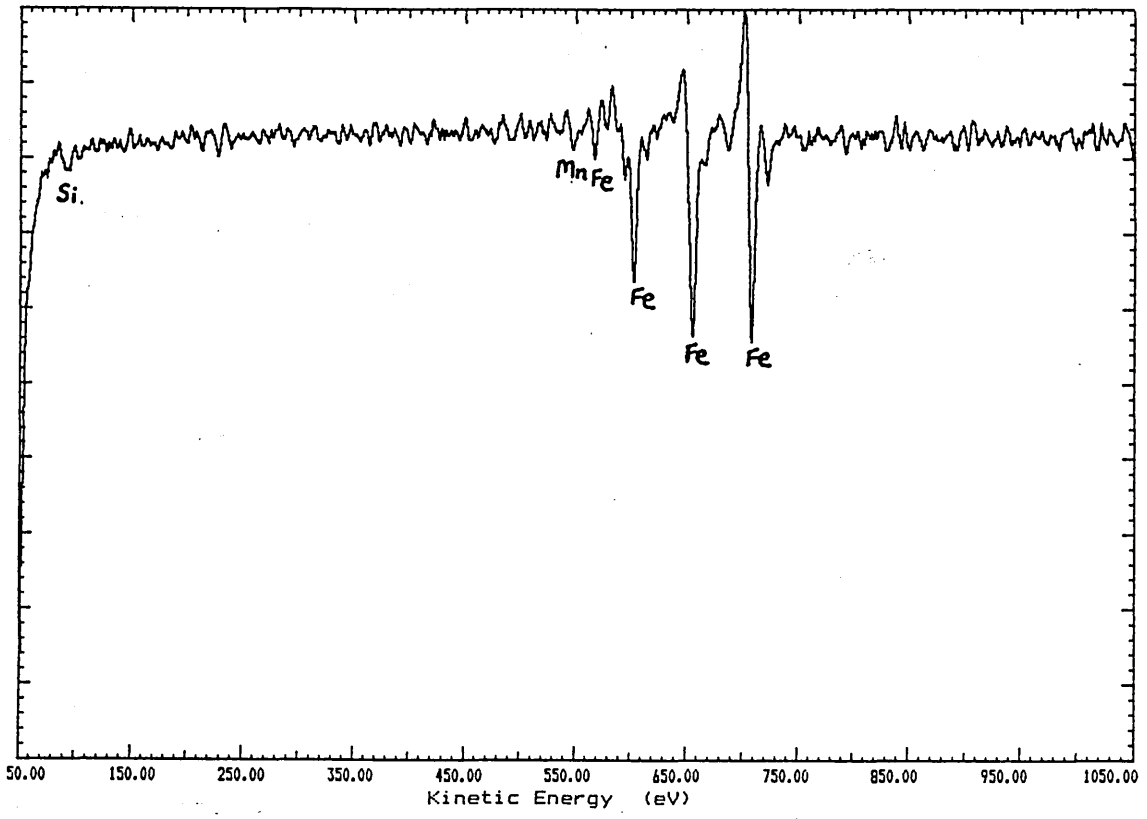

Fig.117 AES spectra for alloy 273,1h.850°C W.Q.
Intergranular: AS FRACTURED

AES Retard Ratio = 4 Max Plotted Count Rate = 8600
Step Size = 0.25 eV. 3 Scans of 4000 channels at 20 ms per chan

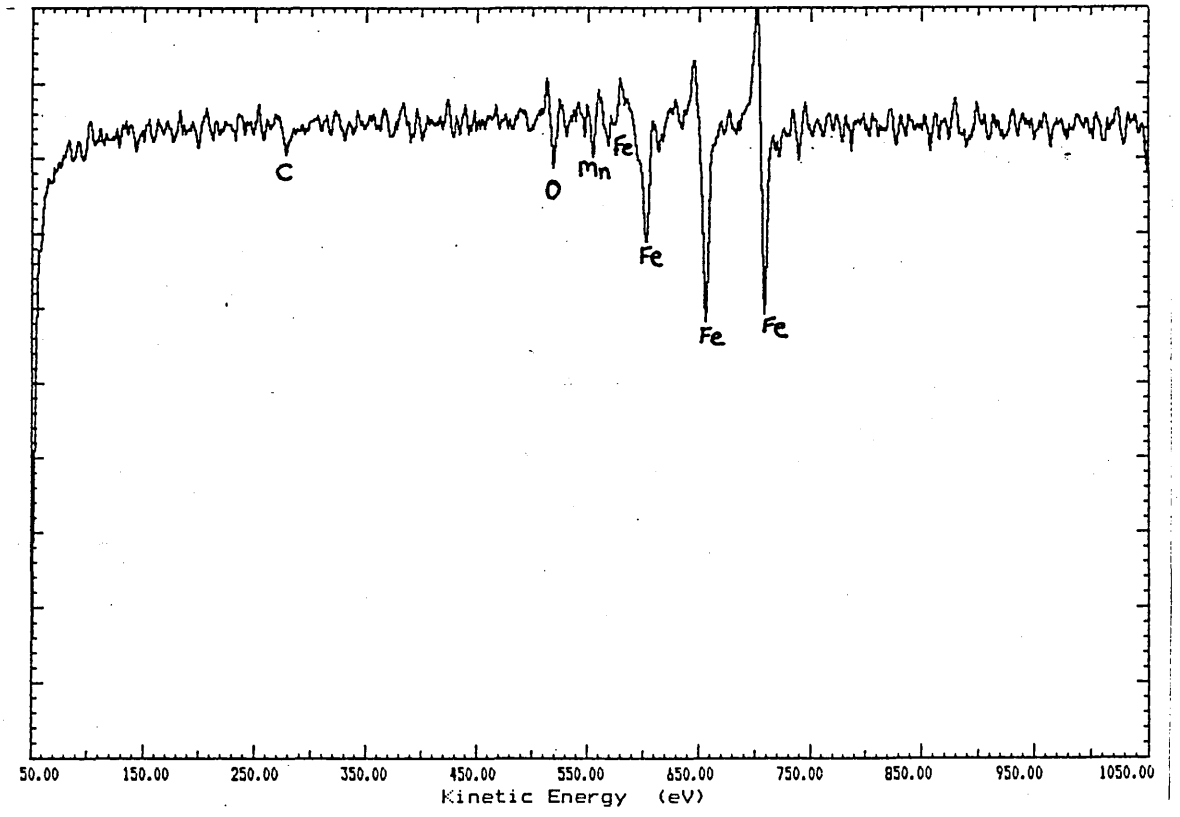

Fig.118 AES spectra as above after ~15 monolayers removed by argon-ion sputtering.

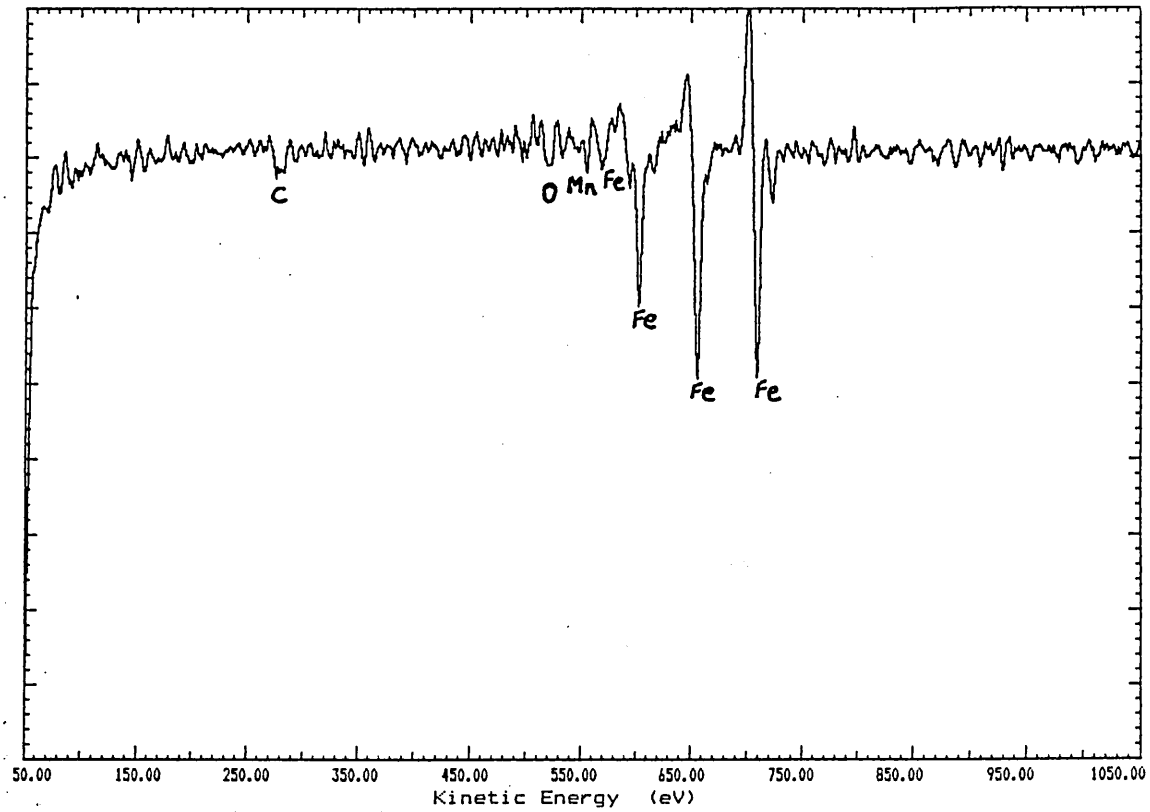

Fig.119 as figure 118 but after ~30 monolayers removed.

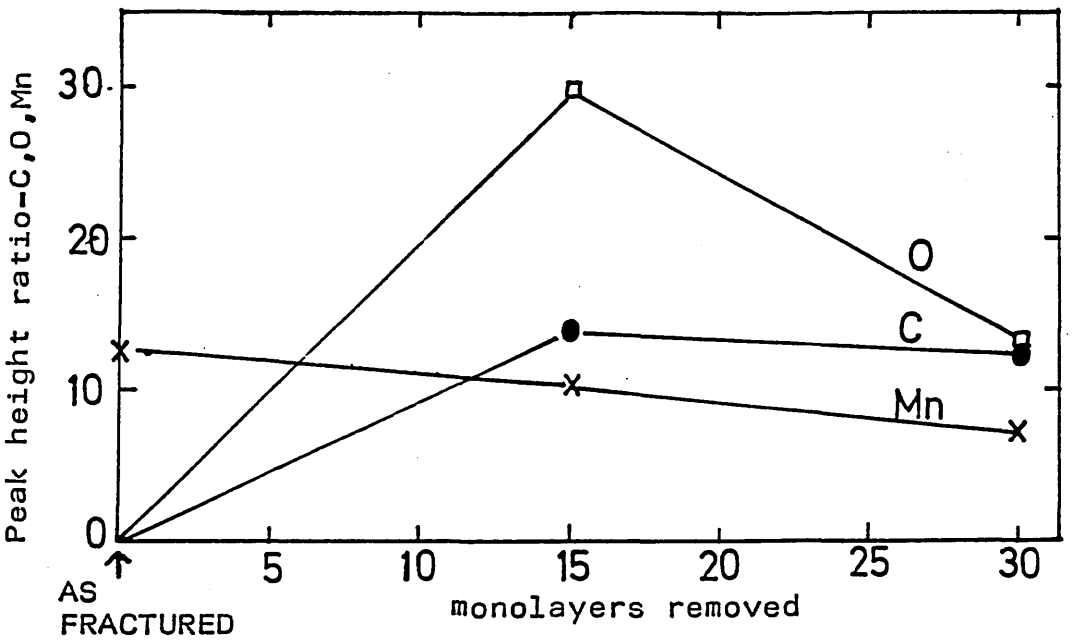

Figure 120 AES sputtering profiles for peak height ratios(% of Fe_{703}eV peak) for alloy 273.

Heat treatment: 1h850°C WQ

Fracture mode: Intergranular

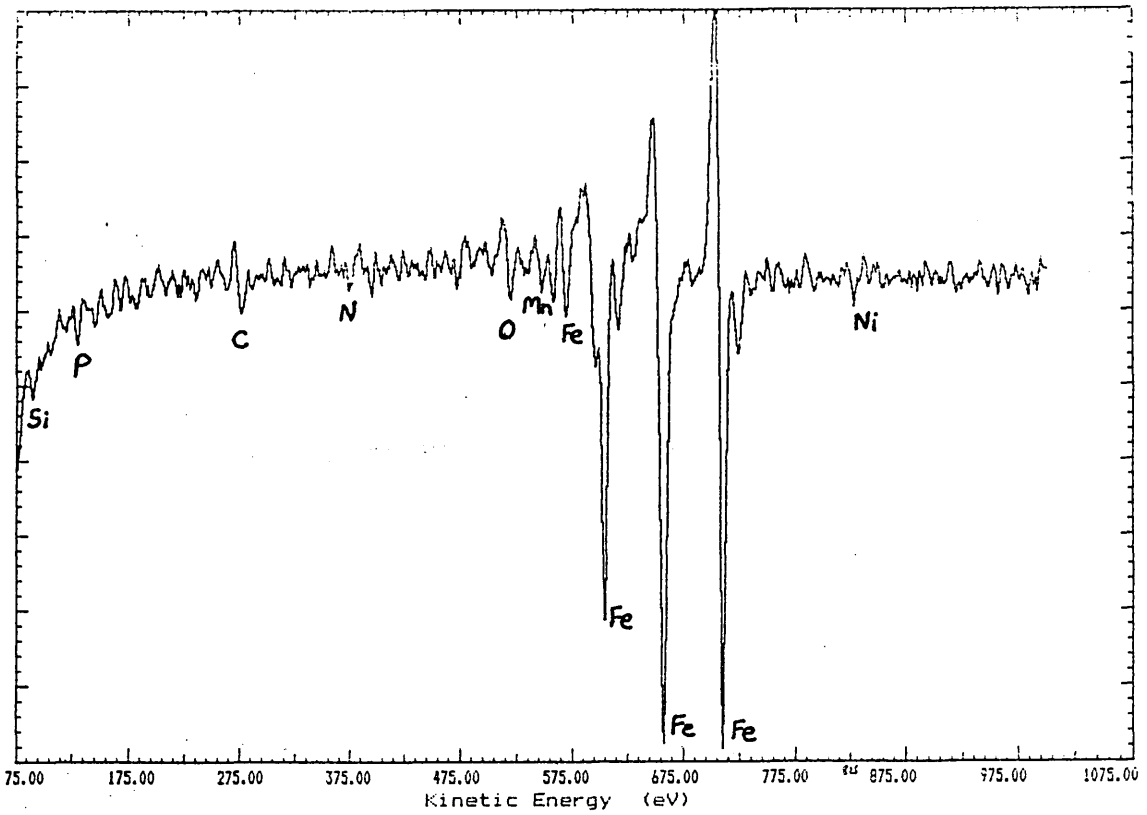

Fig.121 AES spectra for alloy 273,1h.850°C A.C. Intergranular: AS FRACTURED

AES Retard Ratio = 4 Max Plotted Count Rate = 19533
Step Size = 0.25 eV. 3 Scans of 3700 channels at 20 ms per chan

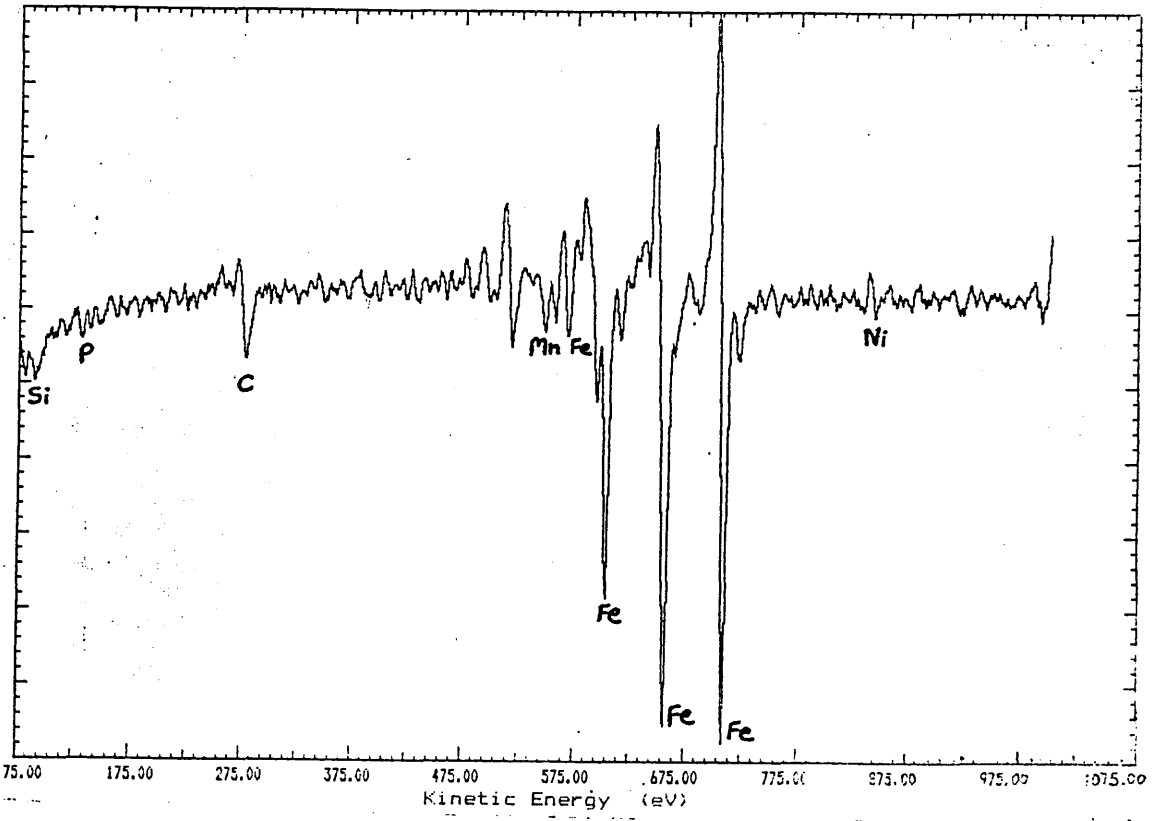

Fig.122 AES spectra as above after ~ 5 monolayers removed by argon-ion sputtering.

Step Size = 0.25 eV. 3 Scans of 3700 channels at 20 ms per chan

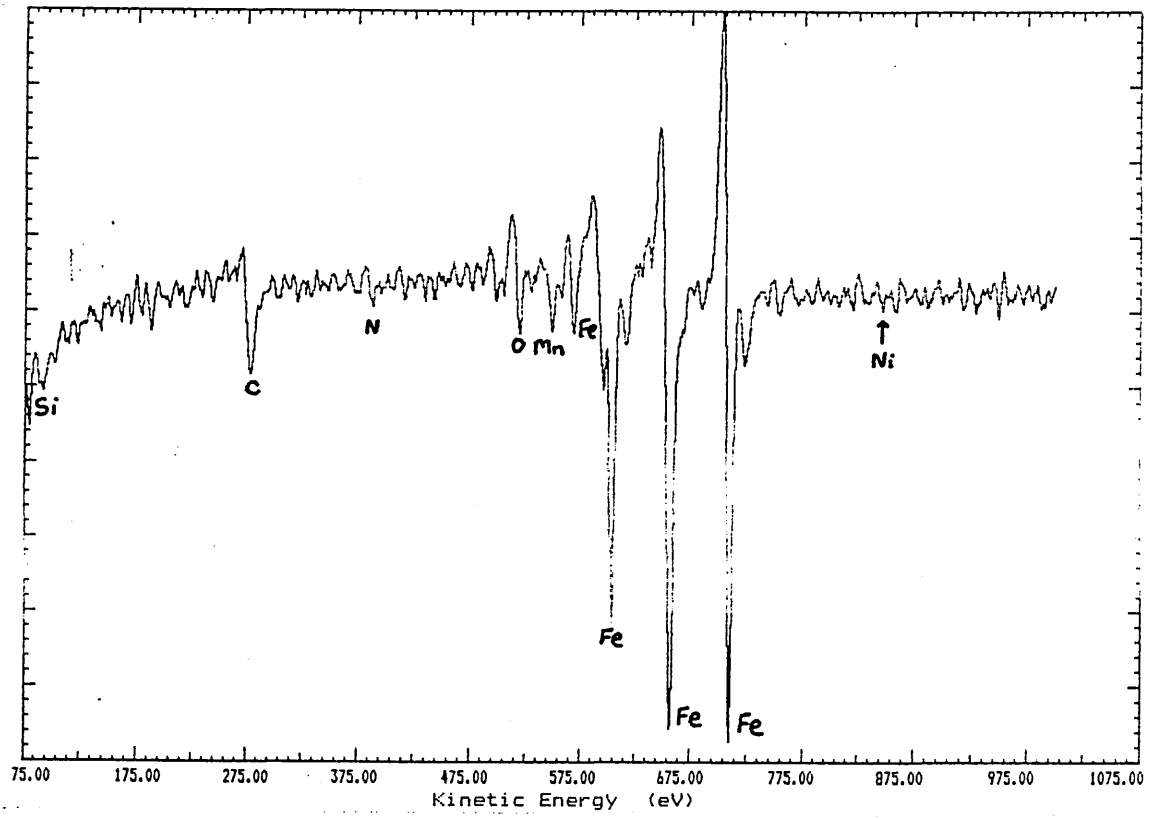

Fig.123 as figure 121 but after ~10 monolayers removed.

AES Retard Ratio = 4 Max Plotted Count Rate = 10200
Step Size = 0.25 eV. 3 Scans of 3700 channels at 20 ms per chan

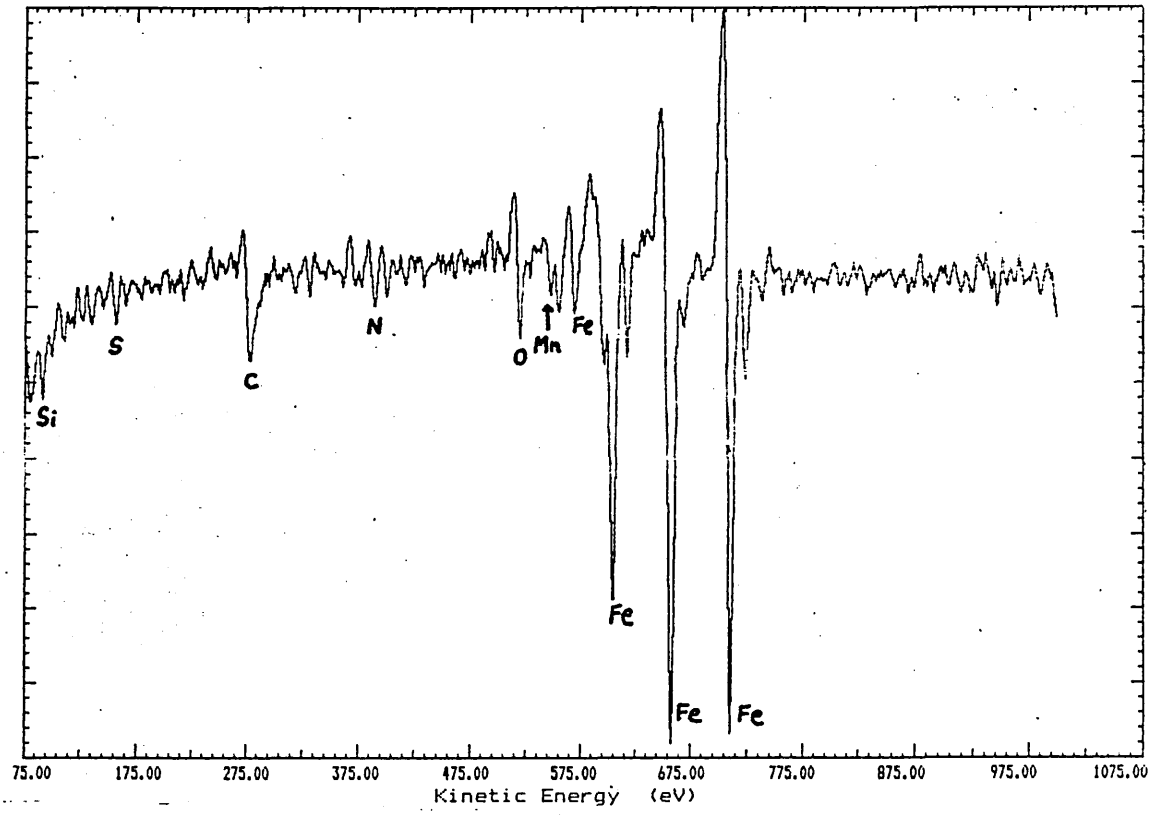

Fig. 124 as above ~15 monolayers.

Step Size = 0.25 eV. 3 Scans of 3700 channels at 20 ms per chan

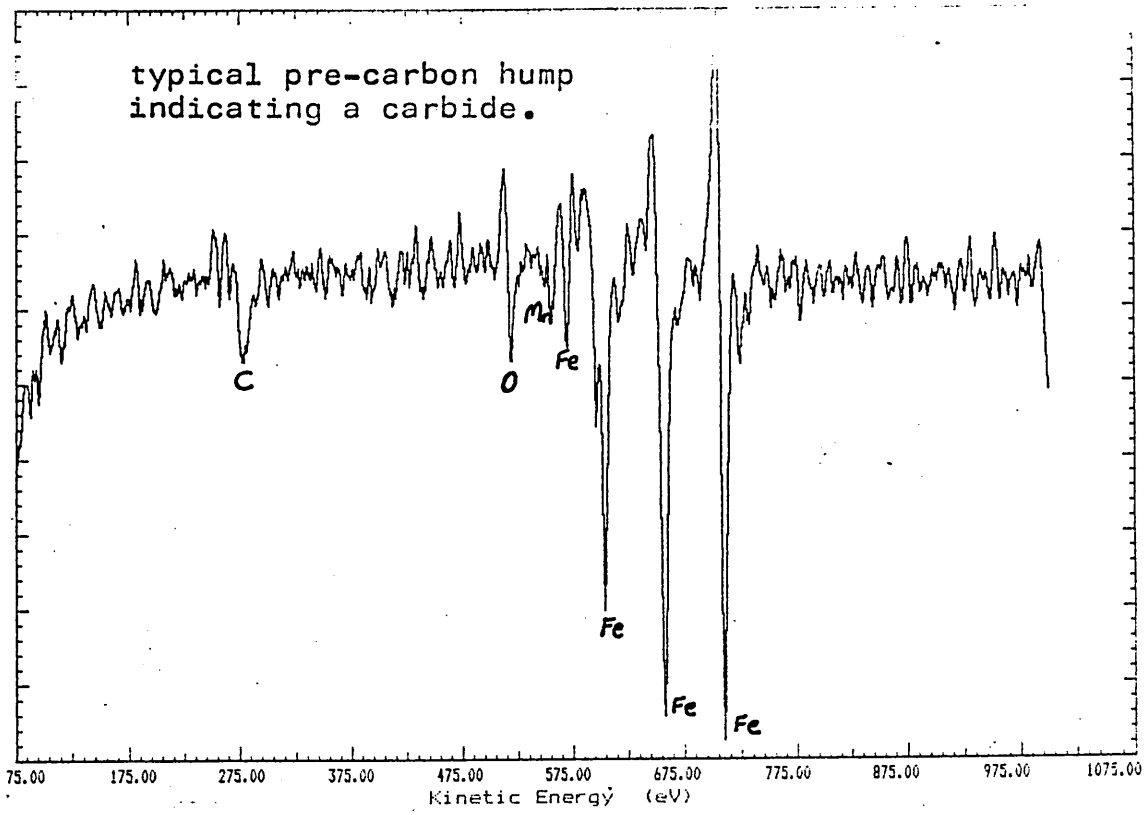

Fig.125 as fig.124 after ~15 monolayers showing a precipitate.

AES Retard Ratio = 4 Max Plotted Count Rate = 3999
Step Size = 0.25 eV. 3 Scans of 3700 channels at 20 ms per chan

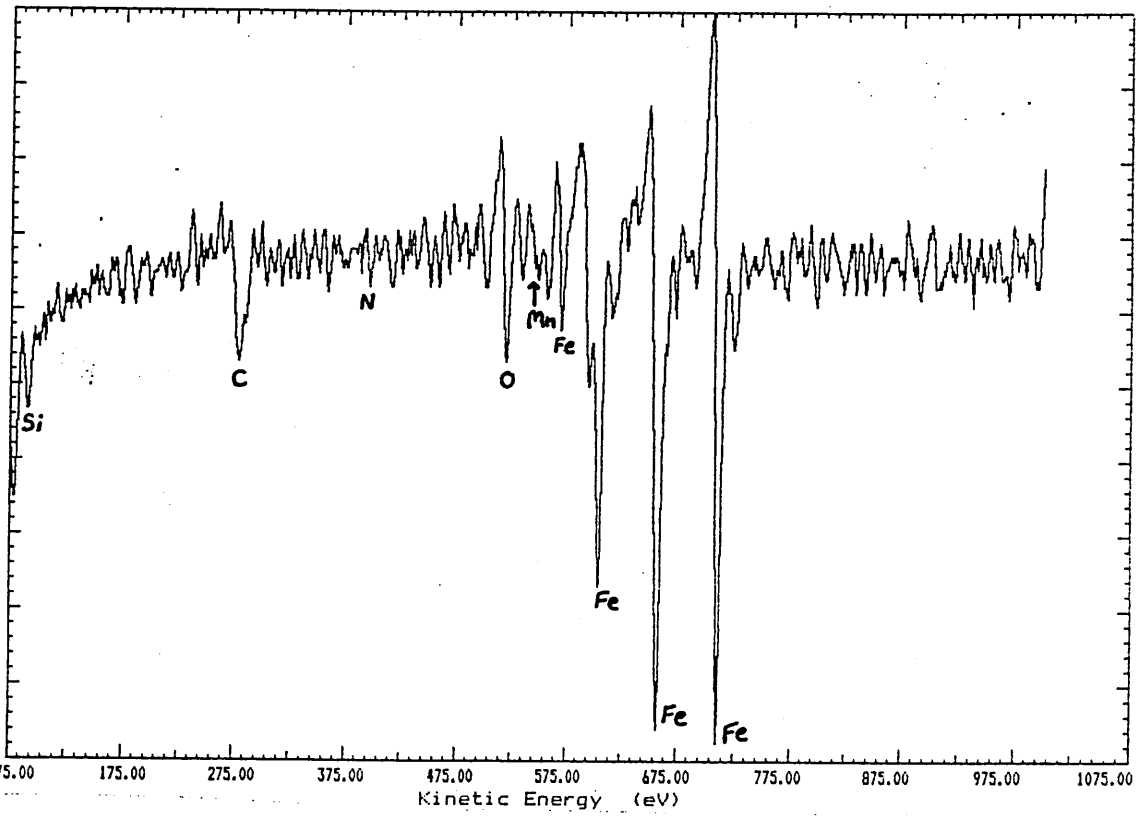

Fig.126 as fig.124 but after ~20 monolayers removed.

Step Size = 0.25 eV. 3 Scans of 3700 channels at 20 ms per chan

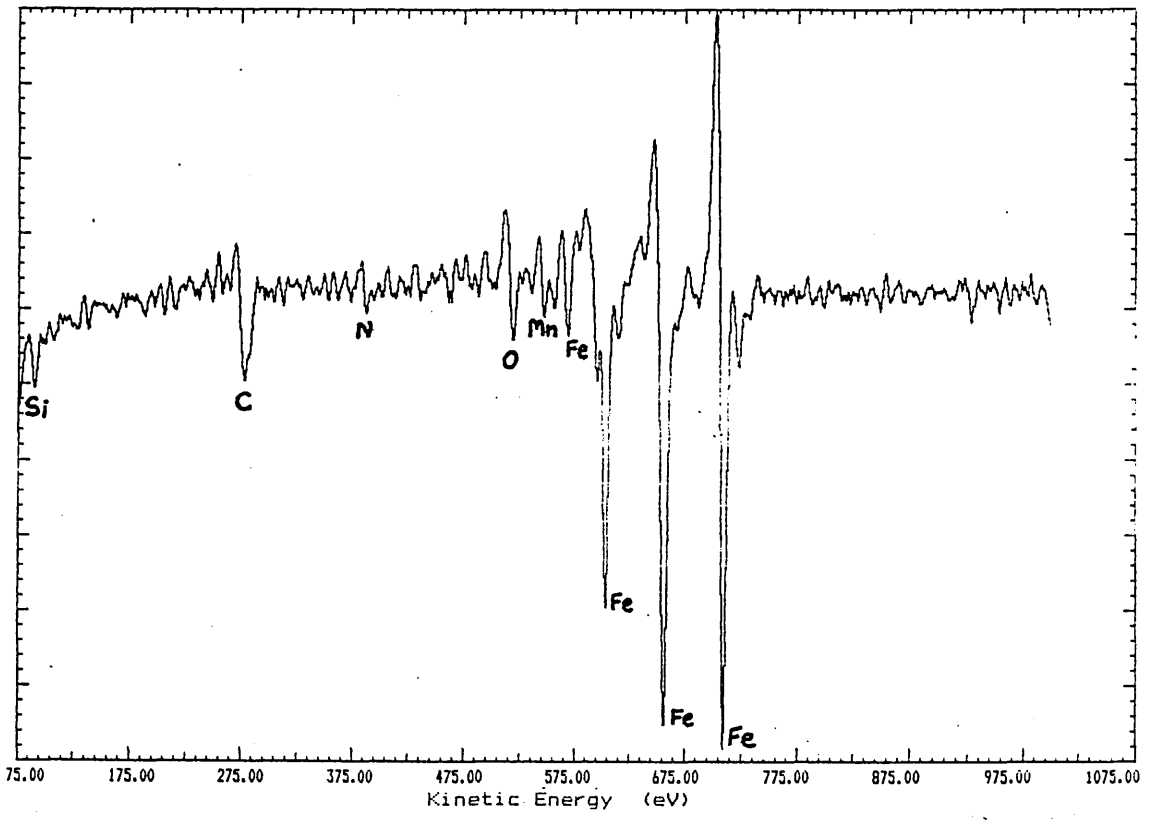

Fig.127 as figure 126 but after ~ 25 monolayers removed.

AES Retard Ratio = 4 Max Plotted Count Rate = 19843
Step Size = 0.25 eV. 3 Scans of 3700 channels at 20 ms per chan

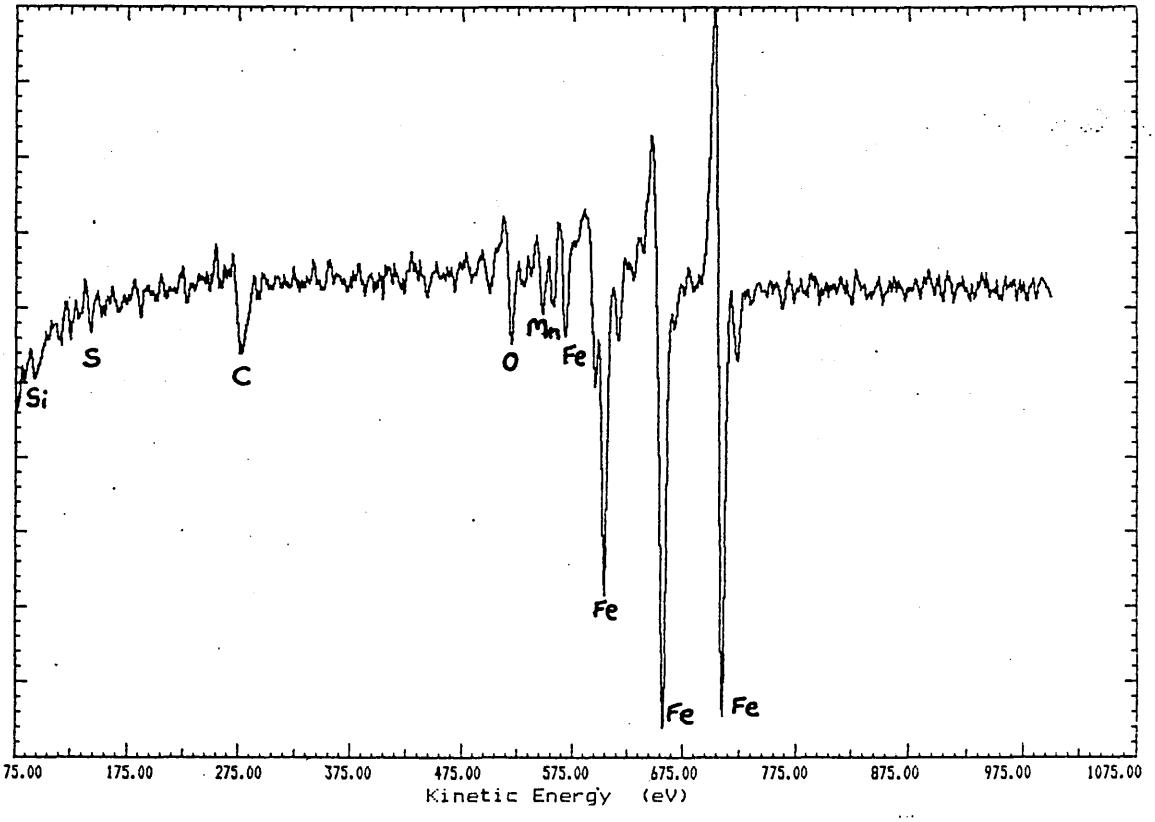

Fig.128 as above but after ~ 30 monolayers removed.

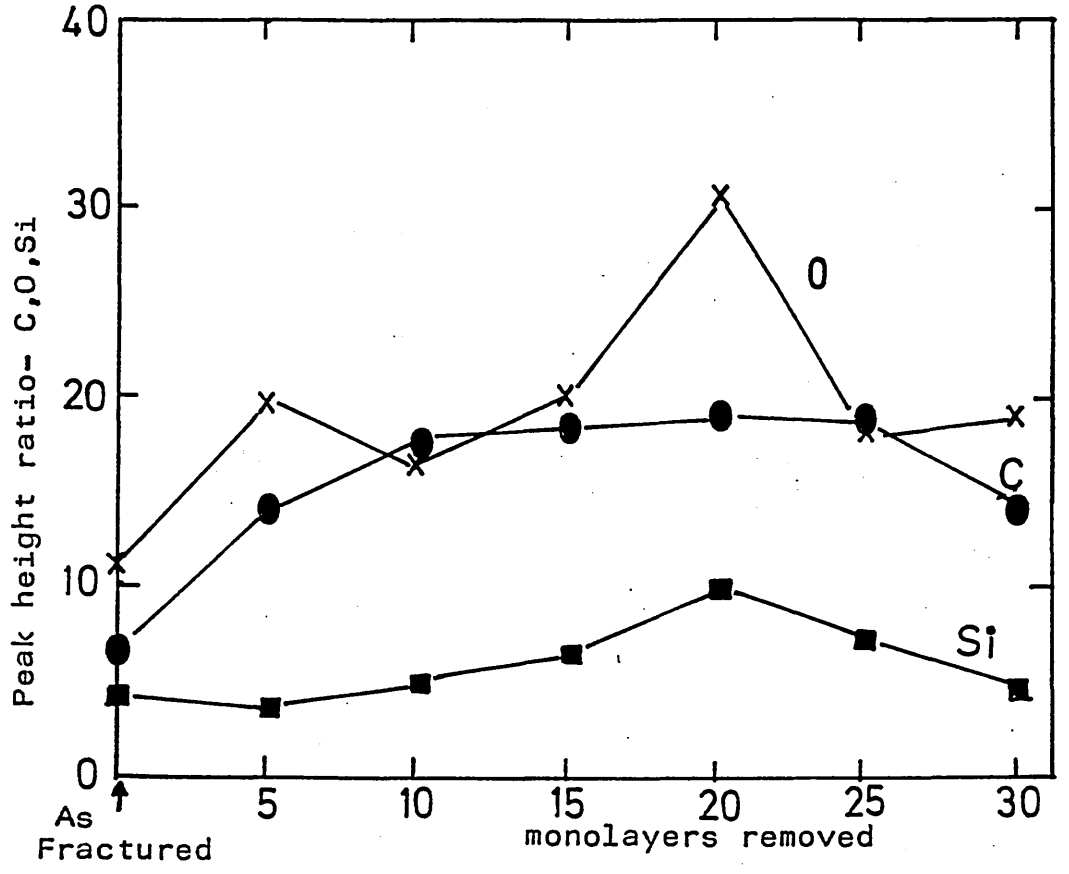

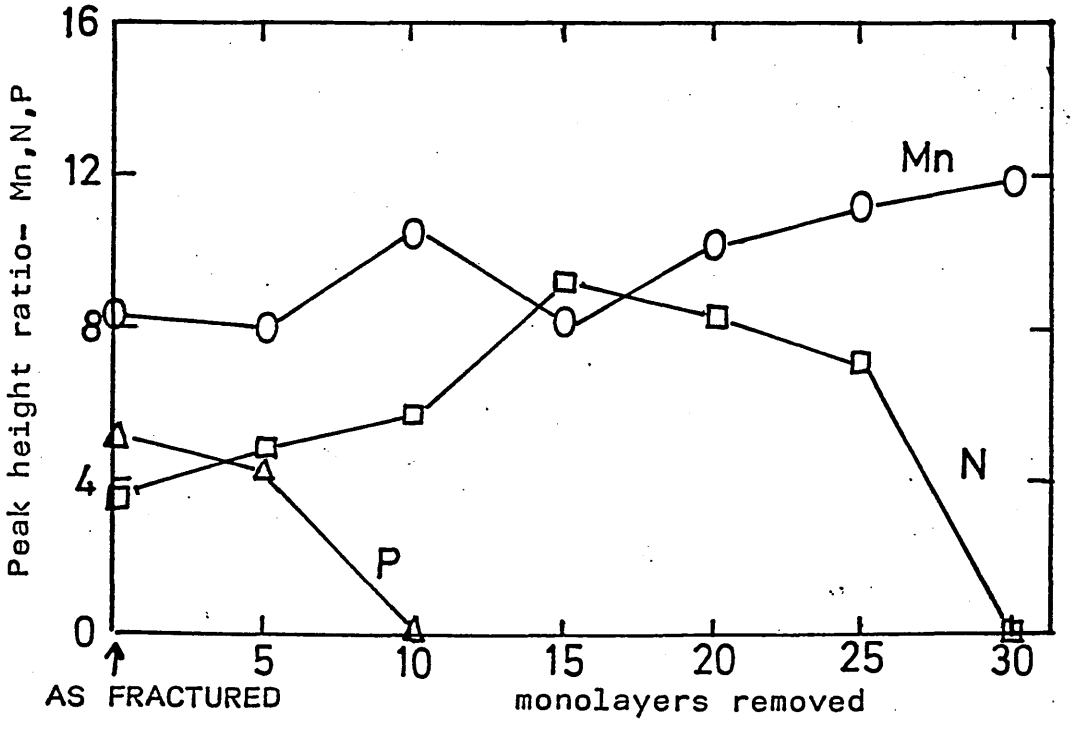

Figure 129 AES sputtering profiles for peak height ratios(% of Fe_{703}eV peak) for alloy 273.

Heat treatment:1h. 850°C AC
Fracture mode: Intergranular

Step Size = 0.25 eV. 3 Scans of 3700 channels at 20 ms per chan

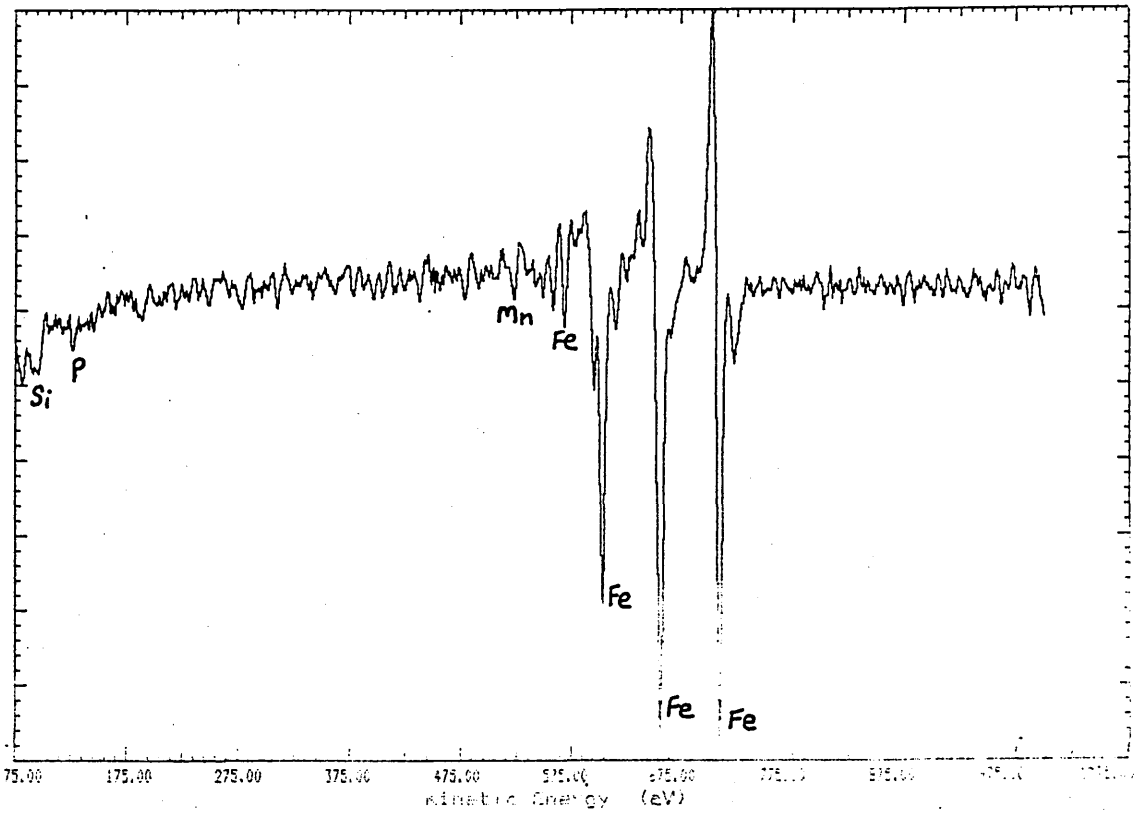

Fig.130 AES spectra for alloy 275, 1h.850°C A.C. Intergranular: AS FRACTURED

AES Retard Ratio = 4 Max Plotted Count Rate = 25466
Step Size = 0.25 eV. 3 Scans of 3700 channels at 20 ms per chan

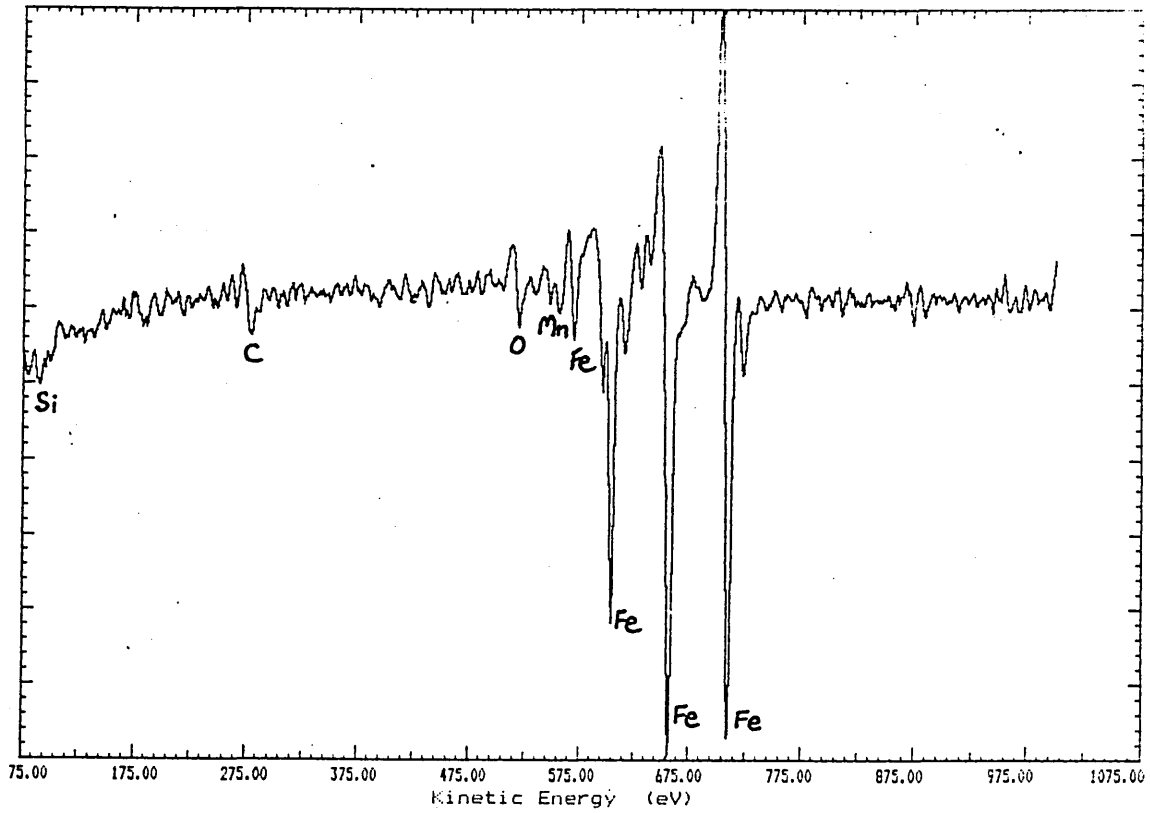

Fig.131 AES spectra as above after ~5 monolayers removed by argon-ion sputtering.

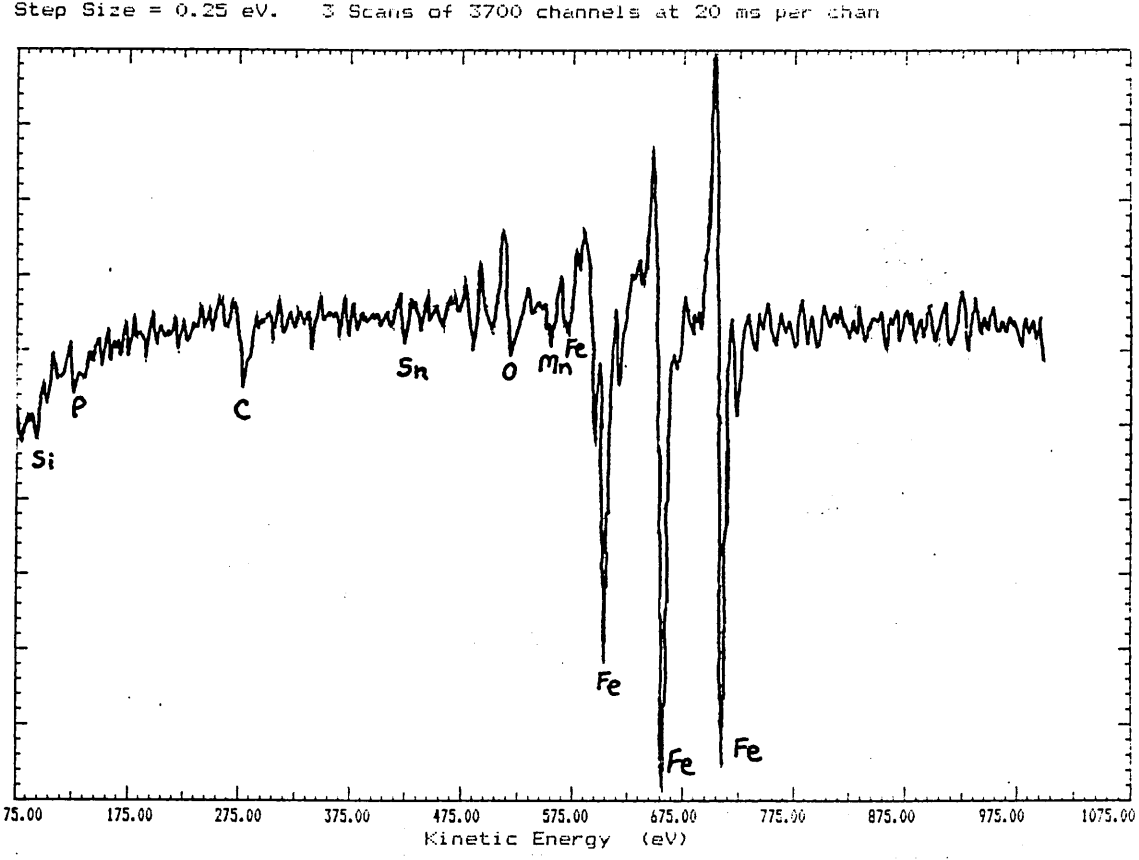

Fig.132 as figure131 but after ~ 10 monolayers removed.

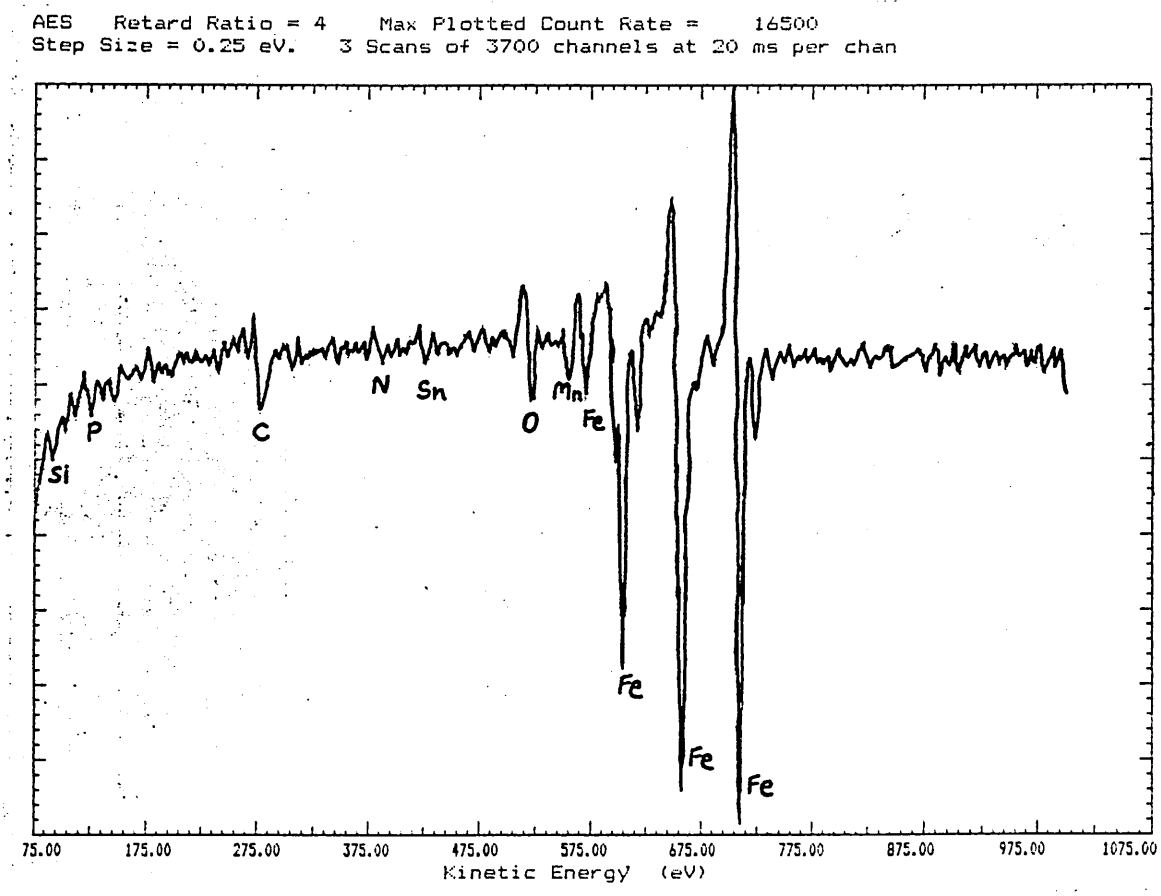

Fig.133 as figure 131 but after ~ 15 monolayers removed.

Step Size = 0.25 eV. 3 Scans of 3700 channels at 20 ms per chan

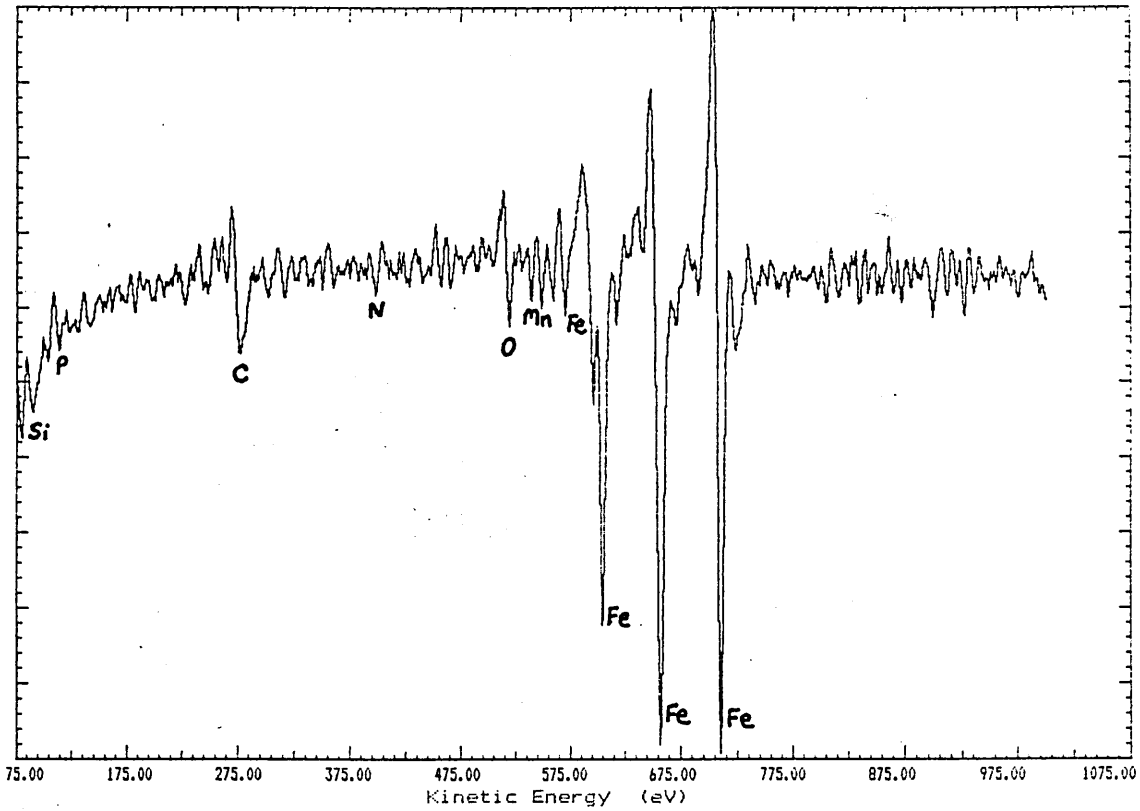

Fig.134 as figure131 but after ~20 monolayers removed.

AES Retard Ratio = 4 Max Plotted Count Rate = 13714
Step Size = 0.50 eV. 7 Scans of 1850 channels at 20 ms per chan

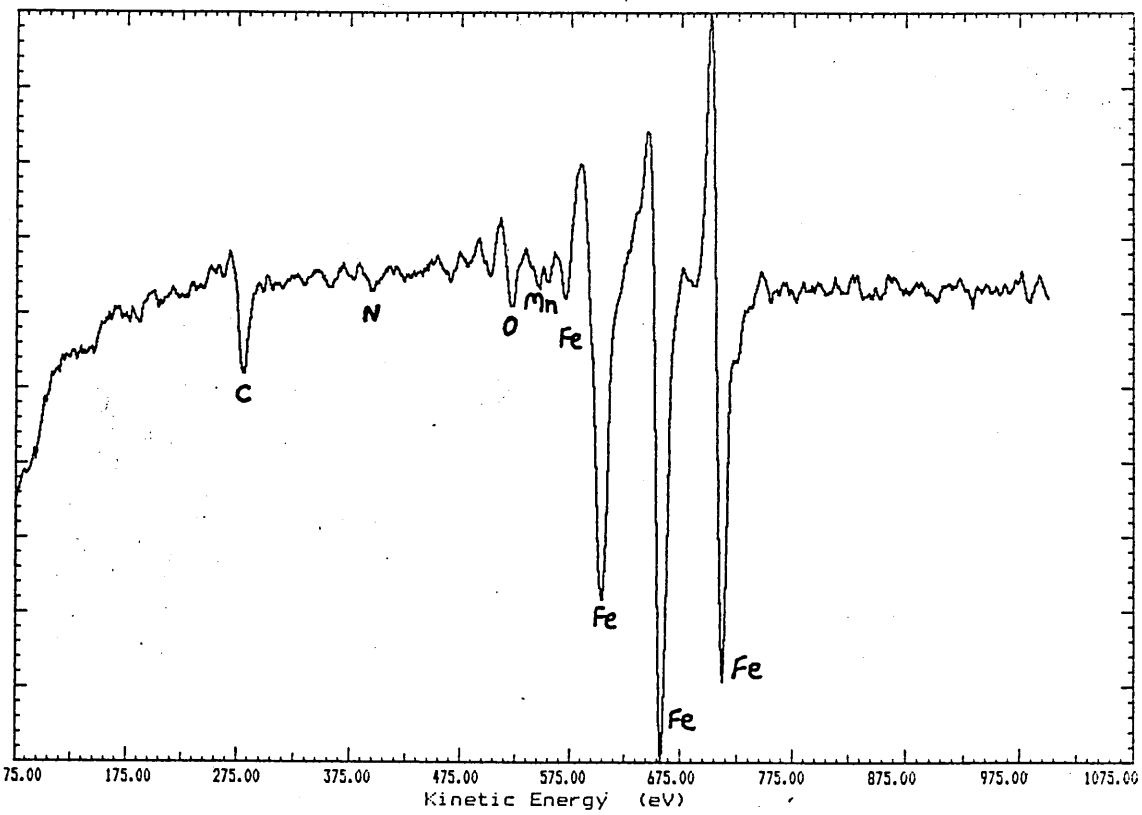

Fig.135 as figure 131 but after ~25 monolayers removed.

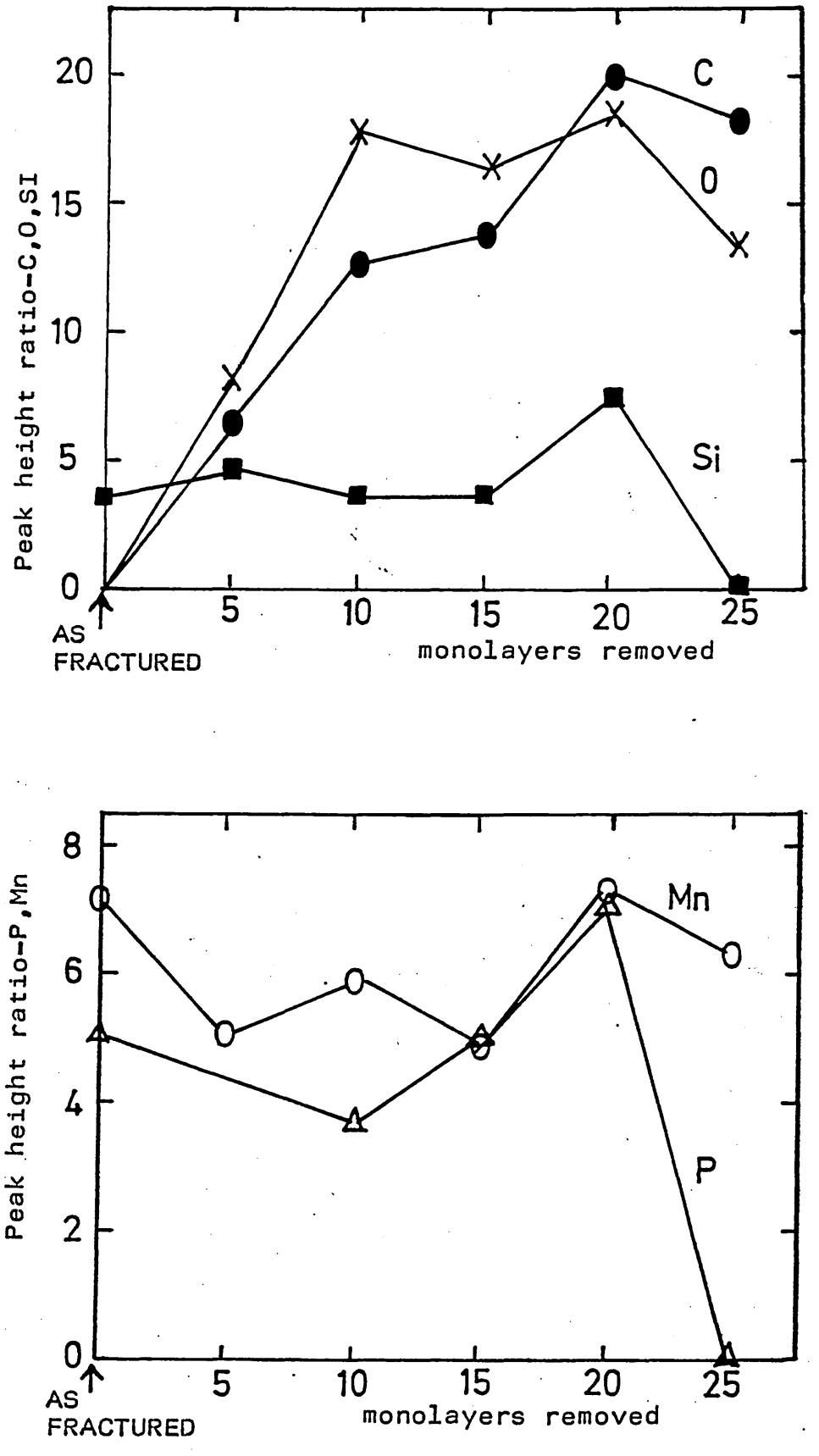

Figure 136 AES sputtering profiles for peak height ratios(% of Fe_{703}eV peak) for alloy 275.

Heat treatment: 1h850°C AC

Fracture mode: Intergranular

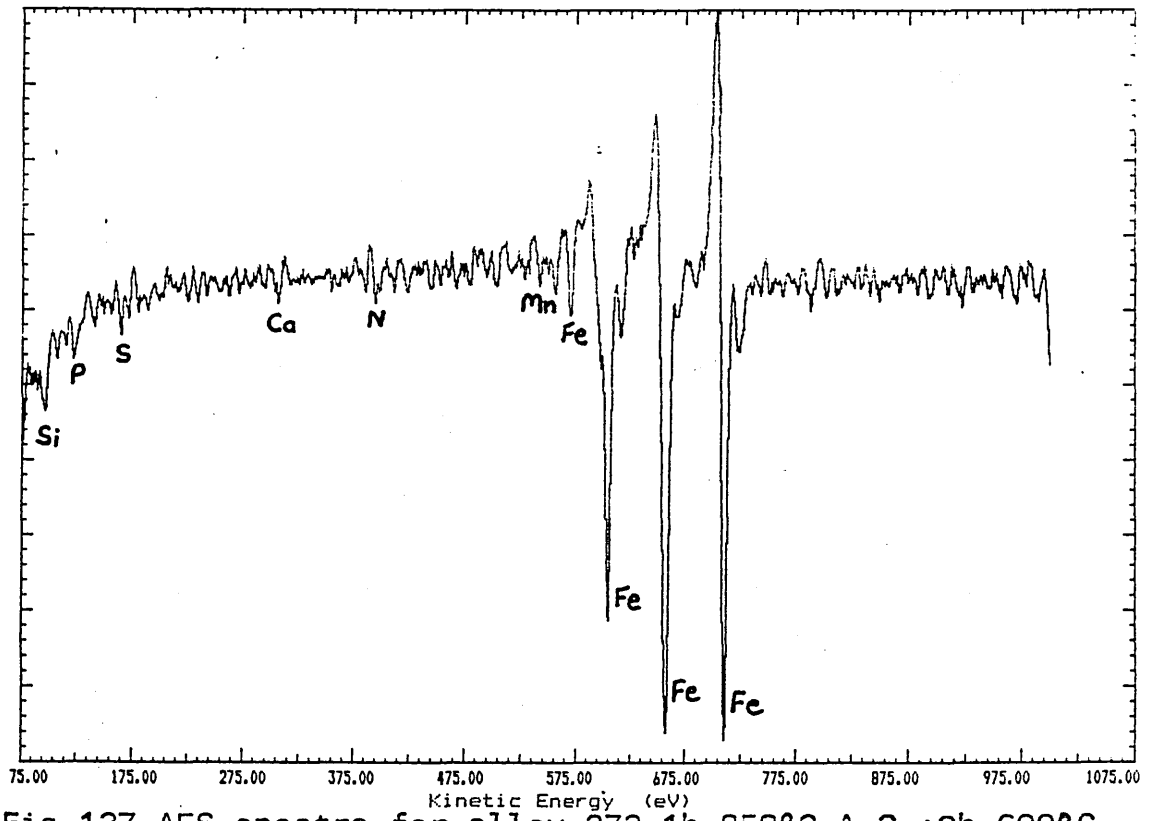

Fig.137 AES spectra for alloy 273,1h.850°C A.C.+2h.600°C cleavage:AS FRACTURED.

AES Retard Ratio = 4 Max Plotted Count Rate = 15299
Step Size = 0.25 eV. 3 Scans of 3700 channels at 20 ms per chan

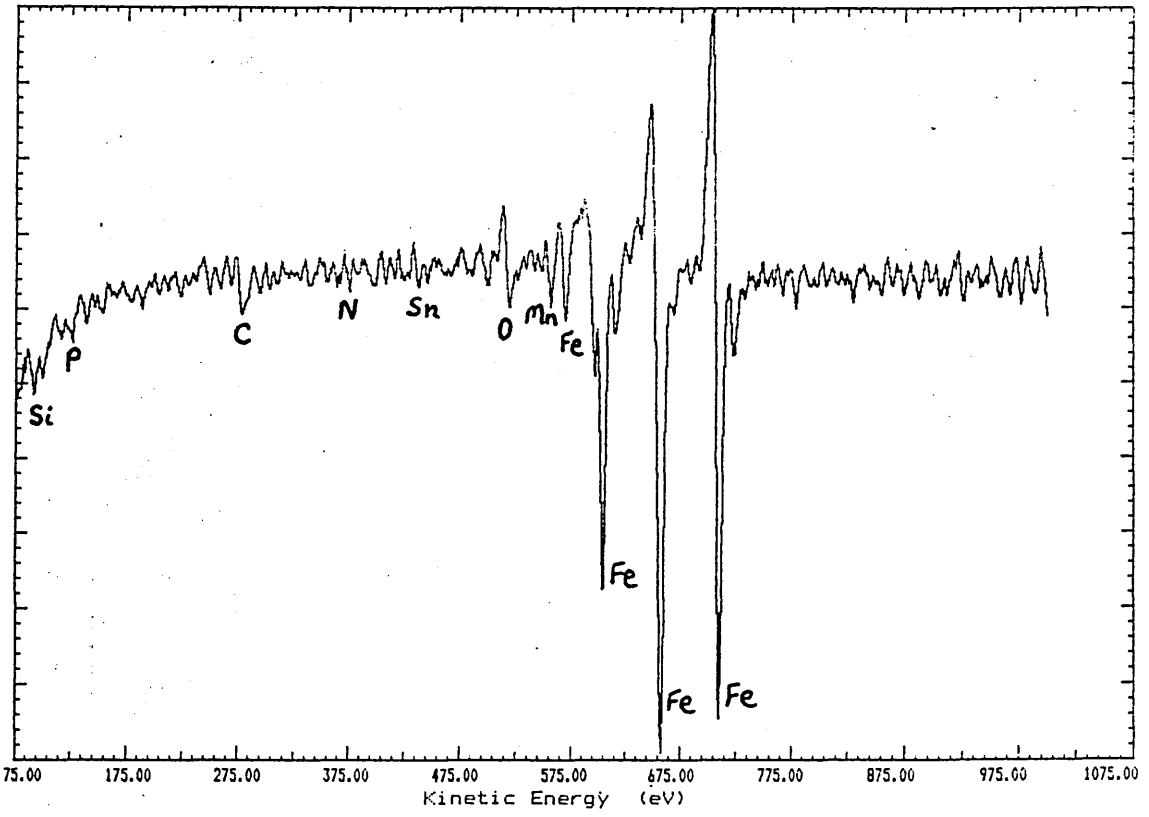

Fig.138 AES spectra as above after ~ 5 monolayers removed by argon-ion sputtering.

Step Size = 0.25 eV. 3 Scans of 3700 channels at 20 ms per chan

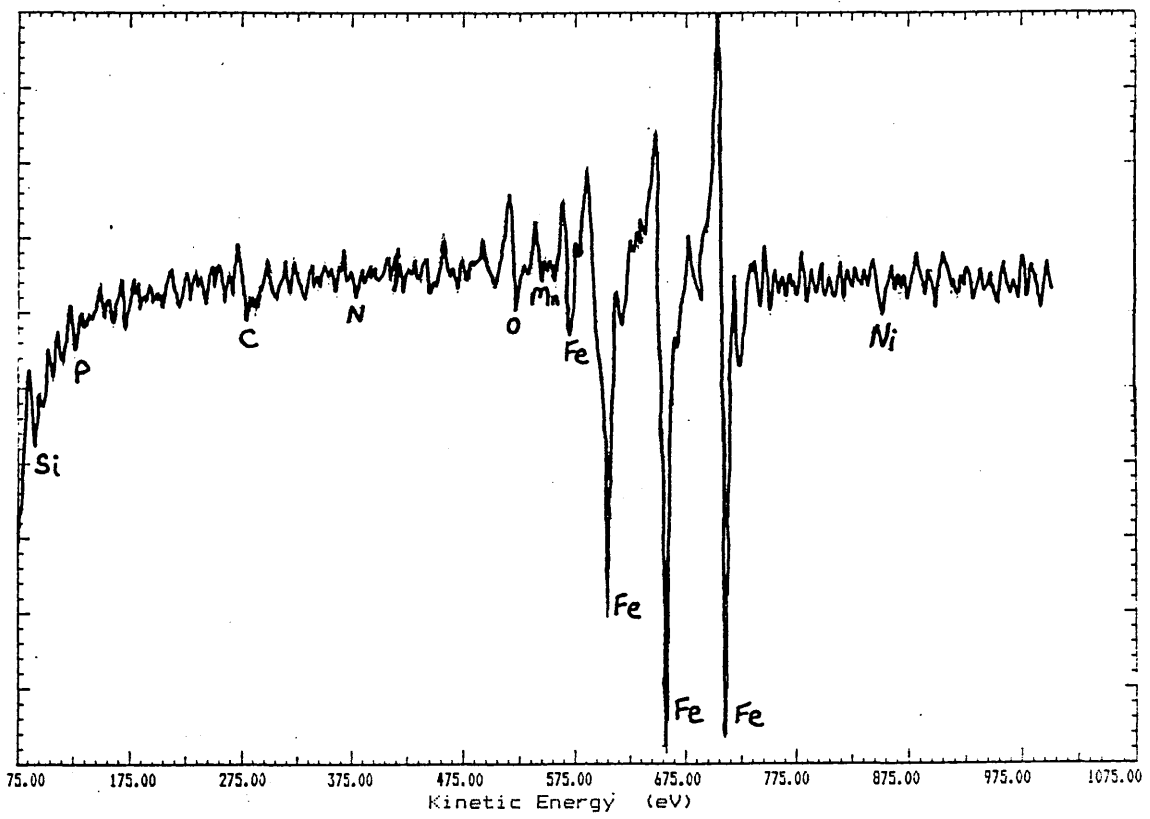

Fig.139 as fig.138 but after ~10 monolayers removed.

AES Retard Ratio = 4 Max Plotted Count Rate = 24033
Step Size = 0.25 eV. 3 Scans of 3700 channels at 20 ms per chan

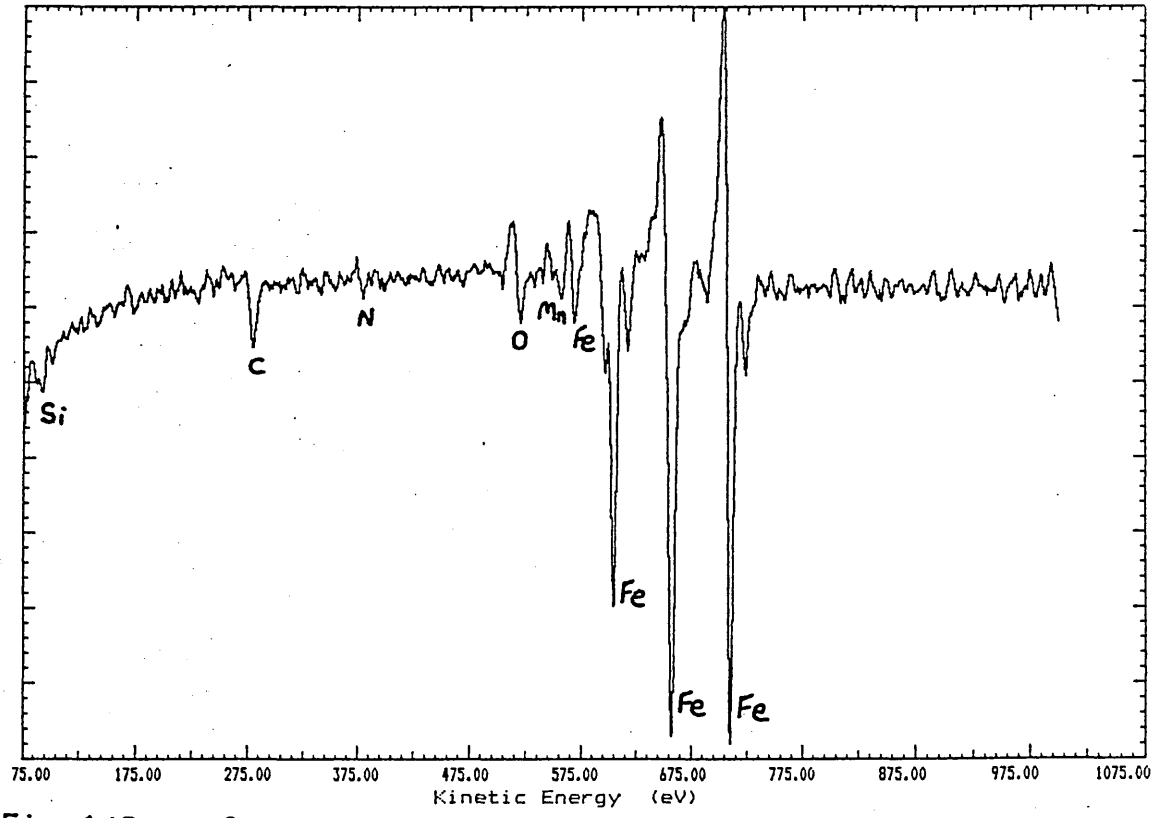

Fig.140 as fig.138 but after ~ 15 monolayers removed.

Step Size = 0.25 eV. 3 Scans of 3700 channels at 20 ms per chan

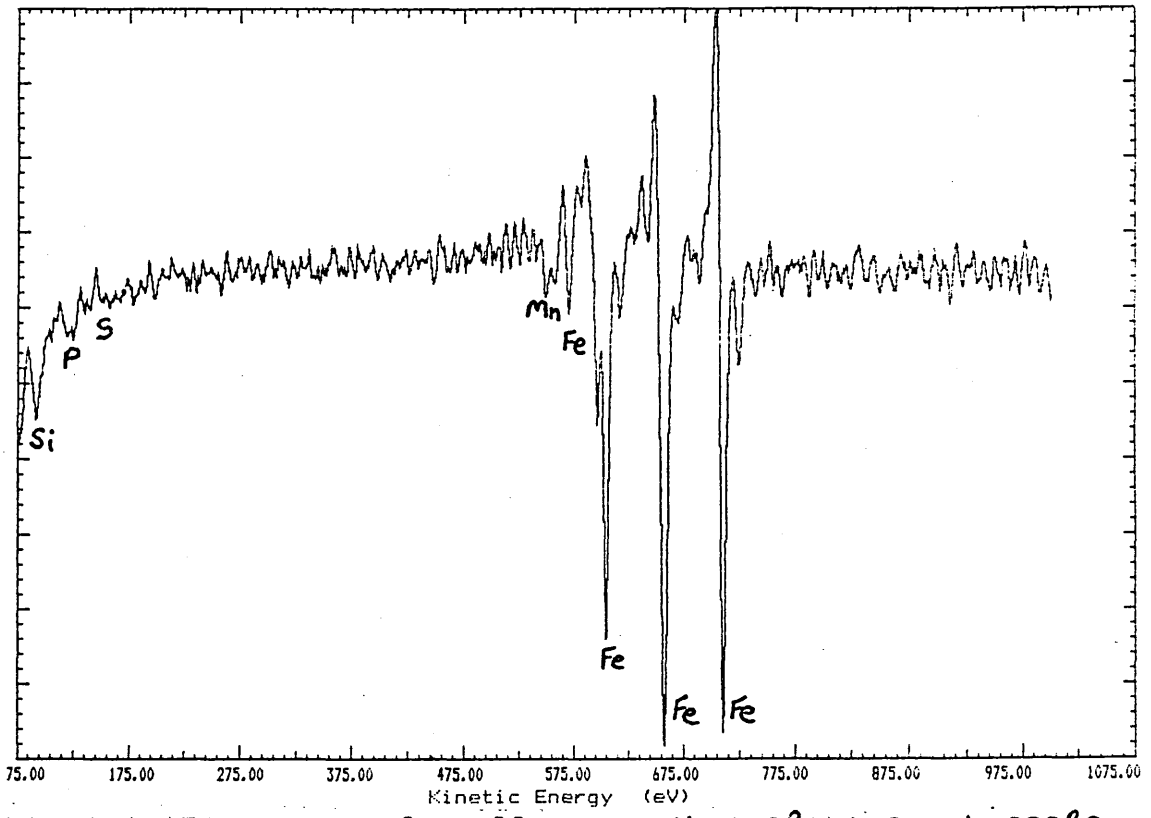

Fig.141 AES spectra for alloy 273,1h.850°C A.C.+2h.600°C Ductile:AS FRACTURED.

AES Retard Ratio = 4 Max Plotted Count Rate = 13233
Step Size = 0.25 eV. 3 Scans of 3700 channels at 20 ms per chan

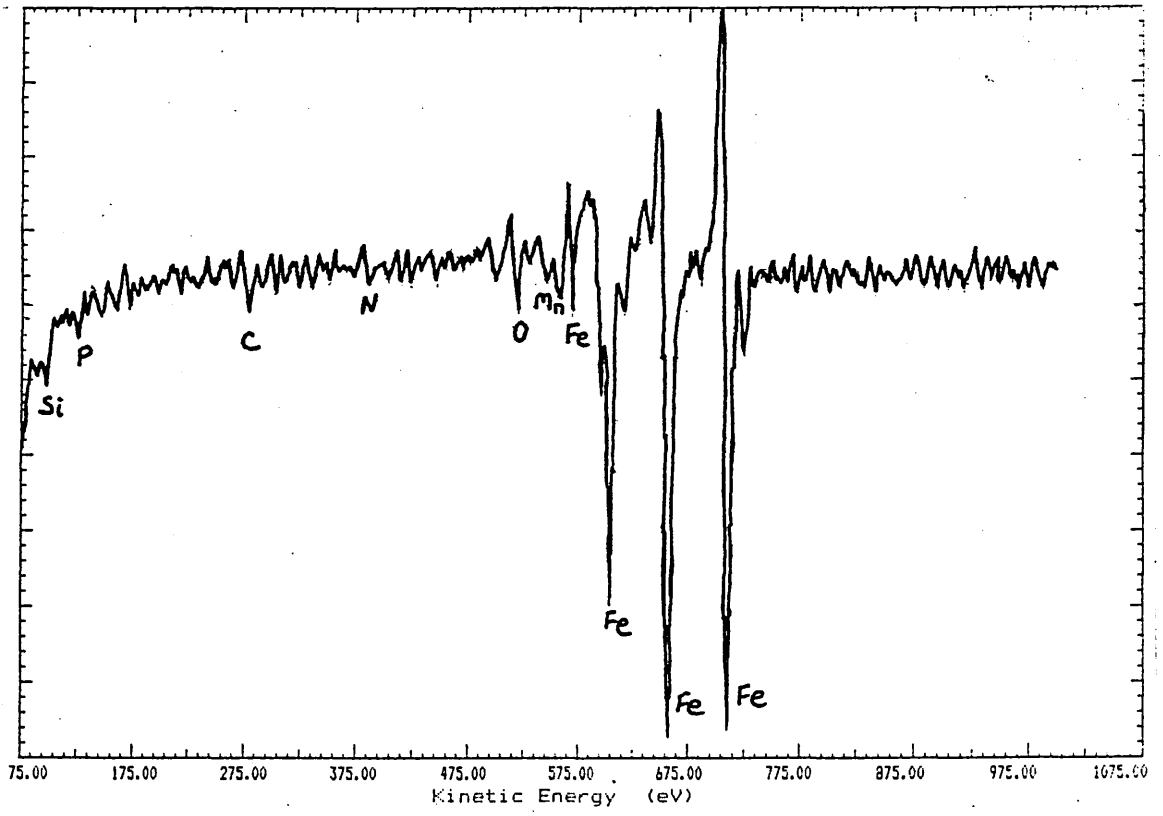

Fig.142 AES spectra as above after ~5 monolayers removed by argon-ion sputtering.

AES Retard Ratio = 4 Max Plotted Count Rate = 11960
Step Size = 0.25 eV. 3 Scans of 3700 channels at 20 ms per chan

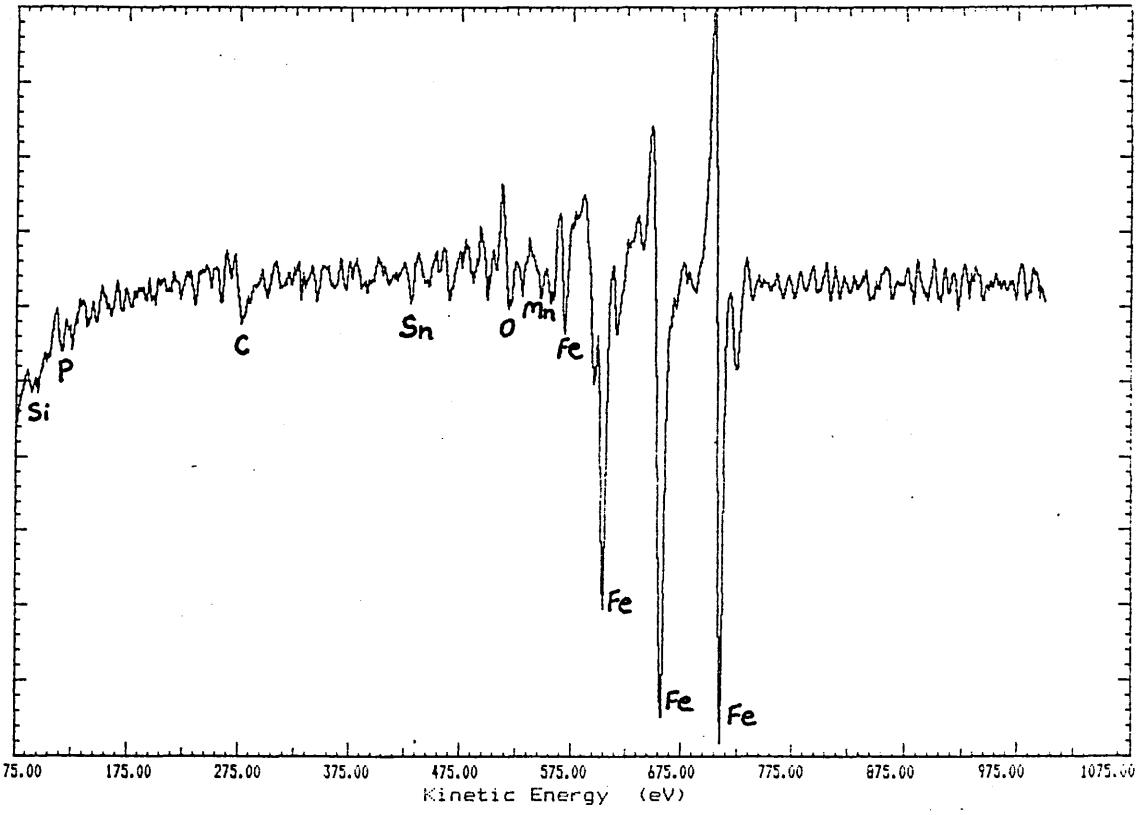

Fig.143 AES spectra as fig.142 but after ~10 monolayers removed.

AES Retard Ratio = 4 Max Plotted Count Rate = 18766
Step Size = 0.25 eV. 3 Scans of 3700 channels at 20 ms per chan

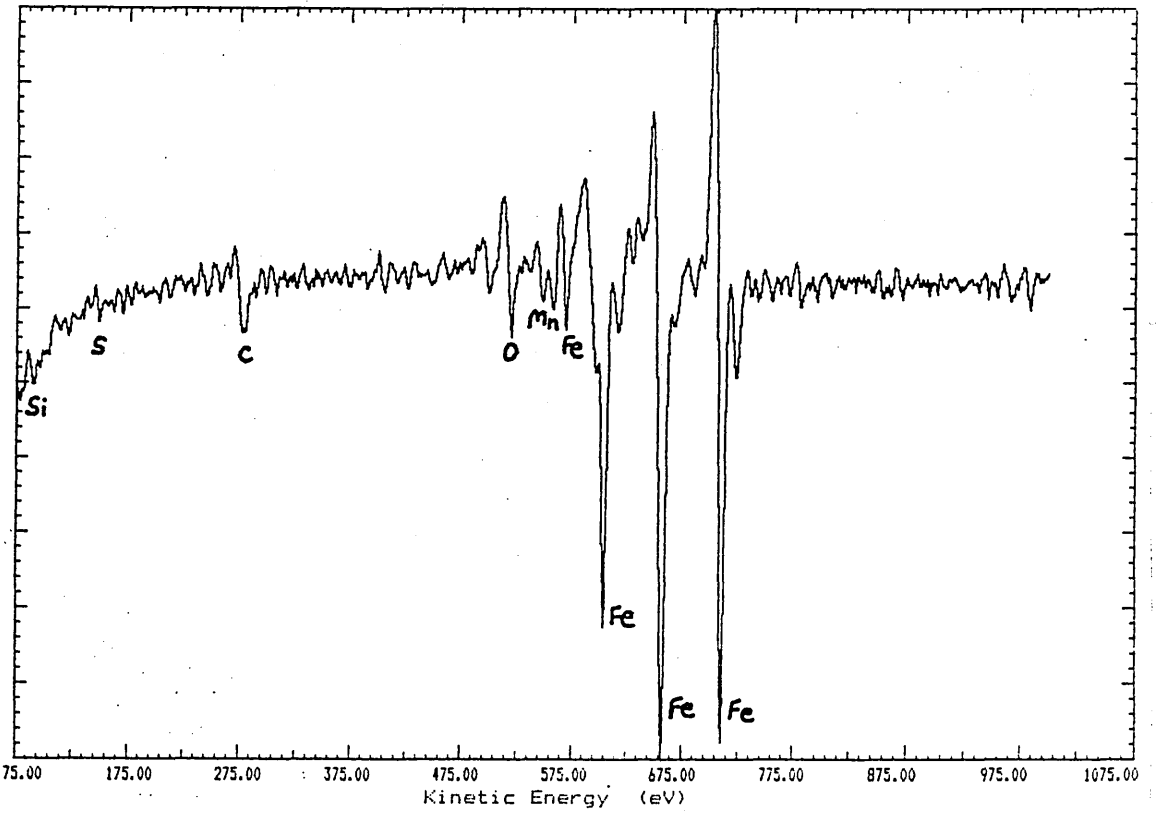

Fig.144 as fig.142 but after ~15 monolayers removed.

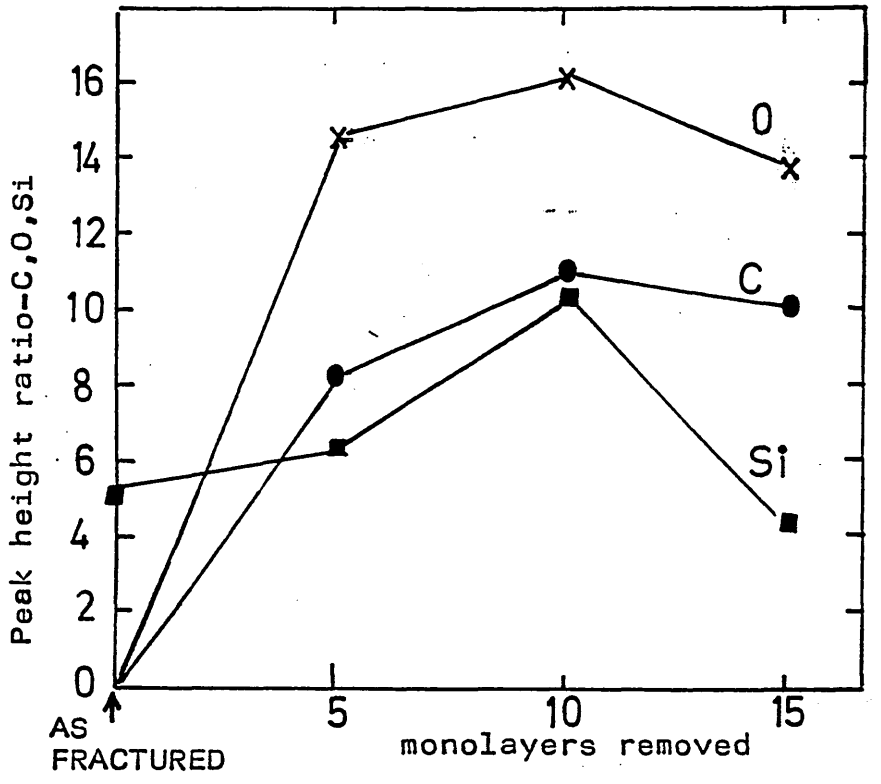

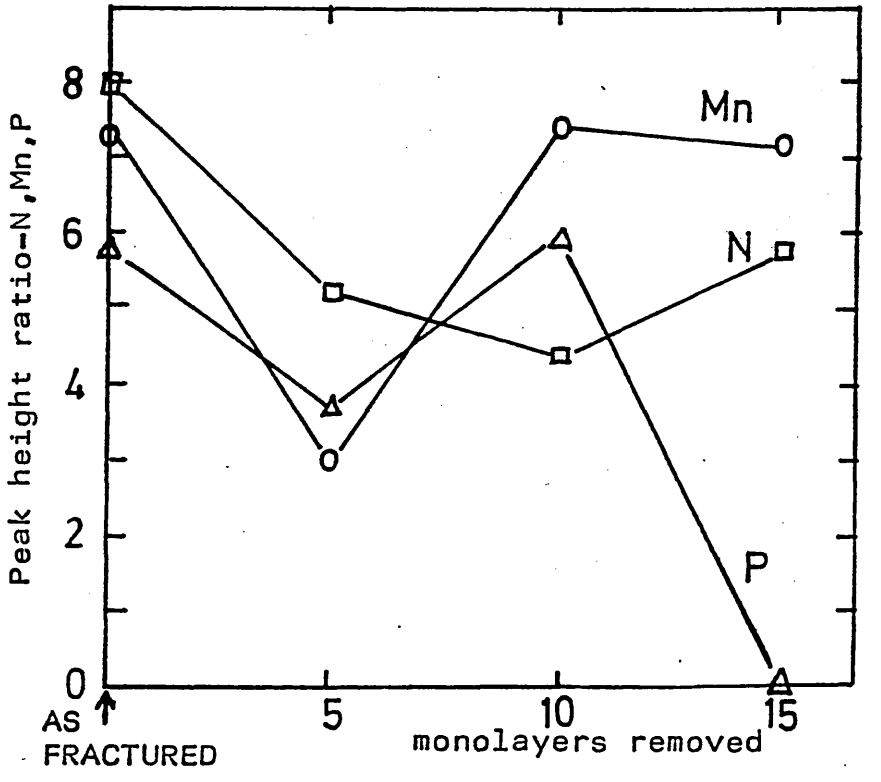

Figure 145 AES sputtering profiles for peak height ratios(% of Fe_{703}eV peak) for alloy 273.

Heat treatment: 1h.850°C AC+2h.600°C WQ
Fracture mode: Cleavage areas.

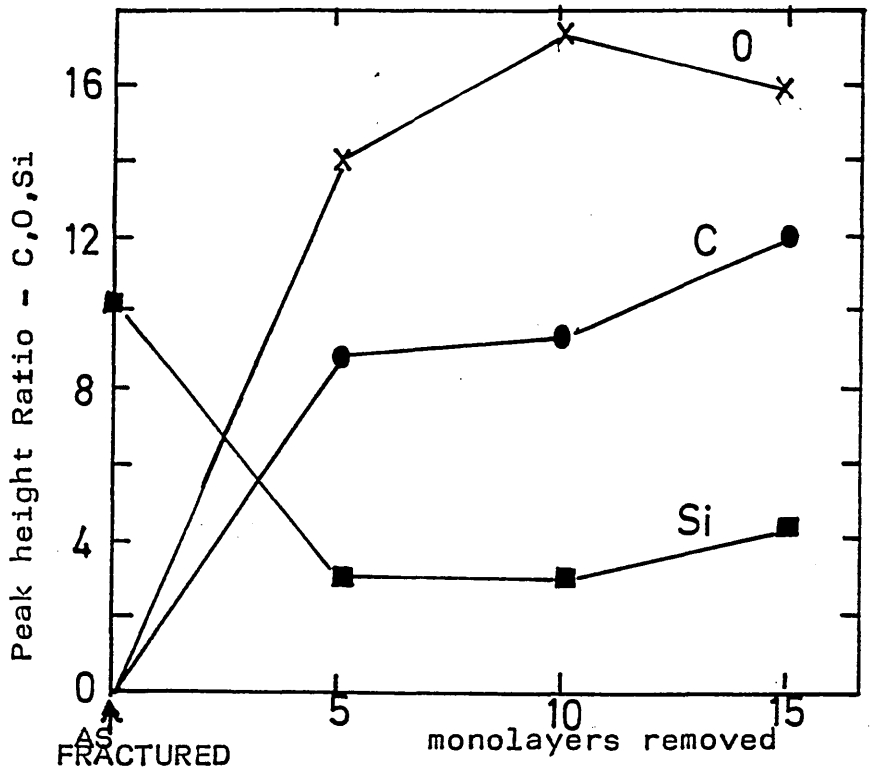

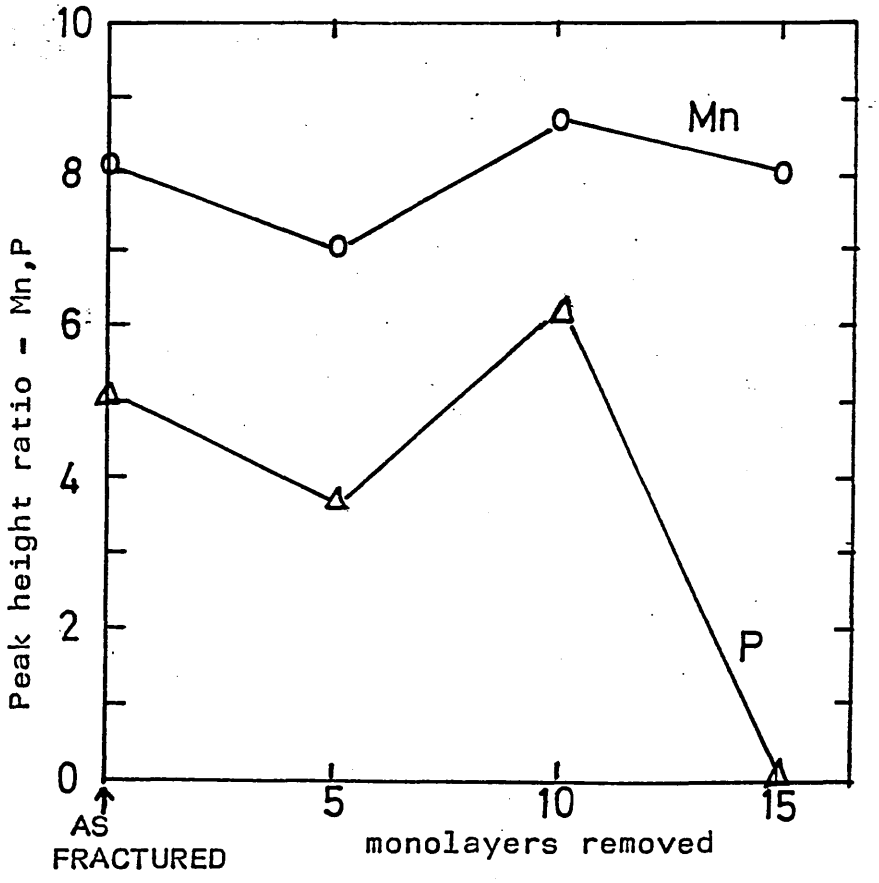

Figure 146 AES sputtering profiles for peak height ratios(% of Fe_{703}eV peak) for alloy 273.

Heat treatment:1h850°C AC +2h600°C WQ
Fracture mode: Ductile Areas

Step Size = 0.25 eV. 3 Scans of 4000 channels at 20 ms per chan

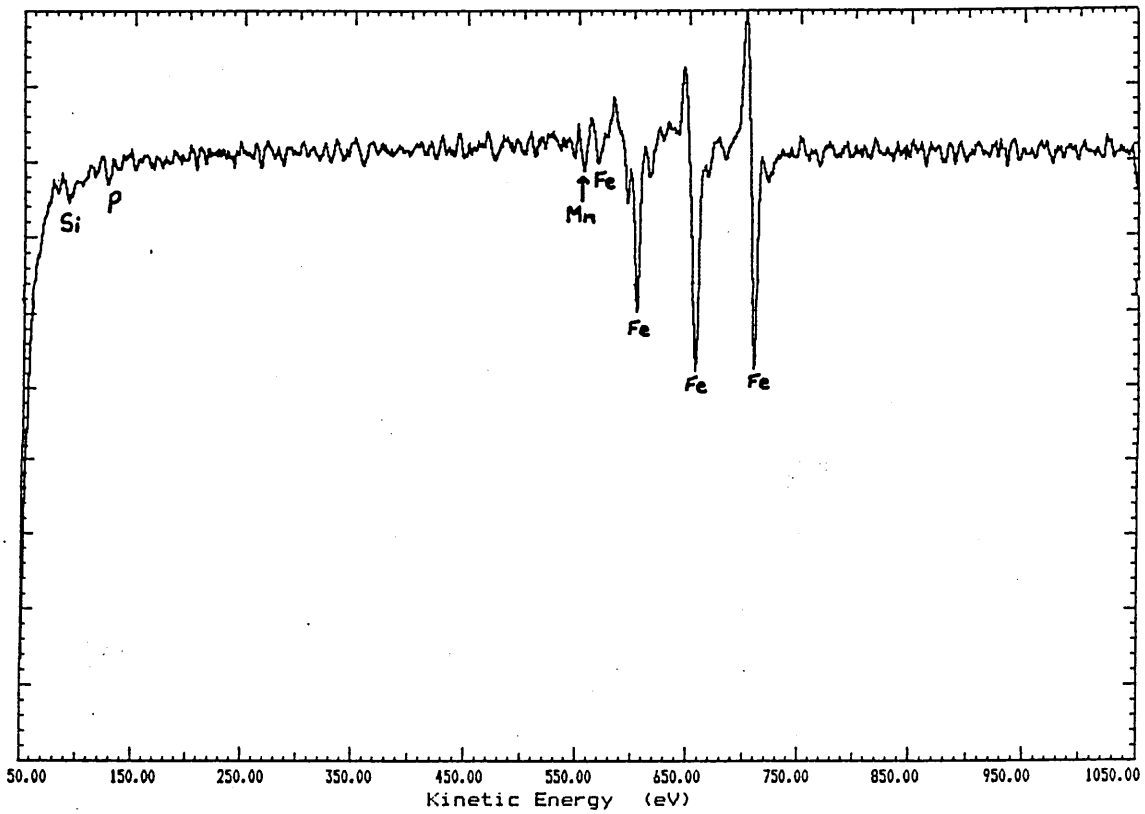

Fig.147 AES spectra for alloy 278,1h.850°C A.C.
Intergranular:AS FRACTURED

AES Retard Ratio = 4 Max Plotted Count Rate = 17433
Step Size = 0.25 eV. 3 Scans of 4000 channels at 20 ms per chan

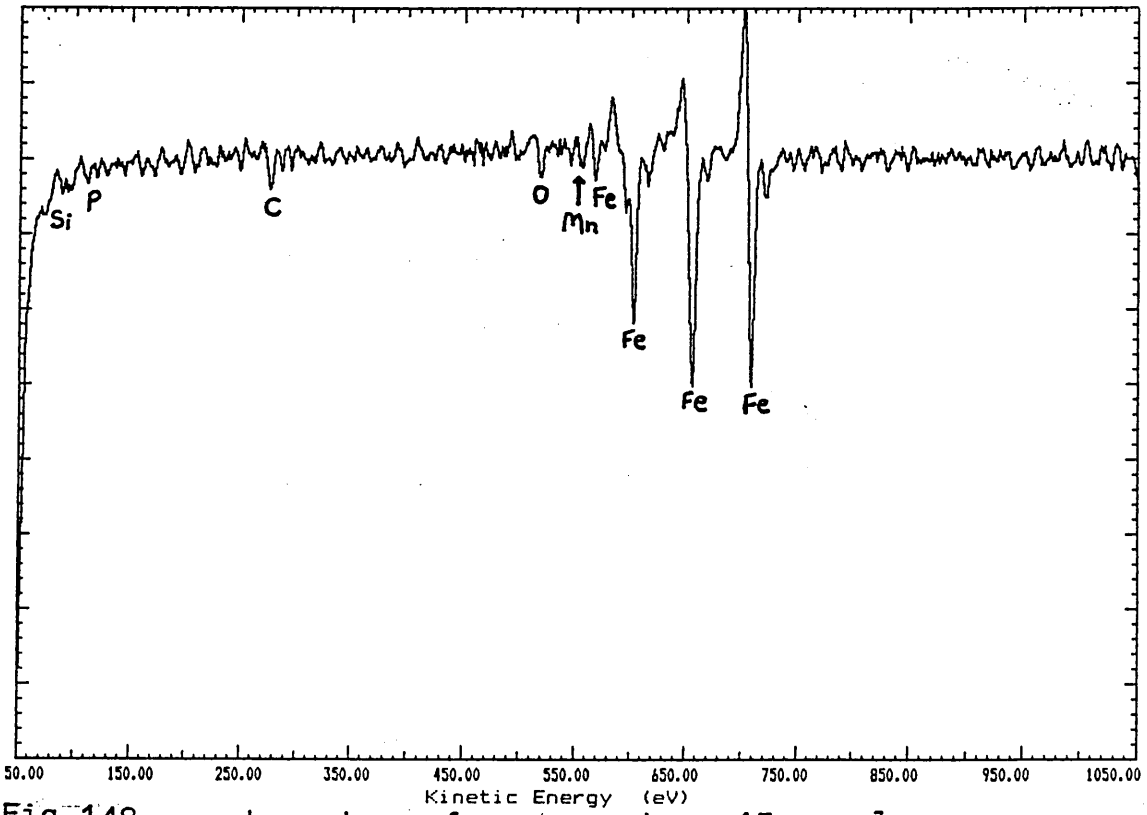

Fig.148 as above but after removing ~ 15 monolayers.

Step Size = 0.25 eV. 3 Scans of 4000 channels at 20 ms per chan

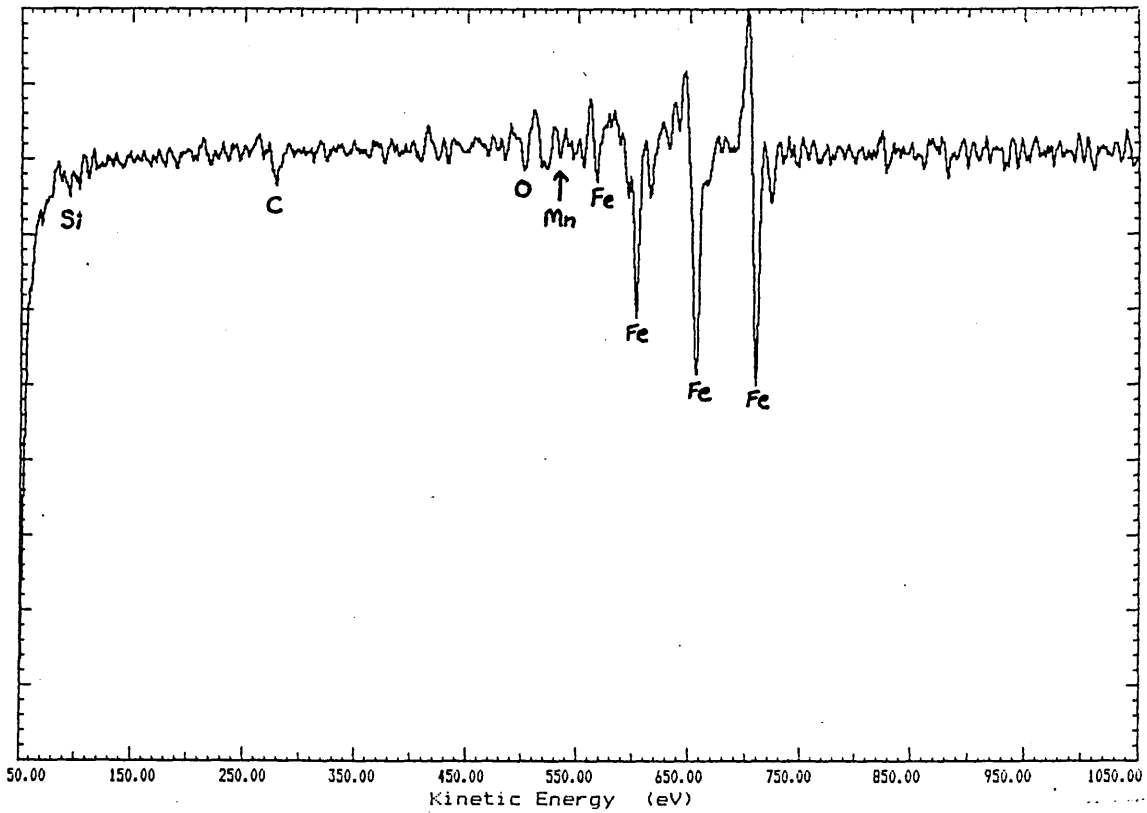

Fig.149 as fig.148 but after removing ~ 30 monolayers.

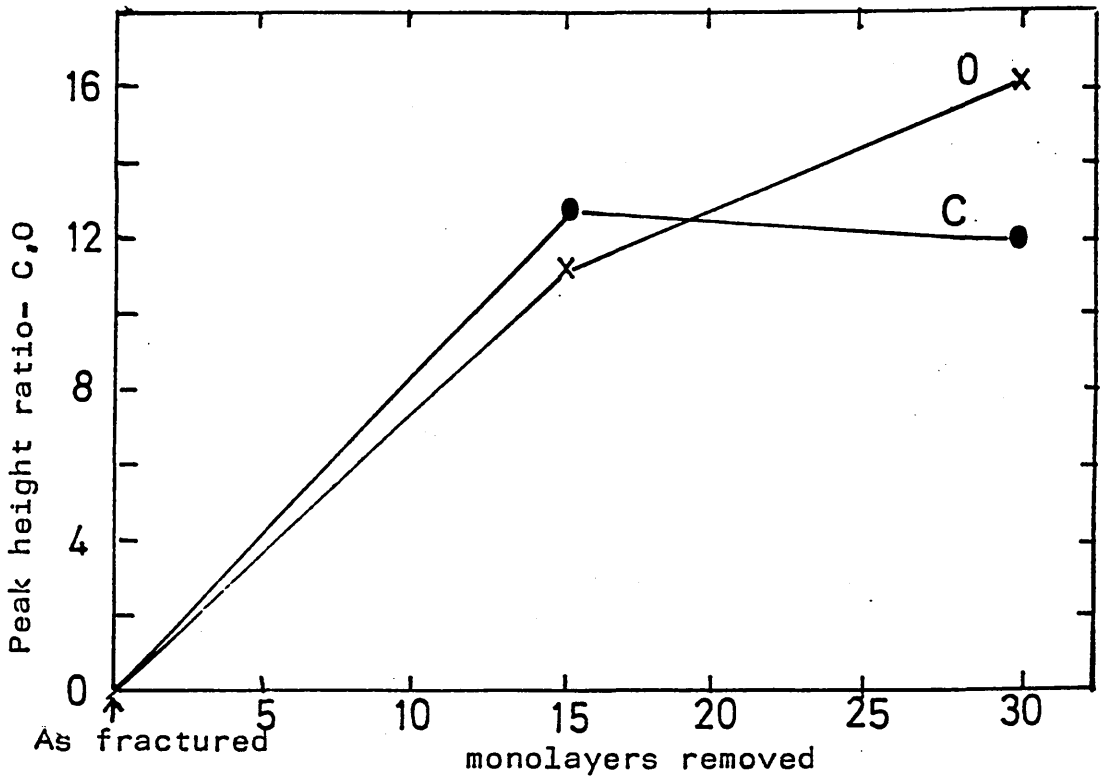

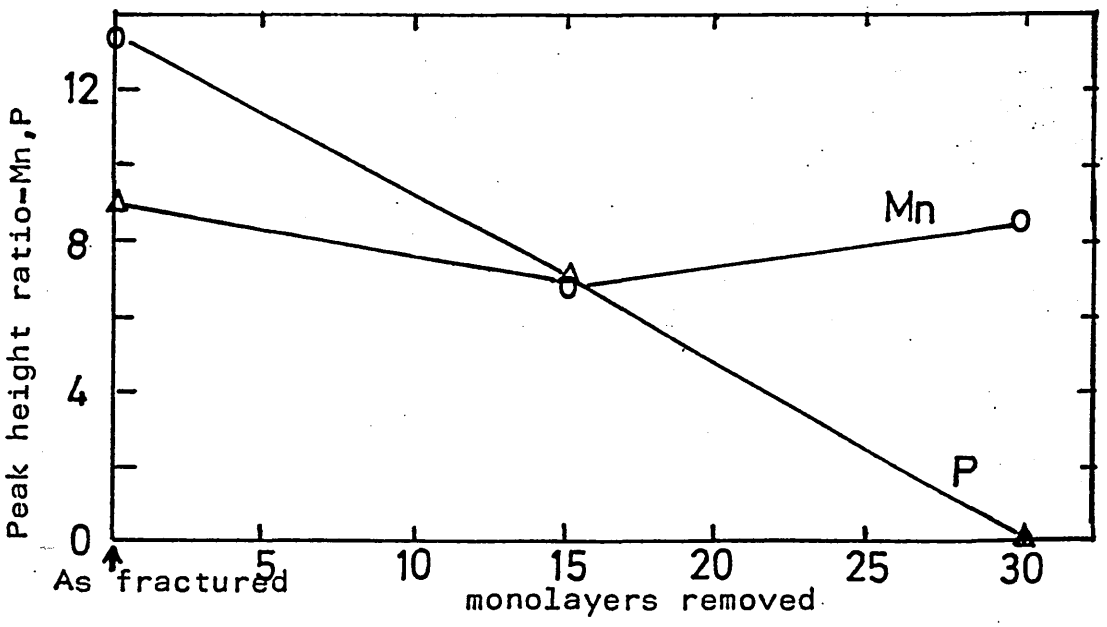

Figure 150 AES sputtering profiles for peak height ratios(%of Fe_{703}eV peak) for alloy 278.

Heat treatment: 1h850°C AC
Fracture mode: Cleavage

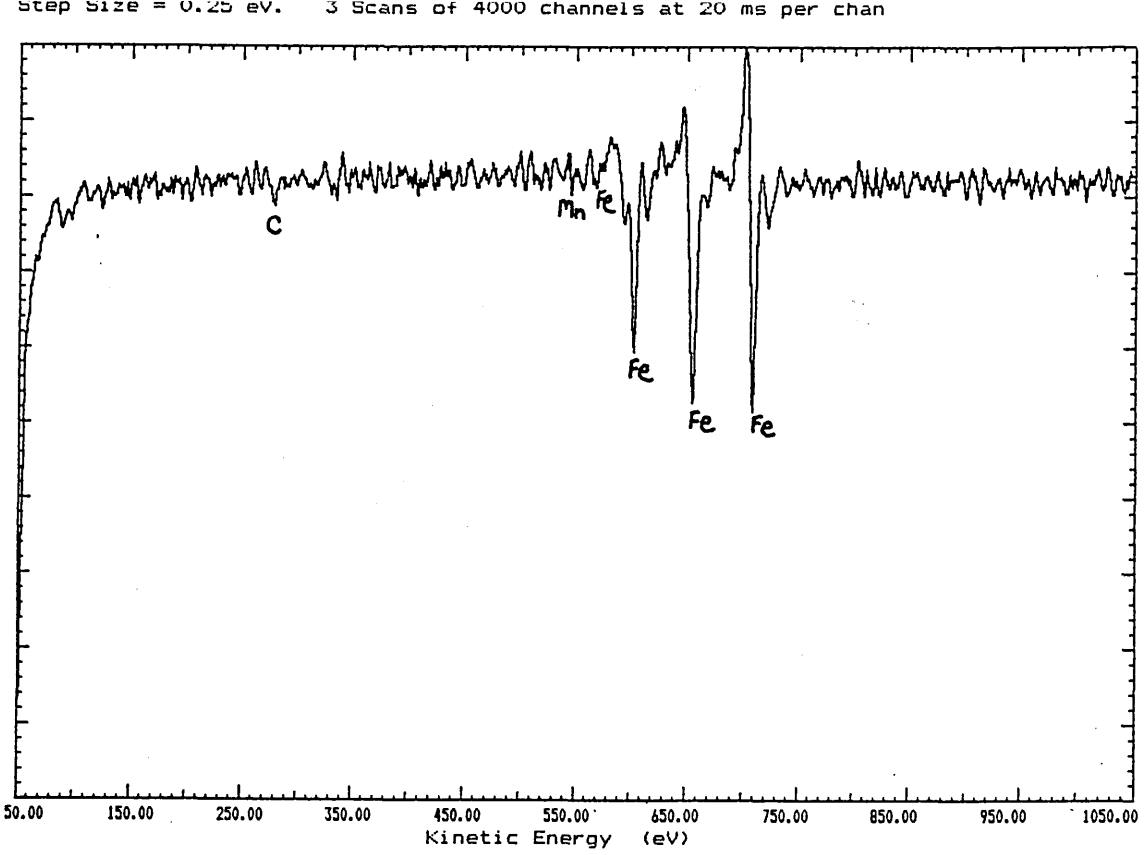

Fig.151 AES spectra for alloy 277, 1h.1160°C IBQ.
Intergranular: AS FRACTURED

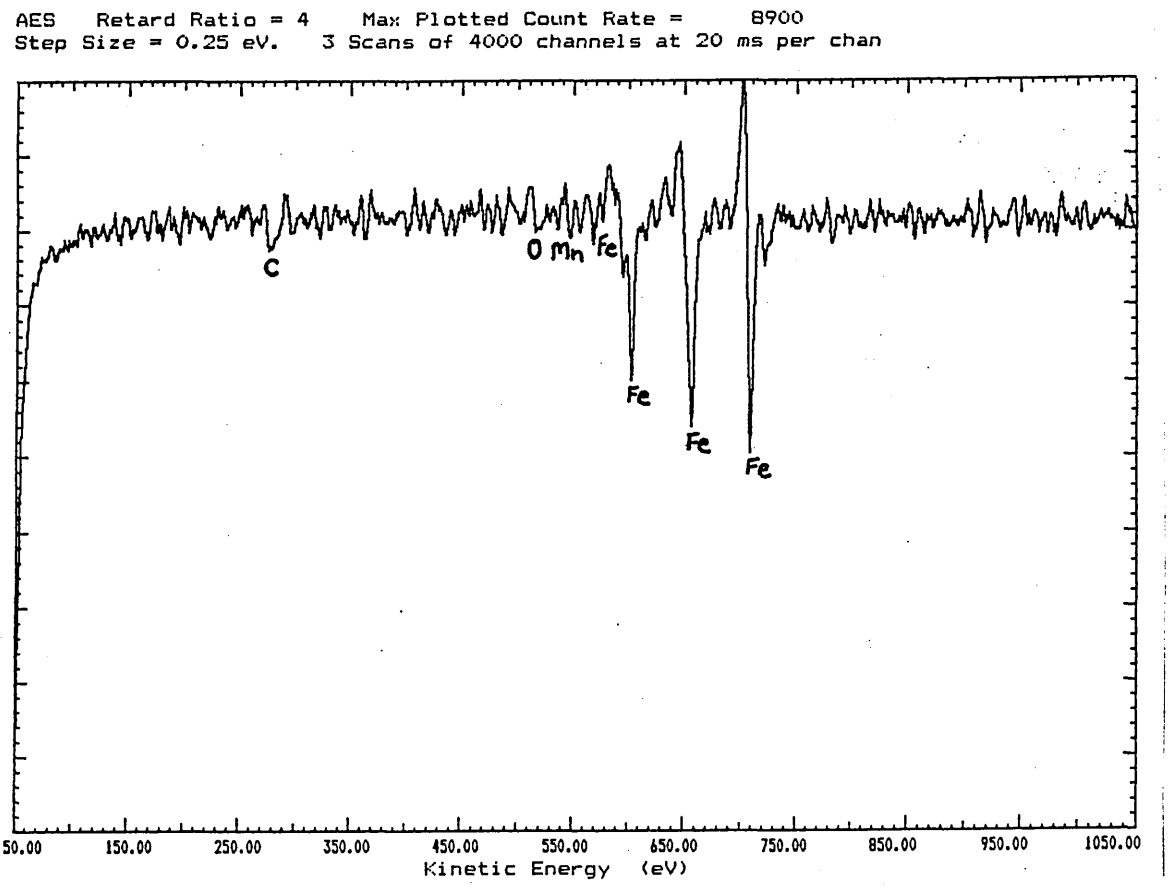

Fig.152 as above but after removal of ~15 monolayers.

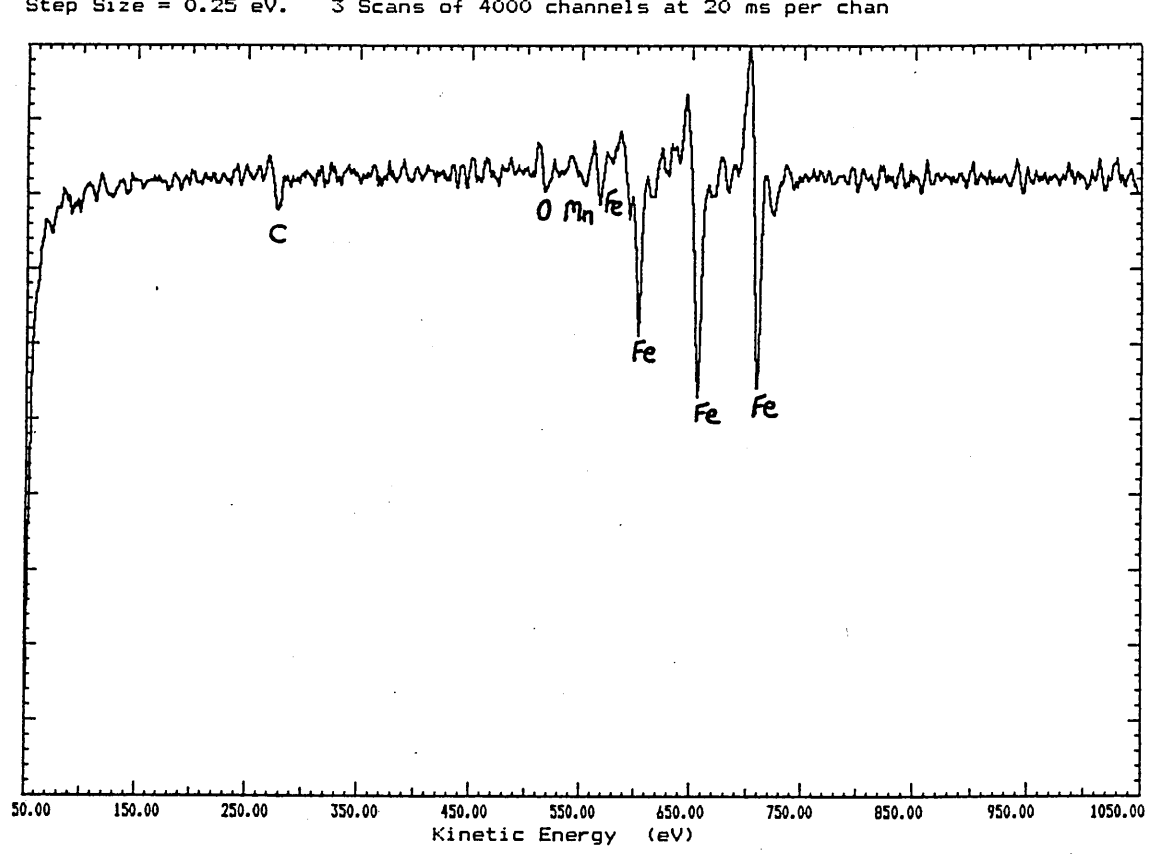

Fig. 153 as fig.152 but after ~30 monolayers removed.

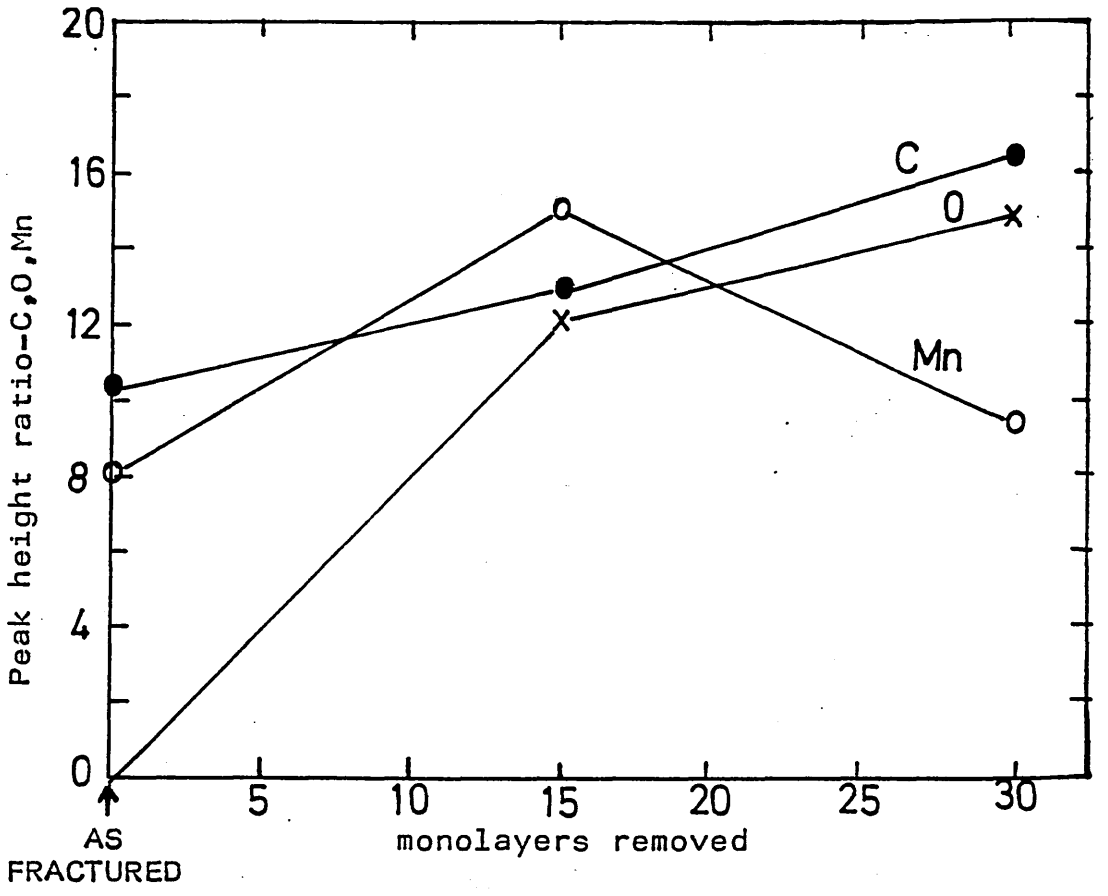

Figure 154 AES Argon-ion sputtering profiles for peak height ratios(%of Fe_{703}eV peak) of alloy 277.
Heat treatment: 1h 1160°C IBQ
Fracture mode: Intergranular

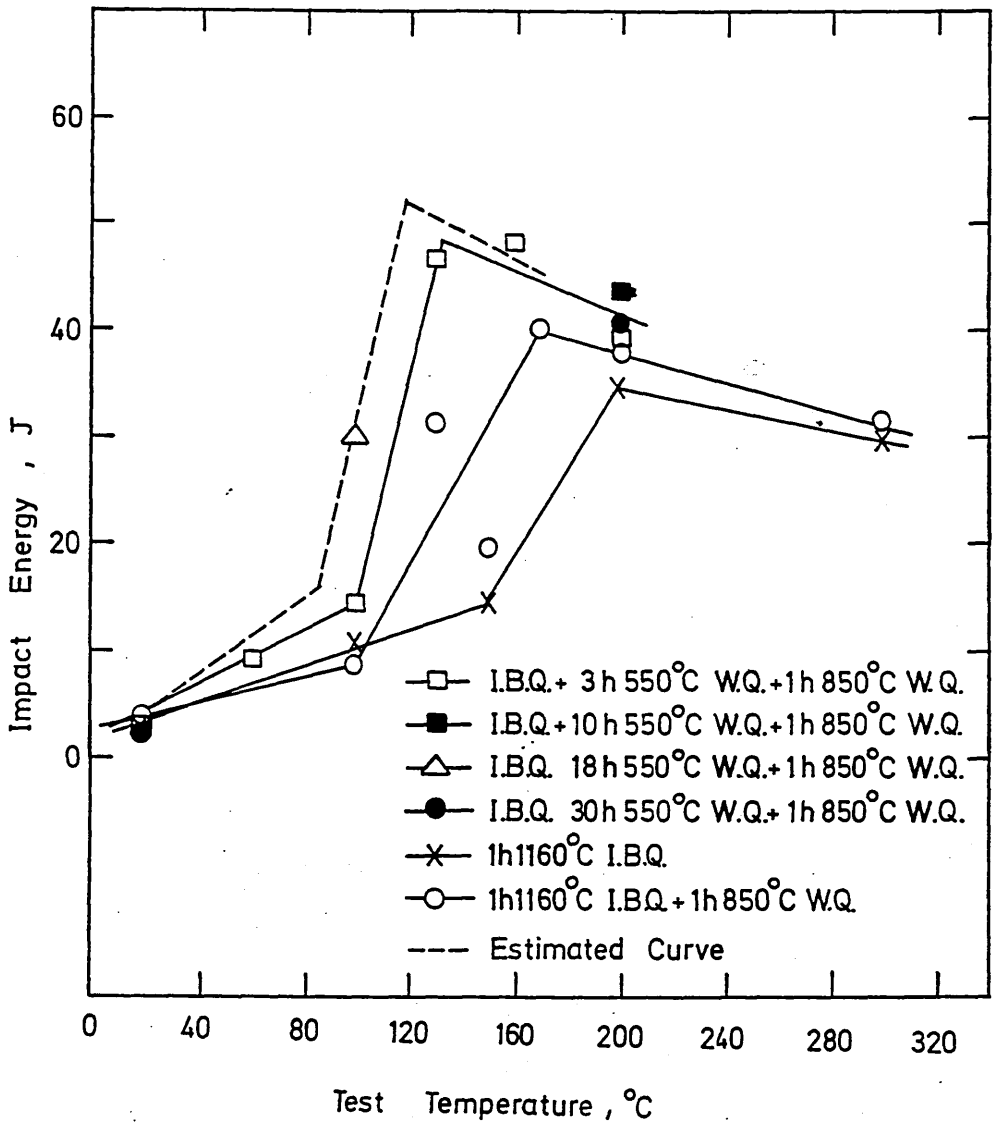

Figure 155 Impact transition curves for alloy 277 in various heat treated conditions.

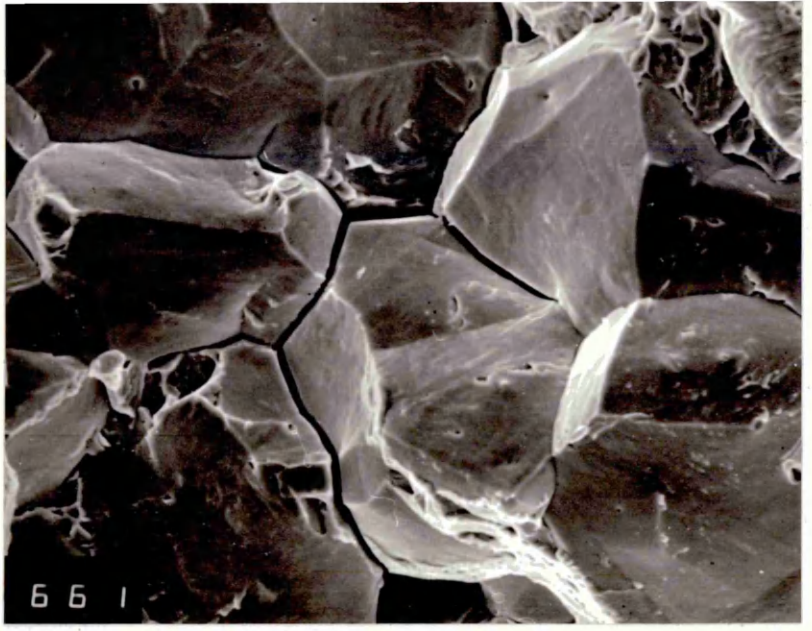

X800

Figure 156 S.E.M. micrograph of alloy 277 in the IBQ condition, tested at room temperature showing intergranular fracture.

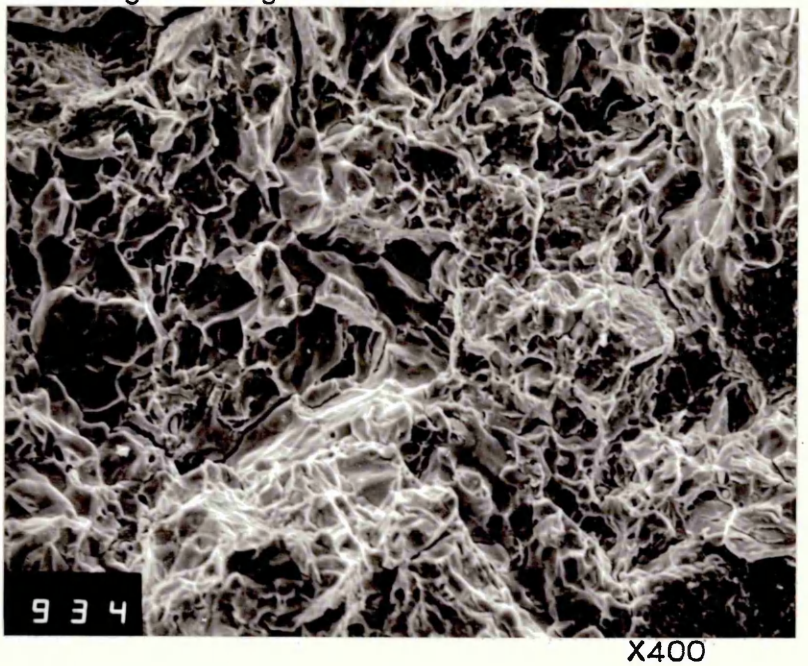

X400

Figure 157 As above but in the IBQ+850WQ condition showing a quasi-cleavage fracture mode.

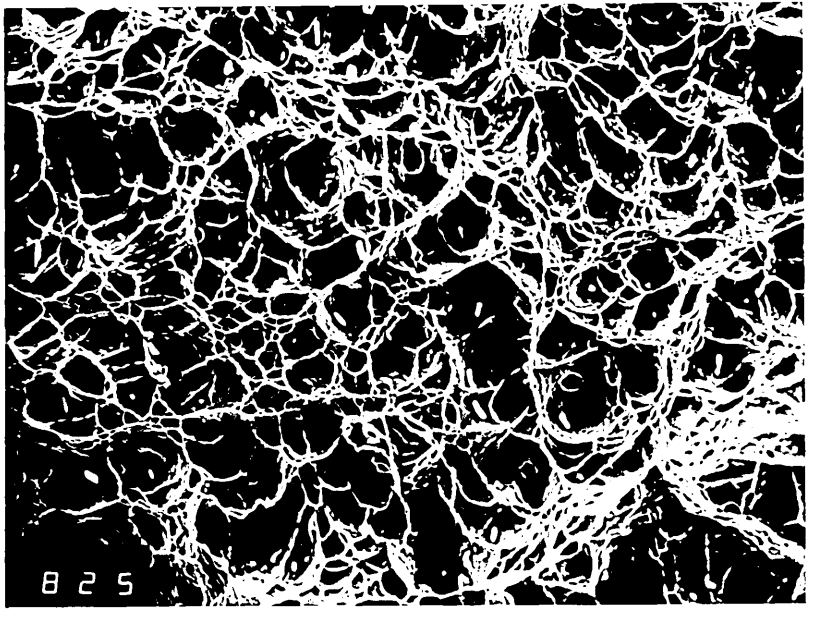

X400

Figure 158 S.E.M. micrograph of alloy 277 in the IBQ condition ,tested at +300°C,showing ductile dimples.

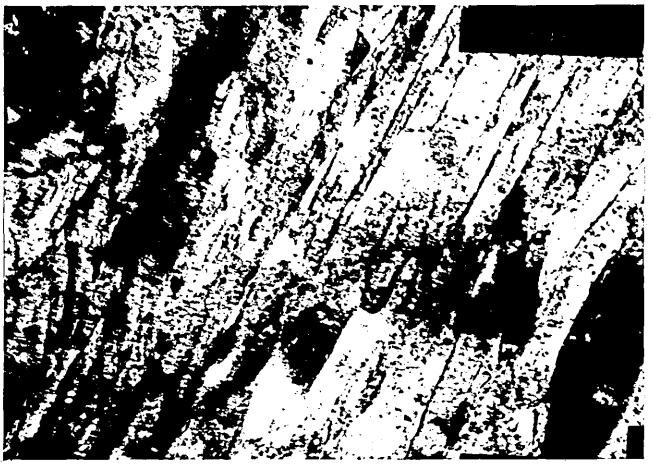

X50K

Figure 159 T.E.M. micrograph of alloy 277 in the IBQ+ 850WQ condition showing the lath martensite structure.

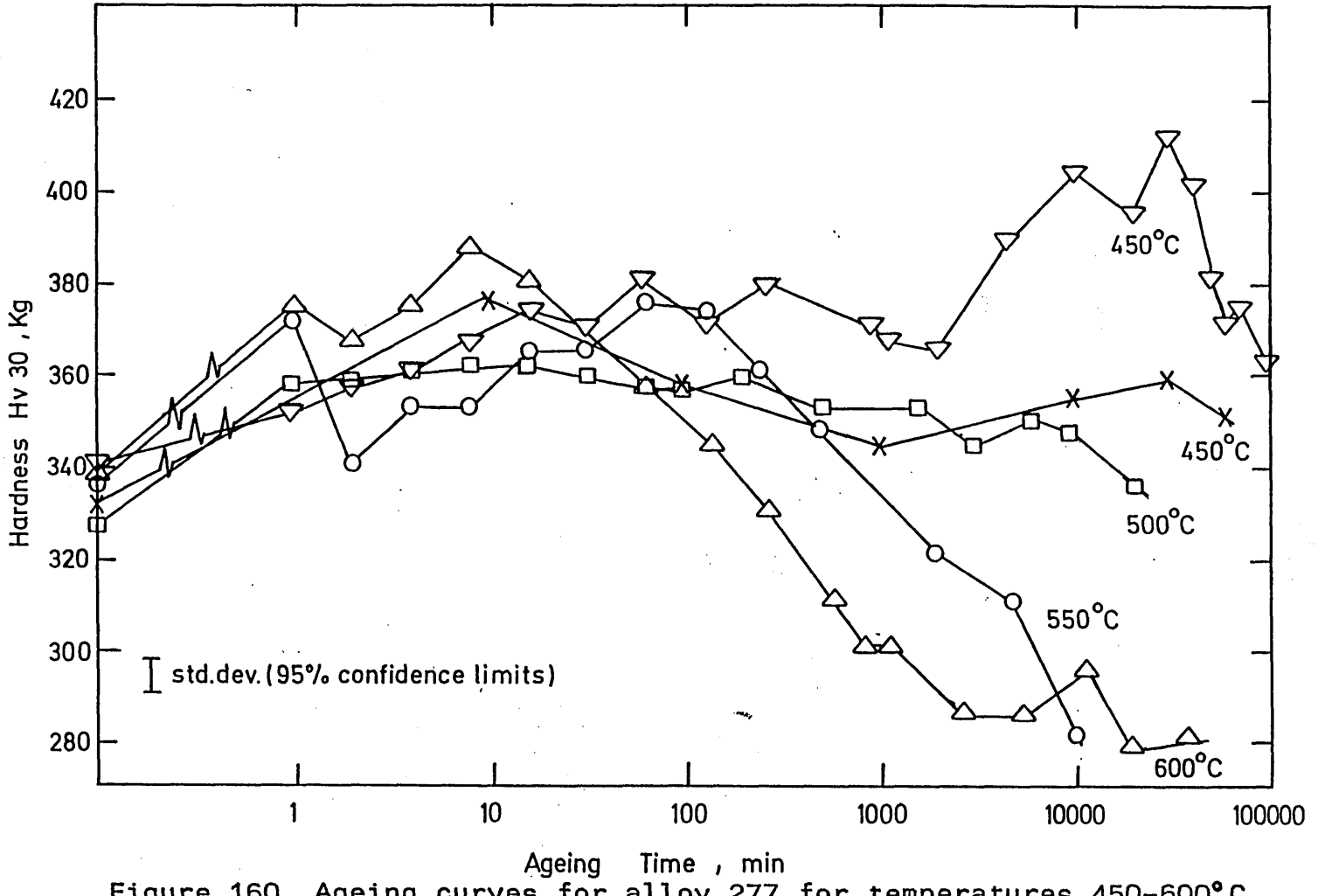

Figure 160 Ageing curves for alloy 277 for temperatures 450-600°C.

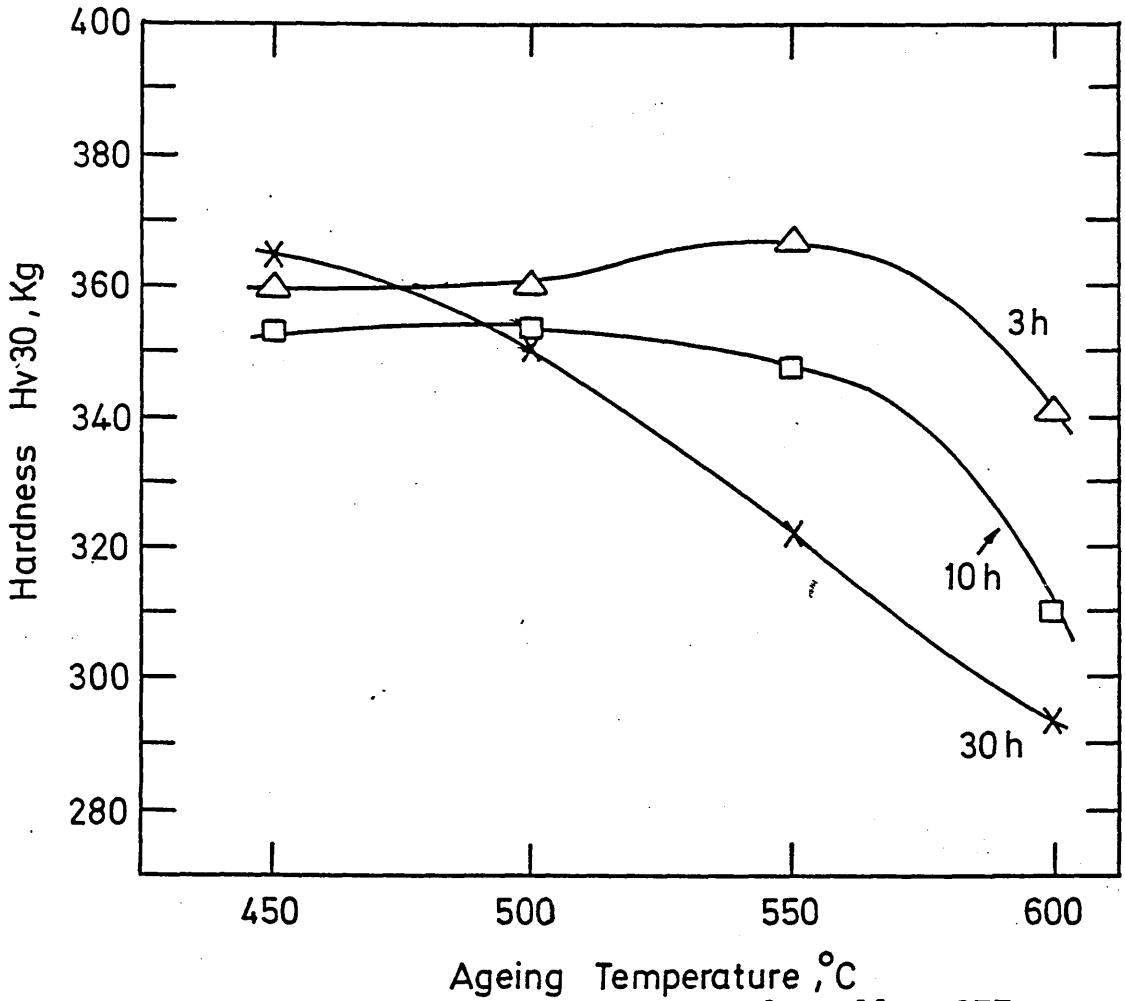

Figure161 Hardness versus ageing time for alloy 277 for 3,10 &30 hours.

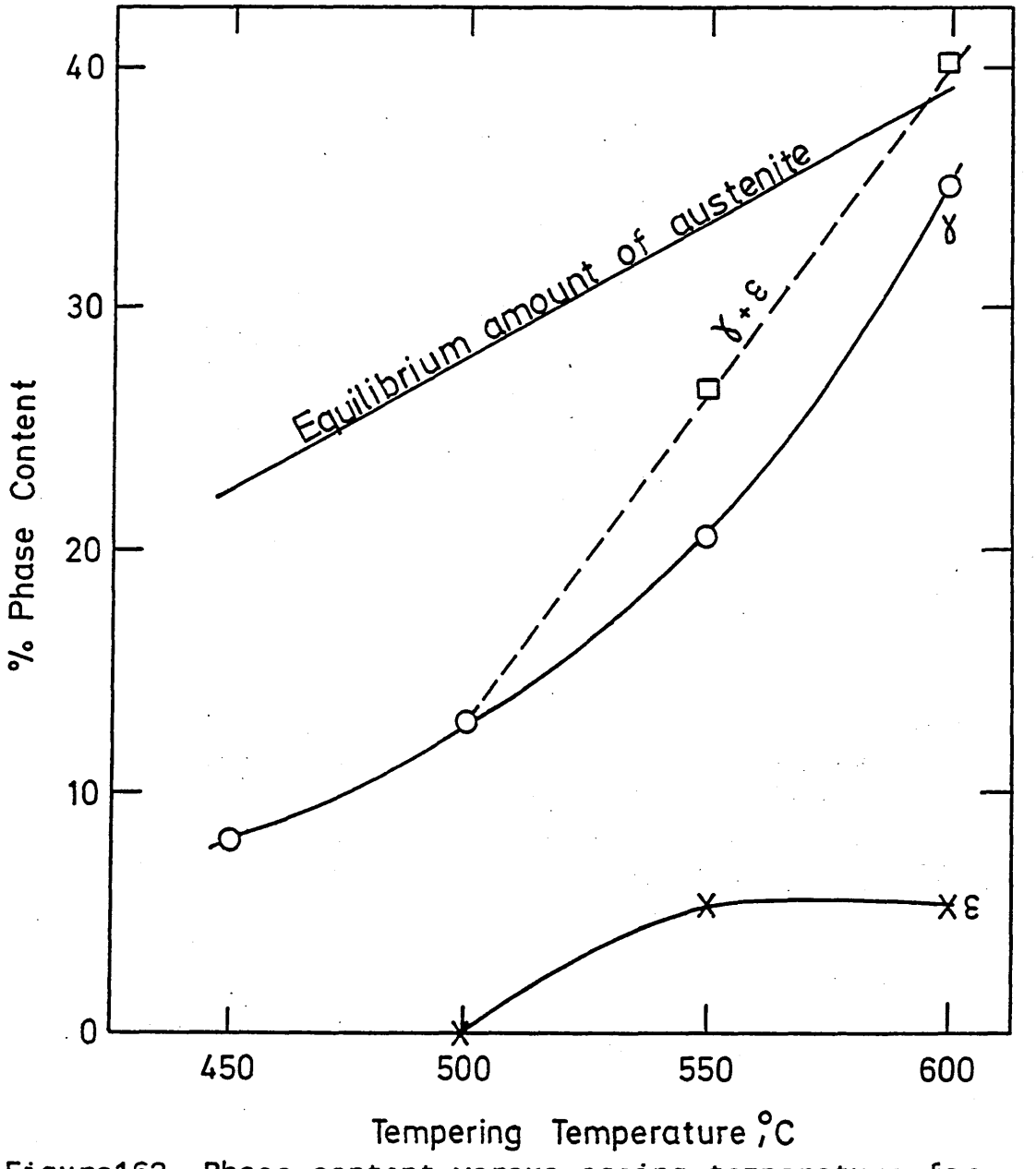

Figure162 Phase content versus ageing temperature for alloy 277.

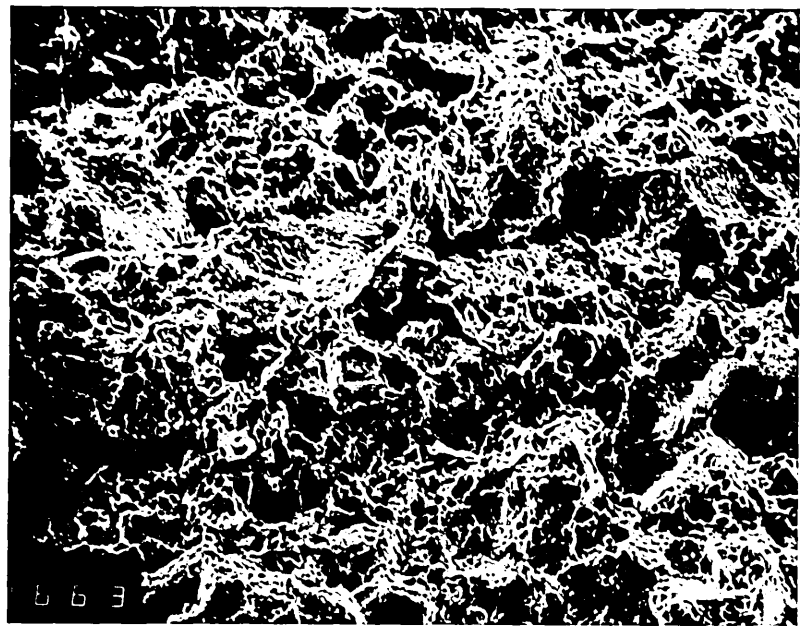

X200

Figure 163 S.E.M. micrograph of alloy 277 in the IBQ+3h550WQ+1h850WQ condition,impact tested at room temperature showing a fine quasi-cleavage fracture.

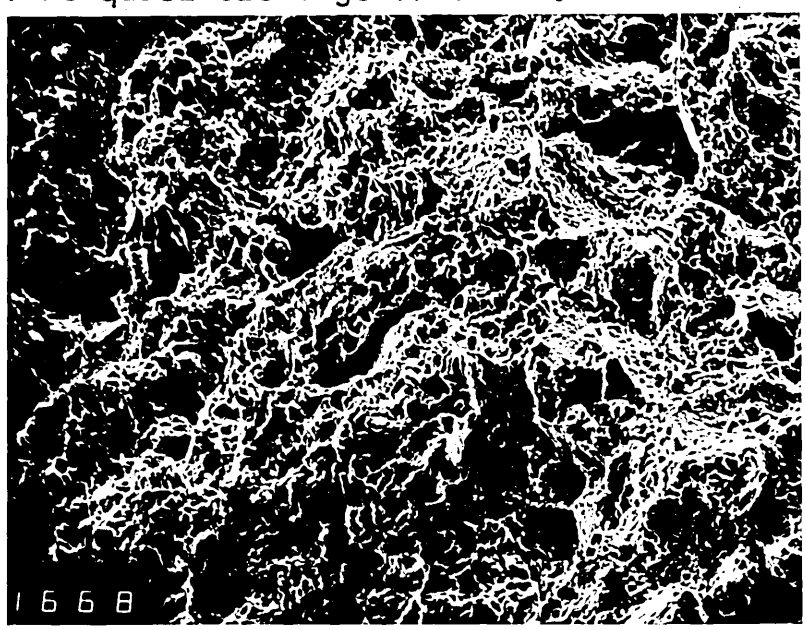

Figure 164 S.E.M. as above but after IBQ+30h550WQ+ 1h850WQ,tested at R.T.and showing fine quasi-cleavage.

X200

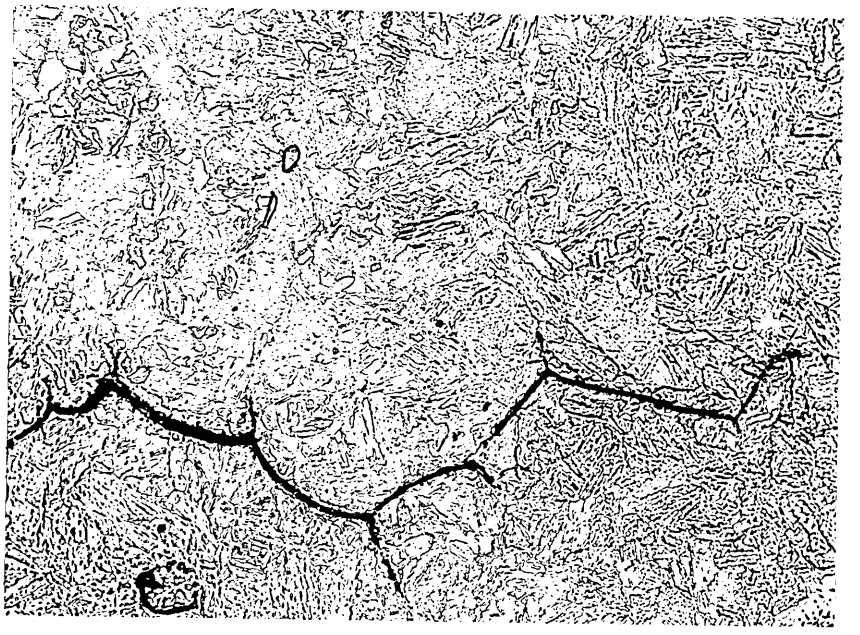

X500

Figure 165 Optical microstructure of alloy 277 in the IBQ+30h550WQ+1h850WQ condition showing quench cracks along prior austenite grain boundaries.

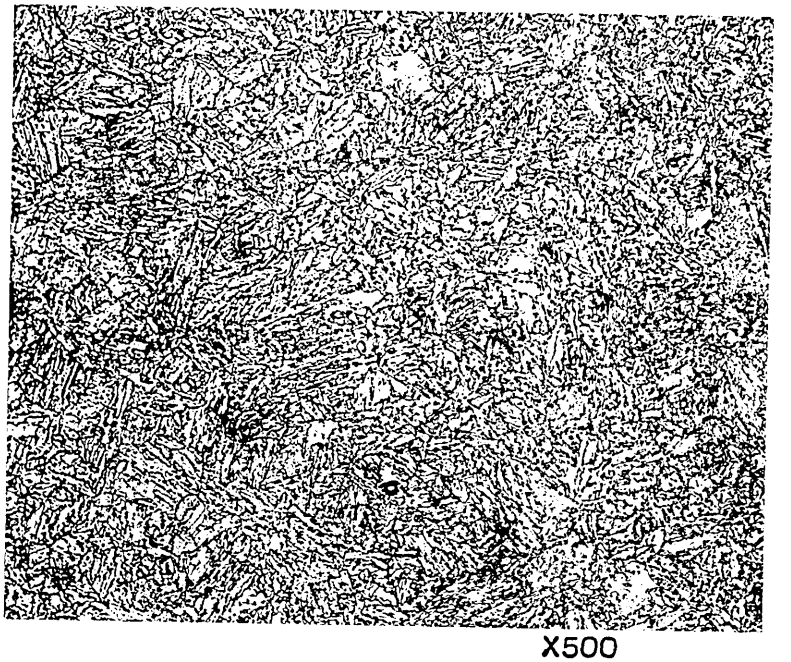

X500

Figure 166 Optical as above but after IBQ+18h550WQ +1h850WQ,showing the fine prior austenite grain size.

X16K

Figure 167 T.E.M. microstructure of alloy 277 after IBQ+3h550WQ+1h850WQ showing the lath structure.

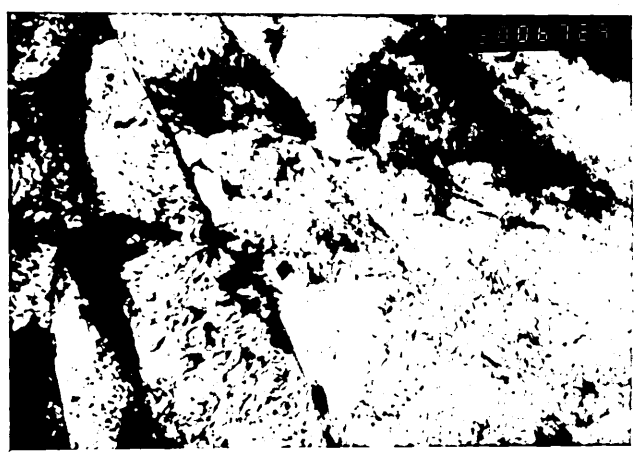

X50K

Figure 168 T.E.M. as above showing grain boundary precipitation of carbides.

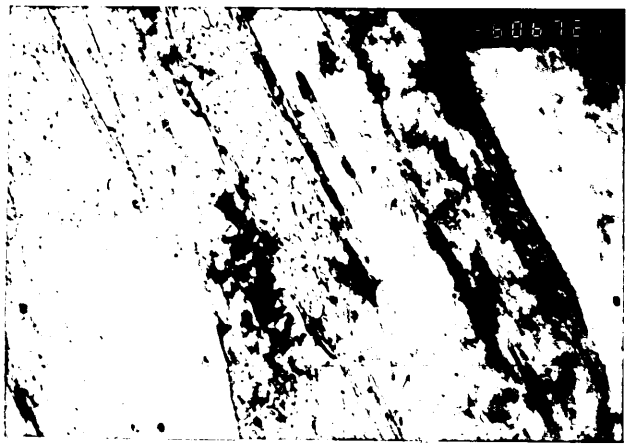

X66K

Figure 169 As fig 168 showing vanadium carbide precipitates.

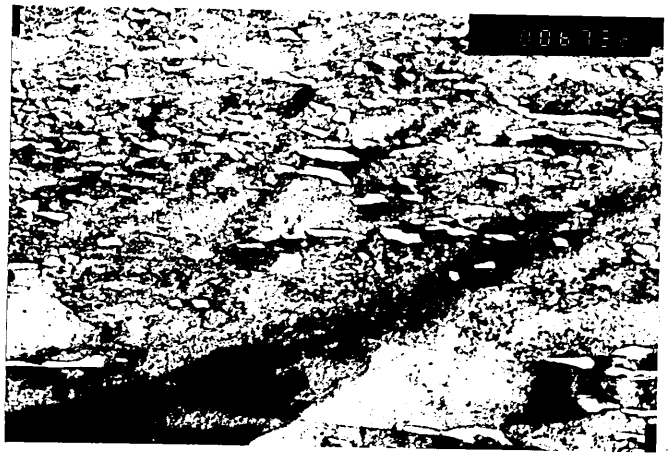

X20K

Figure 170 T.E.M. microstructure of alloy 277 in the IBQ+30h550WQ condition showing reverted austenite.

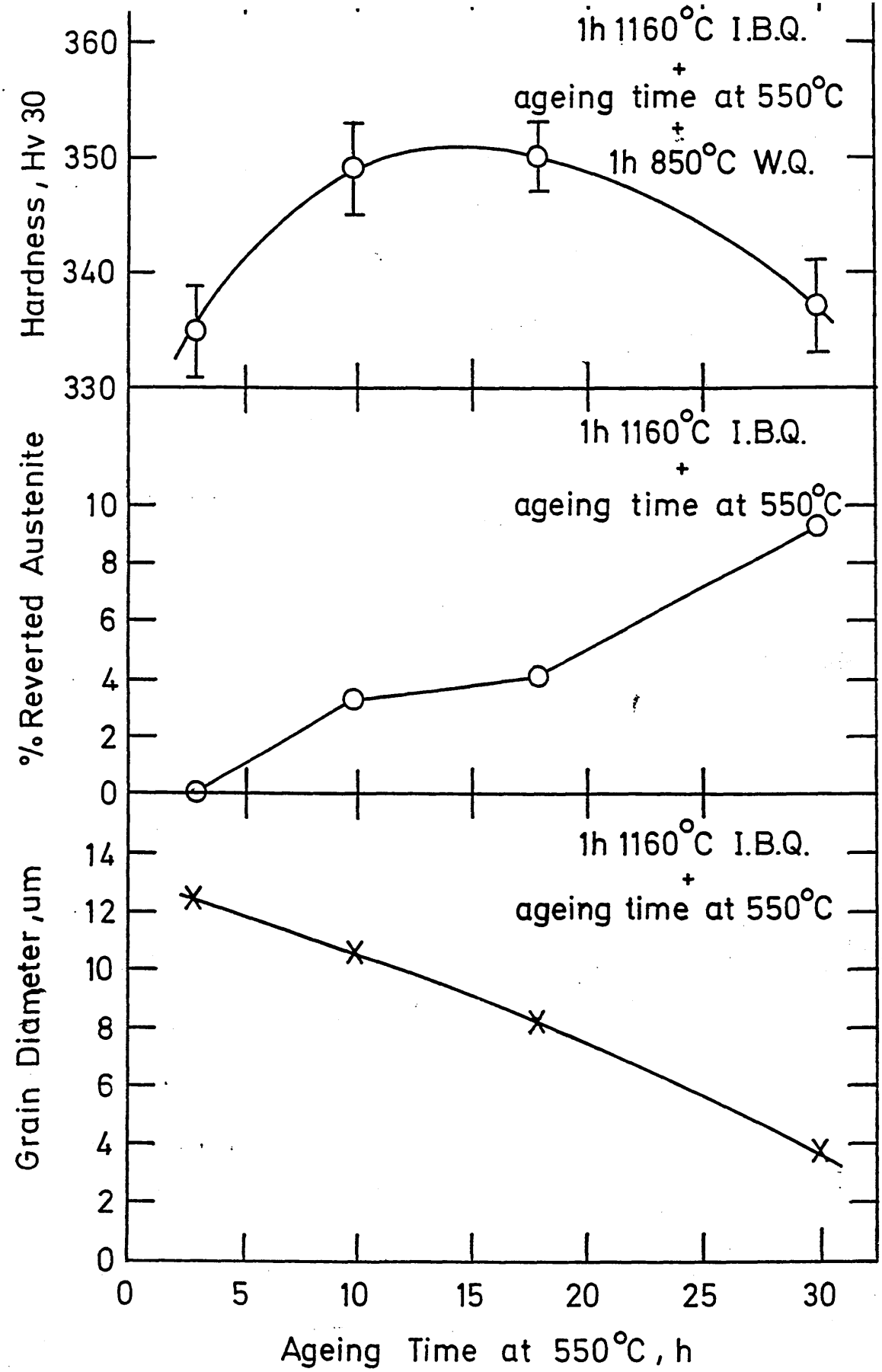

Figure171 The variation of grain size, phase content and hardness with ageing time at 550°C for alloy277.

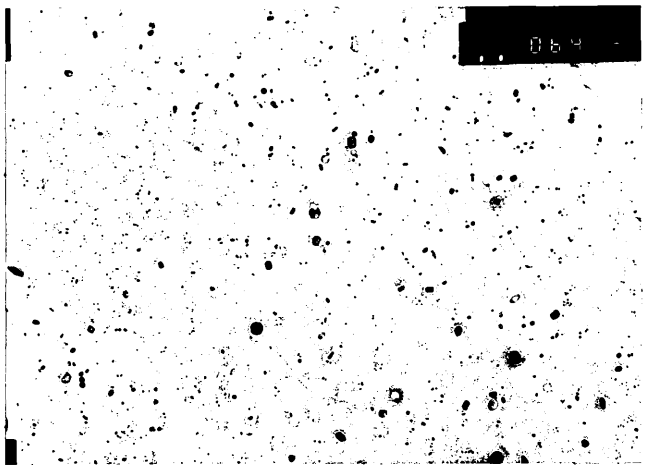

X50K

Figure 172 T.E.M. carbon replica of alloy 277 in the IBQ+3h550WQ+1h850WQ condition showing vanadium carbide precipitation.

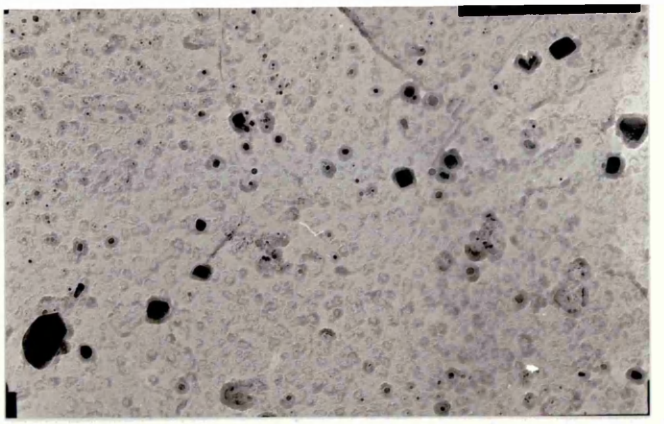

Figure 173(a) X26K

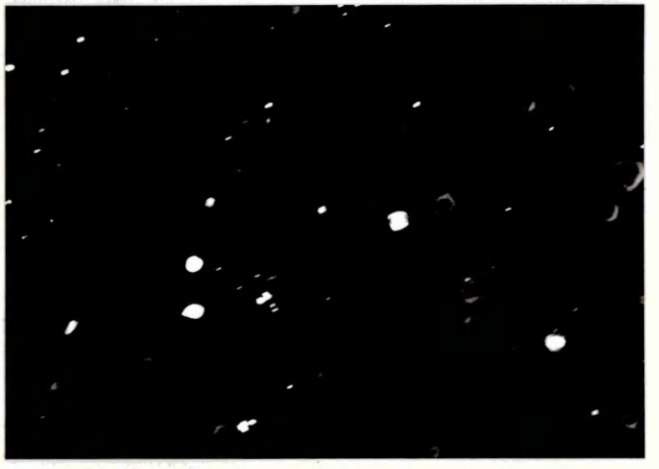

Figure 173(b) Dark field-V_4C_3 X26K

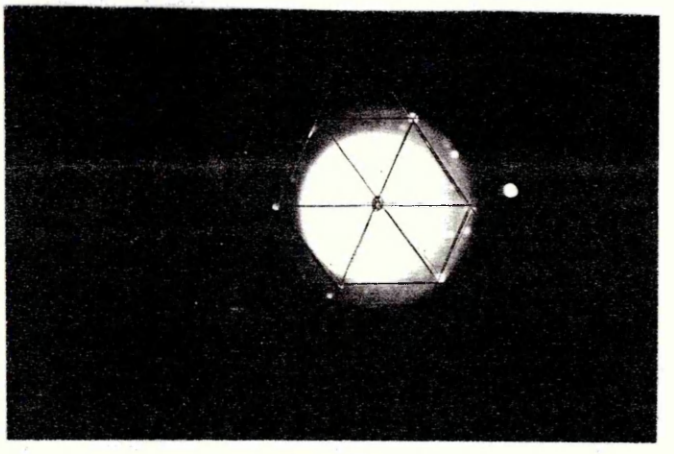

Figure 173(c) $\langle 111 \rangle V_4C_3$

Above show bright and dark field vanadium carbide for alloy 277,with the corresponding diffraction pattern, after IBQ+3h550WQ+1h850WQ.

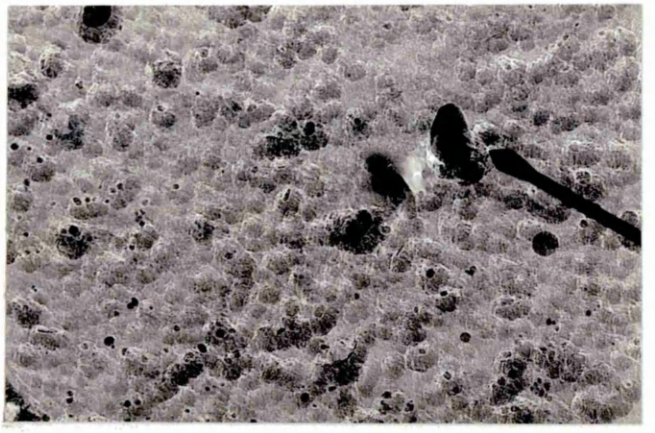

Figure 174(a) carbon replica X75K

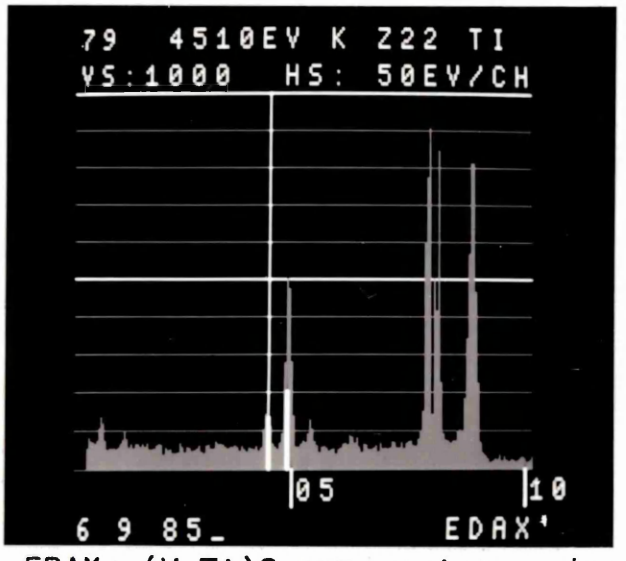

Figure 174(b) EDAX (V,Ti)C ppt.-pointer above

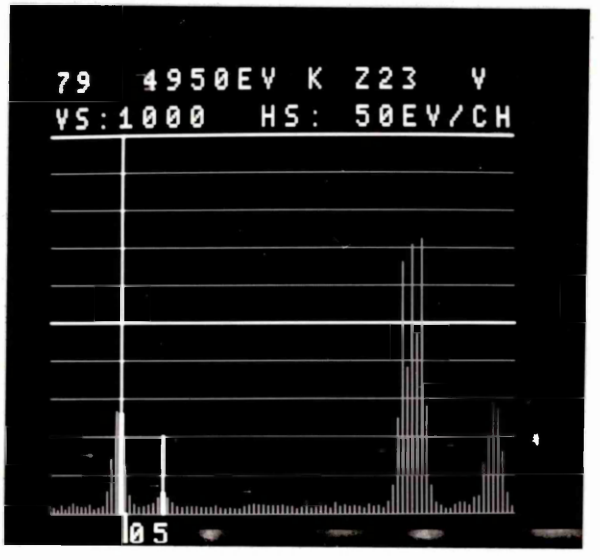

Figure 174(c) EDAX vanadium carbide ppt.

Above are T.E.M. carbon replica and corresponding EDAX spectra for alloy 277 after IBQ+3h550WQ+1h850WQ.

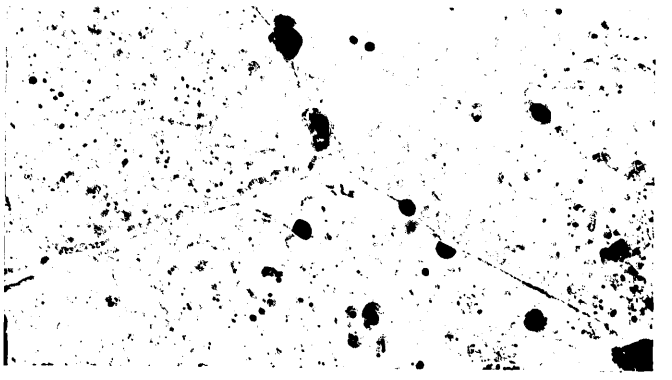

X33K

Figure 175 T.E.M.carbon replica for alloy 277 after IBQ+10h550WQ+1h850WQ,showing ppt's along the grain boundaries.

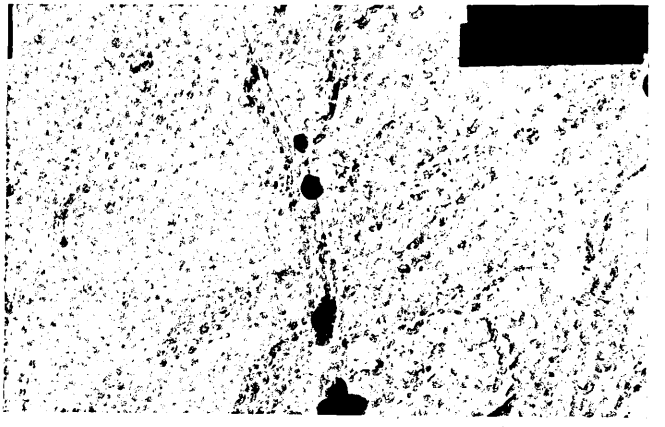

X26K

Figure 176 As above but after 18h@550°C +850WQ

Figure 177 As above but after 30h@550°C+850WQ

X66K

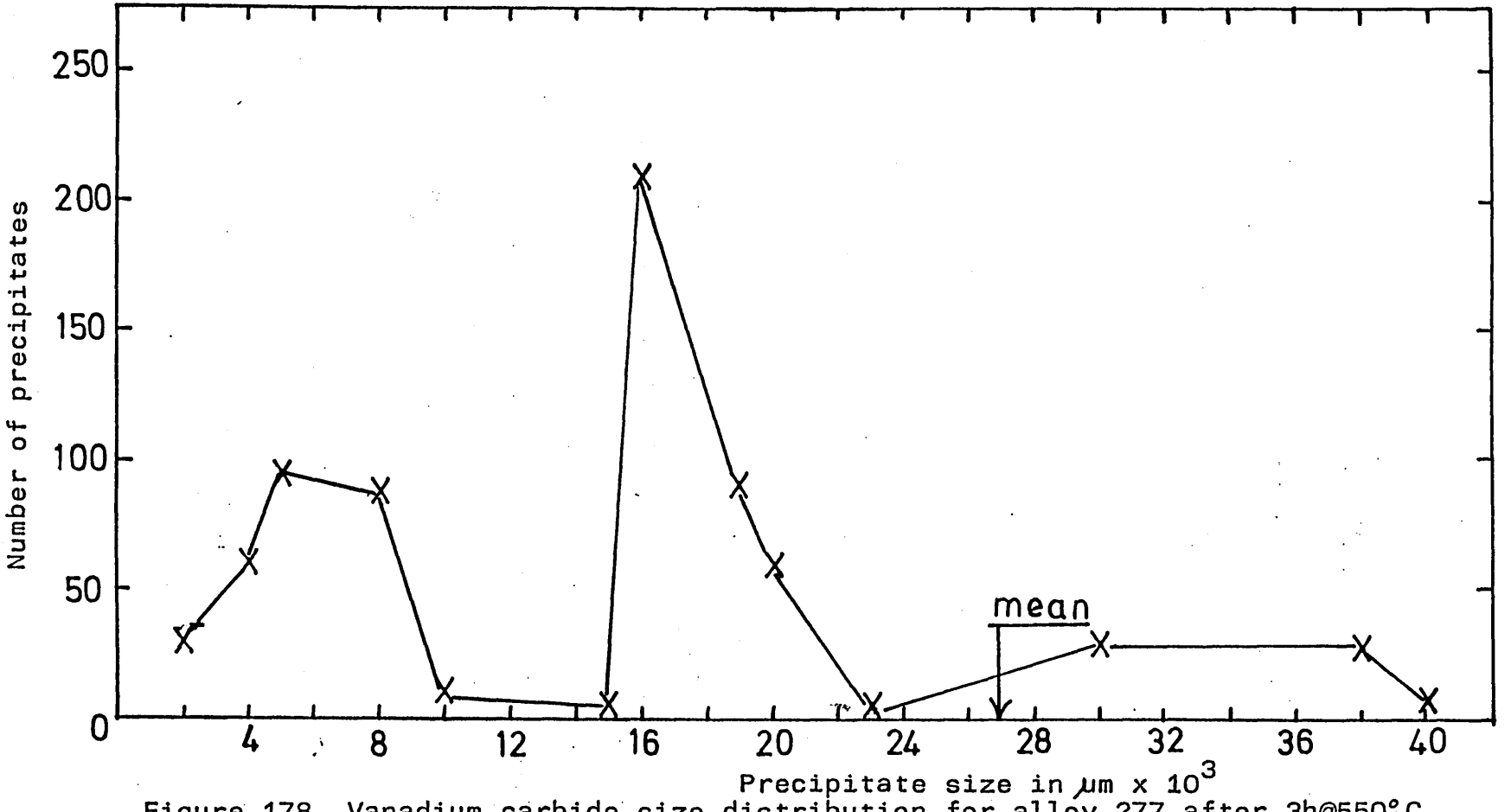

Figure 178 Vanadium carbide size distribution for alloy 277 after 3h@550°C.

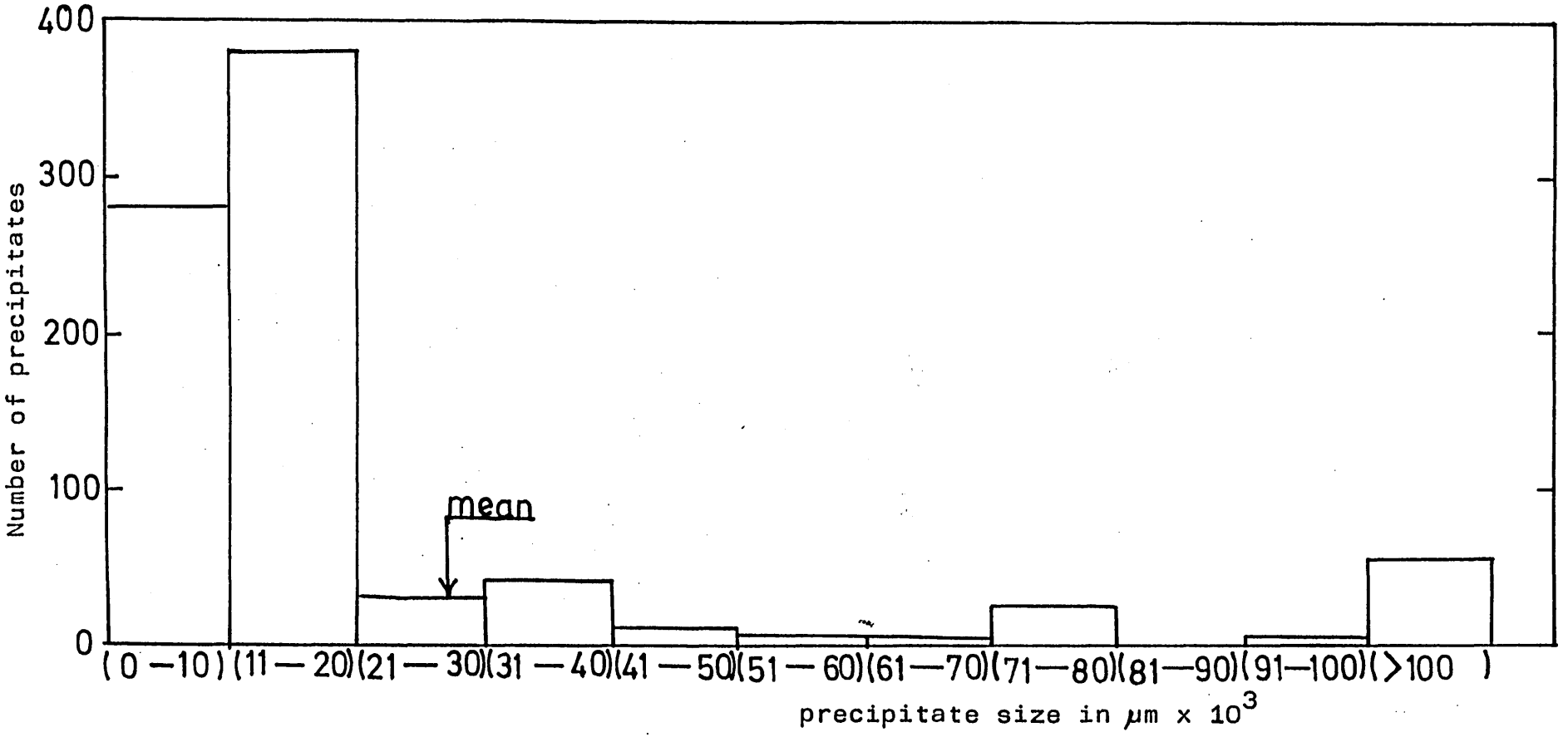

Figure 179 Histogram of vanadium carbide size distribution for alloy 277 after 3h@550°C.

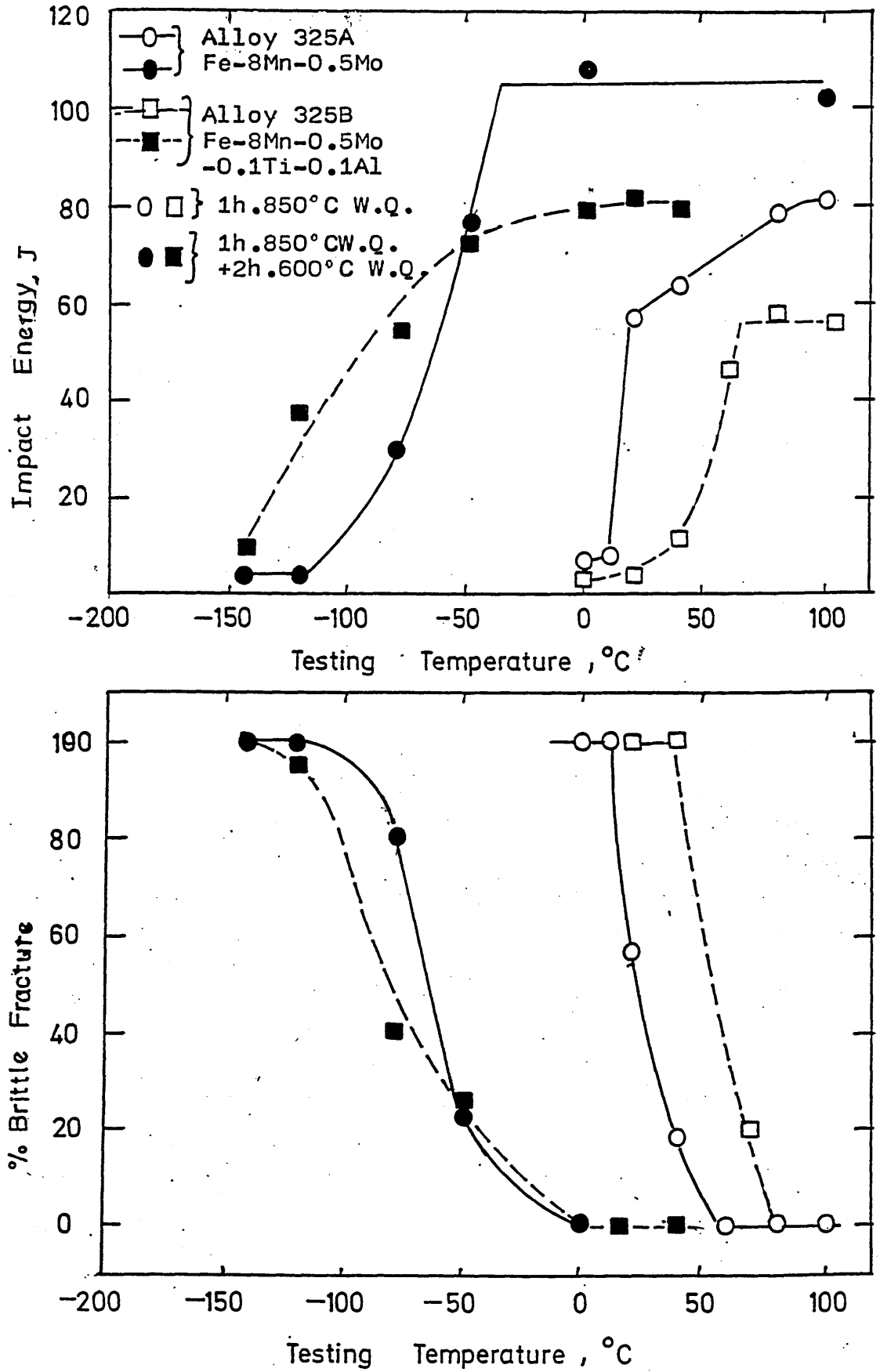

Figure 180- Impact transition curves and DBTT curves for alloys 325A&B of commercial purity.

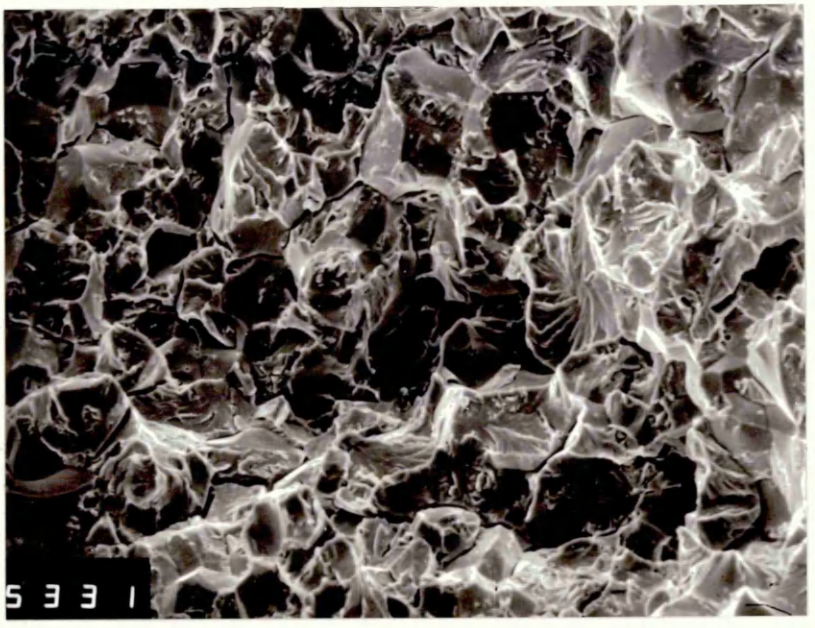

X400

Figure 181 S.E.M. micrograph of alloy 325B in the 1h850WQ condition on a R.T. charpy, showing a mixture of cleavage and intergranular fracture mode.

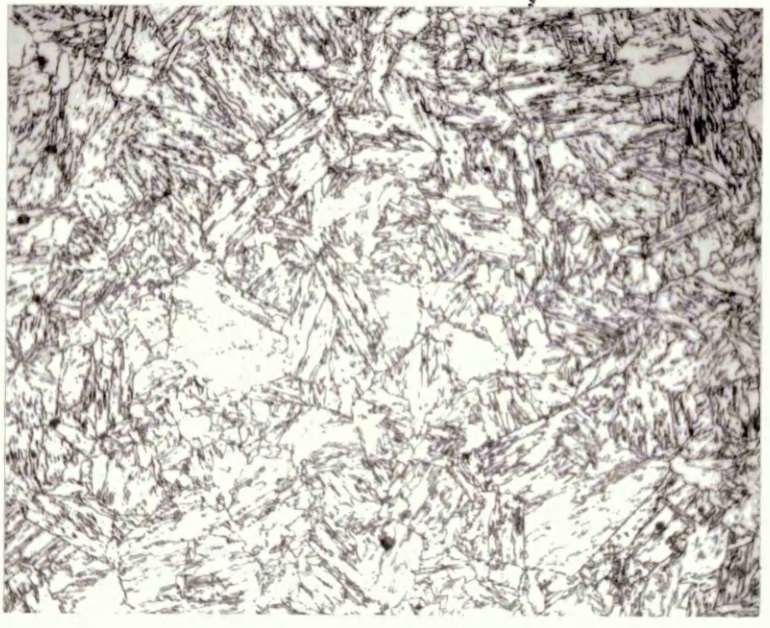

Figure 182 Optical microstructure of alloy 325B in the 1h850WQ+2h600WQ condition.

X500

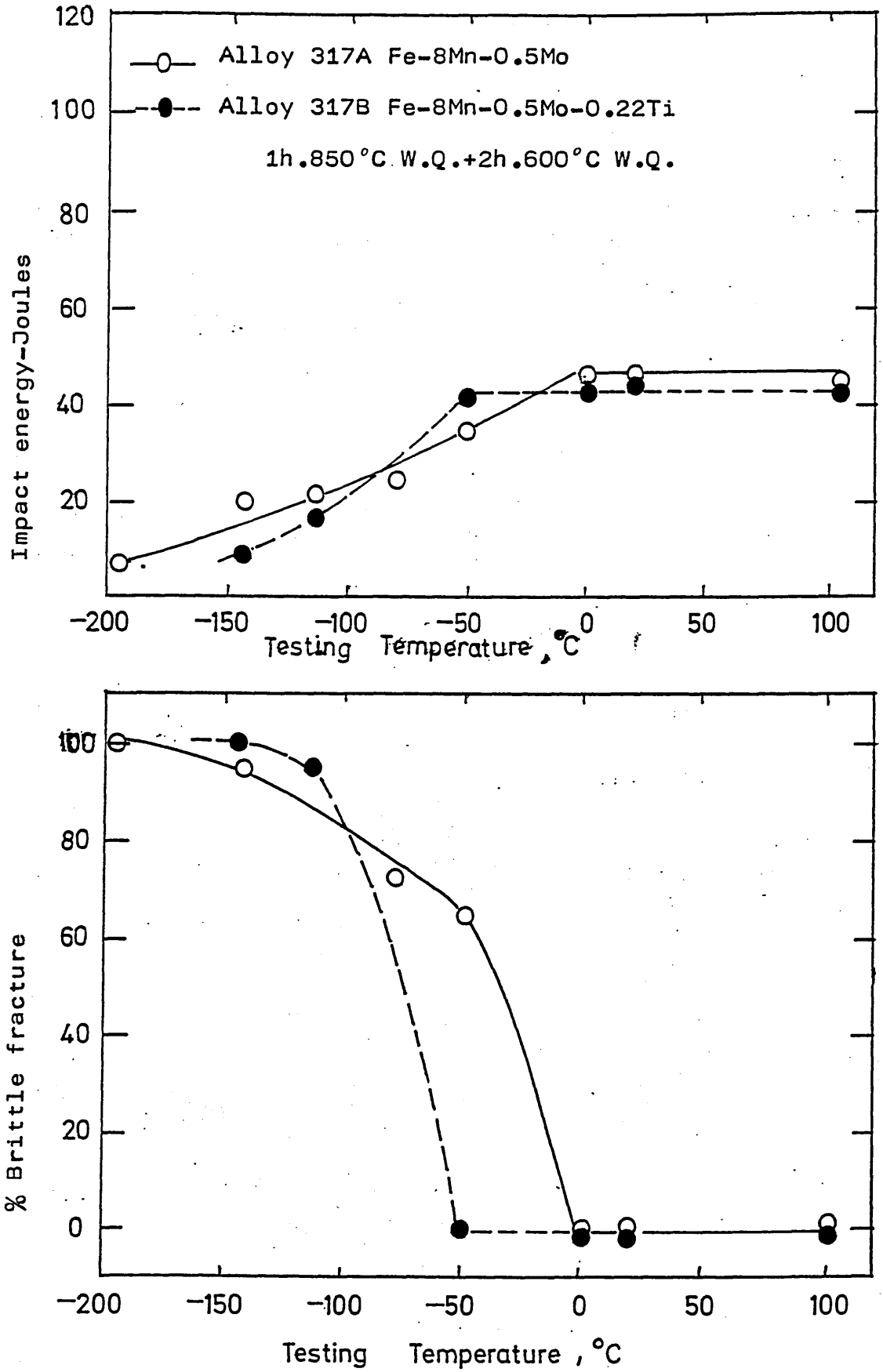

Figure 183 Impact transition and DBTT curves for alloys 317A and 317B of commercial purity; optimum heat treatment.

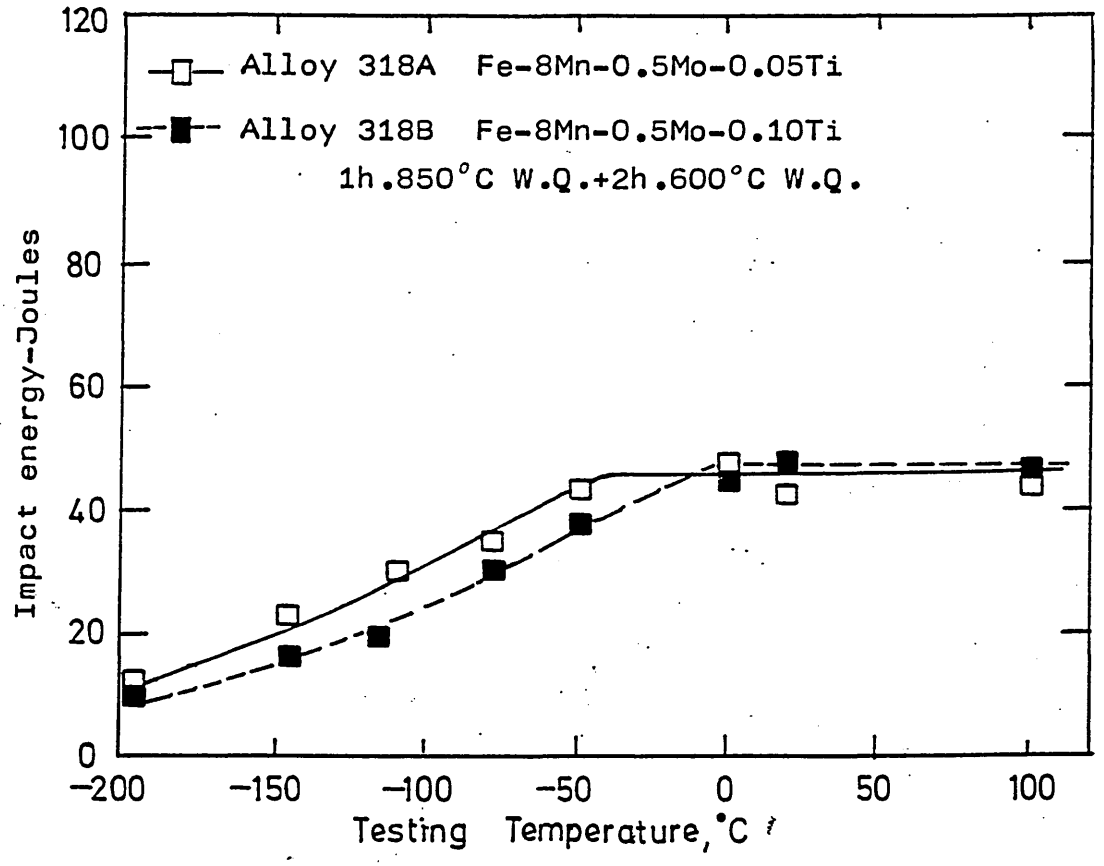

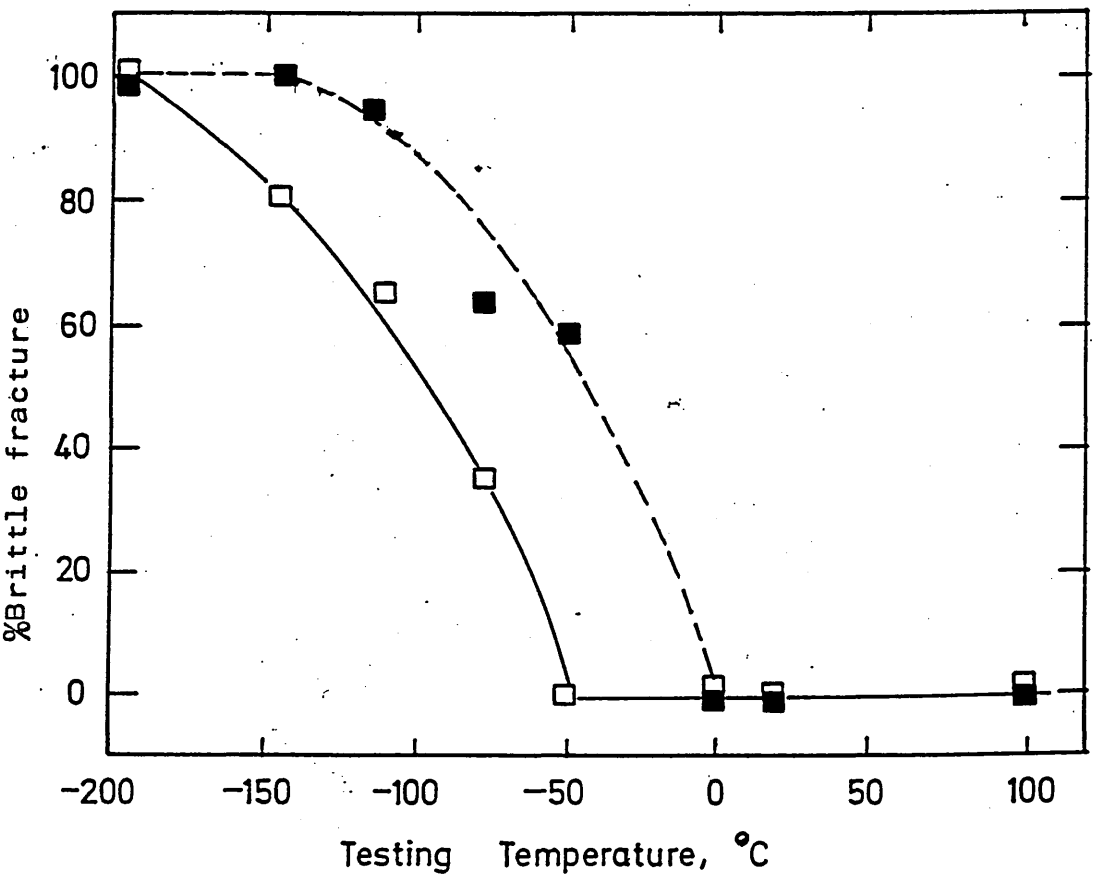

Figure 184 Impact transition and DBTT curves for alloys 318A and 318B of commercial purity; optimum heat treatment.

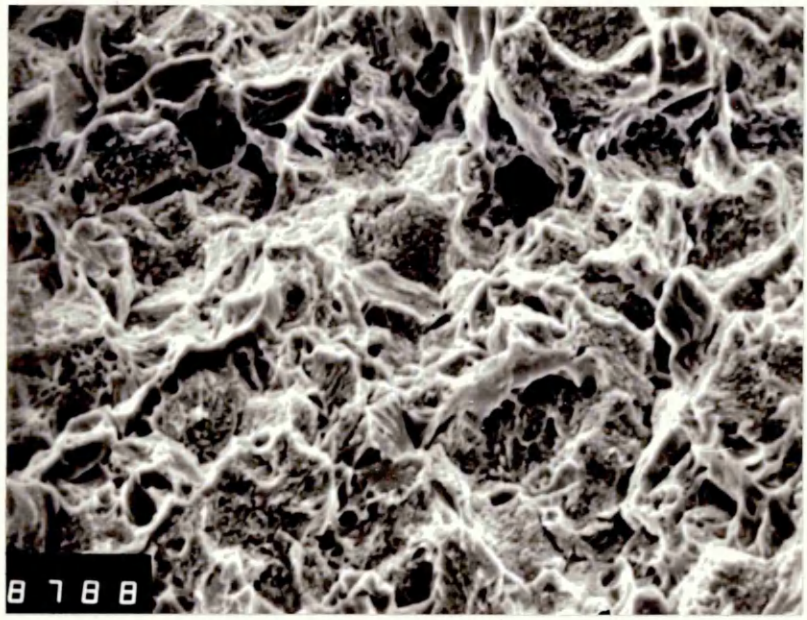

X800

Figure 185 S.E.M. micrograph of the fracture surface of alloy 318A in the 1h850WQ+2h600WQ condition after impact testing at -196°C. The fracture mode is quasi-cleavage/ductile.

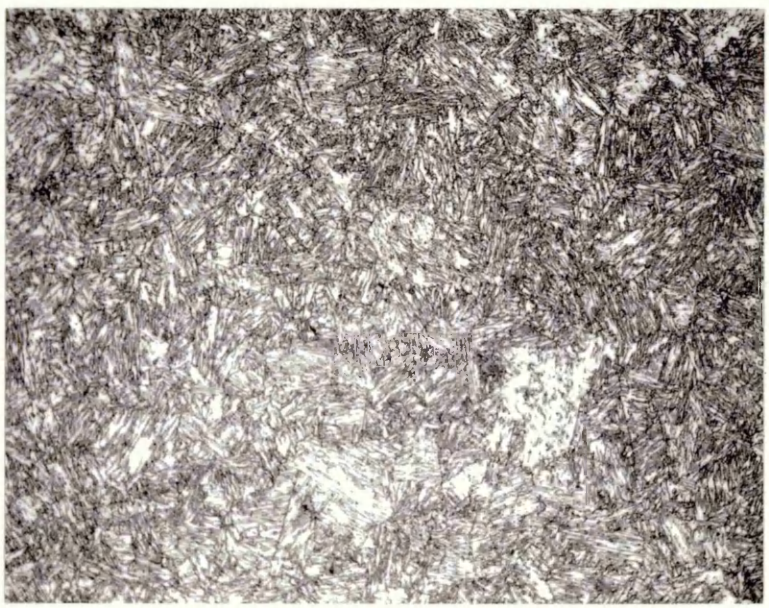

X500

Figure 186 Optical microstructure of alloy 318B in the 1h850WQ+2h600WQ condition showing the typical lath martensite structure.

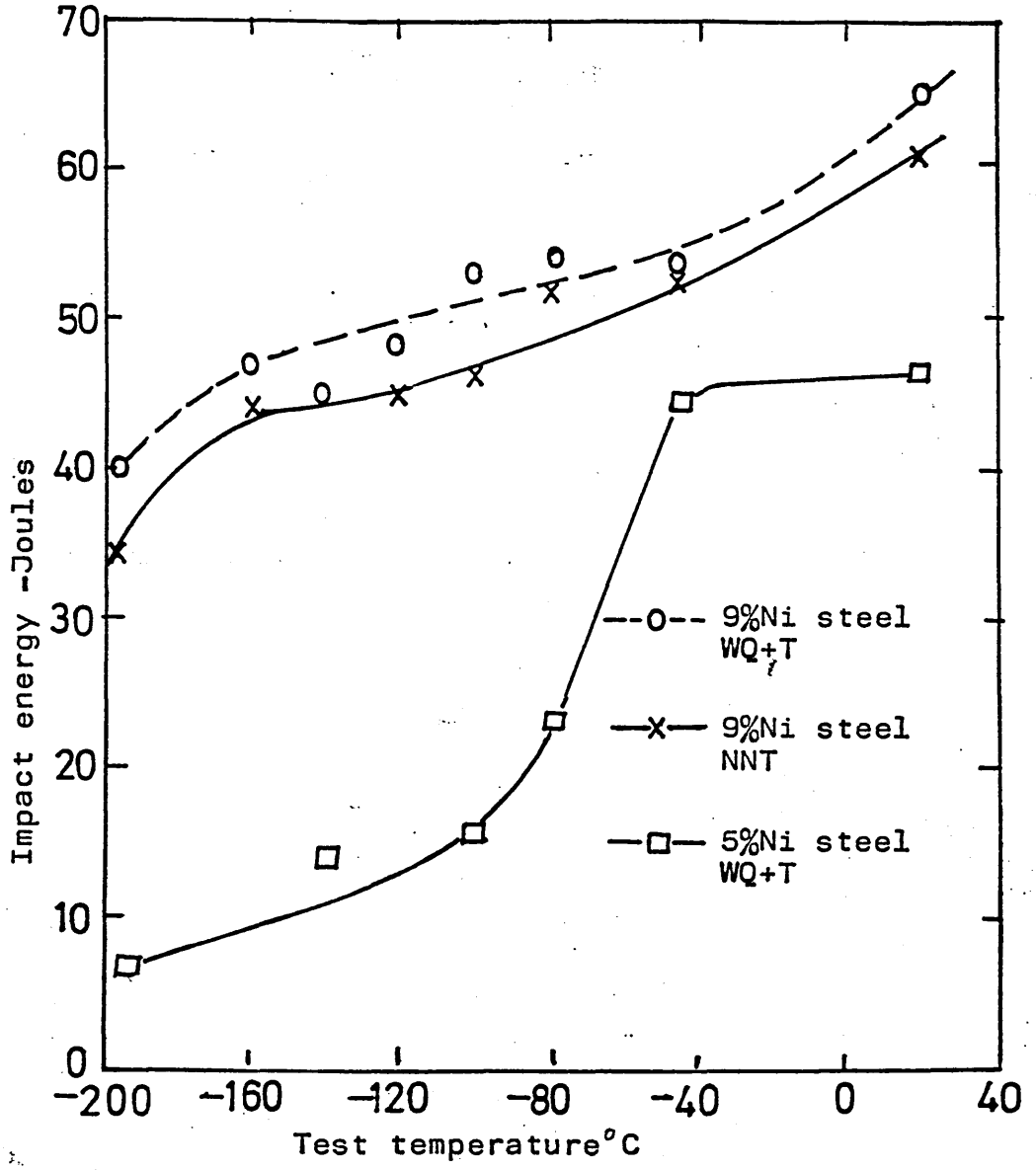

Figure 187 Impact toughness of commercial 9%Ni&5%Ni steels

APPENDIX I

Calculations

(i) Converting Mass Fraction of V into Volume Fraction of Precipitate, f

Using: Density of VC = 5.81 g/ml (assuming stoichimoetric
Density of Fe = 7.9 g/ml VC and not V_4C_3)
Relative atomic mass of V = 50.94
Relative atomic mass of C = 12.01
Mass fraction of V = 0.23%

50.94 grams of V combines with 12.01 grams of C to form 62.95 grams of VC

Therefore 0.23 grams of V forms $\frac{0.23}{50.94}$ x 62.95 grams of VC

Volume fraction of VC, $f = \frac{0.23}{50.94} \times 62.95 \times \frac{5.81}{7.9}$

$= 0.209\%$

Therefore volume fraction = 0.00209

(ii) Substituting into Zener's Equation:

$$D = \frac{8r}{3f}$$

where r = 0.027/2 = 0.0135 microns

The smallest grain size which can be effectively pinned by the dispersion:

$$D = \frac{8 \times 0.0135}{3 \times 0.00209}$$

$= 17.2 \mu m$

Compared to the actual grain size of 12.5μm this is an overestimate as expected.

(iii) Substituting into Gladman's Equation:

The critical particle radius $r^* = \frac{6Rof}{\pi} \left(\frac{3}{2} - \frac{2}{Z}\right)^{-1}$

assuming Z = 2, f = 0.00209, Ro = 6.25μm (12.5/2)

$r^* = 0.05 \mu m$

assuming Z = 1.5, f = 0.00209, Ro = 6.25μm

$r^* = 0.15 \mu m$

The mean precipitate particle size was 0.0135μm radius and so this equation overestimates the precipitate size by a factor of 4 to 11 times.

If we assume the critical particle radius to be our mean particle size of 0.0135μm radius then:

If Z = 2, $\underline{Ro = 1.69 \mu m}$

If Z = 1.5, $\underline{Ro = 0.56 \mu m}$

The actual grain radius was 6.25μm and so the equation underestimates the grain size by a factor of 4 to 11 times.